THE UNIVERSITY OF CHICAGO

A MULTI-WAVELENGTH INVESTIGATION OF YOUNG STELLAR AND PLANETARY SYSTEMS

A DISSERTATION SUBMITTED TO
THE FACULTY OF THE DIVISION OF THE PHYSICAL SCIENCES
IN CANDIDACY FOR THE DEGREE OF
DOCTOR OF PHILOSOPHY

DEPARTMENT OF ASTRONOMY AND ASTROPHYSICS

BY

ADINA DANIELA FEINSTEIN

CHICAGO, ILLINOIS

JUNE 2023

TABLE OF CONTENTS

LIST OF FIGURES

LIST OF TABLES

ACKNOWLEDGMENTS

Thank you to Jacob "J-Ice" Bean for your guidance, support, and trust. When two strong-headed people are put in a room together, there is a $\geq 90\%$ chance it will end poorly. I'm grateful that the outcome in this case was quite the opposite. I will always appreciate our many frank discussions and how you allowed me the freedom to pursue my own interests, even when they were far from your own. Thank you to my committee members Hsiao-Wen Chen, Fred Ciesla, Benjamin Montet, and Brian Nord for sharing your wisdom during our meetings.

Thank you to my entire family - Mom, Dad, Adam, Jeremy, Tali, Laurel, Aunt Thalia, Aunt Susan, Uncle Marty, Gaby, Yoni, and Lindsay - for your love, support, and patience. Thank you to my parents for all that you've done to shape who and get me to where I am today. Thank you to my mom for reading every paper I publish and asking thoughtful questions to gain a better understanding of my passions.

Thank you to Megan M. for being the best office mate and for helping me care for Shmegan (RIP). Thank you to Megan B. for being the best bitch 'n stitch buddy, a constant source of support and encouragement, and so much more that I probably shouldn't write down. Thank you to Celeste for being a constant source of sunshine and encouraging me to keep climbing literally and figuratively. Thank you to Blake, Elyssa, and Josh for hilarious game nights and Super Bowl parties. Everyone in this paragraph has shaped my graduate school experience in the most positive way, and I cannot thank you enough for that.

Thank you to Hsiao-Wen Chen for your endless support and always having time to chat about both science and non-science topics (but mostly non-science). Thank you to Fausto Cattaneo for our virtual and in-person coffee meetings, which always put me in a positive mood for the rest of my day. Thank you to Fred Ciesla for welcoming me into your group, and allowing me to stay even though I rarely contributed anything useful. Thank you to the Bean team - Andreas, Julian, Ben, David, Megan, Rafael, and Madison - for interesting science conversations.

Thank you to Rex and Slinky. You showered me with snuggles throughout not only graduate school but also a global pandemic. I don't know what I would have done without you. Thank you to the Montet family for rescuing Rex and Slinky when they were babies.

Thank you to my wonderful collaborators and friends I've made along the way. I especially want to thank Fred Adams, Eva-Maria Ahrer, Lili Alderson, Megan Andsell, Megan Bedell, Jenny Bergner, Jonathan Brande, Ashley Chontos, Zach Claytor, Louis-Philippe Coulombe, Trevor David, Dan Foreman-Mackey, Oliver Hall, Taylor Hoyt, Gourav Khullar, Rodrigo Luger, Catriona Murray, Michael Radica, Zafar Rustamkulov, Darryl Seligman*, Johanna Teske, and Luis Welbanks. You have all made the ancillary BS of academia worth tolerating. Thank you to all of the mentors who have believed in and gave me the opportunity to pursue my passions: Mady Bernard, Jonathan Lunine, Phil Arras, and Joshua Schlieder.

Thank you to the National Science Foundation Graduate Research Fellowship Program under Grant No. (DGE-1746045) for financial support throughout my Ph.D.

I acknowledge that throughout my graduate studies I have lived and worked on the original homelands and traditional territory of the Kiikaapoi (Kickapoo), Peoria, Kaskaskia, Potawatomi, Ojibwe, Miami, and Očhéthi Šakówi (Sioux) people. I acknowledge my use of telescopes situated on Mauna Kea, in the traditional territory of the Kanaka 'Ōiwi (Hawaiian) people, and on Cerro Pachon, in the traditional territory of the Diaguita people.

ABSTRACT

Intense, high energy stellar irradiation is believed to control the atmospheric mass loss of short-period planets. These effects are most dramatic in the early stages of planetary evolution, when young stars produce higher levels of X-ray and Ultraviolet radiation, and exhibit more short-term high-energy bursts of radiation called stellar flares. Observing how close-in planets react to these environments is key to understanding planetary evolution. In this dissertation, I present four studies of young stellar activity and planetary atmospheres as viewed in UV, optical, and infrared wavelengths.

First, I present a study of stellar flares from five hours of Hubble Space Telescope Cosmic Origins Spectrograph (1070-1360 Å) observations of the ~ 25 Myr M dwarf AU Microscopii (AU Mic). I detect 12 flares in the far-UV "white-light" curve with energies ranging from $10^{29} - 10^{32}$ ergs. To contextualize these observations for AU Mic b and c, I estimate the additional atmospheric mass lost in the presence of flares. I find the atmospheric mass-loss is $\sim 10^8$ g/s, with instantaneous increases by up to 10^12 g/s in the presence of superflares.

Second, I present a study of ground-based optical observations of a transit of V1298 Tau c, a $30 - 40$ Myr super-Neptune planet. I observed a full transit of V1298 Tau c with Gemini-North/GRACES and measure an obliquity of $\lambda = 5^\circ \pm 15^\circ$ via Doppler tomography. The tomographic signal is only seen in the chromospherically driven core of the Ca II IRT, which may be the result of star-planet interactions. I find that excess absorption of the Hα line decreases smoothly during the transit. While this could be a tentative detection of hot gas escaping the planet, I show this variation can also be explained by the presence of surface heterogeneities.

Third, I present a survey of stellar flares in optical/infrared broad-band observations from the *Transiting Exoplanet Survey Satellite* (*TESS*). I developed and applied a novel convolutional neural network of flare detection to 3200 young stars to evaluate flare rates as a function of age and spectral type. I find that flare rates and amplitudes decrease for stars $t_{\rm age} > 50$ Myr across all temperatures $T_{\rm eff} \geq 4000$ K, while stars from $2300 \leq T_{\rm eff} < 4000$ K

show no evolution across 800 Myr. Additionally, I applied this new network to all stars observed during the *TESS* primary mission.

Last, I present the first transmission spectrum of the hot-Saturn WASP-39 b as observed with JWST Near InfaRed Imager and Slitless Spectrograph. The spectrum spans $0.6 - 2.8\mu$m in wavelength and reveals multiple water absorption bands, the potassium resonance doublet, as well as signatures of clouds. I find the atmospheric composition of WASP-39b, favors a heavy element enhancement of $\sim 10 - 30\times$ the solar value, a sub-solar carbon-to-oxygen ratio, and a solar-to-super-solar potassium-to-oxygen ratio. The observations are best explained by wavelength-dependent, non-gray clouds with inhomogeneous coverage of the planet's terminator.

CHAPTER 1

INTRODUCTION

"*It is important to draw wisdom from many different places. If you take it from only one place, it becomes rigid and stale.*"

— Uncle Iroh

1.1 A brief formation history of short-period gas giant planets

Time-series photometric missions such as *Kepler* [64], *K2* [245], and the *Transiting Exoplanet Survey Satellite* [*TESS*; 465] have led to the discovery of over 5,000 exoplanets and 6,000 candidate exoplanets to-date.[1] This informs us that planet formation mechanisms are ubiquitous across the Milky Way galaxy. However, the exact processes that lead to the formation of planets, and in particular gas-rich short-period planets, is not thoroughly understood. There are several open questions about their formation: (I) where did they form within the protoplanetary disk? and (II) how did they end up at short ($< 20\,\mathrm{day}$) orbital periods?

There are two theoretical pathways to forming a short-period gas giant planet. First, the planet could have formed in situ either through gravitational instability [the disk fragments into gravitational bound clumps; 66, 145] or core accretion [a planetary proto-core accretes mass in gas from the local protoplanetary disk; 433, 444, 88]. In situ gravitational instability has been proven infeasible due to the local thermal pressure supporting the material against gravitational collapse close to the host star, where temperatures ad gas surface densities of the inner disk are on the order of $\geq 10^3\,\mathrm{K}$ and $\geq 10^3\,\mathrm{g\,cm^{-2}}$, respectively [392]. Meanwhile, in situ core accretion requires a sufficient amount of material to form a massive core [$\sim 10 M_\oplus$; 437] and have a feeding zone such that the cores can accrete a sufficiently massive atmosphere ($\sim 10 - 300 M_\oplus$). The mass of the core can be defined as

1. NASA Exoplanet Archive, Update 2023 March 1.

$$M_{\rm core} = 2\pi\Sigma_{\rm solids} a \Delta_{R_H}, \tag{1.1}$$

where $\Sigma_{\rm solids}$ is the surface density of solids and Δ_{R_H} is the width of the feeding zone in units of Hill radii [118]. Without replenshing the feeding zone region through material drift and assuming $\Sigma_{\rm solids} \sim 10^3\,{\rm g\,cm^{-2}}$, the core mass growth slows at $\sim 10^{22}\,{\rm kg}$, or comparable to the mass of the Moon. Additionally, these processes are racing against the lifetime of the inner region of the disk [$\lesssim 10\,{\rm Myr}$; 157]. Therefore, it seems unlikely that short-period gas giant planets can form in-situ.

The second leading theory is that gas giant planets form via either a gravitational instability or core accretion farther from the host star ($>{\rm AU}$) and migrate inwards. We can invoke multiple processes which may have resulted in the orbital migration of gas-rich planets to short periods. One such explanation is smooth disk migration, where the recently formed planet creates perturbations in the density profile of the protoplanetary disk [250]. These perturbations can alter the angular momentum of the planet's orbit, resulting in either inward *or* outward migration [45]. A second mechanism could be gravitational scattering by larger planets in the system, which could result in planets on high eccentricity orbits [e; 389]. A third mechanism Kozai-Lidov cycles and tidal friction, which are driven by interactions between the planets and stellar flybys [278, 307, 152] and are likely to affect planets in binary systems or in dense stellar clusters which have sufficient interactions with nearby stars. Each of these mechanisms act on different timescales. Smooth disk migration results in migration timescales of $< 10\,{\rm Myr}$, when the disk is still present and sufficiently massive [292], while Kozai-Lidov cycles act on timescales of

$$\tau \approx P_{\rm planet} \frac{M_\star}{M_{\rm pert}} \left(\frac{a_{\rm pert}}{a_{\rm planet}}\right)^3 (1-e_{\rm pert})^{3/2}, \tag{1.2}$$

where $P_{\rm planet}$ is the orbital period of the planet, $a_{\rm planet}$ is the semi-major axis, $M_\star$ is the mass of the host star, $M_{\rm pert}$ is the mass of the perturbing body, and $a_{\rm pert}$ and $e_{\rm pert}$ are the

semi-major axis, a, and e of the perturbing body around the host star [240]. Depending on the orbital parameters of the planet and perturbing body, τ could be on the order of tens or thousands of millions of years. The resulting e of the orbit can be a hint towards which type of migration processes the gas-giant planet underwent as well.

Theoretically, the atmospheric composition of a gas giant planet could provide context for where the planet formed with respect to its host star. As one moves farther out in the protoplanetary disk, the temperature decreases. The drastic temperature differences will therefore dictate what molecular species exist in the gas state, which feed the atmosphere, and which have frozen out onto grains. One means of doing this is by measuring the carbon-to-oxygen ratio (C/O) of the atmosphere [404].

The C/O can be derived from measurements of CO, CO_2, CH_4, and H_2O. The presence, or lack thereof, provides context for where the planet formed with respect to the H_2O, CO and CO_2 snowlines. Gas-rich planets ($R/R_\oplus \geq 4$) that formed beyond the aforementioned snowlines and subsequently migrated inwards *after* the disk dissipates will have elevated C/O (> 0.8) and low metal enrichment. Meanwhile, gas-rich planets which form in similar locations, yet migrate *within* the disk should have lower C/O (< 0.5) and more metal enrichment [404]. Planets at large orbital separations (e.g. HR 8799; $a > 20$ AU) that may have formed in situ via gravitational instability will have C/O dependent on their formation location [341].

The C/O of gas giant atmospheres has been measured for ~ 30 short-period planets that are transiting via transmission spectroscopy. Measuring the C/O of planets via observations of both transits and eclipses have been enabled by the infrared wavelength coverage of the *Hubble* and *Spitzer* Space Telescopes, which cover a breadth of broad H_2O and CO_2 absorption features (see Table 2 in Hoch et al. [238] for a summary of C/O measurements through 2022). The majority of short-period gas giant planets discovered to-date are either old (> 1 Gyr) or have unconstrained ages [57]. Therefore, their atmospheres likely underwent significant chemical processing or contamination from cometary bombardment [502], making

them no longer reliable tracers of their initial formation conditions. However, we can leverage the fact that we can measure the ages of stars [see review by 515], and by proxy their planets. By identifying and characterizing planets around stars of known young ages, we can begin to piece together a more complete picture of planet formation and evolution.

1.2 A foothold into planetary evolution: The discovery of planets younger than 100 Myr

Kepler, *K2*, and *TESS* have each enabled the discovery of thousands of transiting exoplanets. The transit depth of a planet is related to $d = (R_p/R_\star)^2$. Therefore, these observatories have the capabilities to observe hours-long parts-per-million transit depths in light curves. Automated pipelines [e.g. SPOC; 256, 257] have developed extensive techniques to generate light curves and provide diagnostic products to validate potential transiting exoplanet candidates. These pipelines have a successful track-record of detecting a plethora of planet candidates with transit depths ranging from $20 - 5000$ ppm, and up through eclipsing binaries. Unfortunately, these pipelines are limited to successfully identifying candidates when the host star is relatively quiet (i.e. the noise is dominated by either systematics of photometric limitations). Young stars (< 500 Myr) are anything but quiet, making them particularly challenging targets to detect transiting exoplanets around.

Figure 1.1 provides an example what a young stellar light curve looks like. This light curve is for the 23 Myr M dwarf AU Mic, which hosts two confirmed exoplanets [440, 359]. The full light curve exhibits $\sim 5\,\%$ variability on 4.86 day timescales [440], which originates from starspots rotating in and out of our line of sight. The structure and amplitude of the variability is also seen to evolve on longer timescales. On top of this, there are short-duration high-energy events known as stellar flares (marked in red). The transits of AU Mic b and c are marked by blue and orange vertical lines, and zoom-ins of one transit of each is presented in the bottom of Figure 1.1. The planets have radii of 4.2 and $3.24 R_\oplus$, respectively. Even

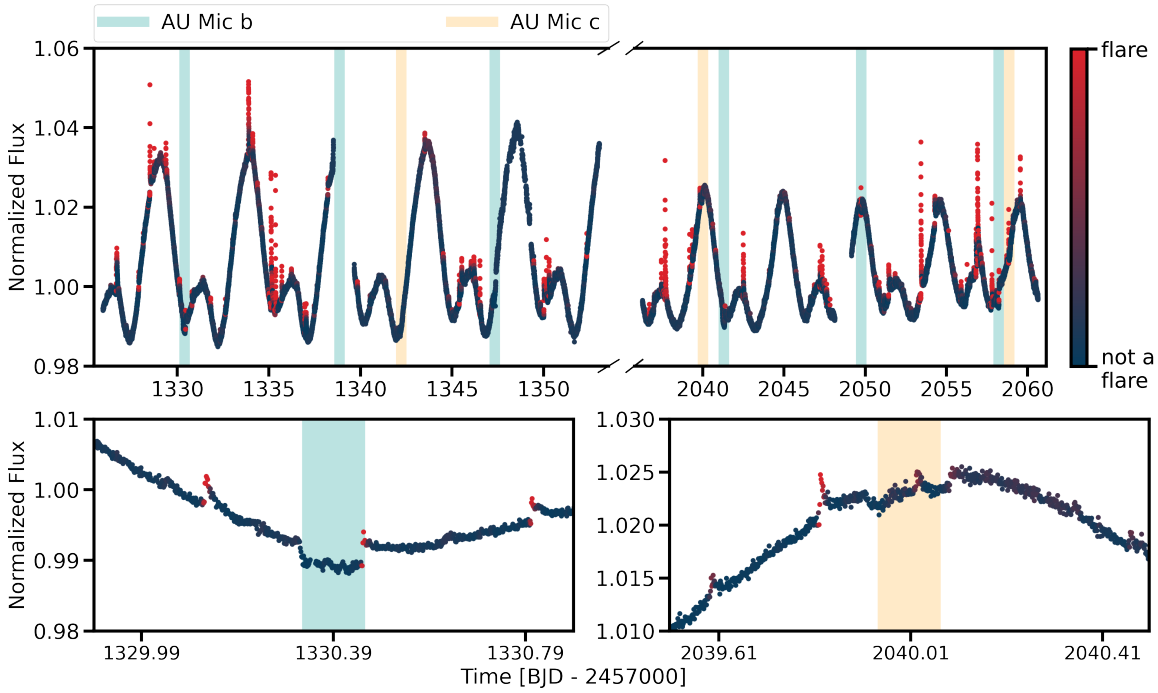

Figure 1.1 An example light curve from *TESS* highlighting the challenges associated with discovery transiting planets around young stars. The top panel presents the *TESS* observations of AU Mic, a 23 Myr system with two confirmed transiting exoplanets [440, 359], from Sectors 1 and 27. Points are colored by if they are a flare (red) or not a flare (dark blue). The 4% modulation seen in the light curve is due to variations in the starspot coverage and configuration between the two stellar hemispheres. The two bottom panels highlight individual transits of AU Mic b (left; teal) and c (right; orange). The transit depths $< 0.5\%$ and can occur simultaneously with flares.

zooming-in on the transits, the signal is overwhelmed by the stellar variability and, for these examples, flares even occur *during* the transits. Therefore, detecting transiting exoplanets around active young stars has been a challenge for the community to overcome.

In order to detect these young transiting exoplanets, we needed two advancements in the field: (I) a reliable and efficient way to model and remove the stellar variability and (II) a large enough sample of young stellar light curves to search. To identify transiting exoplanets orbiting young active stars, time-series modeling of the stellar variability, often referred to as "de-trending" must be implemented. Developing pipelines which automatically and accurately detrend light curves is necessary for the vast amount of light curves *Kepler*

and *TESS* have provided the community. Common detrending algorithms include sliding medians [e.g. 93, 75, 513], sliding means [574, 372], polynomial filters [e.g. 194], and splines [e.g. 553, 351, 316]. Each detrending technique has its strengths and weaknesses and the field has yet to settle on the "best" one which should be used to identify transiting exoplanets in young light curves [a full review and comparison of detrending algorithms can be found in 236]. These methods can be computationally expensive to implement depending on the complexity of the algorithm. Additionally, if the de-trending method is too flexible, it can easily model and remove the transit signal itself. Therefore, the de-trending method on each young active light curve likely needs to be tuned to that specific target, and is likely to be a function of the stellar rotation period [553].

The next challenge becomes the sample of stars. *Kepler* was designed to stare at a patch of sky for a long period of time to determine the percentage of exoplanets that are in or near the habitable zone of a range of spectral types [65]. The majority of these targets were main sequence, or quiet, host stars out of the ecliptic plane. After two of *Kepler*'s reaction wheels broke, the mission was repurposed as *K2*, whose field-of-view was limited to along the ecliptic plane due to the stabilizing torque required by the solar wind pressure to keep the spacecraft pointing stable (enough). For the first time, *K2* successfully monitored stars in young stellar clusters along the ecliptic such as the Taurus-Auriga [$1-2\,\mathrm{Myr}$; 268], Upper Scorpius [$10\pm3\,\mathrm{Myr}$; 431], Pleiades [$112\pm5\,\mathrm{Myr}$; 110], and Hyades [$750\pm100\,\mathrm{Myr}$; 71] stellar associations and clusters, enabling the first detections of young transiting exoplanets. On the other hand, *TESS* was designed to observe $\sim 95\%$ of the entire sky, resulting in tens of thousands of young stars being monitored over its current mission lifetime of 6 years.

The first young transiting exoplanet discovered was K2-33 b [orange triangle in Figure 1.2; 116, 351]. K2-33 b is a $5.04R_{\oplus}$ sized planet on a 5.42 day orbital period. The host star, K2-33, is a type M3.3 star with a rotation period of 6.3 days. K2-33 is an established member of the Upper Scorpius OB association, with an approximate age of $5-10\,\mathrm{Myr}$ [451, 450]. K2-33 b was initially discovered and confirmed from *K2* observations from Campaign 2 (23

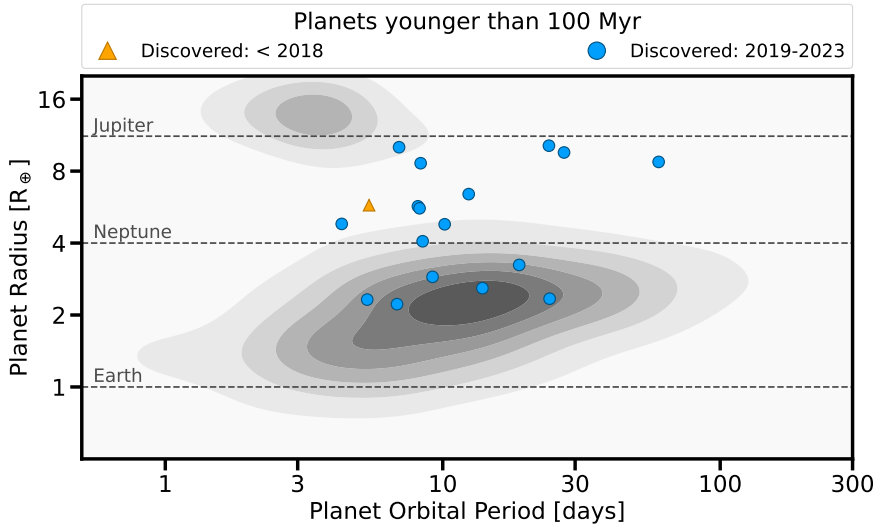

Figure 1.2 Periods and radii of young transiting exoplanets in the context of the older population, highlighting the rarity of planets younger than 100 Myr (points). Triangles represent planets confirmed prior to 2018; circles represent planets confirmed between 2019 – 2023. Over the course of this thesis, the population of young planets discovered has increased from 2 to 18, unlocking a new potential to observe planets shortly after they finished forming.

Aug 2014 - 13 Nov 2014). The discovery of this uniquely young planet opened the doors to future detections of young transiting exoplanets.

Since then, over a dozen more young planets have been discovered both in archival *Kepler* and *K2* data, as well as new *TESS* observations (blue circles in Figure 1.2). These new young candidates orbit high probability members of nearby moving groups and associations [116, 351, 353, 581] or field stars whose ages could be determined photometrically and spectroscopically [117, 115, 397, 440, 469, 79, 359, 67]. For the first time, we have the opportunity to study planets as a function of age and system properties to observe footprints of planetary formation and evolution in real time, enabling us to answer questions about the formation and migration mechanisms fueling the population of short-period gas giant planets.

1.2.1 Young exoplanet atmospheric compositions

Unknown. There have been no confident detections of a young exoplanet atmosphere, nonetheless an understanding its composition.

In theory, transmission spectroscopy, or observing a transit of a planet at different wavelengths to build a spectrum of the atmosphere [499], should be easier for these young planets, as these planets are inflated, and the expected signals are inversely correlated with planetary gravity [121]. However, the inhomogeneities on the stellar surface prove challenging to disentangle from planetary signatures. Both occulted and unocculted active regions can heavily impact the detectability and reliability of planetary transmission spectra [455, 456].

Surface features lead to multiple challenges in planetary data sets for a variety of reasons. Active regions will change along our line of sight given the stellar rotation period. For young stars, these rotation periods can be on the order of < 20 days [108], leading to strong changes over short timescales. Second, active regions have different temperatures from the disk-averaged photosphere (e.g. starspots are colder, while faculae are warmer). This can result in different molecular features present from the star at any given time. Some molecular features which may originate from the star could be H_2O [577], TiO [391], and others [56]. These are all species which could exist in a planetary atmosphere as well.

1.3 A stellar renaissance thanks to exoplanet missions

Large transiting exoplanet surveys are ultimately observing one thing: stars. Through the success of *Kepler* and *TESS*, the community has not only discovered thousands of transiting exoplanets, it has revived the field of stellar astrophysics. Through long term monitoring of a large sample of stars, insights into stellar rotation periods [366] and insights into stellar dynamos [461] have all been achieved in just over a decade. In addition to the aforementioned advancements, we have also begun to further understand phenomenon known as stellar flares.

1.3.1 Stellar flares: What are they and what can they teach us?

The magnetic field of the Sun is believed to be generated by the dynamo, which is located at the interface between the radiative core and convective exterior. Magnetic reconnection provides the energy to accelerate proton and electron beams in the stellar atmosphere and eject stellar plasmas, which result in flare radiation emission and coronal mass ejections (CMEs). Stellar flares are associated with impulsive reconnection events [55], and are often short-lived (lasting seconds to minutes), highly-energetic events. Flares and CMEs are easily observed on the Sun. For other stars, it is assumed that their dynamos are generated similarly, and thus stellar flares are readily observed. There are several geometric configurations which could result in an impulsive flare event. For an example, reconnection events could be the result of emerging flux loops colliding [25], shearing in the stellar corona resulting in field lines being twisted due to different rotational speeds [55], braided field lines [423], or, for young stars specifically, magnetic interactions between the stellar and circumstellar disk field lines [514].

We cannot resolve stellar flares and associated CMEs on other stars. Therefore, we rely on light curve analyses to understand the morphogology and behavior of flare events. Fortunately, stellar flares exhibit a characteristic behavior in a given light curve: a sharp impulsive rise and exponential decay, which is a similar behavior to what is seen on the Sun [e.g. 112]. From this, we can extract information about how long the flare event lasted and the energy produced during the flare, following

$$E = 4\pi d \int_{t_0}^{t_1} \left[(F_f(\tau) - F_q(\tau) \right] d\tau, \tag{1.3}$$

where d is the distance to the star, F_f is the flux during the flare event, F_q is the flux in quiescence, and t_0 and t_1 are the start and end times of the flare event. These two parameters, along with the shape of the flare decay, allow us to understand the flare frequency distributions (FFDs) of stars and help us gain insight into the flare formation mechanisms

of our own Sun.

Adding an extra dimension of observing flares at different wavelengths provides information about how the event propagates through the stellar atmosphere. By observing flares in the X-ray through the near-Infrared (NIR), we gain insights into flare behavior from the corona down to the stellar photosphere. This is enabled by the different formation temperatures of emission lines seen across the electromagnetic spectrum. Some of the first large flare studies were completed in the X-ray and extreme Ultraviolet (EUV) and far UV (FUV). As an example, the Ultraviolet Spectral Characteristics of Low-mass Exoplanetary Systems (MUSCLES) Treasury Survey is a program designed to observe exoplanet host stars in the X-ray and UV to understand their local stellar environments [184]. As a consequence of this monitoring, flares have been identified on both active and inactive M dwarfs [325]. These observations looked at the overall differences in the FFD on each subgroup of M dwarf, and additionally studied the morphology and frequency of the flares in different emission lines. [325] demonstrated there were different slopes in the FFD depending on which emission line was being studied, with a shallower slope in the N V doublet at 1240 Å and a steeper slope in the Si IV doublet at 1400 Å. This indicates different responses of emission from different species to the same event, and hints at a relationship between FFD slope and line formation temperature. However, this study was completed for a relatively small sample of 20 flares across 6 stars. UV campaigns have also been dedicated to understanding the evolution of UV flares and flare rates as a function of stellar age. The HAbitable Zones and M dwarf Activity across Time (HAZMAT) program detected 18 flares on a 40 Myr M dwarf in the Tucana-Horologium association, all with energies $> 10^{30}$ erg [328]. The most energetic flare in the sample ($10^{32.1}$ erg) was accompanied by $15,500 \pm 400$ K blackbody emission, which emitted 18% of its flux in the FUV ($912 - 1700$ Å). This could be harmful to planetary atmospheres.

1.3.2 Large surveys of stellar flares from Kepler, K2, and TESS

More recently, the advent and success of missions such as *Kepler*, K2, and *TESS* have allowed for detailed studies of stellar flare properties as a function of both spectral type and age [114, 225]. [112] identified $\sim 850,000$ flare events across 4,000 stars observed during the primary 4-year *Kepler* mission. From these data, a potential saturation in flare rates was identified as a function of Rossby number, which relates the stellar rotation period and mass. However, the flare catalog of [112] was later noted to be significantly contaminated with other sources of variability [113].

A large number of studies have been completed to specifically understand super flares on solar-like stars using *Kepler* data. [343] analyzed the *Kepler* 1-minute light curves from 120 days of observations and identified 187 superflares on 23 solar-type stars, with energies ranging from $10^{32} - 10^{36}$ erg. For reference, the most energetic flare seen on the Sun was the Carrington event in 1859, which had an energy of $\sim 10^{32}$ erg [80]. [507] expanded this study to analyze 500 days of *Kepler* observations of solar-type stars. They identified 1,547 superflares on 279 G dwarfs, suggesting that superflares with energies $E = 10^{34} - 10^{35}$ erg on solar-type stars occur once in $800 - 5,000$ years, while the most active star in the sample released a superflare every 100 days.

As mentioned in Section 1.2, *K2* allowed for the opportunity to observe stellar clusters of different ages, allowing for an understanding of how flare rates and energies evolve as a function of spectral type. In a series of papers, flare rates were measured in the Pleiades (125 Myr), Hyades (690 Myr), Praesepe (750 Myr), Ruprecht 147 (2.6 Gyr), and M67 (3.6 Gyr) stellar clusters. [251] analyzed the light curves of 1,761 late-K to mid-M dwarfs and identified 751 flare candidates with energies from $10^{32} - 10^{34}$ erg. Of the total number of flares observed, 80% were identified on stars in the Pleiades, and none were observed from M67 stars. [251] identified that the FFD for stars in the Pleiades and Praesepe had similar slopes, suggesting similar flare generation processes. In a follow-up study, [253] analyzed light curves of 2,111 cluster members, and added Hyades and Ruprecht 147 cluster members

to their sample. A total of 3,844 flares were identified across the entire sample. The flare rates were seen to decline with age, and decline faster for higher mass stars. Additionally, they identified a rapid decline in flare rates for M1-M2 dwarfs between Hyades and Praesepe members. The challenge associated with analyzing flares in *K2* data is the cadence of the observations. Data were taken every 30 minutes, which is insufficient for sampling the entirety of the flare and bias results towards only observing the highest energy flares.

Due to the novelty of the *TESS* data, fewer studies have been completed analyzing flare rates and energies thus far. [216] lead the first analysis of flares from 24,809 stars observed in *TESS* Sectors 1 and 2. The stars were observed with a cadence of 2-minutes, which significantly improves the identification and resulting energies of the flares compared to *K2* observations [242]. [216] found that 40% of mid to late M dwarfs released at one flare during the observations, and the fraction of flare stars drops to 10% for early M dwarfs. This could be related to the change in interior structure at M4 dwarfs, where they become fully convective [503]. Similarly to flare searches in *Kepler* observations, [548] completed a designated search of superflares from solar-type stars in *TESS* data. This analysis observed 1,216 superflares on 400 solar-type stars ($\sim$ 2% of the entire sample of stars). The FFD observed with *TESS* is similar to that of *Kepler*. Neither study discussed the ages of the stars analyzed.

1.4 Chapter Summaries

The remainder of the thesis is laid out as follows.

Chapter 2 reports the *Hubble Space Telescope* observations of the 23 Myr active M dwarf AU Mic. The data presented are from over 5 hours of far-ultraviolet observations of AU Mic with the Cosmic Origins Spectrograph (COS; $1070 - 1360$ Å). Over the observations, 13 flares with energies ranging from 10^{29-31} erg s^{-1} occurred, yielding an intense FUV flare rate of 2.5 flares hour^{-1}. These energies and rate are used as priors to understanding the contributions of flares to atmospheric mass-loss to AU Mic b, the innermost planet of the

system. Additionally, I present a novel spectral energy distribution (SED) of AU Mic using these and archival observations ranging from the X-ray to the infrared. The SED is used to model accurate transmission spectra of AU Mic b and c to inform future *JWST* observations.

Chapter 3 reports Gemini-N/GRACES observations of a transit of V1298 Tau c, a $30-40$ Myr, $5.59 R_{\oplus}$ planet orbiting a young K0-K1.5 solar analog. Through this campaign, I report the projected obliquity of V1298 Tau c ($\lambda = 5^{\circ} \pm 15^{\circ}$), suggesting the planet is aligned with the stellar spin axis. The obliquity could only be measured through the Ca II triplet, which may be the result of star-planet interactions. Additionally, there is an excess in Hα absorption that appears to be decreasing smoothly with the transit. This signature could be the result of an extended hydrogen atmosphere around V1298 Tau c, or contamination from stellar surface inhomogeneities.

Chapter 4 presents a novel convolutional neural network (CNN), `stella`, developed to accurately and efficiently detect stellar flares in *TESS* 2-minute data. The CNN takes $1-2$ seconds to identify flares on a single light curve. We applied the network to observations of 3,200 young stars in order to evaluate flare rates as a function of age and spectral type. There is a noticeable decrease in flare rates and amplitudes for stars $t_{\rm age} > 50$ Myr and $T_{\rm eff} \geq 4,000$ K, while stars from $2,300 \leq T_{\rm eff} \leq 4,000$ K show no evolution across 800 Myr. The rotation periods for 1,500 stars in the sample were measured as well. It is noted that there was no phase dependence of where flares occurred with respect to the rotation, suggesting the projected filling factor of stellar active regions remains relatively constant as seen from our viewing location.

Chapter 5 reports the application of `stella` to $\sim 200,000$ stars observed at 2-minute cadence from the *TESS* primary mission. With this data, I test if stellar coronal magnetic fields maintain themselves in a critical state via a delicate balance between the dynamo-driven injection of magnetic energy and the release of that energy via flaring events. A total of $\sim 10^6$ flares were observed in the entire data set. By fitting the FFDs for different mass bins, I find that all main-sequence stars exhibit distributions of flaring events similar

to that observed in the Sun, independent of their mass or age. This may suggest that stars universally maintain a critical state in their coronal topologies via magnetic reconnection events. If this interpretation proves correct, we may be able to infer properties of magnetic fields, interior structure, and dynamo mechanisms for stars that are otherwise unresolved point sources.

Chapter 6 reports the atmospheric characterization of the hot-Saturn WASP-39 b with the *JWST* Near Infrared Imager and Slitless Spectrograph (NIRISS; $0.8 - 2.8\mu$m). These observations reveal multiple water absorption bands, the potassium resonance doublet, as well as signatures of inhomogeneous cloud coverage around the planetary terminator. The precision and broad wavelength coverage of the Near Infrared Imaged and Slitless Spectrograph (NIRISS) with the Single Object Slitless Spectroscopy (SOSS) mode allows us to break model degeneracies between cloud properties and the atmospheric composition of WASP-39 b, favoring a heavy element enhancement ($\sim 10 - 30\times$ solar "metallicity"), a sub-solar carbon-to-oxygen ratio (C/O), and a solar-to-super-solar potassium-to-oxygen ratio (K/O). These observations were executed as part of the *JWST* Early Release Science Program (PI Batalha).

Chapter 7 concludes.

CHAPTER 2

AU MICROSCOPII IN THE FUV: OBSERVATIONS IN QUIESCENCE, DURING FLARES, AND IMPLICATIONS FOR AU MIC B AND C

"It's just as I only now began to fear!"

— Professor H.J. Farnsworth

Magnetic reconnection provides the energy to accelerate proton and electron beams in the stellar atmosphere and eject stellar plasmas, which result in flare radiation emission and coronal mass ejections (CMEs).[1] Decades of multiwavelength observations of solar and stellar flares, from particularly active stars like AD Leo, have provided insights into the underlying magnetic reconnection and plasma mechanisms driving these explosive events [73, 442, 340, 364, 226, 448, 20, 26, 229, 411, 558, 593]. While multiwavelength observational campaigns of flares have been ongoing for decades [229, 411], the more recent development of exoplanet atmospheric science has led to a resurgence of these campaigns for exoplanet host stars [338]. While photometric surveys like Kepler [65] and all-sky surveys like the Transiting Exoplanet Survey Satellite [TESS; 465] provided crucial insight into the frequency of flares as a function of spectral type [401, 114, 343, 325, 216, 241, 164], age [251, 162, 253], and rotation period [138, 137, 136, 243, 503], detailed spectroscopic studies of stellar flares connect broad-band observations to those observed from the Sun.

Observations of individual stars with the Extreme Ultraviolet Explorer (EUVE) provided the first EUV flare observations of other stars. This allowed for the opportunity to compare these events with the behavior of the solar corona. [228] observed two flares from the active M3 dwarf AD Leo simultaneously in optical wavelengths. These data combined with contemporaneous X-ray observations provided strong evidence of the Neupert effect

1. This work is based on [167], which was co-authored by Kevin France, Allison Youngblood, Girish M. Duvvuri, D.J. Teal, P. Wilson Cauley, Darryl Z. Seligman, Eric Gaidos, Eliza M.-R. Kempton, Jacob L. Bean, Hannah Diamond-Lowe, Elisabeth Newton, Sivan Ginzburg, Peter Plavchan, Peter Gao, and Hilke Schlichting. A. Feinstein reduced and analyzed the data presented in this chapter, created the UV flare profile described in Section 2.2.1, and reduced all archival observations to create the SED of AU Mic. P. Wilson Cauley is the PI of the *HST* program GO-16164 which obtained the observations of AU Mic. G. Duvvuri created the DEM model used to estimate the EUV flux of AU Mic in Section 2.3.6. D.J. Teal and E. Kempton generated the 1D atmospheric models of AU Mic b and c in Section 2.4.2. K. France, A. Youngblood, E. Gaidos, P. Gao, S. Ginzburg, E. Newton, P. Plavchan, and H. Schlichting are co-Is on *HST* program GO-16164. All other co-authors provided valuable feedback to improve the quality of the manuscript.

[393, 126], a model of chromospheric evaporation. They also provided evidence that stellar corona are heated via similar mechanisms believed to be operating in the corona of the Sun. [28] completed a two-week long observational campaign with the EUVE of the young solar analogues 47 Cas and EK Dra. They measured quiescent emission that was 2-3 orders of magnitude greater than that of the Sun, with average plasma temperatures in the corona of $20 - 30 \times 10^6$ K. They reported flares with energies of $3 \times 10^{33} - 6 \times 10^{34}$ ergs, which are $1 - 2$ orders of magnitude *more* energetic than the historic Carrington super-flare event on the Sun [80].

Observations from the Measurements of the Ultraviolet Spectral Characteristics of Low-mass Exoplanetary Systems (MUSCLES) survey [184] demonstrated that the baseline FUV/NUV luminosity increases by a factor of $\sim 100\times$ from early K to late M dwarfs. Additionally, even optically inactive M dwarfs exhibit frequent flares in their UV light curves based on the strength of Hα and Ca II [183, 327, 128]. A detailed analysis of flares from both inactive and active M dwarfs from the MUSCLES survey was presented by [328]. This study of Hubble Space Telescope (HST) Cosmic Origins Spectrograph (COS)/Space Telescope Imaging Spectrograph (STIS) light curves revealed that the flares from active stars are an order of magnitude more energetic than inactive stars, but both exhibit the same flare frequency distributions [328, 325], where active stars were defined by a Ca II H & K equivalent width (EW) > 10 Å and inactive stars had EW< 2 Å.

Time-series photometric missions such as Kepler and TESS led to the discovery of $>$ 5000 exoplanets.[2] However, only a small hand-full of these planets are < 100 Myr [116, 351, 115, 117, 50, 397, 352, 469, 79, 359, 353, 67]. Time-series observations in the X-ray/FUV of these host stars have provided insight into the effect of young stellar irradiation on exoplanet atmospheres and may quantify the relative importance of photoevaporation and core-powered mass loss for super-Earths and sub-Neptunes [321, 415, 201, 218, 326, 476].

AU Microscopii (AU Mic) has been the target of extensive observations over the past

2. NASA Exoplanet Archive, Update 2022 April 5.

decade because of its close proximity [9.72 ± 0.04 pc, 192, 440], youth [22 ± 3 Myr, 348], and circumstellar debris disk [263, 314, 315, 368, 29, 173, 439]. Two transiting exoplanets orbiting interior to the debris disk were reported recently [440, 359, 198]. As an M dwarf, AU Mic may provide crucial insights into planetary formation and atmospheric evolution around the most common stellar type in the galaxy [234].

Recent observational and theoretical investigations of AU Mic have constrained its stellar properties that affect the evolution of the short-period planets, including the magnetic field strength, high energy luminosity [106], and flare rate. [273] obtained optical spectroscopic and spectropolarimetric observations to characterize at small and global scales. Zeeman broadening and intensification analysis of Y- and K-band atomic lines yielded a mean field of $\langle B \rangle = 2.2\,\mathrm{kG}$. Preliminary Zeeman-Doppler imaging revealed a potential weak, non-axisymmetric magnetic field configuration, with a surface-averaged strength of $\langle B_z \rangle = 88\,\mathrm{G}$ [273]. This is double the magnetic field strength of $\langle B_z \rangle = 46\,\mathrm{G}$ presented in [359]. A search for long-term activity cycles in the photosphere of AU Mic revealed a possible stellar cycle length of $40 - 42$ years, with average brightness changes of $\Delta V = 0.2\,\mathrm{mag}$ [63].

The EUVE satellite was used to observe multiple flares on AU Mic in 1992. [107] observed two flares with energies $E_{EUV} = 2 \times 10^{33}$ and 3×10^{34} ergs at 65-190 Å with estimated temperatures of 3×10^7 K. Spectroscopic investigations of these flares revealed that the temporal evoluton of Fe XX-XXIV was similar to the photometric light curve. This demonstrated that the hot plasma ($\sim 10^7$ K) may have experienced rapid expansion and adiabatic cooling [140]. The existence of these Fe lines also constrained the differential emission measurement (DEM) models at temperatures between $10^6 - 10^8$ K [373]. Modeling the DEM during different phases of the flares revealed a high-temperature component during the entire event and subsequent decay, with shifts towards higher temperatures at the peak [374].

[460] conducted a survey of late-type dwarfs with Far Ultraviolet Spectroscopic Explorer (FUSE) in which AU Mic was observed flaring twice. Flaring was observed by FUSE in the FUV continuum and in several emission lines including C II at 1036 Å, C III at 977 and

1175 Å, and O VI at 1032 Å, which trace formation temperatures from $4.74 \leq \log(T[\mathrm{K}]) \leq 5.45$. The continuum fluxes were fit with a $\log(T[\mathrm{K}]) \sim 8.0$ thermal bremsstrahlung profile, in contrast to the blackbody profile more typically used to interpret M dwarf flares at NUV wavelengths [277].

The stellar activity of AU Mic specifically has been characterized recently. The system was also observed in two sectors of TESS data, resulting in two $\sim$ 27 day light curves separated by $\sim$ 1 year. Gilbert et al. [198] reported an average flare rate of $\sim$ 2 flares per day with a slight increase in activity after one year. [557] recently conducted an investigation of coronal dimming from coronal mass ejections (CMEs) following flares on AU Mic with archival XMM-Newton observations. Statistically significant dimming events were seen following three flares in the sample.

The activity of AU Mic provides variable and harsh environments for its planets. [17] modeled the space-weather experienced by AU Mic b & c in the presence of stellar winds and CMEs. These simulations indicate that AU Mic b & c reside inside the sub-Alfvénic region of the stellar wind, with average pressures of $10^2 - 10^4\times$ the average value experienced by Earth. [17] presented simulations of extreme CMEs in the system with global radial speeds $\sim 5 \times 10^3 - 10^4\,\mathrm{km\ s^{-1}}$, mass of $\sim 2 \times 10^{18}\,\mathrm{g}$, and kinetic energies between $10^{35-36}\,\mathrm{erg}$. The CMEs increased the dynamical pressure felt by the planets by $4 - 6$ orders of magnitude with respect to the steady-state, and could temporarily shift the planetary conditions from sub- to super-Alfvénic.

In this paper, we present time-series observations of AU Mic with the Hubble Space Telescope (HST) Cosmic Origins Spectrograph (COS) to characterize its flare and quiescent emission in the FUV. This paper is organized as follows. In Section 3.1, we describe the observations, the creation of light curves, and the identification of flares and spectral emission features. We then describe the properties and morphologies of the flares in Section 4.2. We also describe variations of emission line profiles and provide measurements of the continuum flux both in quiescence and during flares. In Section 2.3, we provide a panchromatic spec-

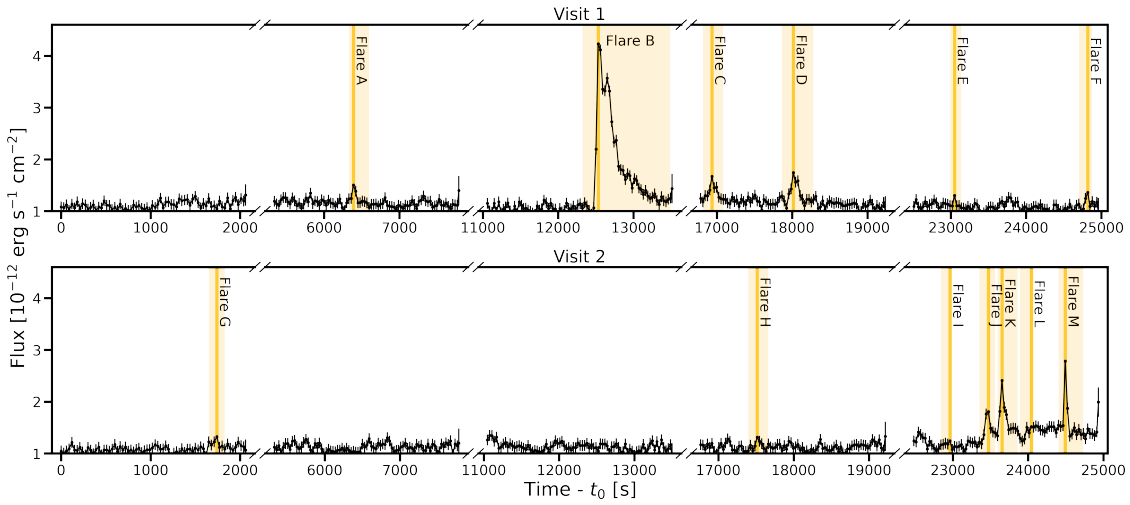

Figure 2.1 Flux-calibrated light curves from two HST/COS visits to AU Mic across the entire wavelength coverage (1064 − 1361 Å). Time of peak flare events are marked with a vertical orange lines. Highlighted yellow regions are excised for the creation of a clean out-of-flare template spectrum. A total of 13 flares were identified, with one double-peaked flare identified in the third orbit of Visit 1 (Flare B) and 5 flares present in the last orbit of Visit 2 (Flares H-L). We present the parameters for each flare in Table 2.1.

trum of AU Mic using a combination of models, and current and archival observations. In Section 2.4, we model the atmospheric mass-loss for AU Mic b and atmospheric retrievals for AU Mic b & c with these new FUV observations. We search for evidence of coronal dimming and an affiliated proton beam during the most energetic flare in our sample in Section 2.5. In Section 4.5, we summarize our results and advocate for future X-ray/FUV observations of flares and JWST observations of AU Mic b & c.

2.1 Observations & Reduction

We observed AU Mic over two visits with HST/COS under GO program 16164 (PI Cauley). We used the COS G130M grating centered at 1222 Å for both visits with $R \sim 12,000 - 17,000$, following the instrumental configuration used in [188]. This configuration provides coverage from approximately 1060-1360 Å with a detector gap from 1210-1225 Å, masking the bright Ly-α emission feature to avoid detector saturation. The same COS setting was

used for both visits. The visits were executed on 2021 May 28 and 2021 September 23 during transit events of AU Mic b. The transits of AU Mic b are a separate ongoing analysis and do not impact the flare results presented here. We note the reference start time for Visit 1 is MJD = 59362.148; the reference start time for Visit 2 is MJD = 59480.629.

2.1.1 Light Curve Creation

AU Mic is well known to be active, with flares observed in the far UV [460] and the optical with TESS broadband photometry [198]. We produced light curves using the `time-tag` markers available in our HST/COS output files. This mode documents every photon event as a function of time and wavelength, allowing for time-series spectra to be extracted.

In order to categorize the observational data into time bins, we used `costools`[3], which is a set of tools for HST/COS data reduction. The `costools.splittag.splittag` routine creates time-separated `corrtag` files for a given number of input seconds. For the primary data reduction, we binned the observations into 30 second exposures. It has been previously established by several sets of authors that the time-resolution can impact measured flare amplitudes and energies [242, 309]. We chose to use 30 second exposures to balance high temporal cadence with sufficiently high signal-to-noise ratio (SNR) per bin. We reduced each new `corrtag` file using the default processing pipeline of `calcos`[4], which provides a set of calibration tools for HST/COS. We extracted 1D spectra (`x1d` spectral data products) from every unbinned `corrtag` file.

There are 402 1D spectra per visit after this reduction, with detector segments a and b for each spectrum covering the full G130M CENWAVE 1222 bandpass. Each 1D spectrum has calculated affiliated errors per each observed wavelength, which we use directly in our error propagation. The wavelength solution per each frame visit is slightly different. To mitigate this issue, we interpolated each 1D extracted spectrum onto the same wavelength

3. `https://github.com/spacetelescope/costools`

4. `https://github.com/spacetelescope/calcos`

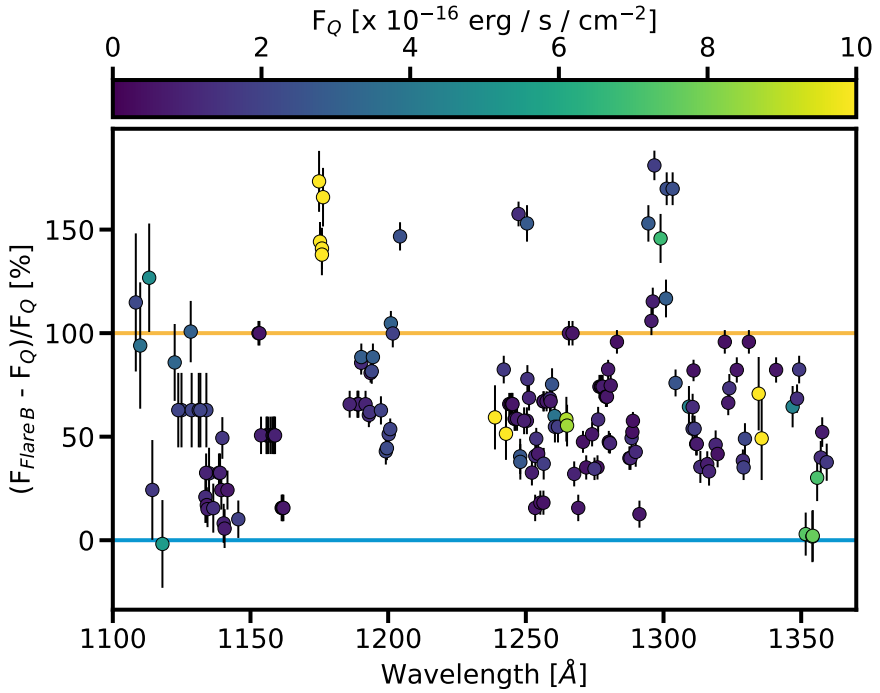

Figure 2.2 Comparison of line flux during Flare B (see Figure 2.1) and in quiescence (F_Q) for all lines identified in the AU Mic spectrum. Points are colored by line flux in quiescence. The values and error bars are presented in Tables 2.3 and 2.4. There is an overall increase in flux for all identified lines during Flare B as compared to the quiescent state. The blue and yellow lines represent no change and a doubling of flux values.

grid with a log-uniform dispersion of 0.009Å bin^{-1}. Our white light curve (flux summed over our entire wavelength coverage) is shown in Figure 2.1. We present our light curve in units of seconds, in accordance with previous FUV flare studies [e.g. 328, 188, 185]. We also created light curves of individual spectral features by isolating emission lines in the 30-s cadence 1D spectra for flare identification and analysis.

2.1.2 Flare Identification

Due to the small data set, we identified flares by-eye in each orbit. Flares were identified as large amplitude outliers in the light curves, followed by a decay. Each candidate flare was required to have at least two data points above the noise level of the orbit when it occurred. To identify flares, we searched two separate light curves: the C III emission line

at 1175.59Å and the Si III emission line at 1294.55 Å (Section 2.7.1; Figure 2.11). This method is consistent with previous studies [e.g. 582]. Flares were more pronounced in the C III and Si III light curves, while some smaller flares were not as obvious in the white light curve alone. In total, we identified 13 flares within both visits to AU Mic, labeled with with capital letters in Figure 2.1. Additionally, we highlight all time bins associated with the flare in the yellow shaded region. The peak of the flare is highlighted by a thick vertical line. We consider all remaining time bins outside of the yellow highlighted regions to be attributed to AU Mic in quiescence. The affiliated spectra are mean-combined to create a quiescent spectrum for AU Mic, presented in Figure 2.12.

2.1.3 Spectral Line Identification

The high SNR and high activity level of AU Mic produces a spectrum rich with emission features, which allow us to create a nearly complete list of present emission features and their measured fluxes, with respect to the databases and published FUV line lists. We searched for known emission features through the CHIANTI atomic database of spectroscopic diagnostics [127, 296], the National Institute of Standards and Technology (NIST) Atomic Spectra Database [279], previous HST/STIS observations of AU Mic [416], and FUSE observations of AU Mic [460].

We present measured flux values, wavelength/velocity offsets compared to rest wavelengths, and full-width half-maximum (FWHM) values for all identified lines in Table 2.3. Measured flux values are presented in units $10^{-15}\,\mathrm{erg\,s^{-1}\,cm^{-2}}$. We measured the line fluxes and FWHMs by assuming each line profile can be modeled by a single Gaussian function convolved with the COS line-spread function. We performed a χ^2 minimization for each line, allowing the mean (λ_{obs}; assuming the potential for non-negligible Doppler shifting), line width, and amplitude to vary. We do not explicitly fit for the continuum around each line, but include a term to account for an offset with respect to the continuum.

This process was completed for the mean quiescent spectrum and for a mean-combined

spectrum of all time bins during Flare B, the largest flare in our sample. We summarize the results of Tables 2.3 and 2.4 in Figure 2.2, by plotting the quiescent vs. Flare B line fluxes. We find that, on average, bright and faint emission lines increase by a constant value of ~ 1.5 during Flare B. Additionally, we note that the strongest emission features in quiescence do not show the strongest increase in flux during Flare B, but rather follow a similar trends as all lines identified.

2.2 The FUV Flares of AU Mic

We have identified 13 flares in our sample. Here, we discuss flare parameters as a function of energy, equivalent duration, and wavelength. Additionally, we compare how line profiles and continua change from quiescence during the five most energetic flares in our sample: Flares B, D, J, K, and M (Figure 2.1).

2.2.1 Flare Modeling & Parameters

For broadband optical/IR white-light flares, the typical flare light curve model consists of a sharp Gaussian rise followed by an exponential decay [569, 114]. We find that the previous model does not fit the FUV light curves well because the flare peak tends to appear more rounded, rather than discretely peaked. This is likely due to the wavelength dependencies in our light curves. Mainly, the peak of the flares in our FUV light curves are not as sharply peaked as the flares in Kepler and TESS. Instead, we develop a new profile to fit wavelength-dependent flares, which combines the [112] and [212] flare profiles and is similar to the newly developed models by [542]. Here, we use a skewed Gaussian profile with respect to time, profile(t), convolved with the white-light flare model. The skewed Gaussian takes the form:

$$\text{profile}(t) \sim \frac{1}{\sqrt{2\pi}\omega}\left(e^{-(t-\xi)^2/(2\omega^2)}\right) \times \left[1 + \text{erf}\left(\frac{\eta}{\sqrt{2}}\right)\right] \tag{2.1}$$

where ξ is the mean time of the distribution, t is time relative to an arbitrary starting point, ω is a free parameter with units of time that sets the amplitude of the distribution, and erf is the error function. It is important to note that Equation 2.1 has units of inverse time, because it will be convolved with respect to time. The parameter η is a renormalized and dimensionless proxy for time, and is defined as

$$\eta = \alpha \left(\frac{t - \xi}{\omega} \right) , \tag{2.2}$$

where α is dimensionless and defines the skew of the distribution. When $\alpha > 0$, the distribution has a steeper rise on the left wing; while a profile with $\alpha < 0$ has a steeper decay on the right wing. For all models, $\alpha > 0$, indicative of a steeper rise.

For completeness, the white-light flare model with respect to time, white-light flare(t), takes the form

$$\text{white-light flare}(t) = \begin{cases} a\, e^{-(t-t_{\text{peak}})^2/(2r^2)} & t < t_0 \\ a\, e^{-(t-t_{\text{peak}})/d} & t \geq t_0 \end{cases} \tag{2.3}$$

where t_0 is the time of peak intensity of the flare, a is the amplitude of the flare with units of flux, r is a parameter that sets the slope of the rise of the flare, and d sets the slope of the decay of the flare. The function that we use to fit the flares in this data set is the convolution of Equations 2.1 and 2.3. After performing the convolution, we calculate best fit parameters by performing a χ^2 minimization, allowing all parameters to freely vary.

Flare B is considered a complex flare because it exhibits a pronounced double-peaked structure, and required a unique analytic function to fit. It is likely the secondary peak originates from a *sympathetic* flare to the primary. Sympathetic flares are typically defined as spatially correlated with the primary flare, and are often seen on the Sun. Theoretically, the reconnection event causing the primary flare can trigger readjustments of the local magnetic field line topology, which can potentially trigger additional reconnection events [530, 423,

Table 2.1 Measured Flare Parameters. The parameter $t_{\rm peak}$ is the peak time of the flare; E is the flare energy; ED is the flare equivalent duration; $N_{\rm flares}$ denotes the number of flare models combined in the best-fit result. The horizontal line separates flares from Visit 1 and Visit 2. The reference start time for Visit 1 is MJD = 59362.148; the reference start time for Visit 2 is MJD = 59480.629.

Flare	$t_{\rm peak}$ [s]	E [10^{30} erg]	ED [s]	$N_{\rm flares}$
A	6388	3.78 ± 0.14	17.4 ± 9.0	1
B	12531	24.1 ± 0.14	688.5 ± 88.0	3
C	16935	4.17 ± 0.32	51.6 ± 20.3	1
D	17985	3.81 ± 0.29	53.9 ± 18.1	1
E	23049	1.19 ± 0.11	1.8 ± 6.8	1
F	24819	1.24 ± 0.11	5.9 ± 6.8	1
G	1740	2.42 ± 0.22	6.4 ± 13.6	1
H	17515	3.51 ± 0.32	1.0 ± 20.4	1
I	22993	2.01 ± 0.18	4.9 ± 11.4	1
J	23473	3.50 ± 0.25	60.3 ± 15.9	1
K	23653	3.64 ± 0.22	100.8 ± 13.6	1
L	23983	1.39 ± 0.11	17.3 ± 6.8	1
M	24493	3.53 ± 0.22	92.4 ± 13.6	1

528, 329, 496]. It is not possible to quantify the spatial correlation between these two flaring events deterministically without the ability to spatially resolve AU Mic. However, based on the short timescale between the two flaring events compared to the typical flare occurrence rate of the star, it is likely that these two events are correlated. The decay of Flare B is also slower than typical decay rates in exponential functions. For these reasons, we model Flare B with three flare profiles: two profiles for the notable double-peaked structure and a third, lower energy flare profile to approximate the prolonged decay. For all other flares, we used a single flare profile.

We computed the absolute flare energies, E, following [114, 225, 328], with the equation,

$$E = 4\pi D^2 \int_{t_0}^{t_1} \left(F_f(\tau) - F_q(\tau) \right) d\tau \tag{2.4}$$

where D is the distance to AU Mic, F_f is the flux during the flare and F_q is the quiescent flux. For this work, we adopt a distance of $D = 9.72\,\mathrm{pc}$ [192]. The parameters t_0 and t_1

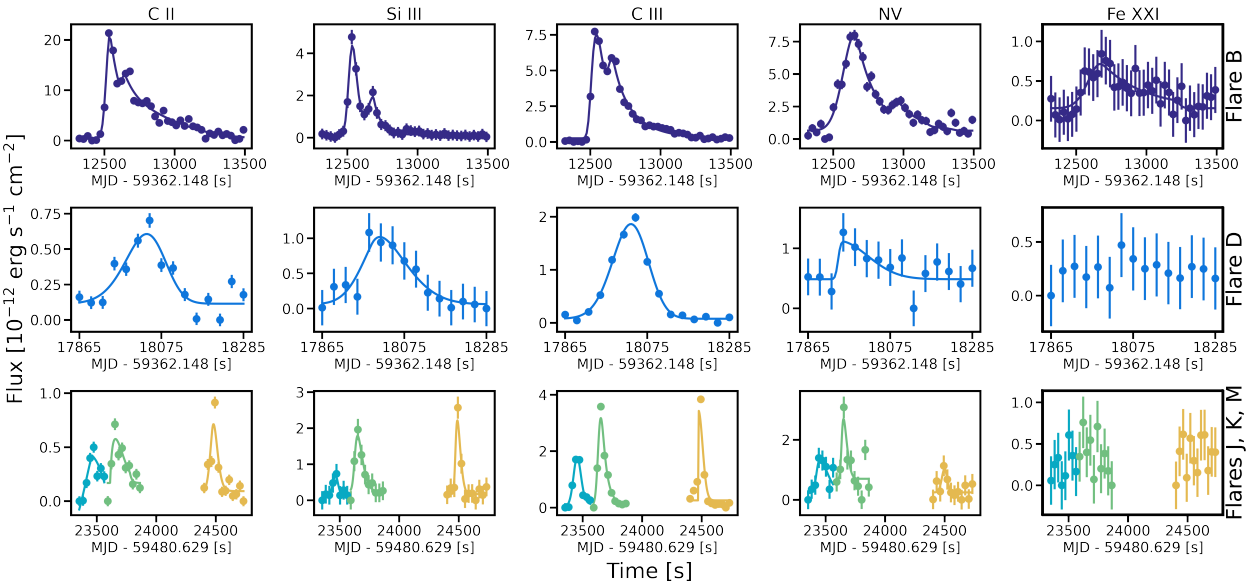

Figure 2.3 A comparison of flares seen in emission lines that originate from different formation temperatures (provided in Table 2.2), moving from coolest to hottest emission line from left to right. The best-fit model for each flare is over-plotted as a solid line. The first and second rows are light curves for Flare B and D. The third row are light curves for Flares J, K, and M (teal, green, and yellow). We were unable to properly model Flare D, J, K and M in Fe XXI due to a lack of obvious flare shape.

represent the initial and final times of the flare, and are calculated when the absolute flux returns to the typical continuum value for the star. Additionally, we calculate the equivalent duration, ED, of the flares as

$$\mathrm{ED} = \int_{t_0}^{t_1} \left(\frac{F_f(\tau) - F_q(\tau)}{F_q(\tau)} \right) d\tau. \tag{2.5}$$

We present the measured absolute flare energies, equivalent durations, and time of the flare peak in Table 2.1. These energies were calculated from the white light flux light curves (Figure 2.1). We find the flares in our sample range from $E = 1.19 \times 10^{30} - 2.41 \times 10^{31}$ erg and ED = 1 to 689 s.

Table 2.2 Flares in Different Emission Lines. $N_{\rm G}$ is the number of Gaussian profiles combined to fit the given ion emission feature.

Ion	λ [Å]	Range [km s^{-1}]	$\log_{10}(T_{\rm form}[{\rm K}])$	$N_{\rm G}$
C II	1335.708	[-80,60]	4.5	2
Si III	1294.55	[-100,100]	4.7	3
C III	1175.59	[-240,230]	4.8	7
N V	1238.79	[-80,80]	5.2	2
Fe XXI	1354.07	[-100,100]	7.1	1

2.2.2 Spectroscopic Light Curves

By creating spectroscopic light curves, we can calculate all of the above flare parameters with the goal of understanding the evolution throughout the stellar atmosphere. We created light curves for the five ions presented in Table 2.2, which are selected to represent a range of formation temperatures from $\log_{10}(T_{\rm form}[{\rm K}]) = 4.5 - 7.1$. In that table, we also present the velocity range [km s^{-1}] over which the data were integrated to create the light curves for each spectral line. We present these light curves in Figure 2.3 for Flares B (top row), D (middle row), J, K, and M (bottom row). We also include the flare model best fits using the analysis presented in the previous subsection, over-plotted as solid lines. Flares D, J, K, and M were each modeled with a single flare profile. Flare B exhibited clear evolution in the double-peaked profile, as well as a decay tail that changed shape between emission features. For this reason, we used a two flare profile for Flare B in the C II and N V, a three flare profile for Si III, and C III light curves, and a single flare profile in the Fe XXI light curve.

Flare Peak Time Offsets in Flare B

In this subsection, we investigate if there are any wavelength dependencies in the time at which Flare B had peak intensity. We complete this analysis for only the doubly-peaked Flare B, for which we have a sufficiently high SNR to re-reduce the data to shorter time-bins. For this analysis, we follow the procedures presented in Section 2.1.1. We reduce the data from Visit 1 Orbit 3 where Flare B occurs using time bins of 3 s. We measure the time

offset of each peak with respect to peak time $t_{\rm WLC}$ of the "white light" flare (Figure 2.1; reported in Table 2.1) to highlight the evolution of both flares. We define the peak time for the primary flare as $t_{\rm WLC,1}$ and the secondary as $t_{\rm WLC,2} = t_{\rm WLC,1} + 120$. We summarize these results in Figure 2.4.

We find that the primary peaks of C II, Si III, and C III are within 1.5σ agreement with $t_{\rm WLC,\,1}$. For hotter emission lines, we find primary peak times of 123 ± 7 s (N V) and 151 ± 41 s (Fe XXI) after $t_{\rm WLC,\,1}$. For the secondary peaks, we find C II, Si III, and C III occur 7 ± 13 s, 31 ± 5 s, and 9 ± 5 s, respectively, after $t_{\rm WLC,\,2}$. As noted above, we did not detect a secondary peak in the Fe XXI light curve, likely due to the low SNR. Additionally, at a faster cadence, the $t_{\rm WLC,\,2}$ is ill-constrained in N V.

We find no clear trends in peak time offsets with respect to emission lines for Flare B. While the cooler temperatures, which trace the transition region, peak earlier than in the white-light curve for the primary peak, the opposite is true for the secondary. We note one reason the general shape of the white-light curve deviates from the typical flare profile could be due to emission lines peaking at different times. This could result in a broader peak, rather than a sharp discreteness between the flare rise and decay.

Energy Contributions

We compare the energies measured in the spectroscopic light curves, E_{SLC}, to energies from the full COS G130M band white light curve, E_{WLC}. We evaluate the contribution of each emission line to the total white-light flare energy (Figure 2.4). We find that all flares in our sample follow similar trends in the energies measured from the spectroscopic light curves. Each flare has the largest energy contribution from C III, followed by C II. For this analysis, we treat Flare B as a single flare.

We find the largest contribution from C III across all flares, where $(E_{SLC}/E_{WLC})_{\rm CIII} = 10 - 21\%$. The energies from C II have the second largest contribution to the total energy, where $(E_{SLC}/E_{WLC})_{\rm CII} = 1 - 7\%$. Interestingly, the weakest contribution of C II is for

the most energetic flare in our observations (Flare B). We find total contributions of Si III and N V to be $(E_{SLC}/E_{WLC})_{\rm SiIII} = 0.05 - 0.15\%$, $(E_{SLC}/E_{WLC})_{\rm NV} = 0.07 - 0.28\%$, respectively, and, for Flare B, $(E_{SLC}/E_{WLC})_{\rm FeXXI} = 0.03\%$.

These trends are suggestive of the energy from the flare being deposited deeper in the upper chromosphere and transition region, while coronal heating is negligibly affected for these observed flares. Simultaneous observations of Flare B in the X-ray would have provided a better constraint on the high energy contribution to the total output, and how the flare affects hotter plasma in the stellar atmosphere.

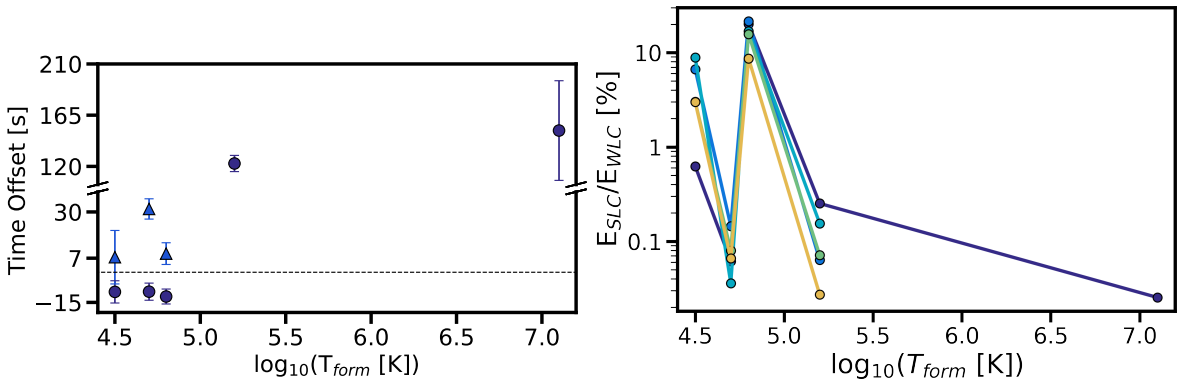

Figure 2.4 Top: A comparison of time offsets for the primary (circles) and secondary (triangles) flare peaks with respect to the peak in the "white-light" for the complex Flare B as a function of formation temperature. We plot the zero-point as a horizontal dashed line and note the time offset of the secondary peak in the in "white light" as a dotted black line. We set the zero-points for the primary and secondary peaks as $t_p = 12531$ s and $t_s = 12651$ s, with respect to the visit start time (MJD = 59362.148). We do not see the secondary peak in N V and Fe XXI. Bottom: A comparison of the measured energies for each flare from the spectroscopic light curves (E_{SLC}) compared to the measured white-light energy (E_{WLC}). All flares have the strongest measured energy in C III ($\log_{10}(T_{\rm form}[{\rm K}]) = 4.8$). Flare B has the highest E_{SLC}/E_{WLC} in C III, likely due to the increased prominence of the second flare at this wavelength (see Figure 2.2).

2.2.3 Line Profiles

In addition to modeling differences in flare morphologies and measuring differences in energies, we evaluate changes in the line profiles of the emission features. In this subsection, we

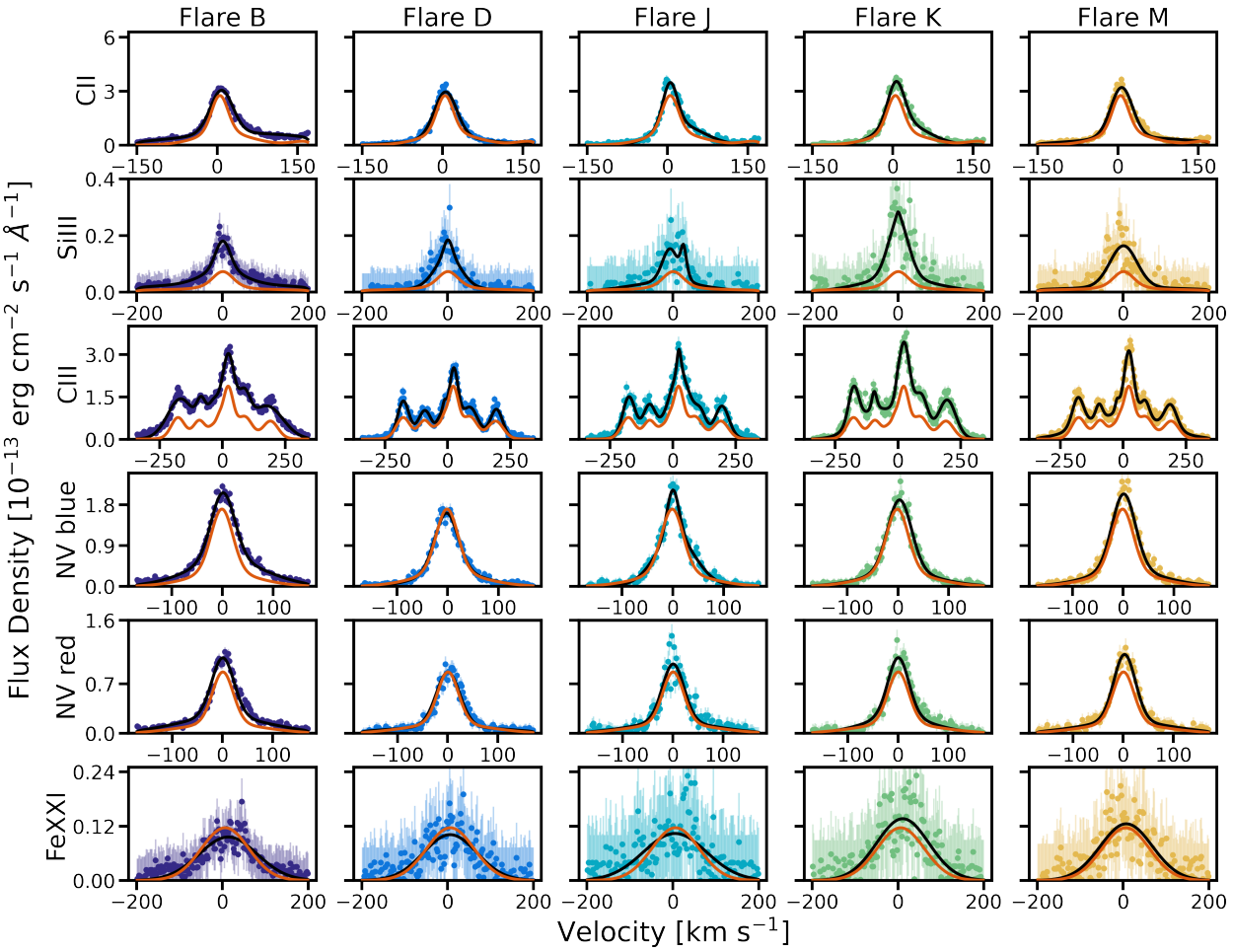

Figure 2.5 A comparison of line profiles in quiescence compared to Flares B, D, J, K, and M (left to right). The best-fit quiescent line profile is plotted in orange; the best-fit in-flare line profile is plotted in black, with the data plotted in color. All line profiles were fit with a multi-Gaussian model, where the exact number of Gaussians in each model is presented in Table 2.2. We find that for Flares B, J, K, and M each ion exhibits a bulk flux increase. Flare D poses the only exception to this, where there is little change in the profiles of C II, N V, and Fe XXI. In Si III, Flares B, J, K, and M all show a bulk increase in the blue side of the line center. In N V doublet, Flares B, J, K, and M all exhibit additional flux in the peak and red-wing of both the blue and red components.

evaluate this for every feature listed in Table 2.2 in quiescence and during Flares B, D, J, K, and M. Each of the profiles are presented in Figure 2.5. Each is modeled with multiple Gaussian profiles convolved with the Line Spread Function (LSF) of COS. The best fitting model is calculated using a χ^2 best fit between the data and the model using `lmfit` [398]. The number of Gaussians, N_G, used for each line profile is listed in Table 2.2 and the best-fit

model is plotted as a solid black line in Figure 2.5. For comparison, the best-fit model for the quiescent line profile is plotted as a solid orange line.

We find that, across all flares explored, the FWHM of the best-fit line profiles increases between quiescence and in-flare. We report the following changes in FWHM between quiescence and Flares B, D, J, K, and M: 10 to 35% for C II, 130 to 293% for Si III, 37 to 94% for C III, −3 to 22% for the blue component of N V, 2 to 29% for red component of N V, and −19 to 17% for Fe XXI. We note that in the blue component of N V, only Flare D was found to have a smaller FWHM during the flare than in quiescence. Additionally, Flares B, D, and J all have smaller FWHM in Fe XXI during the flares.

On average, there is additional redshifted emissions (e.g. C II and N V) and the peak of the line is redshifted during the flares by up to $15\,\mathrm{km\,s^{-1}}$. Additional redshifted emission (30-200 $\mathrm{km\,s^{-1}}$) has been found during other M dwarf flares [460, 229, 328, 325]. This feature is believed to trace material flowing downward toward the stellar photosphere.

2.2.4 Comparison of Continua

We investigate our spectra for changes in the quiescent and flare continua to measure the differences in best-fit blackbody temperatures, which is often assumed to be $\sim 9000\,\mathrm{K}$ [283]. We defined regions of the spectra without any emission features as the continuum [following 188, 185]. The continuum extends across the entire wavelength coverage of G130M. We provide the specific wavelength regions of the continuum in Appendix 2.7.3.

We present our continua for the quiescent state, and Flares B, D, J, K, and M in Figure 2.6. The continuum points are subdivided into 1 Å bins. To characterize the temperature of the continuum, we fit an ideal blackbody at $\lambda \geq 1120$ Å. In the quiescent state, we find a best-fit blackbody of 16,300 ± 500 K; during the flares, we find the best-fit blackbody ranges from 14,900 – 15,700 K. This is consistent with the blackbody emission from an FUV superflare observed by [325] on another young M dwarf and towards the upper end of continua emission seen during 20 M dwarf flares [277]. Given that these high temperatures are

present in the quiescent state of this cool star, it is unclear whether or not a blackbody is the appropriate model to fit to these data.

Thermal bremsstrahlung is a principal emission mechanism for the Soft X-ray emission observed in solar flares [505, 570, 367]. We fit for both the temperature and electron number density in a thermal bremsstrahlung profile at $\lambda \leq 1120$ Å. We found temperatures of $9.1 \leq \log_{10}(T) \leq 11.2$ best-fit the continua increases seen during Flares B, D, J, K, and M (models plotted in Figure 2.6). However, we note these fits converge only for electron number densities of $\sim 10^{22}\,\mathrm{cm}^{-3}$, which is not representative of the stellar chromosphere. Therefore, thermal bremsstrahlung cannot be solely responsible for this feature, and it is unclear what other mechanisms may be contributing to this FUV excess.

We visually inspected the COS images to determine if this was the result of an overall count rate increase on a portion of the COS segment b detector. We found the count rate increase is limited to within the spectral trace, lending confidence to an astrophysical origin of this signal. To investigate further, we attempted to fit the slope with a blackbody function. Specifically, we attempted to fit only the *slope*, rather than the overall flux density values. However, we find that the blackbody fit fails to converge, as the function cannot accommodate the two orders of magnitude change in flux density over ~ 30 Å.

Observations of AU Mic with FUSE found a similar increase in flux during two flares [460]. The best-fit temperature for a bremsstrahlung profile for these data was calculated to be $\log(T) \sim 8.0$. We compare the blue end of our continua ($\lambda \leq 1120$ Å) to the continua presented in [460]. We find the continuum during Flare B has a steeper flux decrease between $1066 - 1115$ Å, decreasing by $\Delta\mathrm{F} = 0.877 \times 10^{-13}$ erg cm^{-2} s^{-1}, while the bigger flare in [460] shows a decrease of $\Delta\mathrm{F} = 0.003 \times 10^{-13}$ erg cm^{-2} s^{-1} from $955 - 1104$ Å.

While we find tentative evidence of thermal bremsstrahlung emission during these flares, we note that this emission mechanism implies a large continuum enhancement at EUV wavelengths that would be several orders of magnitude brighter than bound-bound emission lines and recombination continuua in the EUV (see Section 2.3.6). Such continuum enhancement

was never observed with EUVE during flares from AU Mic [107, 374] or other stars. Similar flare continuua have not been identified in other M dwarf FUV flare observations [325, 188]. Regardless of the physical mechanism producing the FUV continuum rise, it likely extends into the EUV bandpass where it will contribute to the atmospheric escape of AU Mic b and AU Mic c following stellar flares.

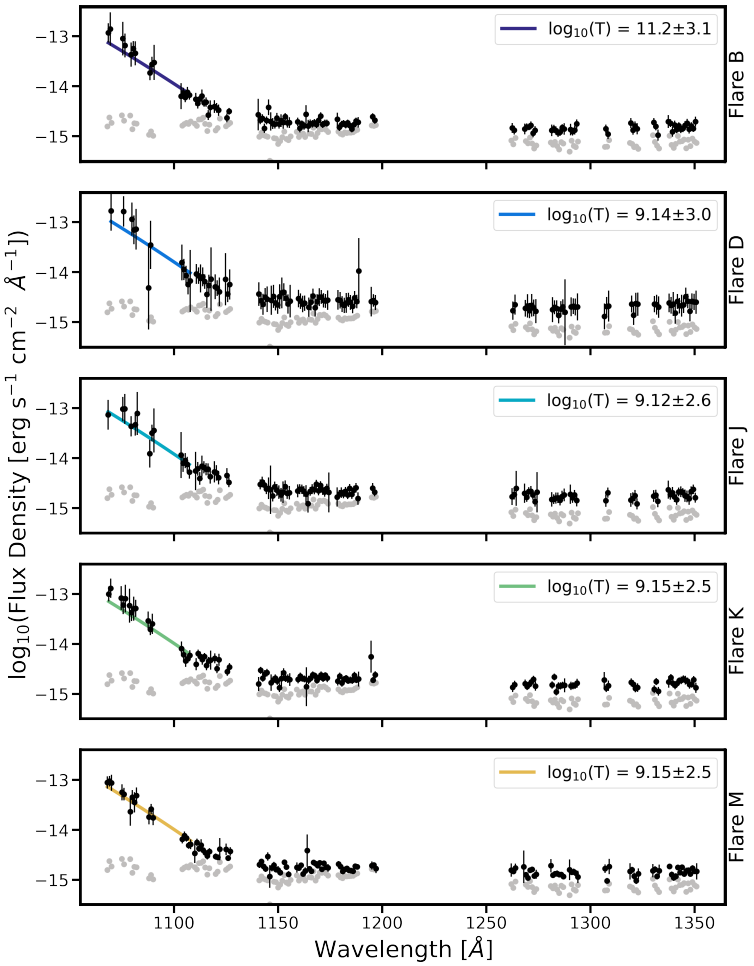

Figure 2.6 The continuum of the mean spectrum for the quiescent state (gray points) and Flares B, D, J, K, and M (black points per each sub-panel). The continuum was visually identified by inspecting regions of the spectrum lacking emission features. For the purposes of this calculation, the spectrum is sub-divided into 1Å bins. We fit an additional thermal bremsstrahlung profile (colored lines) to the continuum of the flare data, as there is an obvious rise at $\lambda \leq 1100$ Å. The resulting best-fit temperature for the thermal bremsstrahlung profile is presented in each sub-panel.

2.3 A Panchromatic Spectrum of AU Mic

AU Mic has been observed across nearly all wavelengths. We performed a systematic search of archival data to construct a panchromatic, quiescent spectrum of this exquisite system – depicted in Figure 2.8. In this section, we describe each data set and models employed for unobserved wavelength regimes in order to create our panchromatic spectrum. We do not include archival EUVE observations due to the low SNR of the spectra, and they do not cover the entire EUV wavelength range.

2.3.1 XMM-Newton Observations

Several observations of AU Mic are available on the XMM-Newotn Science Archive. We used data from Obs.ID 0822740301 (PI Kowalski) which span a wavelength range of $\lambda = 4.02 - 40$ Å. AU Mic was observed from 2018 Oct 10 to Oct 12. This program includes time-series X-ray observations which captured multiple flares. The majority of these data were taken in quiescence. For the remainder of this analysis, we assume that the median spectrum is representative of AU Mic in quiescence.

2.3.2 FUSE Observations

Observations of AU Mic were obtained by FUSE [379, 487] as part of the "Cool Stars Spectral Survey" program. AU Mic was observed on 2000 Aug 26 and 2001 Oct 10 over 905-1187 Å in the time-tagged mode, allowing for the separation of in-flare vs. out-of-flare spectra. The details of these observations are presented in [460], who identified two temporally-resolved flaring events. For the panchromatic spectrum presented in this paper, we removed the in-flare spectra and use the average of all of the remaining quiescent spectra in the FUSE observations.

2.3.3 Ly-α Reconstruction

Ly-α is a key driver in planetary atmospheric photochemistry and must be included in the panchromatic spectrum. However, Ly-α is masked in our HST/COS observations for detector safety (see Osten et al. 410). We note that [580] reconstructed a Ly-α profile for AU Mic in the interest of understanding imprints from the stellar wind on Ly-α observations. In the construction of the SED presented here, we chose to use the model Ly-α profile presented in [174].

[174] used archival STIS observations of AU Mic (1999-09-06; Pagano et al. 416) to detect Ly-α in quiescence and reconstruct its profile following the methods of [587]. The wings of the model Ly-α profile are fainter than measured by COS (see Figure 2.12) because of (i) stellar variability between 1999 and 2021 and/or (ii) differences between the STIS and COS flux calibrations. To account for these differences, we uniformly scale the model profile by a factor of 18 to match the COS wings.

2.3.4 NUV Observations

We retrieved 20 archival observations of AU Mic with the International Ultraviolet Explorer (IUE) in the near-ultraviolet (NUV) covering $1750 - 3450$ Å. Observations were taken from 16 January 1986 to 29 July 1991 as part of programs HC078 [PI Butler; 76] and MC111 (PI Byrne). All observations were taken with low dispersion, large aperture, and exposure times of 1200 s. There were no flares reported in either programs [454, 357], which we verified visually. We used the median of all NUV observations for the baseline quiescence value.

2.3.5 Optical Spectrum

In this subsection, we describe how we reconstructed the quiescent optical spectrum of AU Mic using two methods. In the first method, we obtained 19 publicly available spectra of AU Mic taken from 2019-2021 from the HARPS-N (3789-6912 Å) data archive. In order

to obtain *only* the quiescent spectrum, we removed any spectra with dramatic changes in Hα – indicative of a flaring events/periods of increased stellar activity. Specifically, we removed spectra with (i) strong Hα emission and (ii) asymmetric profiles caused by an increase the blue wing of the Hα flux [344]. This analysis resulted in a data set for the quiescent state which included 11 spectra. We then used the average of this combined data set to produce the optical component of our panchromatic spectrum. We verified that the numerical values of each individual wavelength bin $\delta\lambda$ was consistent with the mean value within $2\sigma\,\forall\delta\lambda$ in the panchromatic spectra.

In the second method, we extended the range of our optical spectra from that which was observed using a PHOENIX stellar model [249]. These models are high-resolution synthetic spectra generated assuming local thermodynamic equilibrium in the stellar atmosphere. Specifically, we selected a model with an effective temperature of $T_{\rm eff} = 3700$ K, surface gravity of $\log(g) = 4.5$, and a solar-type metallicity ([M/H] = 0). The PHOENIX model in our panchromatic spectrum spans from the end of the HARPS-N spectrum to 5 μm, the wavelength cutoff used in the MUSCLES high-level science products [327].

2.3.6 Differential Emission Measure

In this subsection, we describe the methodology by which we estimate the UV and X-ray flux at wavelength regimes not covered by archival observations. Specifically, we calculate the differential emission measure (DEM) which can be used to estimate unobservable EUV flux. Typically, these wavelengths are difficult to observe because of (i) the faintness of the target and/or (ii) photon obscuration from the interstellar medium. We use only the HST/COS observations as inputs to the DEM. W do not use the archival XMM-Newton and EUVE data in our fits. The reason for this is that the scaling between quiescence and during flares for non-simultaneous data most likely does not accurately represent the most recent observations. In order to calculate the DEM model, we follow the methods presented in Section 3 in [146].

This implementation of the modeling takes into account the following procedures:

- It assumes a constant electron pressure across the stellar atmosphere.
- It incorporates the width of the line emissivity function while fitting the DEM model.
- It groups together ions of the same species and calculates the total emissivity across all spectral lines.
- It accounts for multiplets.
- It assumes that the systematic uncertainty, s, can be inferred during fitting by parameterizing it as a fraction s of the DEM predicted flux.
- It calculates a free-bound and two-photon continuum component from H and He.

The inclusion of the continuum is an update to the methods published in [146].[5]

To determine the DEM parameters, we use the measured fluxes for lines marked with an asterisk (*) presented in Table 2.3. These lines are known to have emissivities dominated by gases with temperatures of 10^{4-8} K, and mostly neglects neutral lines. Additionally, these selected lines are not blended with any other known emission line of comparable emissivity and have strong enough emissivities that the line identification routines are reliable. These lines are single resolved lines or multiplets which fit within a 1 Å bin, which ensures all relevant emissivity is added into the model properly. Further selection criteria for reliable emission lines are described in [146].

We use `CHIANTI 10.0.1` [127, 122] to calculate the emissivity functions for all transitions in the `CHIANTI` database. We assumed solar coronal abundances [492] and calculated the emissivity functions from $4 \leq \log_{10}(T) \leq 8$. We fit a Chebyshev polynomial to to reproduce the measured line fluxes. We then ran a Markov Chain Monte-Carlo (MCMC) fit for the coefficients of the polynomial and the estimated systematic uncertainty fraction, s. For the

5. `https://github.com/gmduvvuri/dem_euv`

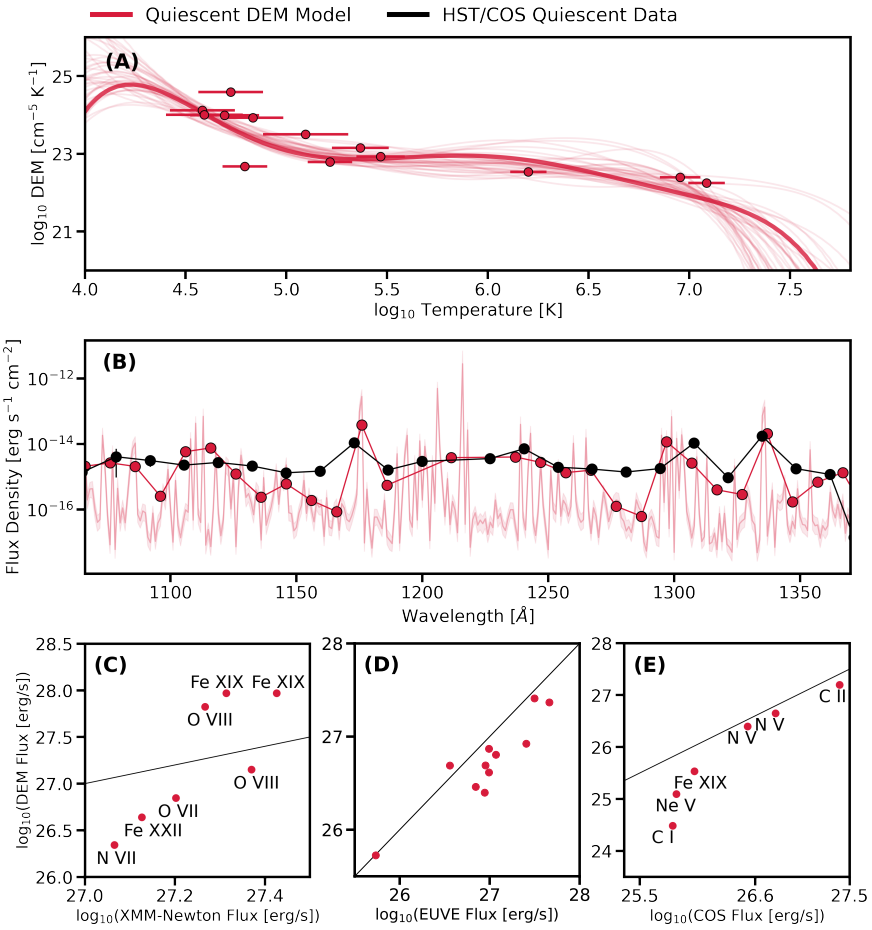

Figure 2.7 A set of Differential Emission Measurement (DEM) models and diagnostic plots. For all of the plots, red lines and symbols represent the DEM models, while black lines and symbols represent the HST/COS data presented in this paper. Panel (A) shows the DEM models of the COS FUV emission lines of AU Mic in quiescence. The average DEM model is shown in the thick line, with individually measured DEM values. The thin lines represent 50 random draws from the models fit with `emcee`. Panel (B) shows the integrated flux in bins of 10Å from the DEM output (red) spectra compared to the HST/COS data (black). The Ly-α line is masked in these bins. The unbinned spectrum is plotted as the pink line with shaded 1σ errors. In Panel (C) we show a comparison of line fluxes from XMM-Newton observations of AU Mic to the DEM modeled spectra. In Panel (D) we show a comparison of line fluxes from EUVE observations [123] of AU Mic to the DEM modeled spectra. These data are for Fe IX - Fe XXIV. In Panel (E) shows a comparison of line fluxes from the presented HST/COS observations to line fluxes. The solid lines in both Panels (C, D, and E) represent a 1-to-1 relationship in the flux.

MCMC, we used 50 walkers and 1200 steps. We visually verified that the walkers were sufficiently randomized after the first 400 steps, which were subsequently discarded. We

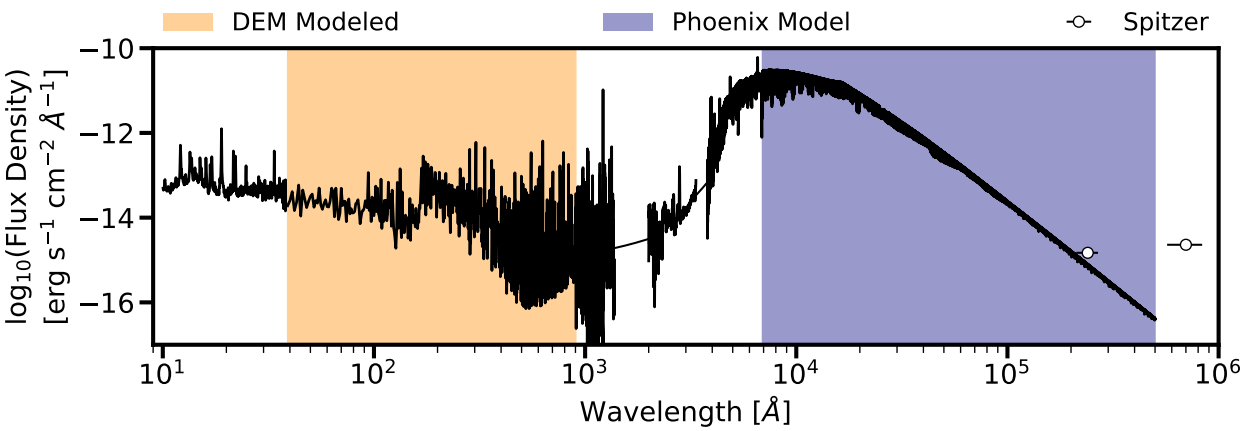

Figure 2.8 A panchromatic spectrum for AU Mic in its quiescent state. The spectra are comprised of archival observations of AU Mic with XMM-Newton (10 - 39 Å), FUSE (900 - 1181 Å), HST/COS (this work; 1064 - 1372 Å), IUE (2000 - 3347 Å), and HARPS-N (3789 - 6912 Å). To fill in gaps in data coverage, we utilize a DEM synthetic spectrum (40-900 Å), a linear interpolation (1372 - 2000 Å and 3334 - 3782 Å), and a PHOENIX synthetic generated stellar atmosphere model (6912 - 2×10^5 Å). For Ly-α (1211 - 1220 Å), we use the reconstructed profile from [174]. We present Spitzer 24 and 70 μm color-corrected detections of AU Mic (white points) for completeness [439]. We do not correct the PHOENIX spectrum for the infrared excess from the debris disk.

present our DEM measurements and functions of AU Mic in quiescence in Figure 2.7. The synthetic spectra generated from the DEM model are shown in red and our HST/COS data are shown in black.

We present several diagnostics to validate our DEM model. First, we subdivide the FUV flux estimated by the DEM models into 10 Å bins and compare to the observations (Figure 2.7, panel B). As is evident in the figure, there is good overall agreement between the estimated and observed flux. We note the model does under-predict largely line-free spectral regions by two orders of magnitude. We attribute these differences to the additional quiescent FUV continuum emission that we describe in Section 2.2.4.

We explicitly did *not* model Ly-α to compare with the reconstruction. The reason for this choice is that the Ly-α is not formed under the physical conditions applicable to the DEM method. Therefore, it would be unphysical to include the DEM-estimated Ly-α. We further validate these methods by evaluating the line flux from specific X-ray, EUV, and

FUV emission lines (Figure 2.7, panels C, D, & E). We find the X-ray, EUV, FUV estimated flux values from our DEM model are generally consistent with the XMM-Newton, EUVE [123], and HST/COS observations.

The DEM presented here is generally consistent with the one presented in [123], as also highlighted in Figure 2.7 Panel (D). However, there are minor differences in the overall shape of this DEM. The [123] DEM model of AU Mic has a well-constrained peak at $\log_{10}(T) = 6.1$ from EUVE measurements and at $\log_{10}(T) = 6.9$ from FUSE and STIS observations. The differences at the high temperature regime ($\log_{10}(T) > 6.5$) may be caused by (i) different observational data sets used to generate each of the DEM models (ii) the differences between the polynomial fit or (iii) more precise laboratory measurements of atomic spectral data since 2002.

2.4 Implications for AU Mic b and c

There is no consensus as to whether stellar flares contribute to or detract from the habitability of a planet. For M dwarf planets specifically, flares may serve as sources of visible light for photosynthesis [8, 384]. They also deliver UV photons needed to initiate prebiotic chemistry [459, 468]. However, bursts of high-energy radiation and stellar energetic particles (SEPs) from flares can remove the atmosphere of a planet and alter its chemical composition [9].

The recent detection of two transiting planets around AU Mic [440, 359] has resulted in significant observational follow-up of the system for planetary and stellar characterization. Several campaigns have ensued to measure the masses of AU Mic b & c via radial velocities, yielding masses from $M_b = 11 - 20 M_\oplus$ and $M_c \leq 22 M_\oplus$ [77, 272, 359, 599]. AU Mic b & c are near a 9:4 mean-motion resonance, which may produce transit-timing variations [359] and a second means to measure the masses of these planets. Transmission spectroscopy in the optical/near-infrared has proven challenging given the strength of the stellar activity of AU Mic [419, 237].

Young and short period transiting planets are believed to host more extended atmospheres

due to the high levels of stellar irradiation [e.g. 293, 412]. This effect is more prominent for stars < 100 Myr because the overall stellar XUV flux is higher. Moreover, young and newly formed planets are likely still undergoing contraction. Therefore the characterization of the the atmosphere of AU Mic b & c are important benchmarks for understanding planetary evolution.

In this section we discuss two potential implications of our observations for the atmospheres of AU Mic b and AU Mic c. In Subsection 2.4.1, we investigate the effects of the measured high-energy luminosity and flares of AU Mic on mass-loss due to photoevaporation. Next, in Subsection 2.4.2, we produce synthetic mid-IR transmission spectra for AU Mic b and AU Mic c using our new panchromatic quiescent spectrum (Figure 2.8).

2.4.1 Flare-Driven Thermal Mass Loss

Recently, several sets of authors have focused on flare-driven atmospheric removal during the first 1 Gyr of the lifetime of a planet. [193] modeled the EUV-driven proton and O^+ escape from an Earth-like planet around Proxima Centauri. They speculated that very large flares could increase the ionization fraction at low altitudes. This would indirectly enhance atmospheric escape. They also demonstrated that very energetic flares produce enhanced rates of hydrogen photoevaporation. [162] modeled H_2 dominated atmospheres in the presence of flares on young G stars following the methods of [415, 413]. They found the inclusion of flares could result in $4 - 5\%$ more atmospheric mass-loss than without accounting for flares. [394] accounted for the X-ray and UV (XUV) contribution of flare flux in atmospheric escape from Earth-like planets around M dwarfs. The XUV flux from flares produced surface water loss for planets with mass $M_p = 5M_\oplus$ in their simulations.

However, the effects of radiation from frequent high-energy flares on short period, young planets has not been fully investigated. Here, we follow methods similar to [162] to evaluate the effects of flares on the photoevaporation-driving mass-loss of AU Mic b & c. We use the modified energy-limited escape methodology presented in [415, Equation 17] and [413]:

$$\dot{M} = \eta \left(\frac{R_p^3 L_{\rm HE}}{4a^2 G M_{\rm Core}} \right). \tag{2.6}$$

In 2.6, η is the dimensionless heating efficiency, R_p is the planetary radius, $L_{\rm HE}$ is the integrated high-energy luminosity of the star from the X-ray through the UV, and $M_{\rm Core}$ is the mass of the core. We make the following assumptions in our model:

- The mass loss efficiency is $\eta = 0.15$ [285].
- The iron mass fraction in the core is $X_{\rm iron} = 1/3$.
- The ice mass fraction in the core is $X_{\rm ice} = 0$.
- We adopt the planetary parameters presented in [359].

To evaluate whether these equations can be used to accurately describe AU Mic b & c, we calculate their Jeans parameter. The Jeans parameter, λ_J, is a quantification of the relative importance of thermal energy and self gravity. It can be calculated using the equation,

$$\lambda_J = \left(\frac{G\, M_p\, m_H}{k_B\, T_{\rm exo}\, R_{\rm exo}} \right), \tag{2.7}$$

where M_p is the mass of the planet, m_H is the mass of a hydrogen atom, k_B is the Boltzmann constant, $T_{\rm exo}$ is the temperature at the exobase, and $R_{\rm exo}$ is the radius of the exobase. We calculate the Jeans parameter, λ_J, for AU Mic b & c using the lower mass estimates from [599]. We calculate $\lambda_{J,b} = 1.8$ and $\lambda_{J,c} = 12.8$ using the following two scaled relationships:

$$\lambda_{J,b} = 1.8 \left(\frac{M_p}{6.7 M_\oplus} \right) \left(\frac{1500K}{T_{\rm exo}} \right) \left(\frac{14 R_\oplus}{R_{\rm exo}} \right), \tag{2.8}$$

and

$$\lambda_{J,c} = 12.8 \left(\frac{M_p}{15.5 M_\oplus} \right) \left(\frac{1000K}{T_{\rm exo}} \right) \left(\frac{6 R_\oplus}{R_{\rm exo}} \right). \tag{2.9}$$

This validates the use of the hydrodynamic escape equation for AU Mic b, but not for AU Mic c [567, 211].

We inject flares using the average flare rate found in the observations presented in this paper ($\sim 2.5\,\mathrm{hour}^{-1}$). We calculate the mass-loss rate for a variety of core masses (5, 8, and 10 $M_{\oplus}$). We also calculate the timescale over which flares may have an impact on the atmospheric masses. We do this by running our model over three scenarios: (1) no flares are present, (2) flares are present for the first 200 Myr, and (3) flares are present for the first 1 Gyr.

We adopt a quiescent luminosity $L_{HE} = 2.71 \times 10^{29}\,\mathrm{erg\,s^{-1}}$. We calculate this value by integrating the DEM modeled spectrum over $1 \leq \lambda[\mathring{A}] \leq 1100$, for which the DEM is reliable. To simulate flares, we adopt a transient L_{HE} that is equivalent to that of a flare. In the ideal scenario, we would estimate $L_{HE,\mathrm{flare}}$ by drawing flares from a fit to the observed flare-frequency distribution. However, since there are only a relatively small sample of flares observed for the system, we adopt a flare-frequency distribution slope of $\alpha = -1.1$ flares day^{-1}. This value is consistent with that observed on low mass ($M/M_{\odot} \leq 0.3$) stars [**?**]. We do not account for thermal bremsstrahlung or the continuum in our calculation of L_{HE}. Our resulting mass-loss rates are presented in Figure 2.9.

First, we calculate the mass loss rates without any stellar flares. We find that the median mass-loss rate for AU Mic b across all assumed core masses ranges from 1.6 to $2.5 \times 10^{8}\,\mathrm{g\,s^{-1}}$ in the case of no flares. These calculations are consistent with the upper limit set by [237] using the metastable infrared He I triplet with NIRSPEC/Keck-II. When we include flares for the first 200 Myr, we find no significant change in the time-averaged mass loss rate, with minimal increases of up to 1.5× the no-flare baseline. When we include flares for the first 1000 Myr, we find the time-averaged mass loss rate increases by 3× the no-flare baseline.

Additionally, we can evaluate instantaneous mass-loss in the presence of super-flares ($L_{\mathrm{flare}} \geq 10^{33}\,\mathrm{erg\,s^{-1}}$) with these simulations. In each simulation, we identify the most energetic flare to be $L_{\mathrm{flare}} \approx 4 \times 10^{33}\,\mathrm{erg\,s^{-1}}$. We find the instantaneous mass-loss increases by six orders of magnitude, up to $\dot{M} \sim 10^{14}\,\mathrm{g\,s^{-1}}$, relative to the no-flare baseline. Given the high duty cycle of AU Mic, where $1/6^{\mathrm{th}}$ of its time (assuming an average $\mathrm{ED}_{\mathrm{flare}} = 5\,\mathrm{minute}$)

is spent flaring, this could indicate that flares are the dominant source of atmospheric mass removal. There are still many open questions which need to be addressed to claim the previous statement. It is unclear what the response time of the atmosphere would be to

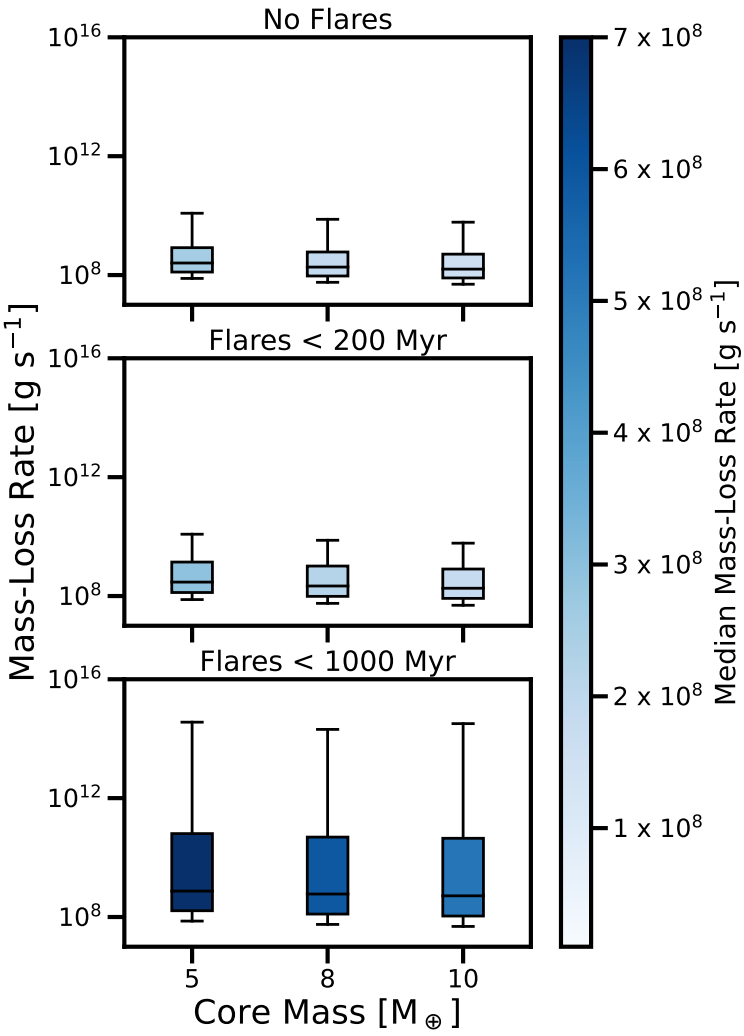

Figure 2.9 Comparison of photoevaporation-driven atmospheric mass loss for AU Mic b. We run our calculations under three different flare evolution scenarios: (Top) No flares present (Middle) Persistent flares during the first 200 Myr (Bottom) Persistent flares during the first 1000 Myr. The box represents the first quartile (Q_1; 25$^{\text{th}}$ percentile), the median (50$^{\text{th}}$ percentile), and the third quartile (Q_3; 75$^{\text{th}}$ percentile). The whiskers mark the interquartile (IQR $= Q_3 - Q_1$), where the lower limit is defined as $Q_1 - 1.5\times$ IQR and the upper limit is defined as $Q3 + 1.5\times$ IQR. The largest spread is seen in the calculation where we inject flares for the first 1000 Myr. The boxes are colored by the median mass-loss rate in [g s^{-1}]. Super-flares ($L_{\text{flare}} > 10^{33}$ erg s^{-1}) can boost mass-loss by up to five orders of magnitude.

being hit by a flare. Additionally, if the atmosphere cannot respond quickly enough to the instantaneous change, then the atmospheric mass loss rate would not increase. This raises the question of if Ly-α or He I at 1083.3 nm transits could be variable in depth/shape.

In context with other planets, Ly-α transits have revealed mass loss rates from $10^8\,\mathrm{g\,s^{-1}}$ [68] to $2.20\eta 10^{10}\,\mathrm{g\,s^{-1}}$ for GJ 436 b ($R_p = 4.2R_\oplus$; $M_\star = 0.812M_\odot$; Addison et al. 4). No Ly-α transit was detected for the 750 Myr planet K2-25 b [473]. Variable Ly-α transits have been observed for HD 189733 b ($R_p = 12.54R_\oplus$; $M_\star = 0.45M_\odot$). [303] observed three transits of HD 189733 b with HST/STIS and constrained the mass loss rate to $10^{9-11}\,\mathrm{g\,s^{-1}}$. [304] observed additional transits one year apart and found changes in the Ly-α transit depth of $\approx 15\%$. They note an X-ray flare was observed 8 hours prior to the deeper transit, although the correlation between events is unclear. [230] recently simulated transits in the presence of flares and CMEs for HD 189733 b. Although the 3D radiation hydrodynamic simulations revealed transit depth increases by 25% for flares-alone and a factor of 4 for CMEs, neither models were able to reproduce the deep transit of HD 189733 b post flare.

Model Limitations

The above calculation only accounts for thermal processes, which does not encapsulate all processes which can contribute to atmospheric mass loss. The thermal escape calculation in Section 2.4.1 can play a major role if AU Mic b is a low-gravity planet with an atmosphere dominated by light atoms, while non-thermal processes can dominate under a range of planetary configurations [335] and have no mass preference. Many of these processes are understood from our own Solar System. From studies of Mars, [96] and [335] defines four primary non-thermal processes.

The first process is photochemical escape, where recombination or charge-charge exchange as the result of stellar ions excites neutral atoms to $v > v_{\mathrm{escape}}$ [294, 95]. The second process is ion sputtering, which is the result of coronal ions impacting atmospheric neutral particles, resulting in ejection [255, 299]. The third process is ionospheric escape driven by energy and

momentum exchange between the solar wind and planetary atmospheres [378]. The fourth process is ionospheric ion pickup, which is the result of both the electric and magnetic fields from the solar wind interacting with and removing ionospheric ions [334, 143].

These non-thermal processes can be driven by coronal mass ejections [295] or interactions with the stellar wind, plasma escaping from the star embedded in the magnetic field [12, 422]. [103] recently simulated the stellar environment for AU Mic b in the presence of stellar winds, estimated from magnetograms derived by [272], and CMEs. These simulations suggest a potential strong stripping of magnetospheric material from the planet. However, the simulations are unable to quantify the rate of mass-loss per CME interaction.

Magnetic shielding from the presence of a magnetosphere may reduce the efficiency of atmospheric removal [335]. However, the magnetic field strength of AU Mic b & c is currently unknown and is essential for understanding these questions. Overall, these non-thermal processes may result in a more significant contribution to atmospheric mass loss than photoevaporation alone. A full calculation coupling both thermal and non-thermal time-dependent processes would need to be completed to fully understand the effect of flares on atmospheric removal, which is outside of the scope of this paper.

2.4.2 Observational Signatures

Stellar activity also affects the chemical composition of planetary atmospheres via photochemistry and atmospheric escape. [98] presented chemistry-climate model simulations that explored the effects of G, K, and M dwarf flares on the atmospheres of rocky planets. They demonstrated that the time-averaged flares and accompanying energetic particles can significantly alter the chemical composition of the atmospheres. The global NO and OH increased by an order of magnitude, while the global O_3 decreased by less than an order of magnitude after 300 days of post-flare evolution in the atmospheres of planets around M dwarfs.

The atmospheres of AU Mic b and AU Mic c could be pristine tracers of their primordial atmospheres, although they may have experienced metal enrichment by accreting comets

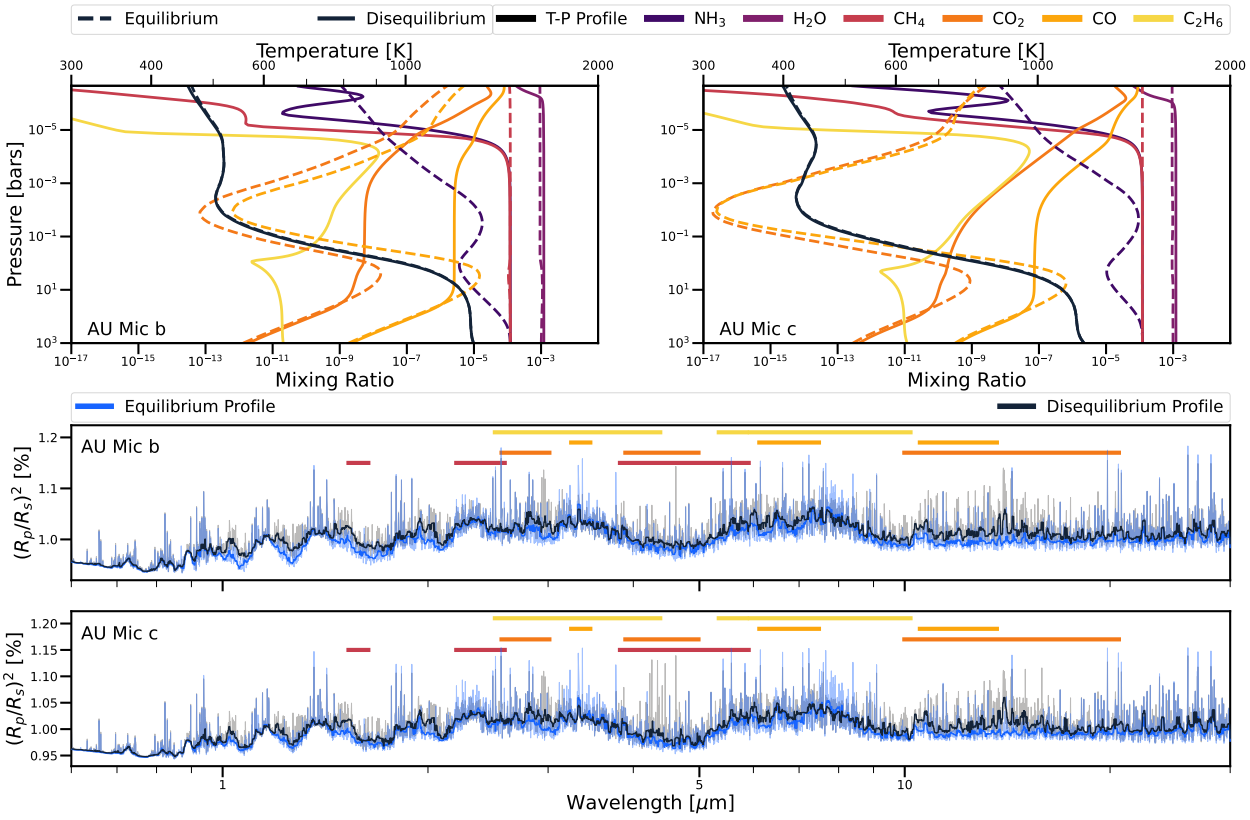

Figure 2.10 Photochemical models for AU Mic b & c. Temperature-pressure profiles (black lines) and mixing ratios (colored) for AU Mic b (top left) and AU Mic c (top right). We model the planets in equilibrium (dashed) and disequilibrium (solid). Normalized transmission spectra as observed from $0.6-12\mu$m for AU Mic b (middle row) and AU Mic c (bottom row). Dominant CH_4, CO_2, CO, and C_2H_6 are labeled in the normalized transmission spectra. These models follow the methods presented in [534] and are evaluated with AU Mic in quiescence.

[502]. Nevertheless, measuring elemental/compound abundances can provide constraints as to where these planets originally formed within the protoplanetary disk [404]. The chemistry and long-term stability depends sensitively on the XUV irradiance of the host star [539, 261]. Here, we model transmission spectra of AU Mic b and AU Mic c in quiescence using the panchromatic spectrum presented in Figure 2.8. We note that AU Mic b & c have the highest Transmission Spectroscopy Metrics (≥ 350, Kempton et al. 267) of all known young transiting exoplanets, making these planets priority targets for future JWST observations.

Here we summarize the methods used for this calculation. We run the `Atmos` 1-D photo-

chemical model for solar composition atmospheres of AU Mic b & c. We use a recently updated version of `Atmos` which is appropriate for atmospheres of sub-Neptune (i.e. hydrogen-rich) composition, as described in Harman et al. [222]. This updated version includes the addition of reactions for nitrogen-bearing species and the hydrocarbon haze prescription from Arney et al. [22, 23]. The temperature-pressure profiles used were computed with the `HELIOS` radiative-convective equilibrium radiative transfer code [347, 346] for AU Mic b & c analog planets with 500 K and 600 K equilibrium temperatures, respectively. The photochemical modeling was conducted using the stellar input spectrum for AU Mic from Figure 2.8, scaled such that the top-of-atmosphere flux corresponds to the orbital distances of each planet as reported by [359]. We then run the resulting atmospheric abundance profiles from the photochemical modeling through the `Exo-Transmit` radiative transfer code [266] to predict the transmission spectra for both planets. For this calculation, we followed the methods presented in detail in Teal et al. [534].

Figure 2.10 shows two `Atmos` disequilibrium (black) and two `FastChem` [526] equilibrium (blue) models for AU Mic b & c, as well as affiliated mixing ratios and temperature-pressure profiles. Both cases use the same temperature pressure profiles, since we do not account for the feedback of disequilibrium chemistry on the thermal structure of the atmosphere.

Although we include hydrocarbon haze formation pathways in each of our `Atmos` models, neither of our atmospheres form significant amounts of photochemical haze. JWST will be able to obtain in-transit spectra from $0.5 - 28\,\mu$m. It is unclear what level of contamination from stellar activity will be present in these data [591, 455]. Any of the instruments on JWST can be used to measure the transit depth and The higher resolution of NIRSPEC compared to NIRISS would make this an ideal instrument to observe H_2O and CO_2 at $\lambda < 5.3\,\mu$m. Additionally, MIRI could be used to look at H_2O, CH_4, and O_3 at $\lambda > 5\,\mu$m.

While any of its instruments can be used to measure the transit depth and distinguish between the equilibrium and disequilibrium models, the primary differences for AU Mic b & c lie at $\lambda < 3\,\mu$m. For AU Mic b at $1 \leq \lambda \leq 2\,\mu$m, we estimate differences in transit

depths of ≈ 200 ppm between the two presented models. While for AU Mic c, we estimate differences of ≈ 70 ppm. For AU Mic b & c at $3 \leq \lambda \leq 5\,\mu$m, we estimate differences transit depths of ≈ 160 ppm. All values predicted by these models are above the estimated noise floor for JWST [363, 490, 491].

[534] identified that uncertainties in the UV continuum of exoplanet host stars are the primary drivers of uncertainties of photochemical models for hazy exoplanets. With the addition of AU Mic's continuum in our panchromatic spectrum, we are able to further constrain our uncertainties. In general, it is challenging to detect the continua of relatively faint M stars. Given the proximity of AU Mic, we were able to obtain a significant detection of an M dwarf continuum. Because of this, AU Mic is an essential benchmark star for understanding UV continua of M dwarfs, and accurately modeling transmission spectra for planets around these types of stars.

2.5 Flare-Affiliated Physical Processes

Coronal mass ejections (CMEs) are eruptive explosions of magnetized plasma that are ejected from the surface of a star. The typical ejection speeds of the plasma make these events potentially detrimental to planetary atmosphere's chemistry and escape rate [500, 588, 541, 98]. [500], [541], and [98] have demonstrated that short-duration bursts of stellar energetic particles (SEPs) from M dwarf flares can lead to significant O_3 depletion on an Earth-like planet without a magnetic field.

High-energy particles can also compress planetary magnetospheres [104, 540], strip the atmosphere [295], and produce harmful atmospheric chemical processes detrimental to surface life. [9] highlights it is the associated XUV and energetic particles that are heightened and accelerated during CMEs that have the potential to control a planet's climate and habitability.

However, it is still unclear as to how M dwarf CMEs differ from solar-type CMEs. [16] model magnetic field configurations and CMEs for M dwarfs. For cases of intermediate and

strong strength magnetic fields, it was seen that CMEs can be fully compressed within the magnetic field. This would result in coronal rain rather than being ejected into the local stellar environment. If this is the case for very active M dwarfs, then CMEs would have potentially negligible effects on short-period exoplanets.

Therefore, understanding the occurrence rate of these processes for AU Mic is vital for understanding the conditions of the accompanying planets. In this section we describe constraints on coronal mass ejections and nonthermal protons in the stellar atmosphere of for AU Mic from our COS light curves.

2.5.1 Coronal Mass Ejections Associated with FUV Flares

Detecting CMEs from spatially unresolved stars is challenging. One promising method to detect CMEs is through the process typically referred to as "coronal dimming" [223, 557]. Coronal dimming is caused by the depletion of plasma in the corona of a star as during a CME [247, 524]. This effect is observed in EUV wavelengths on the surface of the Sun via spectral tracers of coronal plasma with $T \sim 10^6$ K [130, 554, 362]. Recently, [557] searched archival EUV and X-ray observations for CMEs associated with flares on other stars via coronal dimming events. They reported three statistically significant ($\sigma \geq 4.4$) dimming events in X-ray observations of AU Mic with depths ranging from $12 - 24\%$.

Following the methodology outlined in [557], we searched for dimming events in our light curves created from the Fe XII, Fe XIX, and Fe XXI emission lines. These lines form at $10^{6.2}$ K, $10^{7.0}$ K, and $10^{7.1}$ K, and trace the quiet and active corona, respectively. We searched for post-flare dimming during Flare D in these Fe lines. Flare D is the most energetic flare for which we could reliably establish a quiet pre-flare and post-flare flux level in the white-light data. We define the pre-flare flux in the interval $t_0 - t = 17114 - 17595$ s, which is 60 s after Flare C ends. Similarly, we define the post-flare flux in the interval $t_0 - t = 18405 - 19215$ s, which is 120 s after Flare D ends.

We find the pre- and post-flare flux in Fe XII to be $(1.33 \pm 0.58) \times 10^{-13}$ and $(1.31 \pm 0.57) \times$

10^{-13} erg s^{-1} cm^{-2}. We find the pre- and post-flare flux in Fe XIX to be $(4.53 \pm 1.93) \times 10^{-13}$ erg s^{-1} cm^{-2} and $(6.18 \pm 2.03) \times 10^{-13}$ erg s^{-1} cm^{-2}. We find the pre- and post-flare flux in Fe XXI to be $(6.09 \pm 1.25) \times 10^{-13}$ erg s^{-1} cm^{-2} and $(4.97 \pm 1.08) \times 10^{-13}$ erg s^{-1} cm^{-2}. This indicates that the pre- and post-flare flux for all iron lines searched in this paper are within a 1σ agreement with each other. Therefore, there is no evidence for coronal dimming associated with Flare D. However, it is not clear whether this non-detection was due to insufficient sensitivity or the lack of a CME. It would be worthwhile to perform a detailed investigation of these two possibilities, but this is beyond the scope of this paper.

2.5.2 Orrall-Zirker Effect

[409] predicted the existence of additional Ly-α emission during flaring events as a result of nonthermal proton beams. Low-energy (< 1 MeV) protons are challenging to detect because of the lack of affiliated X-ray or microwave radiation. However, it is possible that these protons could interact with and excite chromospheric hydrogen atoms. This process would subsequently result in spontaneous decay and the release of a high-energy photon. The high-energy photons are potentially detectable via flux excess in the red wing of Ly-α [409]. This signature would serve as an observational diagnostic of nonthermal proton beams.

Observations of AU Mic with the Goddard High Resolution Spectrograph on HST on 1991 September 3 provided the first statistically significant detection of the Orrall-Zirker Effect on another star. [582] detected an enhancement in the red wing of Ly-α which lasted approximately 3 s and contained flux of at least 10^{30} erg s^{-1}. The excess was seen from $1220 \leq \lambda \leq 1230$ Å, and is in agreement with the predictions of [409]. Subsequent observations of AU Mic found no Ly-α enhancement, and placed an upper limit on the energy of the beam to $\leq 10^{29}$ erg s^{-1} [472].

To determine if there was an affiliated proton beam in our observations, we searched for enhancement in the blue and red wings of Ly-α, respectively. Specifically, we followed the prescription for the observational requirements of a true event presented in Section 2 of [582].

We created 1 second light curves from the third orbit of Visit 1 to search for an affiliated proton beam around both discrete peaks of Flare B from $1202 - 1204\,\text{Å}$ and $1222 - 1227\,\text{Å}$. Although we discovered a stronger count enhancement in the blue-wing than the red-wing, the overall detection of enhancement was non-significant. Therefore, we conclude that there is no evidence for the Orrall-Zirker Effect in the observations presented in this paper. Future HST-STIS observations of Lyα would be a promising avenue to observe this process in bright stars like AU Mic.

2.6 Conclusions

In this paper, we presented HST/COS observations of 13 flares on AU Mic. Our observations spanned ten orbits over two visits. We summarize our main takeaways below.

1. In Section 4.2, we measured flare energies ranging from $1 - 24 \times 10^{30}$ erg. The latter are comparable to the Sun's Carrington event [80]. We discovered a UV flare rate of $\sim 2\,\text{flares/hour}$, which is significantly greater than the one presented in [198]. This discrepancy is likely due to the difference in bandpasses between HST/COS and TESS. Our findings suggest that the FUV flare rate of low-mass stars is higher than in the optical/IR. This is because lower-energy flares are easier to observe in the UV than optical due to decreased photospheric background level.

2. In Section 2.2.2, we created spectroscopic light curves for a range of atmospheric formation temperatures, and found that all flares have the strongest measured energies at $\log_{10}(T_{\text{form}}[\text{K}]) = 4.8$. We also found a ubiquitous and persistent redshift in the line profiles, which could be due to chromospheric condensation [229].

3. In Section 2.2.4, we estimated a blackbody continuum temperature of $\sim 15,000\,\text{K}$ at $\lambda > 1100\,\text{Å}$. However, it is important to note that the quiescent blackbody temperature is comparable or greater than those measured during Flares B, D, J, K, and

M. Therefore, it is not clear that a blackbody is the best model to fit to the flare continuum.

4. Additionally in Section 2.2.4, we identified a steep increase in continuum flux during the observed flares at $\lambda < 1100\,\text{Å}$. This was best-fit with a thermal bremsstrahlung profile with $9 \leq \log_{10}(T) \leq 11$, similar to the measurements presented in [460]. If this interpretation proves correct, there would be an enhancement of EUV flux from AU Mic. This enhancement could produce an increase in the atmospheric mass loss of AU Mic b & c.

5. In Section 2.3, we created a full panchromatic spectrum of AU Mic with archival XMM-Newton, FUSE, IUE, and HARPS-N observations. For wavelengths that have not been observed ($40 \geq \lambda \leq 900\,\text{Å}$), we fit a differential emission measurement (DEM) model to the COS observations presented in this paper. Similarly, We filled in redward of the HARPS-N observations with a PHOENIX stellar model. This SED will be available for use in atmospheric modeling at `https://archive.stsci.edu/prepds/muscles/`.

6. In Section 2.4.1, we calculated an approximate atmospheric mass-loss rate due to photoevaporation for AU Mic b. In the calculation, we used the estimated high-energy luminosity from our panchromatic spectrum and injected flares with energies ranging from $E = 10^{29-34}\,\text{erg}$. We found that flares could temporarily increase the mass-loss for AU Mic b to five orders of magnitude above the current non-detection limits of $10^8\,\text{g}\,\text{s}^{-1}$ [237].

7. In Section 2.4.2, we modeled the optical through mid-IR transmission spectra for AU Mic b & c using our newly created panchromatic spectrum. Additionally, we modeled the temperature-pressure profiles for both planets in quiescence. We estimate transit depth differences between the equilibrium and disequilibrium models of $\approx 70 - 200\,\text{ppm}$, depending on the wavelength range. These differences could be observable with two transits per planet using JWST.

2.6.1 Future Work

The photoevaporative mass-loss estimated in this work both including and excluding flare events suggests AU Mic b & c could lose 30-50% of their present-day atmospheres. Compared to larger, younger planets [e.g. 115, 469], the planets orbiting AU Mic will not undergo significant radial evolution as the system ages. Atmospheric escape of neutral hydrogen may be observed via the identification of absorption in the wings of Ly-α (e.g., Bourrier et al. 69). It is unlikely that flare-driven atmospheric mass loss would be observed due to geometric constraints on the location of the flare with respect to the orbital plane. And, simulations have shown that the radiation from flares alone produce only minor ($< 0.1\%$) differences in transit shapes [230].

However, it is possible in the presence of a flare and affiliated CME that these processes will be detectable for AU Mic because it is close and bright. Future transit observations of AU Mic b & c would have the required signal-to-noise to confidently detect increases in Ly-α depths. This would correspond to mass loss rates of $\dot{M} \geq 10^{10}\,\mathrm{g\,s^{-1}}$ (Rockcliffe et al. in prep). Unfortunately, contamination in Ly-α from the interstellar medium makes constraining the atmospheric composition of these planets challenging. Simultaneous observations of other dominant atmospheric species such as the metastable He I triplet feature at 10830 Å, or the strong O I and C II lines in the FUV would provide additional constraints on the atmospheric composition.

The effects of flares and XUV irradiation have also been considered for old ($t_{\mathrm{age}} > 1$ Gyr) stars. The contribution of flares to the high-energy radiation has been shown to remove $\sim$90 Earth-atmospheres within a Gyr for old and inactive M dwarfs [185]. The full extent of flare-driven atmospheric removal for more massive planets ($M > 10 M_{\oplus}$) with H_2-rich envelopes such as Jupiter and Neptune has not been fully investigated. Modeling the differences in observed transmission spectra during flares of varying energies would help interpret upcoming JWST observations of AU Mic b & c.

Understanding the contribution of thermal and non-thermal processes to atmospheric

mass loss is unknown for exoplanets. The detection of radio emission from AU Mic b & c would yield constraints on the planetary magnetic field strengths and, in turn, how well shielded the planets are from strong stellar winds and CMEs. While there is weak evidence of radio emission from hot Jupiters [e.g. 302, 120, 390], AU Mic has potential. [264] simulated Alfvén wave-driven stellar wind models to investigate potential auroral signals in the stellar corona from interactions with AU Mic b & c. In the low mass-loss rate ($\sim 27\dot{M}_{\odot}$) scenario, AU Mic b & c are orbiting sub-Alfvénifcally, and AU Mic b could produce time-varying radio emission from $\sim 10\,\mathrm{Mz}$ $-3\,\mathrm{GHz}$ at detectable levels.

The strong FUV continuum increase at $\lambda \leq 1100\,\text{Å}$ is readily seen during flares in our HST/COS observations (Figure 2.6). We tentatively attribute this observational feature to thermal bremsstrahlung emission. Flare observations in the COS FUV modes covering even shorter wavelengths would help constrain the overall contribution of thermal bremsstrahlung to the flare energy output. However, the high-energy luminosity calculated from our DEM model and used as an input to our atmospheric mass-loss calculation does not account for this additional emission. Accurate treatment of this additional emission from thermal bremsstrahlung may result in more stringent constraints on the contribution of flare energies to young atmospheric removal.

2.7 Supplemental Material

2.7.1 Full Spectroscopic Light Curves

We used the C III at $\lambda = 1175.95\,\text{Å}$ and Si III $\lambda = 1294.55\,\text{Å}$ spectroscopic light curves to identify flares in our data set (Figure 2.11). These are the same methods presented in [582].

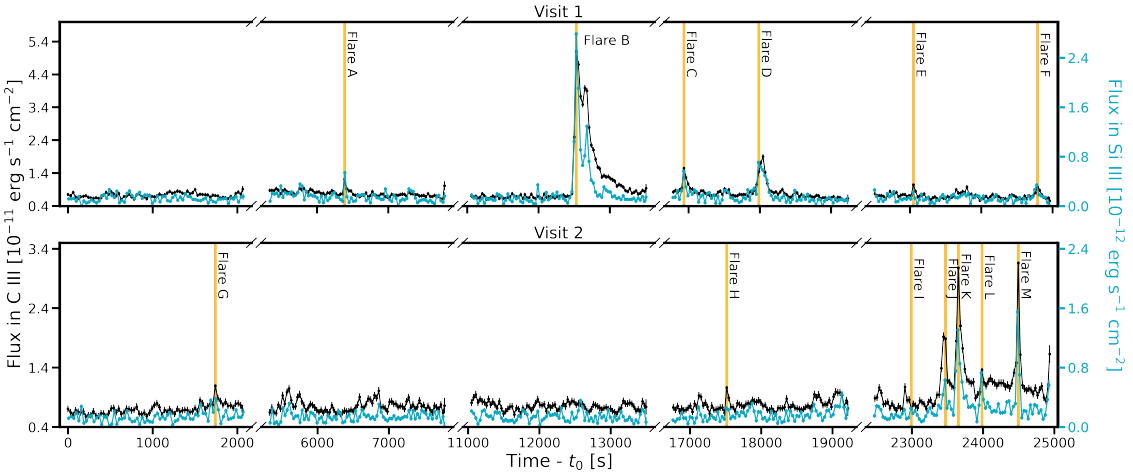

Figure 2.11 Light curves of the C III emission line at 1175.95 Å (black) and the Si III emission line at 1294.55 Å (blue) used to identify flares in the data. Flares identified are labeled with vertical orange lines.

2.7.2 Quiescent Spectrum

We present the entire mean quiescent spectrum for AU Mic, with labeled identified emission features, in Figure 2.12. We grouped dense regions of lines together in the Figure, and provide measured flux values for all identified lines in Table 2.3. Tables 2.3 and 2.4 contain all identified lines with the following parameters: the measured rest wavelength ($\lambda_{\rm rest}$), the observed wavelength ($\lambda_{\rm obs}$), the velocity shift between rest and observed wavelengths in [km s^{-1}], the measured flux in quiescence and during Flare B in 10^{-15}erg s^{-1} cm^{-2}, and the full-width half-maximum (FWHM)[km s^{-1}] of the line in quiescence and during Flare B.

2.7.3 Continuum Regions

We identified the continuum regions of the spectra by-eye, and defined these regions to have no emission features. These are the following wavelength regions we define as the continuum: [1067.506, 1070.062], [1074.662, 1076.533], [1078.881, 1082.167], [1087.828, 1090.035], [1103.787, 1107.862], [1110.500, 1112.946], [1113.618, 1117.377], [1119.548, 1121.622], [1125.255, 1126.923], [1140.873, 1145.141], [1146.285, 1151.544], [1152.602, 1155.579], [1159.276, 1163.222],

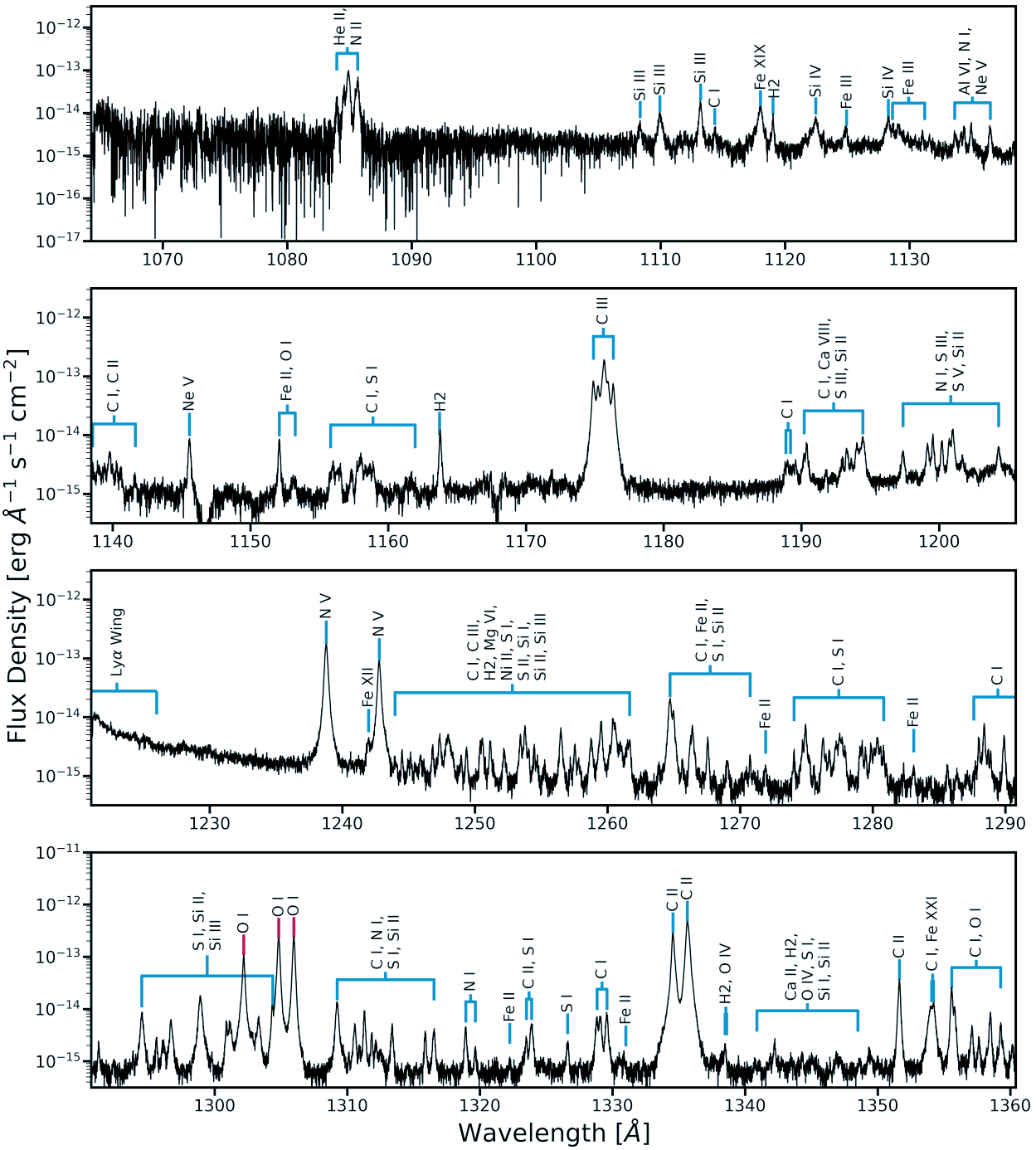

Figure 2.12 The average quiescent spectrum for AU Mic. We removed time intervals that fall within the highlighted yellow regions in Figure 2.1. We labeled all known emission lines seen in our spectrum. Emission features marked with pink lines (O I triplet) are partially contaminated by air glow. We present all measured line centers and flux values for these emission features in Table 2.3.

[1164.565, 1173.959], [1178.669, 1188.363], [1195.162, 1196.864], [1201.748, 1203.862], [1227.056, 1236.921], [1262.399, 1263.967], [1268.559, 1273.974], [1281.396, 1287.493], [1290.494, 1293.803], [1307.064, 1308.703], [1319.494, 1322.910], [1330.349, 1332.884], [1337.703, 1341.813], and [1341.116, 1350.847] Å.

Table 2.3: Complete line list for emission features present in our *Hubble*/COS spectra for AU Mic in quiescence.

Ion	$\lambda_{\rm rest}$ [Å]	$\lambda_{\rm obs}$ [Å]	Velocity Shift [km s^{-1}]	Flux (Quiescent) [10^{-15} erg s^{-1} cm^{-2}]	FWHM (Quiescent) [10^{-15} erg s^{-1} cm^{-2}]
N II	1083.99	1083.99	-2.67	4.26 ± 5.4	0.26 ± 0.02
N II *	1084.58	1084.57	-2.67	8.22 ± 4.54	0.29 ± 0.02
N II	1085.54	1085.56	5.33	16.98 ± 5.17	0.32 ± 0.01
N II	1085.71	1085.66	-13.32	16.98 ± 5.17	0.32 ± 0.01
Si III *	1108.36	1108.35	-2.61	2.22 ± 0.82	0.51 ± 0.03
Si III *	1109.94	1109.95	0.0	3.69 ± 0.75	0.45 ± 0.01
Si III *	1113.2	1113.21	0.0	4.92 ± 0.63	0.3 ± 0.01
C I	1114.39	1114.35	-10.38	1.64 ± 0.59	0.62 ± 0.05
Fe XIX *	1118.06	1118.02	-12.94	5.43 ± 0.52	0.45 ± 0.01
Si IV *	1122.49	1122.47	-5.15	3.29 ± 0.45	0.57 ± 0.02
Fe III	1124.88	1124.94	18.0	2.06 ± 0.44	0.6 ± 0.03
Si IV *	1128.34	1128.3	-12.82	3.06 ± 0.36	0.54 ± 0.03
Al VI	1133.68	1133.62	-17.86	1.26 ± 0.31	0.49 ± 0.03
N I	1134.16	1134.14	-5.1	0.73 ± 0.21	0.3 ± 0.02
N I	1134.4	1134.39	-2.55	0.91 ± 0.21	0.22 ± 0.01
N I	1134.98	1134.95	-7.65	1.52 ± 0.3	0.37 ± 0.02
Ne V *	1136.49	1136.49	0.0	1.38 ± 0.29	0.36 ± 0.01
C I	1138.95	1138.95	0.0	0.97 ± 0.23	0.46 ± 0.03

Table 2.3 continued.

Ion	λ_{rest}	λ_{obs}	Velocity Shift	Flux (Quiescent)	FWHM (Quiescent)
	[Å]	[Å]	[km s^{-1}]	[10^{-15} erg s^{-1} cm^{-2}]	[10^{-15} erg s^{-1} cm^{-2}]
C I	1139.81	1139.78	-7.61	1.61 ± 0.25	0.42 ± 0.02
C I	1140.35	1140.26	-22.83	0.96 ± 0.23	0.48 ± 0.05
C I	1140.62	1140.6	-5.07	0.8 ± 0.23	0.43 ± 0.03
C II *	1141.68	1141.64	-10.14	0.63 ± 0.23	0.46 ± 0.04
Ne V *	1145.58	1145.57	-2.53	1.95 ± 0.22	0.24 ± 0.01
C I	1157.4	1157.35	-12.5	0.93 ± 0.22	0.52 ± 0.03
C III	1174.88	1174.9	4.92	24.01 ± 0.31	0.29 ± 0.01
C III	1175.24	1175.24	0.0	17.09 ± 0.19	0.35 ± 0.02
C III	1176.37	1176.34	-7.38	21.45 ± 0.31	0.31 ± 0.01
S III *	1190.17	1190.2	7.29	1.25 ± 0.14	0.57 ± 0.06
C I	1191.84	1191.79	-14.56	0.99 ± 0.16	0.67 ± 0.06
C I	1193.0	1192.99	-2.42	1.25 ± 0.14	0.51 ± 0.04
C I	1193.29	1193.3	2.42	1.51 ± 0.13	0.32 ± 0.01
C I	1193.68	1193.61	-16.96	0.86 ± 0.11	0.36 ± 0.03
Ca VIII *	1194.04	1194.04	0.0	2.16 ± 0.14	0.43 ± 0.02
Si II *	1194.45	1194.46	2.42	2.96 ± 0.16	0.42 ± 0.01
Si II *	1197.4	1197.37	-7.25	1.96 ± 0.17	0.46 ± 0.02
S V *	1199.2	1199.16	-9.65	2.26 ± 0.16	0.44 ± 0.02
N I	1199.55	1199.55	-2.41	2.3 ± 0.14	0.29 ± 0.01
N I	1200.22	1200.2	-4.82	1.98 ± 0.14	0.29 ± 0.01
N I	1200.71	1200.75	9.64	2.05 ± 0.12	0.33 ± 0.01
S III	1200.99	1200.99	-2.41	3.11 ± 0.14	0.34 ± 0.02
S III *	1201.73	1201.69	-12.04	1.95 ± 0.16	0.77 ± 0.05

Table 2.3 continued.

Ion	λ_{rest}	λ_{obs}	Velocity Shift	Flux (Quiescent)	FWHM (Quiescent)
	[Å]	[Å]	[km s^{-1}]	[10^{-15} erg s^{-1} cm^{-2}]	[10^{-15} erg s^{-1} cm^{-2}]
S V *	1204.3	1204.31	2.4	2.49 ± 0.16	0.53 ± 0.02
N V *	1238.82	1238.79	-7.01	53.45 ± 0.35	0.26 ± 0.0
Fe XII *	1241.95	1241.98	6.99	1.69 ± 0.16	0.56 ± 0.03
N V *	1242.8	1242.79	-4.66	27.19 ± 0.3	0.26 ± 0.0
C I	1244.51	1244.51	0.0	0.58 ± 0.13	0.31 ± 0.02
C I	1246.87	1246.81	-16.24	0.82 ± 0.14	0.32 ± 0.02
C III	1247.41	1247.35	-16.23	1.3 ± 0.14	0.32 ± 0.01
C I	1247.86	1247.94	18.55	2.71 ± 0.21	0.68 ± 0.02
C I	1248.0	1247.99	-2.32	2.7 ± 0.21	0.71 ± 0.02
C I	1249.41	1249.37	-9.26	0.84 ± 0.16	0.36 ± 0.02
S II *	1250.58	1250.56	-4.63	1.51 ± 0.16	0.41 ± 0.02
Si II *	1251.16	1251.16	0.0	1.04 ± 0.15	0.33 ± 0.02
C I	1252.21	1252.21	-2.31	0.86 ± 0.15	0.39 ± 0.02
C I	1253.47	1253.44	-6.92	1.3 ± 0.15	0.36 ± 0.02
S II *	1253.8	1253.78	-2.31	1.5 ± 0.13	0.26 ± 0.01
C I	1254.51	1254.48	-6.92	0.7 ± 0.13	0.29 ± 0.02
Si I	1255.28	1255.27	-4.61	0.51 ± 0.14	0.46 ± 0.03
Mg VI *	1256.37	1256.48	25.33	1.83 ± 0.19	0.32 ± 0.01
C I	1256.5	1256.49	0.0	0.7 ± 0.12	0.24 ± 0.01
Si I	1258.78	1258.78	0.0	1.39 ± 0.17	0.38 ± 0.01
S II *	1259.53	1259.52	-2.3	2.62 ± 0.19	0.34 ± 0.01
Si II *	1260.44	1260.43	0.0	3.86 ± 0.19	0.48 ± 0.02
C I	1261.72	1261.67	-11.46	1.81 ± 0.19	0.54 ± 0.02

Table 2.3 continued.

Ion	λ_{rest}	λ_{obs}	Velocity Shift	Flux (Quiescent)	FWHM (Quiescent)
	[Å]	[Å]	[km s^{-1}]	[10^{-15} erg s^{-1} cm^{-2}]	[10^{-15} erg s^{-1} cm^{-2}]
Si II *	1264.74	1264.72	-4.57	8.82 ± 0.26	0.48 ± 0.01
Si II	1265.0	1264.97	-6.86	8.56 ± 0.24	0.48 ± 0.01
C I	1267.6	1267.56	-9.13	0.95 ± 0.15	0.24 ± 0.01
S I	1269.06	1269.03	-6.84	0.65 ± 0.16	0.46 ± 0.02
S I	1270.78	1270.75	-6.83	0.5 ± 0.13	0.31 ± 0.02
Fe II	1271.98	1271.92	-13.65	0.47 ± 0.14	0.45 ± 0.03
C I	1274.11	1274.07	-11.35	0.63 ± 0.14	0.34 ± 0.02
C I	1274.98	1274.93	-11.34	1.59 ± 0.13	0.25 ± 0.01
C I	1276.29	1276.26	-9.07	1.25 ± 0.15	0.36 ± 0.02
C I	1276.75	1276.73	-4.53	0.77 ± 0.14	0.43 ± 0.03
C I	1279.5	1279.46	-9.04	0.62 ± 0.12	0.28 ± 0.02
C I	1279.89	1279.88	-2.26	0.67 ± 0.11	0.26 ± 0.02
C I	1280.33	1280.35	4.52	1.08 ± 0.12	0.33 ± 0.02
C I	1280.85	1280.82	-6.78	0.63 ± 0.12	0.3 ± 0.02
Fe II	1283.06	1283.09	4.51	0.43 ± 0.14	0.42 ± 0.02
C I	1288.04	1288.01	-6.74	1.0 ± 0.14	0.31 ± 0.02
C I	1288.42	1288.41	-4.49	1.56 ± 0.14	0.23 ± 0.01
C I	1288.71	1288.7	-2.24	0.43 ± 0.1	0.23 ± 0.02
C I	1288.92	1288.89	-6.73	0.43 ± 0.11	0.22 ± 0.02
C I	1289.98	1289.9	-15.7	1.18 ± 0.18	0.25 ± 0.01
C I	1291.3	1291.26	-8.96	0.63 ± 0.16	0.45 ± 0.03
Si III	1294.58	1294.5	-17.88	2.82 ± 0.21	0.34 ± 0.01
S I	1295.65	1295.61	-8.93	0.8 ± 0.17	0.4 ± 0.03

Table 2.3 continued.

Ion	λ_{rest}	λ_{obs}	Velocity Shift	Flux (Quiescent)	FWHM (Quiescent)
	[Å]	[Å]	[km s^{-1}]	[10^{-15} erg s^{-1} cm^{-2}]	[10^{-15} erg s^{-1} cm^{-2}]
S I	1296.16	1296.1	-13.39	0.86 ± 0.16	0.47 ± 0.02
Si III	1296.77	1296.69	-20.08	1.81 ± 0.17	0.33 ± 0.01
Si III	1298.96	1298.93	-8.91	6.83 ± 0.28	0.34 ± 0.01
S I	1300.91	1300.9	-2.22	2.99 ± 0.22	0.63 ± 0.02
Si III	1303.32	1303.31	-2.22	2.44 ± 0.19	0.44 ± 0.01
Si II *	1304.37	1304.37	0.0	2.62 ± 0.16	0.26 ± 0.01
Si II *	1309.28	1309.23	-11.05	4.48 ± 0.24	0.28 ± 0.01
N I	1310.54	1310.57	6.62	1.26 ± 0.16	0.28 ± 0.01
C I	1310.64	1310.56	-17.66	1.77 ± 0.15	0.19 ± 0.01
N I	1310.94	1310.9	-8.83	0.5 ± 0.13	0.45 ± 0.06
C I	1311.36	1311.29	-17.65	1.77 ± 0.15	0.19 ± 0.01
C I	1311.92	1311.85	-15.44	0.73 ± 0.14	0.24 ± 0.01
C I	1313.39	1313.38	-2.2	1.28 ± 0.19	0.27 ± 0.01
C I	1315.88	1315.89	2.2	0.8 ± 0.15	0.23 ± 0.01
S I	1316.54	1316.54	-2.2	1.07 ± 0.17	0.29 ± 0.01
N I	1318.98	1318.93	-10.97	1.08 ± 0.17	0.25 ± 0.01
N I	1319.68	1319.65	-6.58	0.5 ± 0.16	0.38 ± 0.02
S I	1323.52	1323.51	-4.37	0.74 ± 0.15	0.34 ± 0.02
C II *	1323.93	1323.9	-4.37	1.52 ± 0.17	0.31 ± 0.01
S I	1326.65	1326.61	-6.54	0.61 ± 0.15	0.31 ± 0.01
C I	1328.83	1328.83	0.0	1.35 ± 0.13	0.27 ± 0.01
C I	1329.1	1329.08	-2.18	1.89 ± 0.15	0.31 ± 0.01
C I	1329.58	1329.57	0.0	2.17 ± 0.18	0.28 ± 0.01

Table 2.3 continued.

Ion	λ_{rest}	λ_{obs}	Velocity Shift	Flux (Quiescent)	FWHM (Quiescent)
	[Å]	[Å]	[km s^{-1}]	[10^{-15} erg s^{-1} cm^{-2}]	[10^{-15} erg s^{-1} cm^{-2}]
C II *	1334.53	1334.56	6.5	76.88 ± 0.39	0.24 ± 0.0
C II *	1335.71	1335.64	-15.16	149.19 ± 0.44	0.29 ± 0.0
C II *	1351.66	1351.64	-4.28	7.39 ± 0.26	0.19 ± 0.0
Fe XXI *	1354.05	1354.07	2.14	7.68 ± 0.31	0.59 ± 0.01
C I	1354.29	1354.2	-21.36	7.69 ± 0.31	0.59 ± 0.01
C I	1355.84	1355.79	-8.53	7.12 ± 0.28	0.33 ± 0.01
C I	1357.13	1357.11	-4.26	1.31 ± 0.2	0.34 ± 0.01
C I	1357.66	1357.63	-6.39	0.81 ± 0.18	0.36 ± 0.02
C I	1359.28	1359.27	-2.13	1.66 ± 0.22	0.41 ± 0.02

Table 2.4: Complete line list for emission features present in our *Hubble*/COS spectra for AU Mic during Flare B.

Ion	λ_{rest}	λ_{obs}	Flux (Flare B)	FWHM (Flare B)
	[Å]	[Å]	[10^{-15} erg s^{-1} cm^{-2}]	[10^{-15} erg s^{-1} cm^{-2}]
N II	1083.99	1083.99	5.82 ± 21.47	0.17 ± 0.03
N II *	1084.58	1084.57	10.96 ± 17.9	0.33 ± 0.09
N II	1085.54	1085.56	21.37 ± 20.68	0.36 ± 0.04
N II	1085.71	1085.66	21.37 ± 20.68	0.36 ± 0.04
Si III *	1108.36	1108.35	4.81 ± 3.26	0.45 ± 0.04
Si III *	1109.94	1109.95	7.29 ± 3.0	0.36 ± 0.02
Si III *	1113.2	1113.21	11.27 ± 2.58	0.46 ± 0.03
C I	1114.39	1114.35	2.09 ± 2.37	0.49 ± 0.07

Table 2.4 continued.

Ion	$\lambda_{\rm rest}$ [Å]	$\lambda_{\rm obs}$ [Å]	Flux (Flare B) [10^{-15} erg s^{-1} cm^{-2}]	FWHM (Flare B) [10^{-15} erg s^{-1} cm^{-2}]
Fe XIX *	1118.06	1118.02	5.34 ± 2.07	0.5 ± 0.04
Si IV *	1122.49	1122.47	6.19 ± 1.82	0.71 ± 0.07
Fe III	1124.88	1124.94	3.37 ± 1.75	0.58 ± 0.06
Si IV *	1128.34	1128.3	6.21 ± 1.45	0.5 ± 0.05
Al VI	1133.68	1133.62	1.54 ± 1.23	1.68 ± 2.35
N I	1134.16	1134.14	0.9 ± 0.86	0.77 ± 1.18
N I	1134.4	1134.39	1.07 ± 0.86	0.33 ± 0.09
N I	1134.98	1134.95	2.02 ± 1.2	0.29 ± 0.03
Ne V *	1136.49	1136.49	1.62 ± 1.16	0.7 ± 0.17
C I	1138.95	1138.95	1.31 ± 0.92	0.47 ± 0.13
C I	1139.81	1139.78	2.44 ± 0.99	0.38 ± 0.04
C I	1140.35	1140.26	1.06 ± 0.93	0.38 ± 0.07
C I	1140.62	1140.6	0.88 ± 0.93	0.33 ± 0.07
C II *	1141.68	1141.64	0.78 ± 0.91	1.28 ± 2.11
Ne V *	1145.58	1145.57	2.15 ± 0.88	0.27 ± 0.02
C I	1157.4	1157.35	1.41 ± 0.88	0.49 ± 0.06
C III	1174.88	1174.9	66.86 ± 1.45	0.45 ± 0.02
C III	1175.24	1175.24	43.11 ± 0.95	0.52 ± 0.04
C III	1176.37	1176.34	56.99 ± 1.38	0.57 ± 0.02
S III *	1190.17	1190.2	2.35 ± 0.56	0.54 ± 0.13
C I	1191.84	1191.79	1.67 ± 0.63	0.46 ± 0.06
C I	1193.0	1192.99	2.0 ± 0.57	0.48 ± 0.08
C I	1193.29	1193.3	2.44 ± 0.52	1.0 ± 0.99

Table 2.4 continued.

Ion	$\lambda_{\rm rest}$ [Å]	$\lambda_{\rm obs}$ [Å]	Flux (Flare B) [10^{-15} erg s^{-1} cm^{-2}]	FWHM (Flare B) [10^{-15} erg s^{-1} cm^{-2}]
C I	1193.68	1193.61	1.66 ± 0.46	0.54 ± 0.29
Ca VIII *	1194.04	1194.04	3.93 ± 0.58	0.4 ± 0.03
Si II *	1194.45	1194.46	5.72 ± 0.65	0.44 ± 0.04
Si II *	1197.4	1197.37	3.23 ± 0.67	0.53 ± 0.05
S V *	1199.2	1199.16	3.23 ± 0.62	0.51 ± 0.04
N I	1199.55	1199.55	3.4 ± 0.57	0.35 ± 0.03
N I	1200.22	1200.2	3.09 ± 0.56	0.48 ± 0.06
N I	1200.71	1200.75	3.37 ± 0.51	0.58 ± 0.16
S III	1200.99	1200.99	6.44 ± 0.59	0.44 ± 0.04
S III *	1201.73	1201.69	3.95 ± 0.66	0.73 ± 0.1
S V *	1204.3	1204.31	6.2 ± 0.67	0.72 ± 0.06
N V *	1238.82	1238.79	85.24 ± 1.51	0.35 ± 0.01
Fe XII *	1241.95	1241.98	3.16 ± 0.65	0.8 ± 0.15
N V *	1242.8	1242.79	41.19 ± 1.23	0.32 ± 0.01
C I	1244.51	1244.51	0.97 ± 0.52	0.35 ± 0.05
C I	1246.87	1246.81	1.35 ± 0.57	0.4 ± 0.05
C III	1247.41	1247.35	3.42 ± 0.59	0.32 ± 0.02
C I	1247.86	1247.94	3.85 ± 0.83	0.99 ± 0.11
C I	1248.0	1247.99	3.72 ± 0.83	1.16 ± 0.19
C I	1249.41	1249.37	1.37 ± 0.64	0.41 ± 0.05
S II *	1250.58	1250.56	2.69 ± 0.65	0.43 ± 0.03
Si II *	1251.16	1251.16	1.78 ± 0.6	0.33 ± 0.02
C I	1252.21	1252.21	1.13 ± 0.6	0.31 ± 0.03

Table 2.4 continued.

Ion	$\lambda_{\rm rest}$ [Å]	$\lambda_{\rm obs}$ [Å]	Flux (Flare B) [10^{-15} erg s^{-1} cm^{-2}]	FWHM (Flare B) [10^{-15} erg s^{-1} cm^{-2}]
C I	1253.47	1253.44	1.84 ± 0.58	0.37 ± 0.04
S II *	1253.8	1253.78	2.28 ± 0.51	0.3 ± 0.02
C I	1254.51	1254.48	1.01 ± 0.5	0.31 ± 0.03
Si I	1255.28	1255.27	0.61 ± 0.57	1.02 ± 0.88
Mg VI *	1256.37	1256.48	2.51 ± 0.74	0.4 ± 0.02
C I	1256.5	1256.49	1.16 ± 0.47	0.43 ± 0.14
Si I	1258.78	1258.78	2.34 ± 0.66	0.42 ± 0.03
S II *	1259.53	1259.52	4.62 ± 0.76	0.48 ± 0.02
Si II *	1260.44	1260.43	6.25 ± 0.77	0.55 ± 0.03
C I	1261.72	1261.67	2.84 ± 0.74	0.61 ± 0.05
Si II *	1264.74	1264.72	14.0 ± 1.05	0.6 ± 0.02
Si II	1265.0	1264.97	13.36 ± 0.98	0.58 ± 0.02
C I	1267.6	1267.56	1.26 ± 0.59	0.29 ± 0.02
S I	1269.06	1269.03	0.75 ± 0.62	0.44 ± 0.06
S I	1270.78	1270.75	0.76 ± 0.52	0.4 ± 0.06
Fe II	1271.98	1271.92	0.64 ± 0.57	0.48 ± 0.1
C I	1274.11	1274.07	0.96 ± 0.57	0.3 ± 0.03
C I	1274.98	1274.93	2.19 ± 0.54	0.2 ± 0.02
C I	1276.29	1276.26	2.03 ± 0.6	0.35 ± 0.03
C I	1276.75	1276.73	1.36 ± 0.56	0.51 ± 0.08
C I	1279.5	1279.46	1.05 ± 0.47	0.28 ± 0.04
C I	1279.89	1279.88	1.24 ± 0.46	0.26 ± 0.04
C I	1280.33	1280.35	1.64 ± 0.48	0.3 ± 0.03

Table 2.4 continued.

Ion	$\lambda_{\rm rest}$ [Å]	$\lambda_{\rm obs}$ [Å]	Flux (Flare B) [10^{-15} erg s^{-1} cm^{-2}]	FWHM (Flare B) [10^{-15} erg s^{-1} cm^{-2}]
C I	1280.85	1280.82	1.12 ± 0.48	0.4 ± 0.09
Fe II	1283.06	1283.09	0.87 ± 0.56	0.42 ± 0.07
C I	1288.04	1288.01	1.4 ± 0.55	0.31 ± 0.03
C I	1288.42	1288.41	2.34 ± 0.56	0.22 ± 0.01
C I	1288.71	1288.7	0.69 ± 0.39	0.47 ± 0.4
C I	1288.92	1288.89	0.7 ± 0.42	0.26 ± 0.05
C I	1289.98	1289.9	1.68 ± 0.7	0.29 ± 0.02
C I	1291.3	1291.26	0.72 ± 0.64	0.53 ± 0.1
Si III	1294.58	1294.5	7.14 ± 0.86	0.44 ± 0.02
S I	1295.65	1295.61	1.65 ± 0.67	0.53 ± 0.07
S I	1296.16	1296.1	1.89 ± 0.65	0.79 ± 0.2
Si III	1296.77	1296.69	5.07 ± 0.69	0.49 ± 0.03
Si III	1298.96	1298.93	16.83 ± 1.16	0.5 ± 0.01
S I	1300.91	1300.9	6.55 ± 0.89	0.74 ± 0.04
Si III	1303.32	1303.31	6.66 ± 0.78	0.64 ± 0.04
Si II *	1304.37	1304.37	4.76 ± 0.64	0.45 ± 0.05
Si II *	1309.28	1309.23	7.38 ± 0.97	0.49 ± 0.02
N I	1310.54	1310.57	2.07 ± 0.62	0.29 ± 0.02
C I	1310.64	1310.56	2.76 ± 0.62	0.22 ± 0.01
N I	1310.94	1310.9	0.92 ± 0.5	0.7 ± 0.53
C I	1311.36	1311.29	2.76 ± 0.62	0.22 ± 0.01
C I	1311.92	1311.85	1.07 ± 0.54	0.23 ± 0.02
C I	1313.39	1313.38	1.73 ± 0.75	0.32 ± 0.03

Table 2.4 continued.

Ion	$\lambda_{\rm rest}$ [Å]	$\lambda_{\rm obs}$ [Å]	Flux (Flare B) [10^{-15} erg s^{-1} cm^{-2}]	FWHM (Flare B) [10^{-15} erg s^{-1} cm^{-2}]
C I	1315.88	1315.89	1.11 ± 0.61	0.26 ± 0.03
S I	1316.54	1316.54	1.44 ± 0.67	0.31 ± 0.02
N I	1318.98	1318.93	1.6 ± 0.68	0.3 ± 0.02
N I	1319.68	1319.65	0.72 ± 0.64	0.49 ± 0.1
S I	1323.52	1323.51	1.28 ± 0.59	0.71 ± 0.24
C II *	1323.93	1323.9	2.65 ± 0.67	0.37 ± 0.02
S I	1326.65	1326.61	1.14 ± 0.6	0.3 ± 0.03
C I	1328.83	1328.83	1.94 ± 0.54	0.32 ± 0.04
C I	1329.1	1329.08	2.58 ± 0.6	0.39 ± 0.04
C I	1329.58	1329.57	3.23 ± 0.73	0.33 ± 0.02
C II *	1334.53	1334.56	131.83 ± 1.74	0.36 ± 0.01
C II *	1335.71	1335.64	222.51 ± 1.96	0.37 ± 0.01
C II *	1351.66	1351.64	7.61 ± 1.01	0.21 ± 0.01
Fe XXI *	1354.05	1354.07	7.83 ± 1.21	0.71 ± 0.03
C I	1354.29	1354.2	7.87 ± 1.21	0.71 ± 0.03
C I	1355.84	1355.79	9.31 ± 1.1	0.43 ± 0.02
C I	1357.13	1357.11	1.85 ± 0.78	0.42 ± 0.03
C I	1357.66	1357.63	1.26 ± 0.7	0.43 ± 0.05
C I	1359.28	1359.27	2.29 ± 0.87	0.46 ± 0.03

CHAPTER 3

Hα AND CA II INFRARED TRIPLET VARIATIONS DURING A TRANSIT OF THE 23 MYR PLANET V1298 TAU C

Young planets provide valuable insights into the early stages of planet formation and evolution. Through transit missions like *K2* [245] and *TESS* [Transiting Exoplanet Survey Satellite; 465] the population of young transiting planets (here defined as < 100 Myr) has grown to approximately a dozen [116, 351, 50, 397, 352, 440, 469].[1] These planets are key to understanding planetary migration, atmospheric evolution, and measuring atmospheric mass-loss rate due to photoevaporation.

3.0.1 Obliquity Measurements

Close-in transiting exoplanets have brought into question the mechanisms in which they get there. Measuring the obliquity, λ, or the relative angle between the spin of the star and orbit of the planet [291], can yield insights into different migratory paths. A low-obliquity hints at a smooth disk migration history [202, 176], while binary companions or nearby stars in stellar birth clusters can torque planets to a high obliquity over millions of years [152].

Such measurements have only just begun for young systems. The recently discovered 20 Myr planet AU Mic b [440] has been the subject of significant follow-up. All independent studies have measured a low obliquity [5, 237, 361, 419], suggesting the planet formed beyond the ice-line within the protoplanetary disk and experienced a smooth migration inward.

Similar studies of spin-orbit alignment have been completed for DS Tuc Ab, a planet in a slightly older (35-45 Myr) system, in a known binary [397, 377, 598]. The results from both studies concluded the planet has a low obliquity and that the migration was not significantly torqued through Kozai-Lidov oscillations by DS Tuc B. This is additionally supported by the fact that the age of the system is younger than the timescale required for Kozai-Lidov interactions [377]. V1298 Tau has no known companions and thus any spin-orbit

1. This work is based on [163], which was co-authored by Benjamin T. Montet, Marshall C. Johnson, Jacob L. Bean, Trevor J. David, Michael A. Gully-Santiago, John H. Livingston, and Rodrigo Luger. A. Feinstein is the PI of the Gemini-N program GN-2019B-FT-215, which obtained the observations of V1298 Tau. A. Feinstein reduced and analyzed the data presented in this chapter and modeled the Hα variability in the presence of stellar inhomogeneities. M. Johnson is the lead developer of `MISTTBORN`, the doppler tomography software used in this work. All other authors are co-Is on the Gemini-N program GN-2019B-FT-215.

misalignment would hint towards potential torquing of the disk due to neighboring stars in the birth cluster.

3.0.2 Photoevaporation & Young Stellar Activity

Photoevaporation of young close-in planets is one of the leading explanations for the "radius gap" of transiting planets [415, 189, 552, 46]. This gap is between a bimodal distribution of small planets, centered at 1.3 and 2.4 $R_{\oplus}$ with a distinct lack of planets in between. However, early studies did not account for the ages of the systems; [57] presented the first analysis of the planet-radius distribution while accounting for such ages. They found tentative evidence of an age dependence of the planet radius distribution, demonstrating that the number of super-Earths ($R/R_{\oplus} < 1.8$) increases with age, assuming a fixed radius gap location. This could be attributed to a core-powered mass-loss mechanism [218], which may continue for the first 1 Gyr [477]. However, the general contributions of atmospheric removal from photoevaporation and core-powered mass-loss is currently unknown. While photoevaporation rate is a function of flux, these young transiting planets have short orbital periods and allow us to probe the most dramatic environments for atmospheric removal.

Atmospheric photoevaporation is driven by the high energy irradiation from young stars [293, 412]. The effects are particularly dramatic in the first 100 Myr where stellar XUV emission is higher and planets are still contracting, which makes their atmospheres more vulnerable to mass loss [452, 158]. Using *GALEX* observations, [510] found that early M stars remain at high, saturated levels of NUV and FUV flux for the first ∼650 Myr. The same relation was found of K stars [464].The activity lifetime for low-mass stars is longer than that of solar-type stars. However, the higher levels of XUV flux makes photoevaporation more efficient for planets around low-mass stars [477], thus the evolution of planetary radii is faster [414].

An increase in magnetic activity leads to elevated UV/X-Ray radiation in young stars, manifests itself in larger spot coverage, and results in increased photometric variability [159].

Several detailed studies of T Tauri stars have estimated that spots cover 29-41% of the less spotted hemisphere and 61-67% of the more spotted hemisphere [206], with the extreme case of LkCa 4 with of $\sim 80\%$ spot coverage [214]. Larger studies of young stars have also seen a lack of phase dependence for flares, another proxy for magnetic activity, indicating similar levels of high spot coverage across both hemispheres [162]. For detailed spectroscopic studies of young planets (e.g. studying their spin-orbit alignment or atmospheric characterization), it is crucial to understand the underlying starspot and active region coverage.

3.0.3 V1298 Tau

V1298 Tau is a 23 Myr pre-main sequence K star ($M_\star/M_\odot = 1.101$; $R_\star/R_\odot = 1.345$) hosting four known transiting planets [115, 117] observed in *K2* Campaign 4 [245]. V1298 Tau is the first known young transiting multi-planet system. V1298 Tau was first identified as a young star via strong X-ray emission observed with *ROSAT* and strong Li I 670.8 nm absorption [575, 576]. V1298 Tau belongs to a young association in the foreground of the Taurus-Auriga star-forming complex [405] with an estimated age of 20-30 Myr based on comparison to empirical and theoretical isochrones [333, 117]. V1298 Tau c ($R \sim 5.59 R_\oplus$) and d ($R \sim 6.41 R_\oplus$) are predicted to evolve to sub-Neptunes ($< 4 R_\oplus$) or super-Earths ($< 2 R_\oplus$), depending on the XUV evolution of the host star, after 5 Gyr [115, 447]. The light curve for V1298 Tau also shows strong starspot variability, with a peak-to-trough amplitude of $\sim 6\%$ [117]. Therefore, any in-transit spectra need to be carefully searched for the signatures of contaminating ARs and spots.

V1298 Tau b is seen to be well aligned through both a clear Rossiter-McLaughlin signal and Doppler tomographic analyses (Johnson et al. in prep). Additionally, David et al. (in prep) reports detections of excess Hα absorption during transits of planets V1298 Tau b, hinting at highly extended atmospheres, which is expected for young planets.

Particularly, the excess absorption dominates in the red wing of the line and enhanced absorption at transit ingress of V1298 Tau b, which is confined to the core of the line. As the

transit continues, there is an excess in absorption in the wings of the line and more so on the red side. The excess absorption during ingress could be the planet occulting a bright stellar surface or limb feature. Several observations during transits of V1298 Tau c and V1298 Tau d suggest tentative evidence for excess Hα absorption (David et al. in prep). Observations do not span full transits, and therefore it is challenging to attribute the excess to the planets alone.

Here, we present a spectroscopic analysis during a full transit of V1298 Tau c, the innermost known planet in the system. We measure the spin-orbit alignment of the planet via Doppler Tomography and explore potential signs of atmospheric escape through changes in Hα. The paper is presented as follows: Section 3.1 describes our observations and data analysis through both Doppler tomography and detailed line work. We present our results in Section 4.3. Section 4.4 discusses potential sources of the Hα variations observed including center-to-limb variations, underlying starspots and faculae, and an extended planetary atmosphere from V1298 Tau c, and the source of the Ca II Infrared Triplet (IRT). We present our interpretation and future work in Section 3.4. We conclude by putting V1298 Tau c in context with other young planets and a summary of our key findings in Section 4.5.

3.1 Observations & Methodology

Due to the youth and high levels of stellar activity for V1298 Tau, we took several approaches to interpreting our observations. We observed other young active stars to compare spectral line variations to those seen in V1298 Tau. An updated ephemeris for V1298 Tau c was obtained from recent *Spitzer* observations (Livingston priv. comm.).

3.1.1 GRACES Observations

We obtained data with GRACES [Gemini Remote Access to CFHT ESPaDOnS Spectrograph; 100] mounted on Gemini North at the Gemini Observatory on UT 2020 January

22 through the Fast Turnaround program. GRACES has a wavelength coverage of 400-1000 nm and a resolving power of R $\sim$ 81,000. To obtain an optimal signal-to-noise of approximately 300 at 600 nm, we observed V1298 Tau at 360 second exposures. V1298 Tau was monitored for approximately 6 hours in total, resulting in 53 exposures for this analysis. Observations were taken under photometric conditions. Our observations cover the entire transit of V1298 Tau c. Five exposures at the beginning and six at the end are out-of-transit (OOT). We note that a transit of V1298 Tau d ended approximately 12 minutes before our observations began.

Data Reduction

Raw and reduced spectra were provided by Gemini-N. The spectra were reduced using the OPERA[2] pipeline [360, 535]. The OPERA pipeline completes several pre-reduction stages including creating master calibration images, a bad-pixel mask, and calibrating the instrument profile, aperture, and wavelength. The pipeline then extracts spectra from the original CCD images, and normalizes and telluric-corrects the spectra. However, we found a custom reduction of the data provides cleaner spectra for our analysis, via visual inspection.

We extracted each spectrum through the box-extraction method. We dark-subtracted and flat-corrected the spectra using master frames created by taking a median of all available dark and flat exposures. Cosmic rays were identified and removed using `ccdproc` [105], an extension of `astropy` [27, 453] that tracks bad pixels in images.

To extract individual orders, we used five equally spaced columns across the frame and identified local minima across each column. The minima corresponded to regions between the orders. A second-degree polynomial was then fit to each of the five points in a given row to trace and extract the order. We visually inspected that each model corresponded to a single order, and did not cross over into a different order. We discretized the models and ensured the box was the same width across the orders. We then box-extracted 23 orders in

2. Open source Pipeline for ESPaDOnS Reduction and Analysis

each exposure.

To correct for the blaze, we removed the first and last 350 data points and created a 95^{th}-percentile filter using `scipy` with a window length of 150 data points. For stars with broad lines, such as V1298 Tau, this is a standard procedure for identifying the blaze when there is no distinct continuum available [434, 376]. An 8^{th}-degree polynomial was fit to this filter and divided out of the spectra, resulting in our final corrected and flattened spectra (Figure 3.1). The number of cut data points and window length were visually found to result in the cleanest fully reduced spectra. Barycentric-corrected wavelengths, errors, and order numbers were taken from the OPERA-reduced data [535] and mapped onto our extracted spectra. Spectra of the same orders from different exposures were interpolated onto the same wavelength grid with three times the original wavelength resolution.

Doppler Tomographic Analysis

Doppler tomography relies on a transiting planet creating perturbations in rotationally broadened stellar line profiles that trace the orbit of the planet. Unlike typical radial velocity observations, which rely on tracing changes in the photocenter of lines, the Doppler tomography method allows us to resolve this perturbation in high resolution spectra. Here, we used the Doppler tomographic code `MISTTBORN`[3] [260, 259]. In summary, this method compares line profiles between in-transit (IT) and OOT generated models. The initial guess for the line profiles are created by convolving a line list from the Vienna Atomic Line Database [286] with a Gaussian line profile and are rotationally broadened given the $v \sin i$ of the system. `MISTTBORN` is flexible, such that after given an initial guess it fits for the line profile and allows it to take on an arbitrary best-fit shape. An average line profile is extracted from each order of each observation and is weighted by the signal-to-noise. The tomographic signal is determined by subtracting the IT from the average line profile across all OOT observations.

In addition to following the methods presented in [260], we focused on detailed analysis

3. `https://github.com/captain-exoplanet/misttborn`

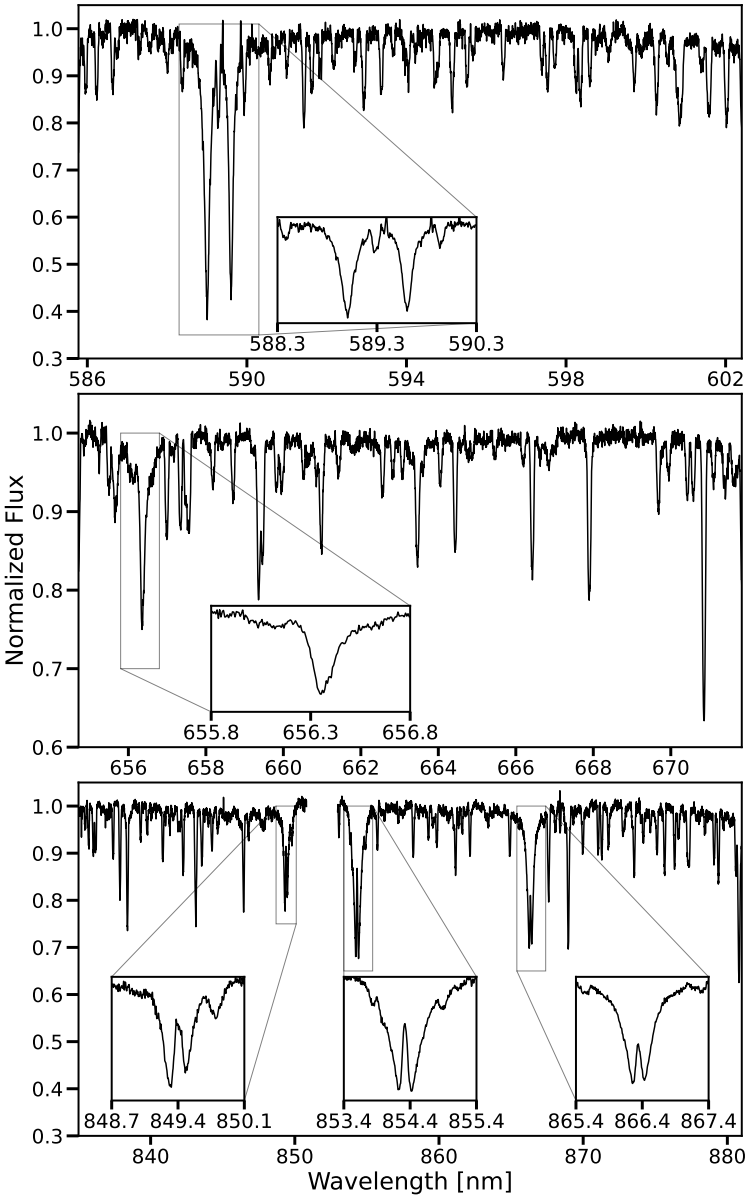

Figure 3.1 Example extracted spectra for V1298 Tau obtained with GRACES on Gemini-North. The bottom panel contains spectra from two different orders to highlight the Ca II IRT at 849.8, 854.2, and 866.2 nm. Inset panels highlight relevant lines used in this analysis including the Na I doublet (top), Hα (middle), and Ca II IRT (bottom).

of the Fraunhofer lines [186], which trace photospheric activity, and tried to extract the tomographic signal from just these lines. Each feature was compared to a median template created from the OOT observations. Of all the lines, Hα and the Ca II IRT at 849.8, 854.2, and 866.2 nm were the only lines that showed variation throughout the night. All other lines

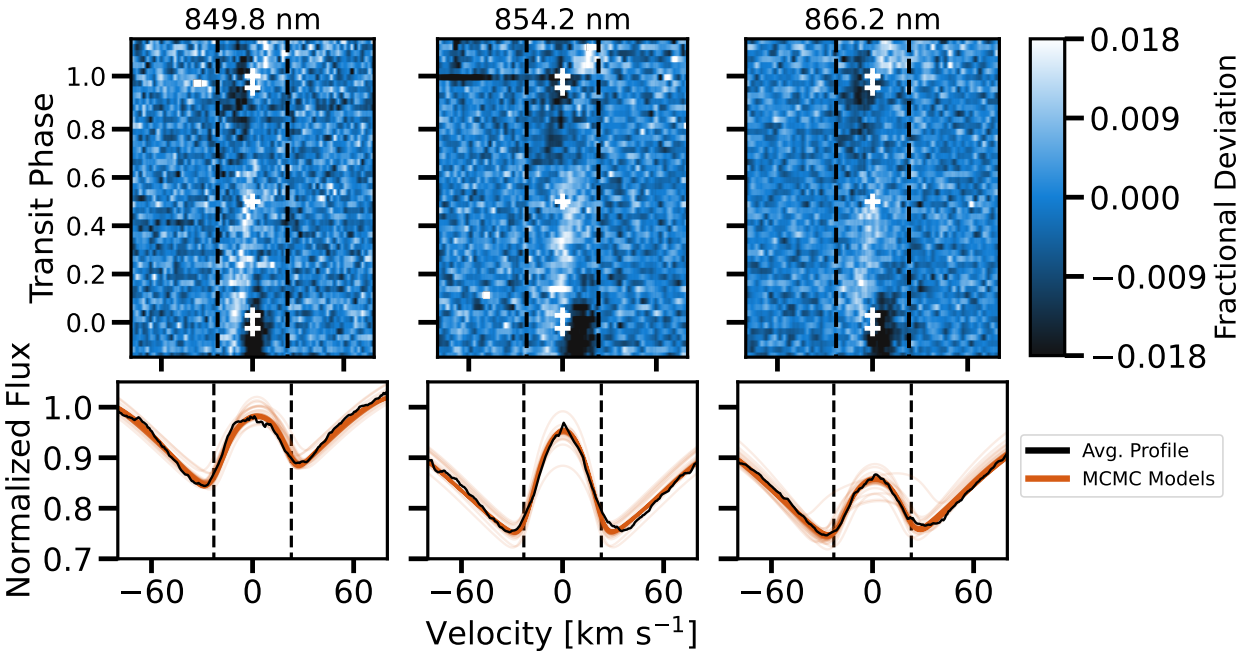

Figure 3.2 Top: Tomographic signal for each line in the Ca II IRT. Signals are plotted in the rest frame of the star. Excess absorption is shown in white and traces the transit. White pluses represent the four contact points of the transit and transit midpoint. Vertical dashed black lines represent $\pm\, v \sin i$. Bottom: 200 randomly selected MCMC fits (orange) used to derive the projected obliquity, λ, of V1298 Tau c, compared to the average line profile (black). Our MCMC best-fit parameters and associated priors are presented in Table 3.1.

appeared stable (see examples in Figure 3.4).

3.1.2 Veloce-Rosso Observations

As part of our analysis, we place the Hα variability of V1298 Tau in context of other young stars of similar activity levels. During 7 nights between UT 2020-11-08 to 2020-11-26, we observed five young M dwarfs ($T_{\rm eff} = 3323 - 3584$ K)[4] with the Veloce-Rosso Spectrograph [199] mounted on the Anglo-Australian Telescope. The targets were originally identified as high-probability ($> 94\%$) young moving group candidates using `BANYAN-`Σ [190], which uses *Gaia* kinematics to assign membership, and were presented in [162]. Three of the targets (TIC 333680372, 246897668, and 178947176) are high-probability kinematic members of the

4. $T_{\rm eff}$ taken from the *TESS* Input Catalog v8 [TIC; 522].

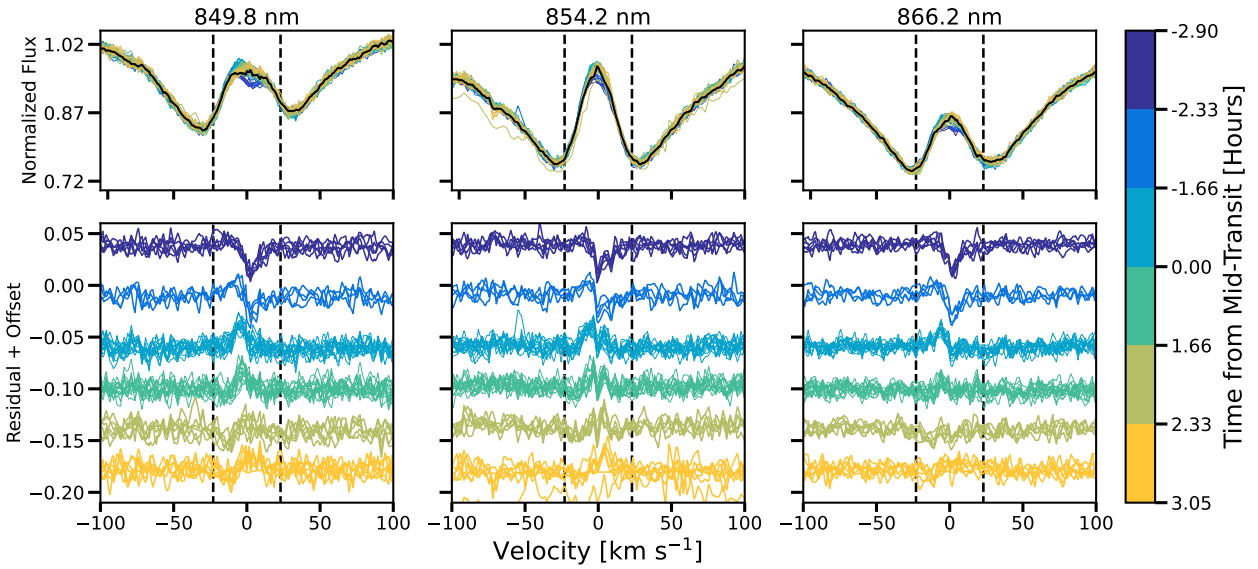

Figure 3.3 Zoom-in of the core and wings of each of the calcium triplet lines. Top: Normalized spectra. The OOT template is plotted as a solid black line. Bottom: The calcium feature with the OOT template subtracted out. There is a deficit in the red side of the core at the beginning of the night (purple), which quickly disappears. An excess in the blue can be seen during the beginning of the transit (dark blue) and slowly disappears through the remainder of the observations (teal to yellow). Lines are binned by time to mid-transit, where the transit duration is 4.66 hours; purple and yellow lines are OOT observations. Vertical dashed black lines represent $\pm v \sin i$, centered at the core of each calcium feature.

AB Doradus Moving Group ($t_{age} \approx 150$ Myr) and the other two (TICs 146522418 and 427346731) are high-probability kinematic members of the β Pictoris Moving Group [$t_{age} \approx 25$ Myr; 48].

`BANYAN-`Σ probabilities are strictly based on kinematic arguments and do not guarantee these stars are members of assigned known groups. However, the rapid rotation seen in the *TESS* photometry for these stars is consistent with young ages. Spectroscopic youth indicators, such as strong Hα emission are present in all of our observations, providing further evidence these stars are likely young and potentially members of the AB Doradus and β Pictoris moving groups.

Targets were observed for a total of 70-120 minutes per night of observation, with exposure times ranging from 300-600 seconds. Data were taken simultaneously with observations of a

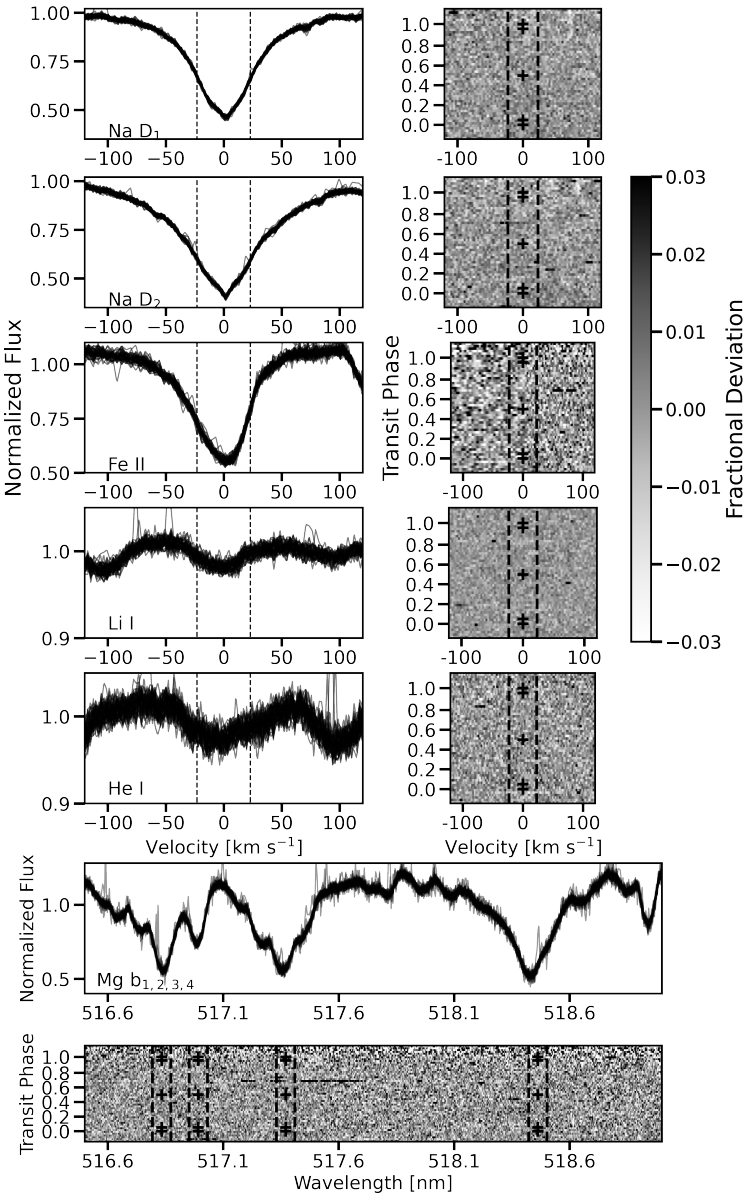

Figure 3.4 Spectral features (line plots) and associated waterfall plots for additional lines where we do not see a Doppler tomographic signal. Each line plot is labeled with the feature and the affiliated waterfall plot is located directly below. We present the Fe II line at 546.6 nm in the third row, Li I in the fourth row, and He I in the fifth row. The last two rows trace over several nanometers to cover the Mg I $b_{1,2,3,4}$ lines. Lines are colored by time of observation similarly to Figure 3.3. Waterfall plots represent deviations from a median OOT template from our observations. White pluses represent the four contact points of the transit and transit midpoint. Vertical dashed black lines represent $\pm\, v \sin i$.

laser comb, used for precise wavelength calibration [385]. The laser comb was additionally used to trace individual orders for box extraction. The observed targets have no known

transiting planets. We reduced all spectra using methods similar to those described in Section 3.1.1. The wavelengths were mapped using a pixel-to-wavelength reference made available by the Veloce-Rosso team.[5]

Targets were observed simultaneously with *TESS*. Due to the youth of these stars, it was possible some observations were taken during flare events. The *TESS* 2-minute light curves were searched for flares using the convolutional neural networks developed by [162]. These neural network models assign a probability that a given event is a flare or not. We considered events "true flares" when they were assigned a probability ≥ 0.9. Times of flares were cross-matched with our observation; spectra that were taken during identified flare events were removed from this analysis.

3.2 Results

Because we found our spectra to show little variation over the night, we could not use all spectral features to extract a Rossiter-McLaughlin or Doppler tomographic signal. Of the Fraunhofer lines checked, including the Mg I triplet at 517 nm, and Na D_1 and D_2 (Figure 3.4), the tomographic signal was only seen in the Ca II IRT at 849.8, 854.2, and 866.2 nm.

3.2.1 Ca II Infrared Triplet

Doppler Tomography

The Doppler tomographic analysis of the Ca II IRT is shown in Figure 3.2. The fractional deviation compares the difference between the Ca II IRT lines of each observation with a median profile from all OOT data. Bright areas represent regions of excess absorption, here due to the planet crossing the surface of the star, tracing from the bottom left to top right and approximately from the beginning to end of the transit. The transit signal is seen

5. `https://newt.phys.unsw.edu.au/~cgt/Veloce/Veloce.html`

independently in all three lines. We fit for the tomographic signal in the core of the Ca II IRT lines using `MISTTBORN` [260]. The line profile model in `MISTTBORN` accounts for the distortion of the line shape during the planet's transit and is a function of the parameters presented in Table 3.1. We do not account for differential rotation or macroturbulence.

`MISTTBORN` is typically used to model individual lines and not spectral features with cores. Here, we combined the line core with an upside-down Gaussian to model the regions around the core, presented in Figure 3.2. For Ca II at 854.2 nm, we set the central velocity of the Gaussian equal to the fitted line center; the other two Gaussian line centers were allowed to vary due to noticeable asymmetry in the lines. We used `emcee` [203, 178] to fit each line. We ran our MCMC fit with 350 walkers and 750 steps. After visual inspection, we removed 150 burn-in steps. We verify our chains have converged via visual inspection and following the method of [196]. The parameters, fit results, and priors are given in Table 3.1.The median Ca II IRT and 200 randomly selected MCMC examples are shown in the bottom row of Figure 3.3.

From this, we measure a projected obliquity of $\lambda = 5^\circ \pm 15^\circ$. We find the Doppler tomographic signal is driven by changes in the core of the Ca II IRT, formed in the stellar chromosphere (Figure 3.3). The individual lines (top row) and residuals with a median OOT template (bottom row) are colored by transit phase of V1298 Tau c. The changes in the lines are visible by eye, and are more pronounced in the residuals. There is very little difference between each observation in the wings of the lines (regions outside of $\pm\, v \sin i$).

Weighted Mean "Light Curves"

Comparing the weighted contributions of spectral features of IT to OOT observations has been used to infer the presence of planetary atmospheres, in particular the Na I D lines [92, 585]. For this, we follow a similar approach to [40]. Per each spectral feature, we calculate:

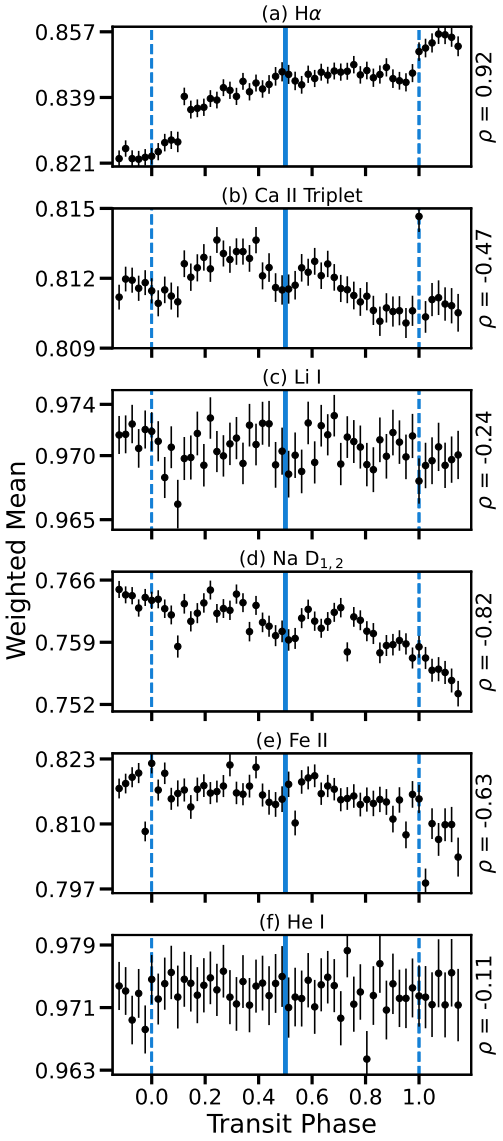

Figure 3.5 Weighted mean "light curves", $\overline{x}$, and affiliated errors, $\sigma_{\overline{x}}$, of the (a) Hα, (b) Ca II IRT, (c) Li I at 670.7 nm, (d) the Na I doublet at 589 nm, (e) Fe IIat 546.6 nm, and (f) He I at 587.8 nm. The Spearman's correlation value, ρ, for each feature is presented on the right hand side. Note the scale for each subplot was chosen to optimize the entire region and error bars are comparable. The solid line marks t_{mid} and the dashed lines represent t_1 and t_4. An increase in weighted mean corresponds to excess absorption in the spectral feature. There is a visible increase in Ca II with transit ingress and egress, while no such trend is seen in the Li I. This provides additional confidence the deviations in Ca II is planetary in nature. The spectra for additional lines are presented in Figure 3.4.

$$x_i(F_j, \sigma_j^2) = \sum_{j=0}^{m}(F_j/\sigma_j^2) \;\; / \;\; \sum_{j=0}^{m}(1/\sigma_j^2) \tag{3.1}$$

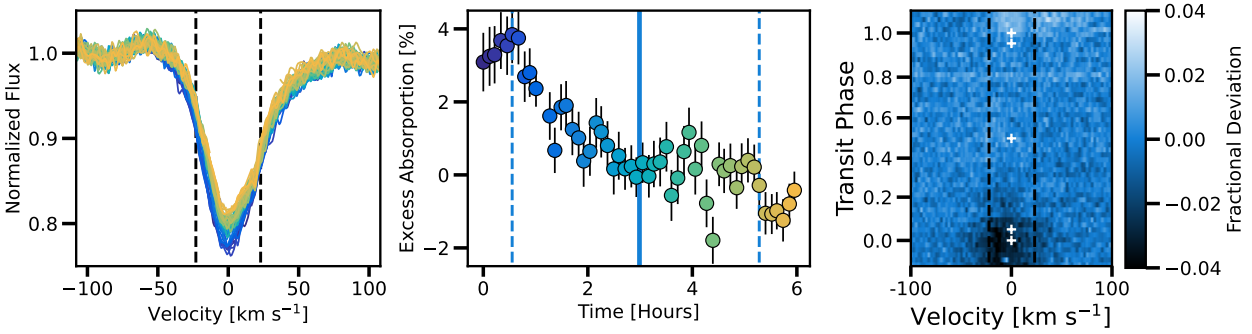

Figure 3.6 Demonstration of variation in Hα observed in our observations. Left: Normalized spectra colored by observation time. Purple and yellow represent the beginning and end of the night, respectively. The smooth variation in depth of the Hα feature is clear. Middle: Measurement of excess absorption seen in Hα as a function of time. The color of points correspond to color of the spectra in the left plot. The solid line corresponds to t_{mid}. The dashed lines correspond to transit contact points t_1 and t_4. Right: Tomography of Hα colored by fractional deviation from the OOT template. White pluses represent the four contact points of the transit and transit midpoint. Vertical dashed black lines in the left and right panels represent $\pm\, v \sin i$.

where x_i refers to a specific spectral feature, F_j is the flux array and σ_j^2 is the variance array for j observations. The total weighted mean "light curve" across multiple spectral features is then given by

$$\overline{x}(F_j, \sigma_j^2) = \sum_{i=0}^{n} x_i \tag{3.2}$$

where n is the total number of combined features (e.g. for the Ca II IRT, $n = 3$). In a similar manner, such that the associated standard deviation for a given feature is:

$$\sigma_i(\sigma_j^2) = \sum_{j=0}^{m} \frac{1}{\sigma_j^2} \tag{3.3}$$

where σ_i refers to errors for a specific spectral line and σ_j^2 is the variance array for j observations. The total weighted standard deviation across i spectral features is calculated as:

$$\sigma_{\overline{x}}(\sigma_j^2) = \left(\sum_{i=0}^{n} \sigma_i \right)^{-1/2} \tag{3.4}$$

We compare a weighted mean of the the Ca II IRT lines to various other lines and activity indicators, such as Li I at 670.7 nm, the Na I doublet at 589 nm, and the He I line at 587.8 nm; the results are shown in Figure 3.5. An increase in weighted mean can be interpreted as excess absorption in the spectral feature.

Li I has been seen to remain relatively stable in the presence of high levels of activity and photometric spot variations [418, 417, 516], with a potential abundance increase in the presence of the more-spotted hemisphere [175]. We measured the Li I equivalent width, and found the average to be 140 mÅ, which is consistent with other K0-K1.5 stars of this age [576]. As a comparison, we use Li I as a control to what is intrinsically occurring in the stellar chromosphere. We test for correlations between transit phase and the light curves for Li I and Ca II IRT in Figure 3.5 by calculating the Spearman's rank correlation coefficient [519]. This test assess how well two data sets can be described using a monotonic function. A correlation coefficient of ± 1 implies an exact monotonic relationship, while 0 implies no correlation. We find correlation values of -0.24 and -0.65 for Li I and Ca II IRT respectively, implying Ca II IRT is slightly more correlated with transit phase than Li I. Li I could be enhanced from flare events; however, we see no evidence of such event in other spectroscopic features affected by flares [e.g. variations in the blue wing of Hα; 344].

Correlations Between Spectral Features

We evaluate other known activity indicators, such as Na I doublet, Fe II, and He I (subplots d - f in Figure 3.5). We calculated the Spearman's correlation value for each to be -0.80, -0.63, and -0.11, respectively. High Spearman's correlation values could be due to long term stellar activity trends seen in the data. This could be particularly true for the Na I doublet. Although trends in the weighted mean is similar to Ca II IRT, there is no evidence of a

Doppler tomographic signal in the lines (Figure 3.4). For completeness, we also evaluate the Spearman's correlation value for Hα (subplot a in Figure 3.5) and find it to be 0.93, indicating a strong correlation with transit phase. We further inspect the Hα signal below.

We additionally evaluate the Spearman's correlation value between each of the spectral features in Figure 3.5. In order to look for correlations in the features, rather than long term trends, we fit a first degree polynomial to each weighted mean light curve. From the trend-removed light curve, we found the correlation between each line. The correlation values are shown in Figure 3.7. The median correlation value between all the lines is 0.1, which indicates there is very little to no correlation. The lines that are most strongly correlated are Hα and the Ca II IRT. Once the long term trend is removed from the Hα, there is a clear upwards "bump", similar to what is seen in Figure 3.6. Due to the strong correlation between that "bump" and the increase that is seen in the Ca II IRT, which is planetary in nature, this could indicate that the trend in Hα is also originating from V1298 Tau c.

3.2.2 Hα Variations

The Hα variations are shown in Figure 3.6. The leftmost panel is the Hα line and surrounding continuum used in our analysis. By eye, there is a clear trend in decreasing absorption throughout the night. To quantify this trend, we calculate the equivalent absorption (EA) of each line, defined as:

$$\mathrm{EA} = -\sum_{i=0}^{n} \frac{F_i}{F_{out}} - 1 \tag{3.5}$$

where F_i is the line flux for one observation and F_{out} is the median template of the OOT observations. The equivalent absorption for Hα is shown in the middle panel of Figure 3.6. There is a trend of decreasing excess absorption throughout the night, with potentially sharp features after V1298 Tau c is fully visible across the stellar surface. This could be the presence of an extended hydrogen atmosphere. However, given the long term trend and minimal OOT

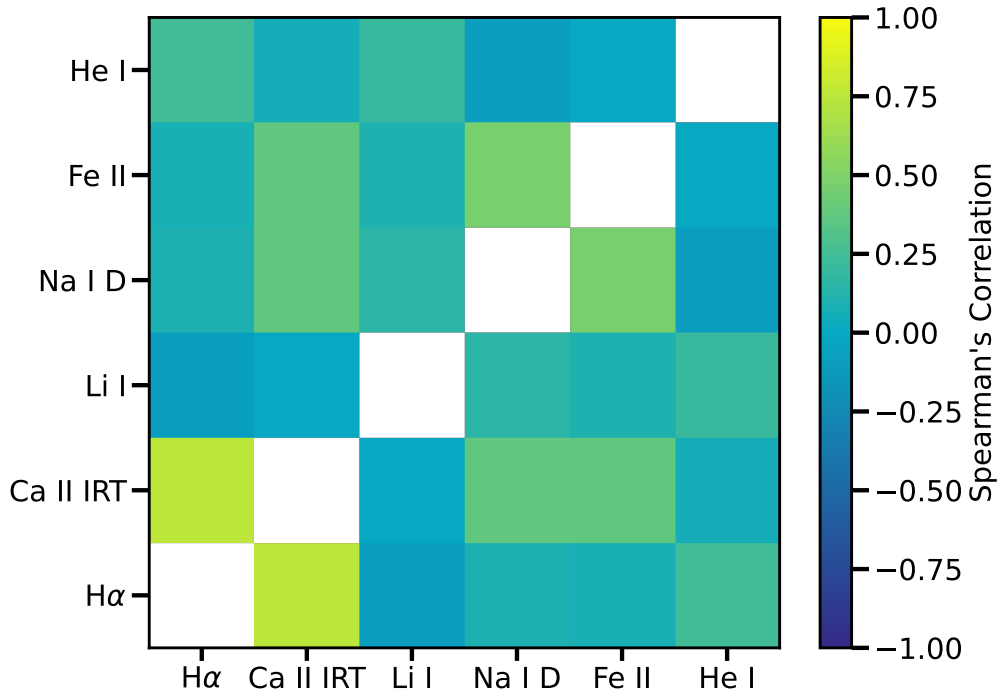

Figure 3.7 The Spearman's correlation value for spectral features presented in Figure 3.5. The average Spearman's value across all spectral features is 0.1, indicating that there is no correlation.The strongest correlation exists between Hα and the Ca II IRT.

observations, it is challenging to disentangle this signature from general stellar activity.

The Doppler tomographic analysis is shown in the rightmost panel of Figure 3.6. Dark and light regions at the beginning and end of the night are the result of over-subtraction from the template, which is constructed from these specific observations. There is no clear tomographic signal seen between $\pm\ v \sin i$, as was seen in Figure 3.2. This is likely due to stellar activity dominating the long-term trend in Hα seen over the night. The excess absorption seen in the middle panel is therefore most likely stellar activity.

Comparison to Veloce-Rosso Targets

The EA of Hα was additionally calculated for the young stars in our Veloce-Rosso sample using Equation 3.5. We note that the activity of M and K stars are comparable at ages $\leq$ 1 Gyr [493, 464]. Thus, this comparison will help provide a stellar context for the Hα

variations. The results are shown in Figure 3.8. We note that the Hα for targets observed with Veloce-Rosso is in emission, while V1298 Tau clearly shows Hα in absorption without a significant core component.

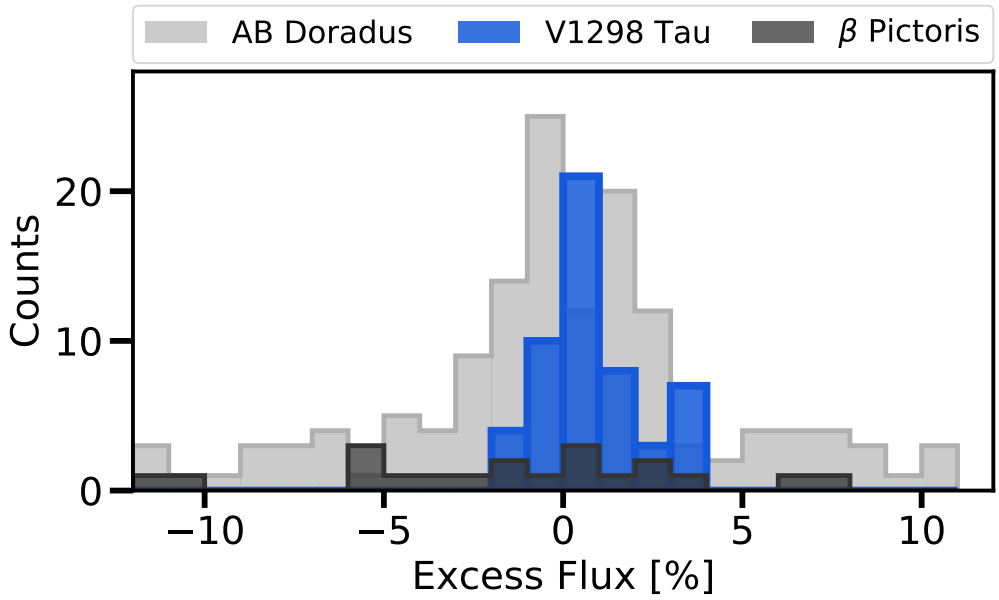

Figure 3.8 Comparison of Hα variations observed in V1298 Tau (purple) with five young M stars observed with Veloce-Rosso. The levels of Hα emission in these young stars varies on the order of a few percent over a few hours. The Hα for V1298 Tau is correlated with time, hinting this may be the signature of an escaping hydrogen atmosphere. However, observations of other young active stars show similar trends over a single night. The Hα excess variations of V1298 Tau trace the distribution of AB Doradus members. This is likely because the relative activity of a 23 Myr K star is comparable to a 150 Myr M star. The light gray histogram are members of AB Doradus moving group (t_{age} = 150 Myr); dark the gray histogram dark gray points are members of the β Pictoris moving group (t_{age} = 25 Myr). Veloce-Rosso observations during flare events were removed. Each bin represents 1% variation in excess flux.

A median template of Hα was created per star per night of observation. The excess flux variation is calculated by comparing each exposure to the median template. This is similar to the way excess Hα flux for V1298 Tau was calculated. There is clear variation for all young stars, with excess variation extending out to $\pm$10%. The predominant amount of excess flux varies between $\pm$3%, which follows the trend seen for V1298 Tau. We additionally found stars in our sample exhibit smooth increasing or decreasing Hα variation over a single night,

in a similar way to V1298 Tau (Figure 3.6, middle panel). This demonstrates the behavior of Hα in young stars can change dramatically over a night.

The average strength Hα emission for young stars is comparable to what is seen in our Veloce-Rosso sample. AB Doradus and other confirmed young moving group members have Hα EWs ranging from -10 to 0, where negative values indicate emission [467]. Confirmed β Pictoris moving group members were seen to have Hα EWs ranging from ~ -15 to 0 for M0-M9 stars [509]. [494] measured Hα EWs in 336 young low-mass stars (K5-M9; $t_{\rm age} \sim 22-200$ Myr) with values ranging from ~ -20 to 2, where earlier spectral types tend towards positive EWs. The values for our Hα EA measurements fall well within the ranges for other young stars with ages between $t_{\rm age} \sim 23-150$ Myr. In the context of other young stars, the variations seen in V1298 Tau can be solely attributed to youth and general stellar activity.

3.3 Discussion

We speculate on several different explanations for the observed Hα variations, such as limb darkening, the presence of star spots, and the presence of an extended Hα atmosphere from V1298 Tau c or V1298 Tau d.

3.3.1 Center-to-Limb Variations

The underlying wavelength dependence of limb darkening can create signals masquerading as those expected from planet atmospheres [109]. We model center-to-limb variations (CLVs) to address this possibility. A synthetic spectrum was obtained from the [81] grid of stellar atmospheric models generated with `ATLAS9` [289]. Based on stellar parameters presented in [117], we chose a model with $T_{\rm eff}$ = 5000 K and $\log(g) = 4.00$ with solar metallicity. Spectra with different limb darkening values were generated using `spectrum` [208] with a wavelength step size of $\Delta\lambda = 0.002$Å. The spectra were additionally rotationally broadened

($v \sin i \sim 23$ km s^{-1}) following the formalism of [207]. A total of 50 synthetic spectra were generated from $u = 0 - 1$, where $u = 0$ is the edge of the stellar disk and $u = 1$ is the center. We sampled limb angles at $\Delta u = 0.02$; $u = 0.0$ was replaced with $u = 0.001$ [109].

We created a discretized stellar surface with $R_{pixels} = 20001$, filled with concentric circles for each value of u as prescribed by [566]. An example of the modeled stellar disk and accompanying spectral feature for one of the Ca II IRT lines at 849.8 nm is shown in Figure 3.9. Variations in line depth as a function of u are highlighted in the inset panel. We model the transit of V1298 Tau c with a radius of 19 pixels, maintaining an $R_p/R_\star = 0.03$ and at an impact parameter of $b = 0.2$ [115]. The spectrum at each step is the summation of all unocculted elements.

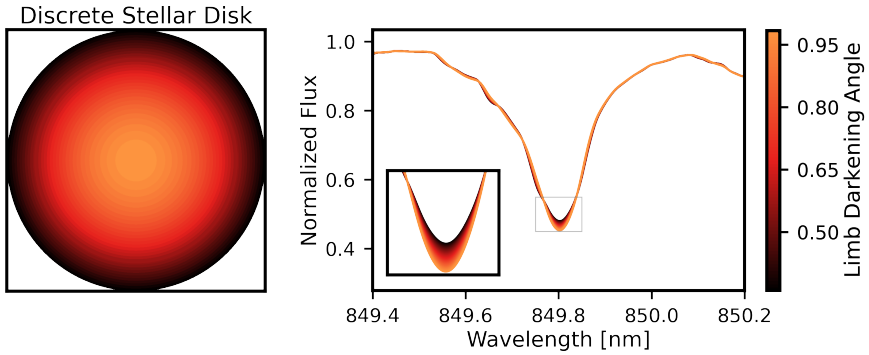

Figure 3.9 Modeled stellar disk and accompanying spectra for V1298 Tau at different limb darkening angles. The original spectrum was taken from the grid of stellar atmospheric models from [288]. Spectra were then generated at different limb darkening angles using `spectrum`. We accounted for rotational broadening due to high $v \sin i$of V1298 Tau. The averaged affect of limb darkening over the entire stellar surface is negligible with respect to the Hα variation seen during our observations.

We find that CLVs for this system induce changes in the spectral features on the order of 10^{-5}. These effects are negligible compared to the observed 8 ppt signal (Figure 3.5). The CLV testing described above does not account for non-local thermodynamic equilibrium effects. Although it would be more rigorous to include such calculations, the magnitude of the variations is negligible compared to the contribution of ARs [83]. Therefore, the behavior seen here is not attributable to CLV.

Next, we account for potential limb-brightening in the core of the Ca II IRT lines, following the methods presented in [109]. First, we create a difference light curve (DC) with a modified version of Equation 9 to account for three, instead of two, lines:

$$DC_{\rm core}(t_i) = \frac{1}{3}\sum_{j=0}^{3} LC_j(t_i) - \frac{1}{3}\sum_{j=0}^{3} LC_{C_j}(t_i) \tag{3.6}$$

where t_i is an observation, LC_j is the mean weighted light curve of each of the three individual Ca II IRT line, j, and LC_{C_j} is the mean weighted light curve for the continuum around each Ca II IRT line. Due to there being many lines near the Ca II IRT, we select the continuum region as 0.5 nm on either side of the lines. We find the effect of limb brightening to be on a similar scale to that in [109], but does not exhibit the same trend. While limb brightening could be responsible for this signal, it is near-impossible to distinguish between variability from the planet and CLV-induced changes, and therefore we rule out limb-brightening as the source of this variability.

3.3.2 Stellar Nature of the Variability

Due to Hα being a tracer of stellar activity, we must explore the possibility that the observed excess absorption variations are strictly stellar in nature. The smooth variation over our observations was seen in similar observations for targets in our Veloce-Rosso sample. Additionally, young stars are believed to have significant photospheric inhomogeneities, seen in the original light curve of V1298 Tau. Similar night-long trends in activity have been seen for other young planet hosts [377] and the trend in the excess Hα absorption during our observations can be explained by stellar activity alone.

Spot & Faculae Modeling

We use `starry` [330], an analytic solution to time series of planet transits and stellar surfaces based on applications of spherical harmonics, in combination with `spectrum` to recreate the

Hα absorption with starspots and surrounding facular regions. We follow the methods discussed in Section 3.3.1 and add in the presence of two starspots with surrounding facular regions. We take a stellar spectrum model of the same log(g) and metallicity as V1298 Tau at 5500 K and 4500 K for the faculae and spots respectively. Although these $T_{\rm eff}$ may not accurately represent all starspot/facular regions, they provide a reasonable estimation for determining changes in line depths/profiles in the presence of such features [82].

We created `starry` models as a function of rotation that are 2500 $\times$ 2500 pixels in size. Then we discretized the surface to indicate values of either surface (orange), starspot (red), or facula (yellow); examples are shown in the top row of Figure 3.10. The approximate area of spot to facula is 60%, similar to that in [84] and the associated modeled photometric variability (Figure 3.10, middle) corresponds to variability seen in the original *K2* light curve [117]. Forward modeling of *K2*/ *TESS* light curves also suggests the variability is driven more strongly by starspots than faculae [258]. We weighted the spectra by the area of each feature (spot, facula, or surface) and accounted for limb-darkening.

The configuration explored in our toy model is just one of many potential solutions and was not fit to the original *K2* light curve, but rather captures a general scale of spot variability. Therefore, it should not be taken as the ground-truth configuration [331]. A six-hour window is highlighted in the photometric variability in red (Figure 3.10, middle), which corresponds to the Hα excess absorption seen in the bottom row of the same figure. Our observations (gray) show a decrease in excess Hα absorption of 4.29% over six hours; this model (red) has a similar trend, decreasing by 4.37% over the simulation.

3.3.3 Planetary Nature of the Variability

We speculate on several different planetary configurations that may be the source of the Hα and Ca II IRT variations seen over our observations. Each scenario is evaluated separately, although the ground truth could be the result of some combination from each.

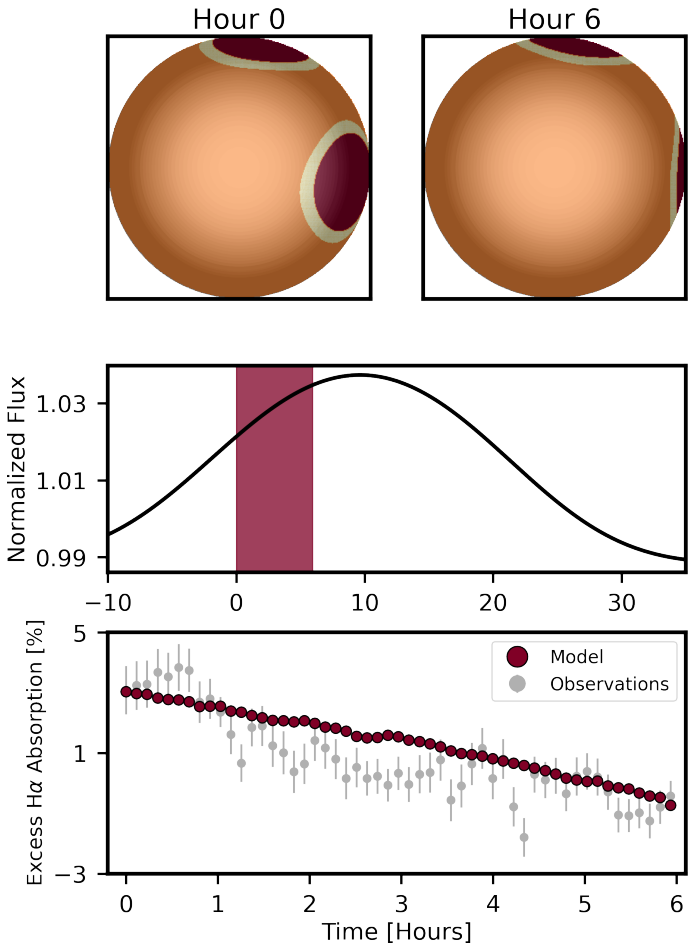

Figure 3.10 Toy spot and facula model created using `starry` of a potential configuration on V1298 Tau that produces similar levels of Hα variation to that seen in our observations. Top row: Surface maps at the beginning and after 6 hours of rotation. Dark red regions represent starpots; bright yellow represent surrounding facular regions; orange is the surface. Maps are limb-darkened. The starspots and faculae comprise of $\sim 20\%$ of the visible surface at the start. Middle row: Normalized light curve of this starspot configuration. Variation amplitudes match those that are present in the original *K2* observations [117]. Shaded red region represents the 6 hour window for the above rotation configurations. Bottom row: Measured Hα excess absorption at each rotation time step. Identifying individual starspots is a degenerate issue; this is one configuration that is able to reproduce a similar trend in Hα excess absorption over the timescale of our observations.

Extended Hα Atmosphere of V1298 Tau c

Given the age of the system and current X-ray irradiation, V1298 Tau c is predicted to evolve significantly from $5.59 R_\oplus$ to a final radius of $1 - 5.55 R_\oplus$ given the different mass

and X-ray activity level assumptions [447]. It would therefore not be surprising to detect a highly extended atmosphere from our target. We note that slight "bumps" in the measured Hα equivalent width at transit ingress and egress for V1298 Tau c (Figure 3.6; middle panel) could be attributed to the planet, while the overall slope is dominated by stellar activity. We fit a line between the equivalent widths for ingress and egress to represent the activity longer-term trend and measured a depth in the excess absorption of 1.85%. Assuming spherical symmetry, this would correspond to an atmosphere with a thickness of 1.28 R_J.

Hα Tail from V1298 Tau d

With updated *Spitzer* ephemerides, we also find that the transit of V1298 Tau d ended 12 ± 15 minutes before our observations (Livingston priv. comm.). V1298 Tau d is a $6.41 R_\oplus$ planet on a 12.4 day period and is predicted to evolve to $1.5 - 6.4 R_\oplus$ in 5 Gyr [447]. If an atmospheric tail is present from V1298 Tau d, it could be contaminating our observations at the beginning of the night. The first seven observations ($t_{\rm MJD} = 58870.725 - 58870.753$) show a relatively stable Hα excess absorption of 5% before decreasing. This could very well mean that our initial observations are catching the tail end of an inflated hydrogen atmosphere around planet d.

In this scenario, we can estimate the extent of the hydrogen atmosphere. If we assume the transit of the extended atmosphere continues for the first 2.5 hours, up until the excess Hα absorption temporarily flattens out, we see the signal change Δ5%. A 5% signal would correspond to an atmosphere thickness of 2.36 R_J. Assuming the atmospheric signal continues for 2.5 hours, this would correspond to a tail length of 5.85 R_J. The remaining observations would be affected by the transit of V1298 Tau c, with a potential active region crossing resulting in increased noise in our Hα measured EAs between $t_{\rm MJD} = 58870.871 - 58870.908$ (corresponding to 3.504-4.392 hours in the middle panel of Figure 3.6).

Ca II IRT from V1298 Tau c

We investigate if the Ca II is an extended ionized atmosphere of the V1298 Tau c. We evaluate the behavior of the Ca II IRT transmission signal in both the star and planet's rest frames (Figure 3.11) and evaluate the transmission signal for Hα (rightmost column). The variations in Ca II IRT are seen to vary with planet orbital phase in both rest frames. We can rule-out that the Ca II IRT is part of an extended atmosphere from V1298 Tau c because it is seen in emission and is not at rest in the planet's rest frame. The Hα line changes also are not at rest in the planet's rest frame and highlight the $\pm\, v \sin i$ change in absorption over the night.

Close-in planets interact with their host star's magnetic field lines, which have been seen to manifest as changes in flux from the cores of chromospherically driven lines. Such changes have previously shown variations with the planet's orbital phase [86]. [508] showed that the equivalent width of Ca II H & K varied consistently with the orbital phase of HD 179949 b over 5 years of observations, which is indicative of a magnetically-driven star-planet interaction. They also found a strong correlation between Ca II H & K and the mean emission from the chromospheric core of the Ca II IRT. Similar studies have been conducted for HD 189733 b, where no clear evidence of star-planet interactions were seen via a similar analysis of Ca II H & K [156]. Following studies using 10 years of spectral observations of HD 189733 b found Ca II H & K variations corresponding to transits, but with a leading phase offset of $\Delta\phi = 40 - 53^{\circ}$ [297, 85].

It is possible the Ca II IRT variations in our observations are driven by star-planet interactions. Given the increased magnetic activity of young stars and the close proximity of young planets, these interactions may be expected. However, with limited orbital phase coverage it is difficult to say if this is the case. Multiple transits of V1298 Tau c are required to determine if the Ca II IRT varies regularly with orbital phase. Simultaneous observations Ca II H & K would also prove useful here.

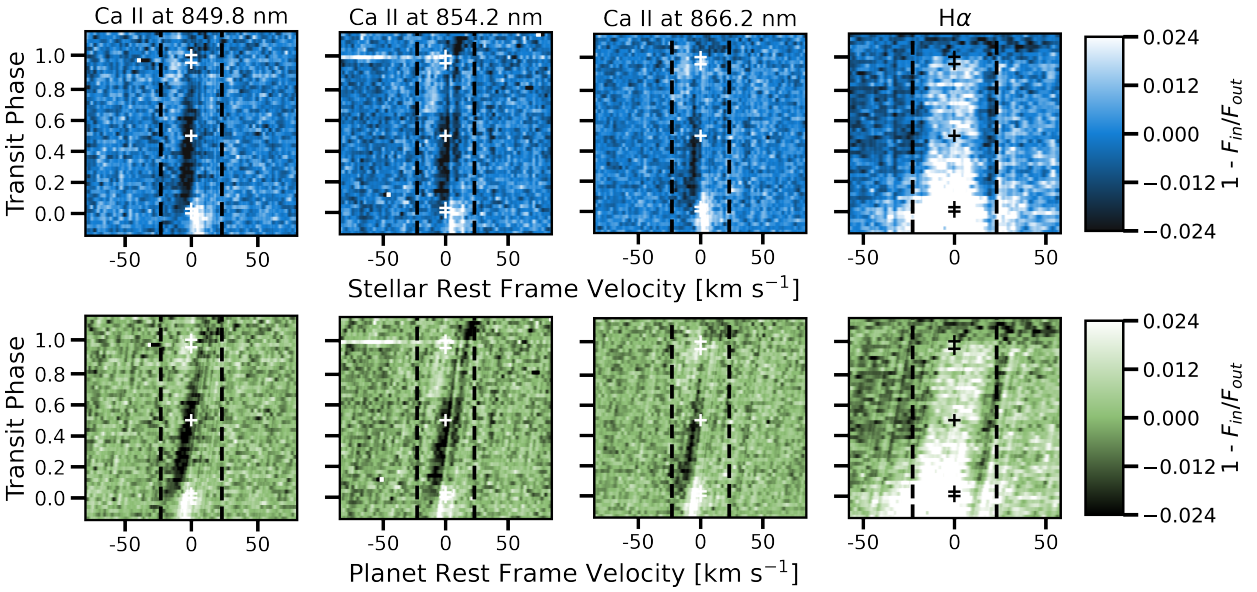

Figure 3.11 Comparison of transmission signal for both Ca II IRT and Hα in the stellar rest frame (top; blue) and V1298 Tau c's rest frame (bottom; green). Here, white represents absorption and black represents emission, which is not physical in transmission spectra. The excess in Ca II IRT stretches more so from $\pm\, v \sin i$ (vertical dashed black lines) in the planet's rest frame velocity, indicating the signal is stellar in origin. Pluses represent the four contact points of the transit and transit midpoint.

3.4 Interpretation & Future Work

3.4.1 Interpretation

In Section 3.3.1, we explored the possibility of our observed Hα trend to be the result of CLV. We can confidently rule this out as being the source of the equivalent width variations due to the small effect we find ($\approx 10^{-5}$) compared to our observed signal (8 ppt).

There appears to be slight indications of a transit in Hα (Figure 3.6) with an underlying long term stellar activity trend. However, there is no visible Doppler tomographic signal. The change in excess Hα absorption is also consistent with that seen for other young stars (Figure 3.8). We also find no evidence of Hα changes in the planet's frame of reference (Figure 3.11, rightmost column). We also show such Hα variations can be explained by a stellar surface with 20% coverage by starspots and faculae (Figure 3.10). A 20% inhomogeneity

coverage, like that at the start of our toy model, is possiblle for young stars.

With no previous constraints on an extended atmosphere from V1298 Tau c or V1298 Tau d, it is difficult to address how much this could be contaminating our OOT observations at the beginning of the night. However, since the Hα excess absorption variations are seen in other young stars and they can be explained solely by the presence of stellar inhomogeneities, we speculate the Hα is most likely stellar in nature.

We only find the Doppler tomographic signal in Ca II IRT. If this is driven by star-planet interactions, then it would be expected to be seen in other lines that originate in the chromosphere. Since our observations do not contain any other such lines (e.g. Ca II H & K), we cannot definitively say this is the case. It is still unclear as to why we do not see variability in other strong lines, specifically the Na I doublet (Figure 3.4).

3.4.2 Future Work

While we speculate on several independent scenarios, the ground truth could very possibly be some combination of all presented interpretations. The observations presented here alone are insufficient to distinguish between them. Multiple transits observed with both Ca II H & K and Ca II IRT could help answer why the Doppler tomographic signal is only seen in this feature of our observations. If it is the result of star-planet interactions, there will be periodic equivalent width variations corresponding to the period of V1298 Tau c [e.g. HD 179949 b; 508].

Since Hα is known to contaminate transmission spectra [455] via the presence of stellar inhomogeneities and young stars are extreme cases of these surfaces [e.g. 214], a detection of an extended Hα atmosphere is very challenging. Multiple observations of V1298 Tau c transiting over different stellar surface phases need to be observed to try and recover this signal. Additional OOT observations may be required to understand the general activity of Hα for this active young star. If the 5% variations of Hα from our observations are stellar in nature, which we believe they are, then more OOT observations will help build a better

spectral template to compare IT observations to.

He I at 1083.3 nm

Starspot and AR contamination has a much less significant effect ($\approx 0.1\%$) for He I at 1083.3 nm [407]. Several detections of atmospheres have been made through observations of He I [e.g. 355, 518, 15, 420]. [213] conclude that planets around active stars are good candidates for searching for He I atmospheric signatures and signs of atmospheric escape. This would also be ideal for young planets, not still embedded in debris disks [237], as stellar inhomogeneities are lower in contrast at longer wavelengths [527]. Additionally, simultaneous observations of V1298 Tau c in Hα and He I will allow us to further understand if the trend in our observations originates from the planet or is dominated by underlying stellar activity.

Ground-based follow-up of V1298 Tau c and other transiting planets in this system using NASA Keck + NIRSPEC could allow for the first detection of an extended young atmosphere in He I. If the greatest variations we will see are driven by chromospheric lines, then transits of V1298 Tau c in the UV may prove more fruitful. Observations using the Hubble Space Telescope + Wide-Field Camera 3 would allow for a full characterization of planetary atmospheres and the high-energy flux from the young active host star. Future James Webb Space Telescope observations of transits of V1298 Tau c as well as V1298 Tau b and d would offer unprecedented detail of the composition as well as characterizing the extension of the young atmospheres. Observations of all three planets would allow for a detailed comparison of atmospheric composition and mass loss for planets of different radii in the same harsh stellar environment.

V1298 Tau and *TESS*

Additionally, *TESS* will observe V1298 Tau during its extended mission from September - November 2021. Simultaneous spectroscopy with this guaranteed photometry would allow for a confident removal of stellar activity and first potential detection of an extended Hα or He I

atmosphere. The resulting *TESS* light curves will show much lower variability amplitudes by virtue of spot contrast that would not be obtainable by ground-based photometry at the *TESS* wavelength coverage. Additionally, *TESS* overlaps in wavelength coverage [600-1000 nm; 465] with Hα, Ca II IRT, and He I, making it easier to compare the spectral response in simultaneous data sets.

X-ray observations of HD 189733 provided evidence of an intense flaring event 3 ks after the eclipse of HD 189733 b [579]. These observations lead to speculation that the flare was the result of magnetic interactions between the star and planet. There is evidence of flares from V1298 Tau in the *K2* light curve [115] and future *TESS* light curves at a higher cadence may display similar flare trends. Any phase dependence of flares with planet transits could be evidence of star-planet interactions and are unlikely dependent on stellar surface spot coverage [162].

3.5 Conclusions

We have presented a Doppler tomographic and spectral analysis of V1298 Tau, a 23 Myr K star, during a transit of its innermost known planet, V1298 Tau c.

1. We measure an alignment of V1298 Tau c of $\lambda = 5^\circ \pm 15^\circ$ from the Ca II IRT at 849-866 nm. This is the only spectral feature with an obvious transit signal, hinting that measuring the spin-orbit alignment of young planets may be more feasible at near-infrared/infrared wavelengths.

2. V1298 Tau c adds to a growing list of young planets with low obliquities, including V1298 Tau b (Johnson et al. in prep), indicating these planets undergo smooth migration shortly after they formed. Multi-planet systems tend towards being well-aligned at all ages [10] and we have demonstrated that the V1298 Tau system is no exception.

3. Variations in Ca II IRT could be an indication of star-planet interactions. More transit observations of V1298 Tau c in Ca II H & K and Ca II IRT may be able to firmly assess

whether this is the case.

4. The excess absorption in Hα corresponds well to variations seen in other stars of younger and slightly older ages. The variations can also be replicated solely via the presence of starspots and faculae, leading us to believe stellar activity is the origin of the signal and it is not from an extended young atmosphere.

5. These observations alone are insufficient to characterize any potential extended atmosphere from V1298 Tau c. More transits are required to disentangle stellar from planetary signals. Future observations in the UV, for more chromospheric lines, and NIR/IR, where starspots are at lower contrast, may prove more optimistic for characterizing young planetary systems.

6. There is still much work to be done to understand the nature of the variability seen in our spectra. The data[6] used in this analysis can be found on the Gemini Archive.

6. Gemini Program GN-2019B-FT-215 on the Gemini Data Archive: `https://archive.gemini.edu/searchform/`

Planet Parameters	849.8 nm	854.2 nm	866.2 nm	Combined	Prior
λ [°]	$13.6^{+16.9}_{-8.8}$	$-0.5^{+9.3}_{-22.7}$	$4.2^{+5.8}_{-13.8}$	$4.9^{+15.0}_{-15.1}$	$\mathcal{U}$[-180, 180]
T_0 [MJD]	$58846.09709^{+0.00008}_{-0.00019}$	$58846.09720^{+0.00018}_{-0.00018}$	$58846.09716^{+0.00017}_{-0.00015}$	$58846.09715^{+0.00016}_{-0.00019}$	$\mathcal{G}$(58846.097156, 10^{-5})
Period [Days]	$8.24964^{+0.00019}_{-0.00012}$	$8.24962^{+0.00021}_{-0.00011}$	$8.24953^{+0.00013}_{-0.00020}$	$8.24959^{+0.00022}_{-0.00018}$	$\mathcal{G}$(8.24958, 10^{-5})
$R_p/R_\star$	$0.03923^{+0.00034}_{-0.00013}$	$0.03926^{+0.00063}_{-0.00012}$	$0.03869^{+0.00052}_{-0.00088}$	$0.03921^{+0.00033}_{-0.00062}$	$\mathcal{G}$(0.039208, 10^{-3})
$v \sin i$ [km s^{-1}]	$23.59^{+0.97}_{-0.73}$	$23.92^{+0.61}_{-1.25}$	$23.45^{+0.99}_{-1.71}$	$23.65^{+0.87}_{-1.17}$	$\mathcal{G}$(23.0, 1.0)
$a/R_\star$	$13.188^{+0.15}_{-0.136}$	$13.187^{+0.003}_{-0.005}$	$13.218^{+0.185}_{-0.088}$	$13.189^{+0.133}_{-0.047}$	$\mathcal{G}$(13.19, 0.01)
impact parameter, b	$0.20^{+0.11}_{-0.12}$	$0.21^{+0.12}_{-0.09}$	$0.22^{+0.10}_{-0.09}$	$0.21^{+0.11}_{-0.10}$	$\mathcal{G}$(0.20, 0.05)
eccentricity, e	$0.11^{+0.03}_{-0.01}$	$0.09^{+0.02}_{-0.05}$	$0.09^{+0.03}_{-0.04}$	$0.10^{+0.03}_{-0.04}$	$\mathcal{U}$[0, 0.5]
periastron, ω [°]	$90.18^{+59.52}_{-65.7}$	$87.27^{+59.61}_{-63.2}$	$86.4^{+51.07}_{-56.23}$	$87.84^{+57.05}_{-61.78}$	$\mathcal{U}$(-180, 180)
limb darkening, u_1	$0.41^{+0.21}_{-0.10}$	$0.86^{+0.13}_{-0.49}$	$0.63^{+0.25}_{-0.26}$	$0.55^{+0.38}_{-0.19}$	$\mathcal{U}$[0, 1]
limb darkening, u_2	$0.21^{+0.12}_{-0.14}$	$0.30^{+0.21}_{-0.15}$	$0.35^{+0.20}_{-0.09}$	$0.30^{+0.19}_{-0.17}$	$\mathcal{U}$[0, 1]
line center [km s^{-1}]	$-1.31^{+0.02}_{-0.68}$	$-7.29^{+0.19}_{-0.02}$	$-14.72^{+0.67}_{-0.11}$	—	$\mathcal{U}$[-20, 20]
Gaussian Parameters					
mean, μ, [km s^{-1}]	$4.99^{+0.19}_{-0.26}$	—	$-12.57^{+1.55}_{-0.99}$	—	$\mathcal{U}$[-20, 20]
width, σ	$39.36^{+3.55}_{-0.72}$	$57.66^{+1.43}_{-2.37}$	$53.30^{+1.74}_{-1.75}$	—	$\mathcal{U}$[35, 60]
scaling factor	$23.56^{+1.62}_{-0.38}$	$41.53^{+1.92}_{-2.71}$	$36.99^{+2.28}_{-1.68}$	—	$\mathcal{U}$[10, 50]
core scaling factor	$0.176^{+0.005}_{-0.012}$	$0.24^{+0.003}_{-0.003}$	$0.145^{+0.003}_{-0.004}$	—	$\mathcal{U}$(0, 1]
model y-offset	$1.04^{+0.01}_{-0.0}$	$1.00^{+0.01}_{-0.01}$	$0.99^{+0.01}_{-0.01}$	—	$\mathcal{U}$[0.5, 1.5]

Table 3.1 Doppler Tomographic Modeling Results for the Ca II IRT. Ca II at 852.4 nm was symmetric about the core so the mean of the underlying Gaussian, μ, was not fit separately from the line center.

CHAPTER 4

FLARE STATISTICS FOR YOUNG STARS FROM A CONVOLUTIONAL NEURAL NETWORK ANALYSIS OF *TESS* DATA

"*While observing a group of solar spots on the 1st September, I was suddenly surprised at the appearance of a very brilliant star of light, much brighter than the sun's surface.*"

— R. Hodgson

Young stars are appealing targets for studying the early stages of stellar and exoplanet evolution. Stellar flares are energetic events caused by the reconnection of magnetic field lines and there is evidence that they abound on very active coronal sources, such as pre-main sequence stars [55].[12] Flare rates are of particular interest due to their effects on the early stages of exoplanet evolution. They have been seen to cause phenomena such as increased photoevaporation of inner protoplanetary disks [55] and irreparable chemical changes to exoplanet atmospheres [556]. Flares can also expedite atmospheric erosion [295], particularly over the first few hundred million years, when the atmospheres of young planets are still contracting [415].

The advent of high-precision time-series photometric missions, e.g. *Kepler/K2* [65] and the *Transiting Exoplanet Survey Satellite* [*TESS*; 465], have allowed for detailed studies of stellar activity across both spectral type and age [e.g. 114, 225]. Using data from the 4-year *Kepler* mission, [112] identified $\sim 850,000$ flares across 4000 stars spanning G0 - M4 spectral types and found a potential flare saturation limit as a function of Rossby number. It was later noted this sample may have significant pollution due to variable stars in this sample [113]. More recently, [216] conducted a flare search of all two-minute cadence stars observed in Sectors 1 and 2 of *TESS*. Of the entire sample, they found 1228 flaring stars with a total

1. This work is based on [160] and [162], which was co-authored by Benjamin T. Montet, Megan Ansdell, Brian Nord, Jacob L. Bean, Maximilian N. Günther, Michael A. Gully-Santiago, and Joshua E. Schlieder. A. Feinstein selected the stellar sample, identified membership to nearby young moving groups and associations of these targets, and analyzed and fit all of the data presented in this chapter. A. Feinstein and M. Ansdell developed the convolutional neural network (CNN) with additional input from B. Nord. M. Günther provided the training set for the CNN model. B. Montet, J. Bean, M. Gully-Santiago, and J. Schlieder provided useful conversations and valuable feedback on the manuscript.

2. An alternative title for this work was "MACARONI: Multi-messenger dAta driven flare statistiCs for young stArs from a machine learning artificial intelligence convolutional neuRal netwOrk aNalysIs of tess data" and the ridiculousness of this title should be noted for posterity.

of ~ 8700 flares, with the most flares occurring on $>$ M4.5 dwarfs.

Stars are known to spin-down as they age [515]. The generation of magnetic fields is driven by the conversion of kinetic to magnetic energy through dynamo theory. [401] and [78] found flare rates decrease with rotation period, a proxy for age [403], and flare energy. Additionally, [401] found that the magnetic energy released by superflares identified in *Kepler* data can be explained by the magnetic energy stored near starspots, concentrated regions of magnetic field lines [144]. More recently, [251] identified and analyzed *K2* data for the Pleiades, Praesepe, and M67 and found a decrease in flaring activity with an increase in age. There was a sharper decrease in activity for stars with higher effective temperatures, $T_{\rm eff}$.

Using short-cadence *K2* light curves, [138] explored the relation between starspots and flares. The identified flares appeared to show no correlation with the phase of the spot grouping, i.e. the spottier hemisphere had similar flare counts to the less spotty hemisphere. [138] also noticed that faster rotators showed greater flaring activity. Repeating similar studies, [137] looked at 167 M dwarfs and [136] looked at 158 G-M main sequence stars in *TESS* short-cadence light curves observed in Sectors 1-13. Again, they found no correlation between the spot phase and flares at any energy.

[474] conducted a similar study with a sample of 119 main-sequence stars observed during the *Kepler* mission. Within this sample of stars, [474] found that low-amplitude flares are correlated with spot groupings. However, the superflares followed similar trends and were detected across all spot phases. Detailed studies of the Sun have revealed that low-amplitude flares are associated with the presence of sunspots [597]. While [474] found similar trends to that of the Sun, [138, 137, 136] did not.

The previously discussed flare detection studies relied on detrending a light curve and using outlier detection heuristics for identifying flare events. Most detection algorithms apply similar statistical criteria to those defined in [89] on a detrended light curve. The criteria defined in [89] predominantly rely on at least three consecutive cadences that lie $\geq 3\sigma$ above the median of the light curve. [216] relied on fitting a spline to the underlying

stellar variability and identifying flare candidates as at least six minutes (three cadences) of flux 3σ above the detrended light curve flux. [138, 137, 136] removed the underlying spot modulation and marking at least two consecutive cadences $\geq 2.5\sigma$ above the median light curve as a potential flare. [474] used a RANdom SAmple Consensus (RANSAC) algorithm, which identifies and subtracts inliers (the underlying light curve) before searching for outliers above a given detection limit [561]. The outliers are flagged as flare candidates.

However, light curve detrending has the potential to remove low-energy flares because aggressive spot variability models can include cadences that may belong to these flares. In turn, this could bias flare detection towards the highest energy flares and affect modeled flare energies. For example, [114] do not find flares below $\sim 10^{33}$ ergs across a range of spectral types. This is additionally true for having a set outlier cut, where low-energy flares may not lie above this threshold. Because individual flares are believed to originate from the same physical processes, they exhibit similar time evolution [55] and therefore similar characteristic shapes in photometric data. Although at some point there will be a noise level to the flare amplitudes we are able to detect, this proves promising for using machine learning algorithms to identify such a feature.

Machine learning algorithms comprise a set of techniques in which models are derived primarily from the data presented to them. Generically, the key informative or distinguishing features of these data must also be presented to the algorithms. However, in a subset of techniques, deep learning algorithms can be presented with raw data, and the models themselves identify the critical informative features.

Several instances of machine learning have already been applied to time series data for planetary and stellar studies. [504] trained CNNs to identify exoplanet transits and present discoveries of new planet candidates. [19] expanded upon these techniques by including centroid positions of the stars to train their CNN. All three methods relied on detrended light curves and hand-labeled transit events. [429] also used CNNs to search for new exoplanet candidates and trained their network on simulated data with underlying stellar variability.

They trained on light curves with underlying photometric variability.

As young stars are more rapidly rotating than main-sequence stars, it may be expected that these stars exhibit higher flare rates. Due to the high magnetic activity and spot coverage of rapidly rotating stars [375, 382], pre-main sequence (PMS) and young ($t_{\rm age} < 800$ Myr) stars may prove to be excellent targets for understanding the relationship between starspots and flares. Here, we present the results of a CNN trained to identify flares in short-cadence *TESS* data as applied to young stars observed in Sectors 1-20 of *TESS*. The CNN is part of the new open-source software package, `stella`[3]. Our analysis is aimed to better understand flare statistics down to low energies, how they relate to spot groupings, and general trends in flare rates with respect to age and spectral type.

The paper is presented as follows: Section 4.1 will discuss the details of creating and validating the CNN. Section 4.2 will describe the young stellar sample, rotation period measurements, and flare identification used in this work. Section 4.3 will present our analysis of the newly identified flares with relation to spots and Section 4.4 will provide a discussion on these results and implications for exoplanets. We will conclude in Section 4.5.

4.1 The Convolutional Neural Network: `stella`

Neural networks learn features from a training data set that consists of input examples with corresponding classifying labels. When presented with samples labeled by a given class, supervised learning techniques are used to optimize the network weights such that they collectively identify sets of features relevant for those classes. Neural networks are often referred to as "deep learning" because they consist of a series of hierarchical computational layers, where each layer is made up of a series of neurons, or scalar valued units [6]. The input to a neuron is calculated by weighting the outputs from neurons in the previous layer, then adding a bias term and applying a non-linear activation function [481]. The activation function is a key component of a neural network because it enables the network to solve

3. JOSS submitted; `https://joss.theoj.org/papers/70892fb54a060e00c5707d0111b13e06`

non-linear problems. For classification problems (such as used in this work), the final output of a neural network is normalized to a value between 0 and 1, which represents a ranking (but not necessarily a probability, see Section 4.1.5) of the input example belonging to the positive class (in our case, flares).

Fully connected neural networks are not designed to explicitly account for spatial structure in data. Neurons in a Convolutional Neural Network (CNN), in contrast, are only connected to local regions in the preceding layer, allowing them to detect local features in the data. CNNs are promising for astronomical purposes as they can be optimized for computer vision tasks. This means the algorithms can identify patterns and features within complex data sets without requiring prior information on said features. Stellar flares exhibit characteristic shapes in time and flux space and therefore training a CNN to identify this specific feature is promising. In CNNs, a convolution layer applies filters to the data, resulting in feature maps from each layer [305]. The weights in a given filter increase when they see certain types of features in the data that they have been optimized for, and this information is then fed into the next layer. The number of feature maps, as well as the complexity of the detected features, typically increases with network depth. Pooling layers aggregate values within small neighborhoods (strides) of neurons along the input by calculating and outputting a summary statistic (e.g., mean, median, max) [284]. Pooling is primarily used to reduce the number of input pixels to the next layer. This allows the feature maps in the next convolutional layer to have a wider view of the input but at lower resolution and without increasing the number of trainable parameters.

Neural networks are useful for scientific research for several reasons. First, they can in many cases outperform physically parameterized modeling or human inspection techniques in their prediction accuracy: this is attributed to their flexibility in identifying critical data representations that are indicative of important aspects of the data with which they are presented. Moreover, unlike human vetting, deep learning models are systematic, which is important for calculating metrics like occurrence rates. Neural networks are also typically

fast in the inference stage: once models are trained, it can take just seconds to apply to hundreds of thousands of new examples; similarly, they are sometimes upgradable, such that improved models can be quickly re-trained and applied to new data. However, networks can suffer from challenges with bias and uncertainty quantification. The data sets used to train a network contain biases, which the network is optimized to represent. Additionally, there are an increasing number of methods for quantifying errors in networks, but it is an area of active study to provide accurate and interpretable error estimates.

4.1.1 Data preparation: Training, Validation, and Test Sets

The *TESS* targets used in training, validating, and testing the CNN are taken from [216], who searched for flares in the first two sectors of the *TESS* mission. The light curves consist of integrated flux measurements taken at two minute cadence over roughly 27 days; they were made publicly available with the first *TESS* data releases through the Mikulski Archive for Space Telescopes (MAST). Similarly to [216], we split each light curve into individual orbits, and normalized the Simple Aperture Photometry flux (SAP flux) separately for each orbit.

For supervised learning tasks, neural networks require input data that are uniformly sampled to train properly. For the inputs to the CNN implemented here, we used a data set of one-dimensional time series where all elements have the same number of 2-minute cadences. We found that a length of 200 cadences provided enough information about the baseline flux surrounding a given flare. Longer baselines often predicted high probabilities for both rotational signatures and flares instead of just flares. This baseline also provided ample flare and non-flare sets to train, validate, and test on. Following the methods of [429], we ensured all known flare peak times from the [216] catalog were centered at the 100^{th} cadence (i.e. centered). Each of these light curve snippets are hereafter referred to as a "sample." All of the discussed steps (e.g. training and ensembling a series of CNN models)

in this section are incorporated into the open-source Python package `stella`.[4] `stella` and the CNN architecture described here, is specifically tailored for finding flares in *TESS* short-cadence light curves and should not be applied to other photometric time-series data.

4.1.2 Labels

We used a binary labeling scheme of "flare" and "non-flare" for the samples (see Figure 4.1 for examples of the samples). For the flare examples, we used the peak times of flares identified by [216]. Non-flare samples were centered on locations in the light curves at least 100 cadences from a flare. Our final training set contains 5389 hand-labeled flare examples and created 17684 non-flare examples for a 30% positive class data set. We then randomly divided the data set into training (80%), validation (10%), and test (10%) sets. We used the validation set to tune the network and train hyperparameters and then used the test set to evaluate the final model performance (Section 4.1.4).

Due to the detection limitations of the flare identifying methods used in creating the training set, we encountered a few issues. First, not all flares, particularly those at low-energy, were identified in the original catalog and therefore have a "non-flare" label in the training set (Figure 4.4; false negatives). Second, we found the catalog is off in peak flare time for some cases and therefore have been classified as false positives when evaluating the validation set. This is because the flare was not at the center cadence of the example.

4.1.3 Network Architecture & Training

Our CNN architecture, shown in Figure 4.2, is implemented in `tf.keras`, which is TensorFlow's [1] open source, high-level implementation of the Keras API specification [101]. The network consists of a one-dimensional convolutional column with global max pooling and dropout, the results of which are flattened and fed into a series of fully connected (or "dense") layers ending in a sigmoid function that produces an output in the range [0,1]. This

4. `https://github.com/afeinstein20/stella`

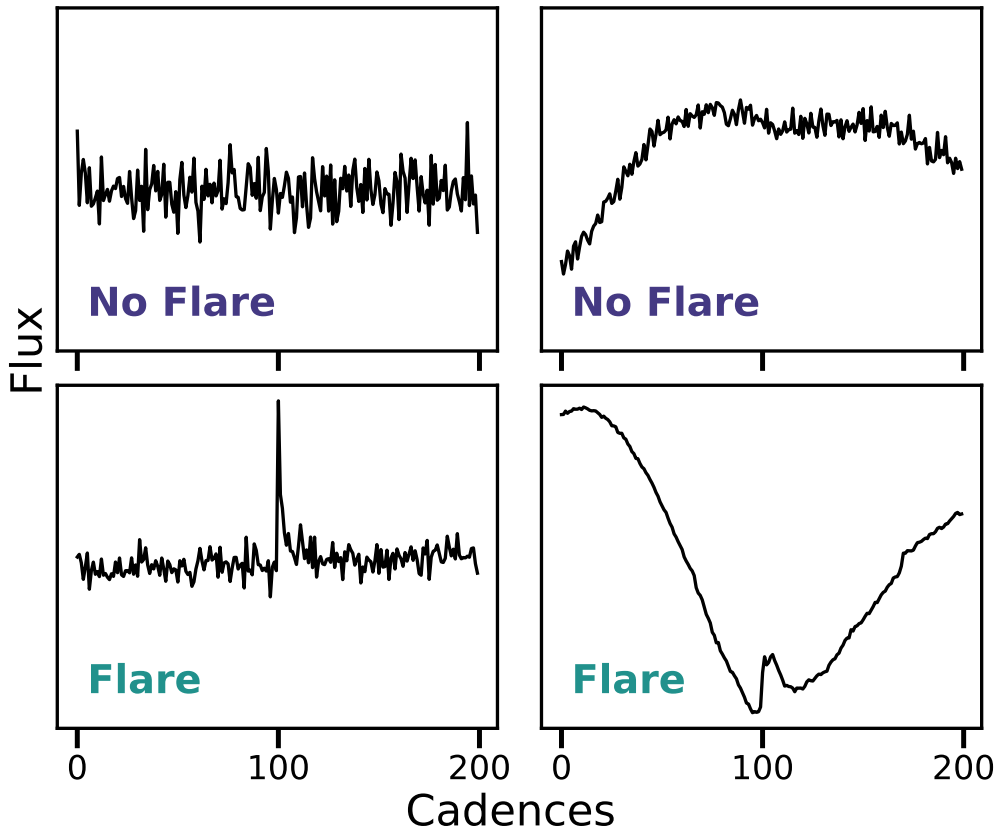

Figure 4.1 Samples in the training set. Using flares identified in [216], we created a training set of non-flares (top) and flares (bottom), each of equal 200 cadence length. The light curves were not normalized. We include within the non-flare cases some examples of obvious spot modulation (upper right) so the CNN will ignore this variability and focus on the characteristic flare shape.

output loosely represents the "score" of how likely a given example is a flare (1) or non-flare (0) event.

The usage of global max pooling and dropout are standard practices with state-of-the-art CNNs [e.g., ImageNet; 231] to improve model performance. Max pooling downsamples the feature maps in a given layer by "pooling" (taking the maximum of) the output neurons within a given region, which can reduce the number of model parameters while increasing generalization [e.g., 310]. Dropout helps prevent model over-fitting by randomly "dropping" (or setting to zero) some fraction of the output neurons in a given layer during training to prevent the model from becoming overly dependent on any of its features [520].

Training neural networks involves inputting samples and then minimizing a cost function that measures how far off the network's predictions are from the truth. This is done through back propagation, which updates the model parameters to reduce the value of the cost function. For model training, we used the Adam optimization algorithm [269] to minimize the binary cross-entropy error function. The Adam optimizer was run with a learning rate of $\alpha = 10^{-3}$ (this controls the degree to which the weights are updated with each iteration), exponential decay rates of $\beta = 0.9$ and $\beta = 0.999$ (for the first and second moment estimates), and $\epsilon = 10^{-8}$ (a small number to prevent any division by zero in the implementation).

4.1.4 Model Evaluation

The exact model architecture, kernel sizes, etc. were chosen based on a trial and error approach to avoid over-fitting the model. Over-fitting was evaluated using four standard machine learning metrics: accuracy, precision, recall, and average precision. Accuracy is the fraction of correct classifications by the model for both classes (flares and non-flares), at a given threshold for deciding when the model output becomes a positive class; we use a threshold of 0.5 for our accuracy calculations and overall analysis. Precision is the fraction of flares classified as flares that are true flares, while recall is the fraction of true flares recovered by the model. The average precision summarizes the precision-recall curve as the weighted mean of precisions achieved at each threshold, i.e. it is the area under the precision-recall curve evaluated across various threshold values, not just 0.5, as the precision is.

We use model ensembling to produce a distribution of 10 independently trained versions of the same model with different random parameter initializations. We then average the predictions across the 10 models and evaluate the above mentioned metrics to establish more robust classifications. Diagnostic plots for the performance of the 10 `stella` models are shown in Figure 4.3. The left column demonstrates the evolution of the accuracy (top) and loss (bottom) functions for both the training and validation sets. As the accuracy converges towards 1 and the loss towards 0, we note that the models are not being over-fit

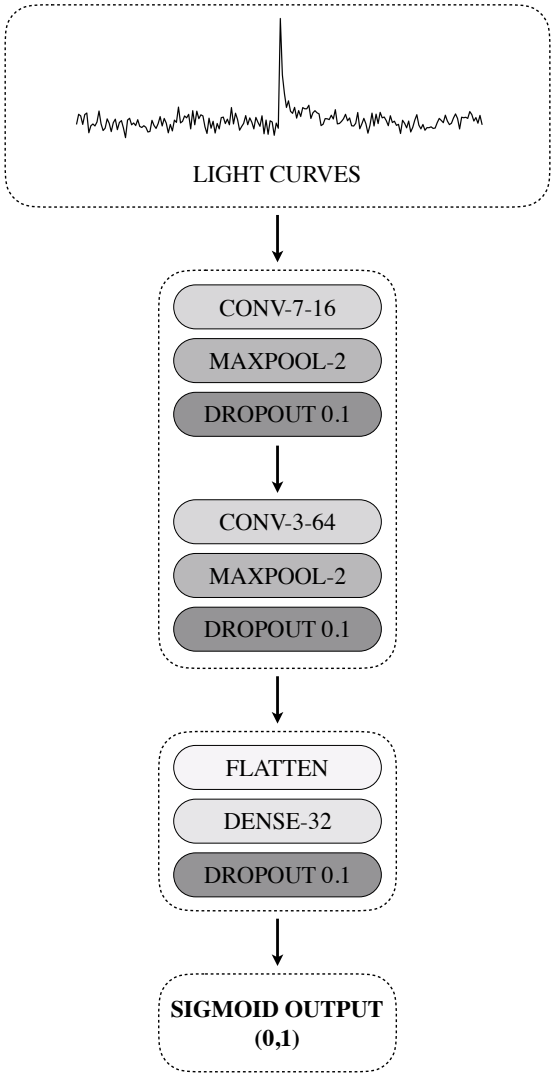

Figure 4.2 The architecture of the `stella` CNN. The training set consists of "flare" and "non-flare" cases, where flares are in the center of a 200-cadence section of the light curve. "CONV-<kernel size>-<number of filters>": a 1D convolutional layer with affiliated parameters. "MAXPOOL-<pool size>": 1D max pooling tensor. "DROPOUT-<dropout fraction>": Drops out fraction of input units to prevent over-fitting. "DENSE-<units>": Creates densely-connected layers of specified units. "SIGMOID OUTPUT": "score" of being part of the positive class.

to the data. The receiver operating characteristics (ROC; top right) visualizes the trade-off of true- and false-positive rates identified in the validation and test sets. The ROC is summarized by the area under the curve (AUC), where an AUC ~ 1 reveals the classification

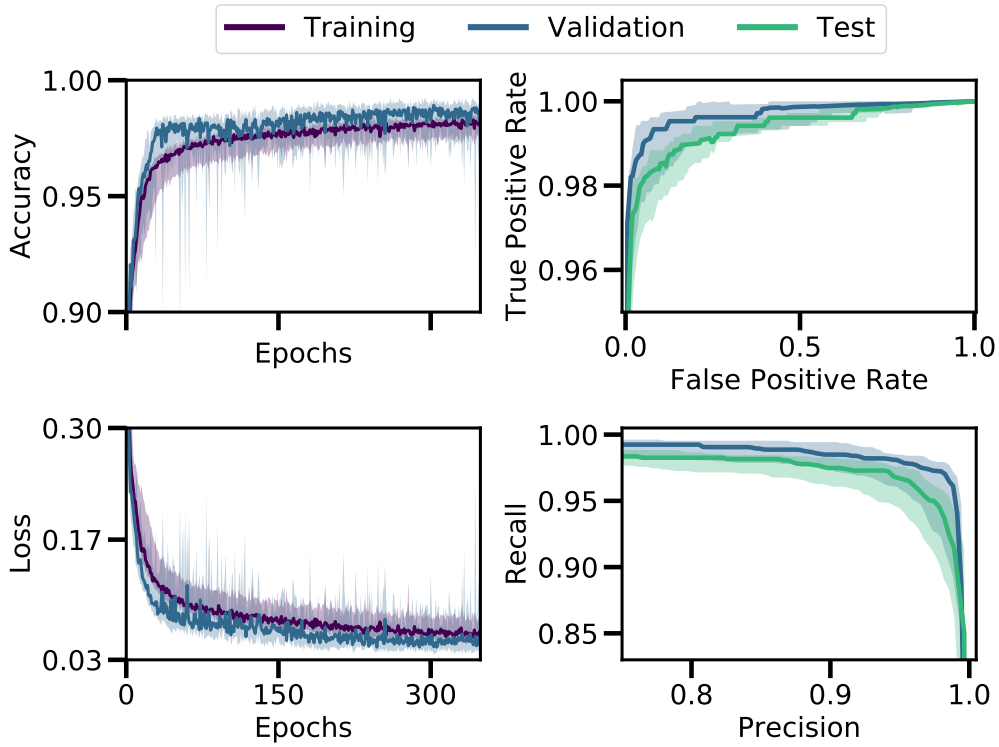

Figure 4.3 The results of training 10 `stella` models demonstrated through several standard metrics. Each model was initialized with a different random seed. The left column demonstrates the evolution of the accuracy (top) and loss (bottom) functions for the training and validation sets over the number of epochs trained on. The right column evaluates the performance of `stella` on the validation and test sets through the receiver operating characteristics (ROC; top) and the precision-recall curve (bottom). The line represents the median curve. The shaded regions represent the 5^{th} and 95^{th} percentiles across the 10 models.

was successful. We obtain an AUC of 0.997 ± 0.002 and 0.993 ± 0.002 for the validation and test sets, respectively. The precision-recall curves for the validation and test sets are shown in the bottom right of Figure 4.3.

Ensembling makes comparisons between different model architectures more robust because it averages over the stochastic differences in the individual models due to their different random parameter initializations. Moreover, ensembling improves model performance because the individual models can perform slightly better (or worse) in different regions of input space, in particular when the training set is small and thus prone to over-fitting. The ensembled results for the test set are: 0.9844 (accuracy), 0.9878 (precision), and 0.9419

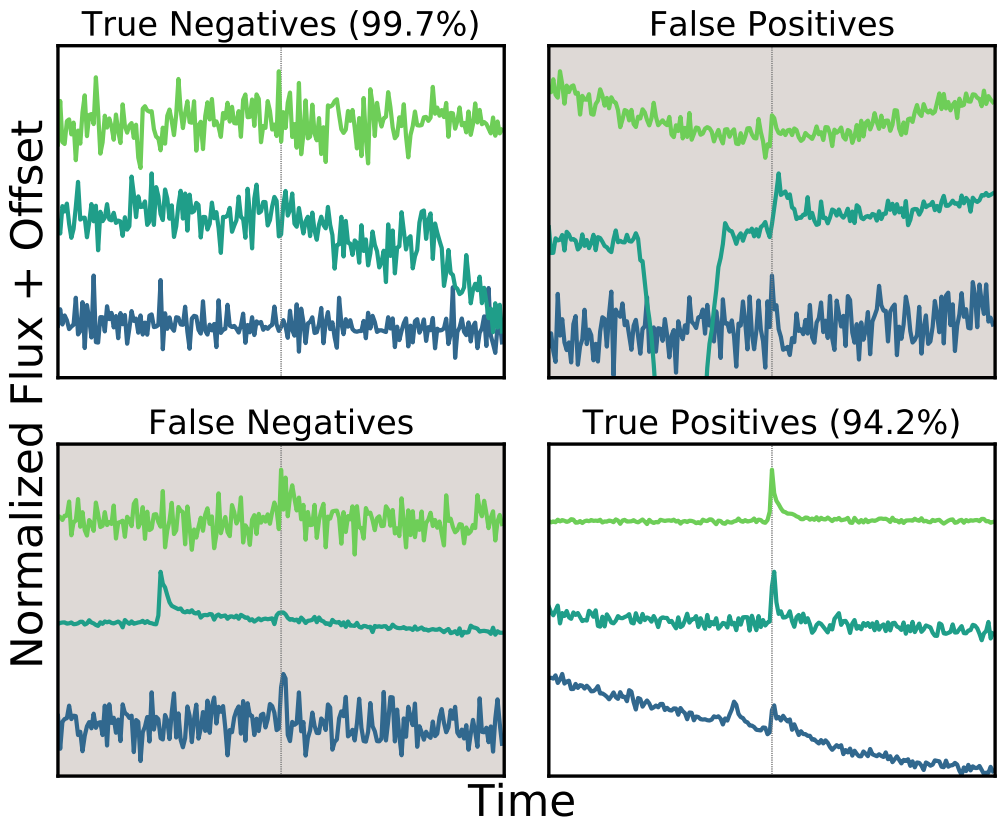

Figure 4.4 The confusion matrix for the `stella` test set. The vertical gray dashed line shows the location of the flare. These samples have been re-scaled so the relative sizes are meaningless; they are offset for clarity. The flares identified as false negatives tend to have flare shapes that deviate from typical positive samples and are probably under-represented in the training set. False positives have flare-like shapes, and could either be noise structures identified as flares or true flares which were unlabeled in the test set due to limitations of previous flare-identifying techniques. The percentages represent the percent of that class recovered in the validation set.

(recall). The average precision is 0.9923. We show the confusion matrix with examples of typical light curves in each category in Figure 4.4.

Additionally, we run a k-fold cross-validation on the combined training and validation sets. Cross-validation is a method of evaluating model generalization performance that is more robust than using training and test sets; in k-folds cross-validation, the data are instead split repeatedly into k parts of equal size and multiple models are trained (here we use k = 5). We show the results of this in Figure 4.5 to illustrate how the model performance

changes with flare amplitude; as expected, smaller flares are more difficult to classify.

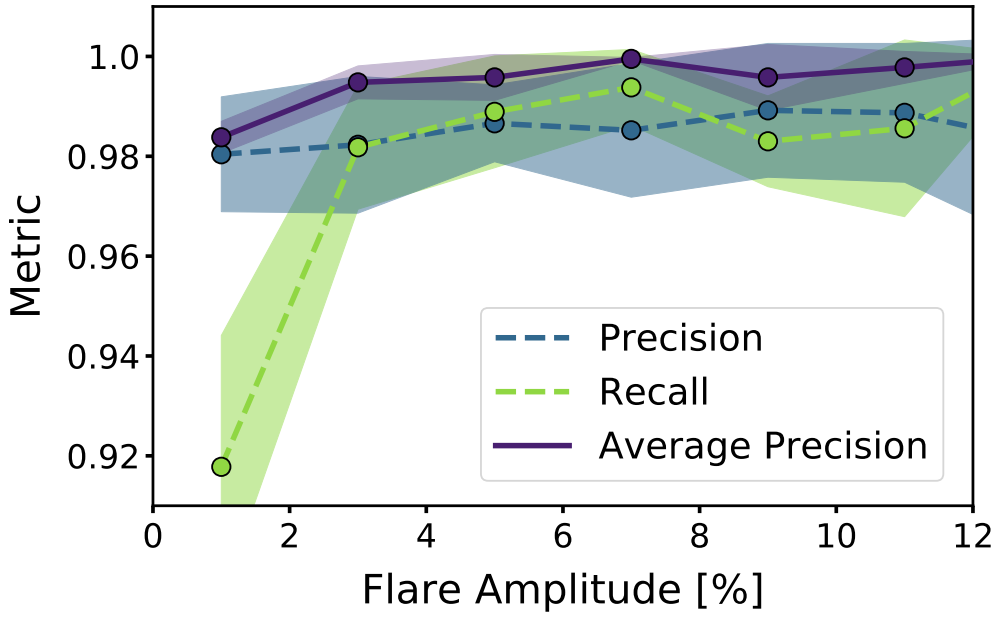

Figure 4.5 The results of how each evaluation metric (legend) changes with flare amplitude. The lines are the averages of the cross-validation k-fold results, while the shaded regions show their standard deviations in each amplitude bin. We use a threshold of 0.5 to calculate the recall (dashed green line), while the average precision (solid purple line) does not require choosing a threshold value.

4.1.5 Determining Probabilities of Events

The output of a neural network classifier is in general not a probability [399], but rather a ranking or score of a given example being associated with the positive class (in our case, a true flare). In some cases, however, the network output may happen to be calibrated such that it is a good estimate of the probability. To test whether this is the case, we calculated the fraction of models across our ensemble that return the flare classification (assuming a threshold of 0.5) for each example in the test set. We then made a histogram of these values with bins spaced such that there were the same number of targets in each bin. For each bin, we then calculated the fraction of true flares using the known labels and compared this value to the fraction of flare classifications by the model: if the model output happens to

be calibrated, then these two values should match in each bin. The results are shown in Figure 4.6, which illustrates a monotonically increasing function near the one-to-one line, indicating that the model is indeed fairly well calibrated and we can use our model output as a rough estimate of probability. We note that there is no measure of uncertainty associated with each classification.

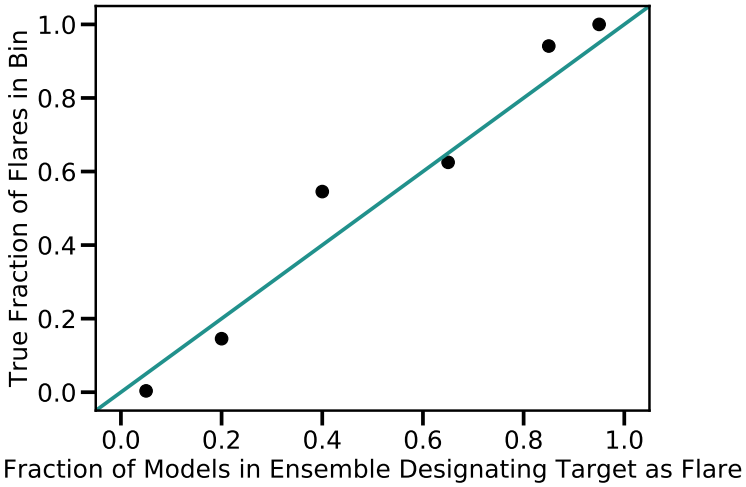

Figure 4.6 The output of the CNN is not a probability and needs to be calibrated to such. Here, we demonstrate that the output value of the CNN (x-axis) corresponds very well to the true fraction of flares (y-axis) and thus no calibration needs to be completed. The output of the `stella` CNN can be taken as a true "probability." A one-to-one line is plotted in teal.

4.2 Analysis

We applied the trained CNN to young stars observed at *TESS* short-cadence for flare identification. Young stars are known to be more active than main sequence stars. Tracing the evolution of flaring activity can provide insight into the first few hundred million years of a star or planet's life.

4.2.1 Selecting the Young Stellar Population

The young stars selected for this sample are high-confidence ($> 50\%$) members of nearby young moving groups, young open clusters, OB associations, and star forming regions (see Table 4.1). Each of these stellar populations are comprised of coeval stars with common kinematics spanning a broad range of masses [602]. The ages of the stellar populations evaluated in this study range from $\sim 1 - 800\,\mathrm{Myr}$. Thus they are powerful tools for understanding stellar properties as a function of age and sample key early times in the formation and evolution of stars and planets.

Population	Age [Myr]	Count	Age Ref.
AB Doradus	149^{+51}_{-19}	283	[48]
Argus	40-50	38	[600]
β Pictoris	24 ± 3	144	[48]
Carina	45^{+11}_{-7}	78	[48]
Carina-Near	$\sim$200	57	[601]
Columba	42^{+6}_{-4}	129	[48]
ϵ Chamaeleontis	$3.7\ ^{+4.6}_{-1.4}$	14	[387]
η Chamaeleontis	11 ± 3	3	[48]
Hyades	750 ± 100	61	[71]
IC2391	50 ± 5	7	[42]
IC2602	$46\ ^{+6}_{-5}$	22	[132]
Lower Centaurus Crux	15 ± 3	338	[431]
Octans	35 ± 5	80	[386]
Platais 8	$\sim$60	13	[438]
Pleiades	112 ± 5	11	[110]
Taurus	1-2	11	[268]
Tucana-Horologium	45 ± 5	182	[48]
TW Hydrae	10 ± 3	33	[48]
Upper Centaurus Lupus	16 ± 2	436	[431]
Upper CrA	10	6	[190]
Upper Scorpius	10 ± 3	13	[431]
Ursa Major cluster	414 ± 23	3	[262]
χ For	$\sim$500	9	[441]

Table 4.1 Number of Stars from Each Young Stellar Population

After compiling a list of candidate young stars by aggregating selected *TESS* Guest

Investigator proposals and data from Faherty et al. [154], we used `astroquery` to access *Gaia* DR2 to retrieve proper motions, parallaxes, radial velocities (when available) for the stars [191, 192]. We used derived effective temperatures, $T_{\rm eff}$, for the stars from the *TESS* Input Catalog (TIC) V8. We used `BANYAN-`Σ[5] to reconfirm and assign population memberships [190]. Using the stars' kinematics, `BANYAN-`Σ derives a Bayesian probability of membership to 27 known coeval populations. We include stars with membership probabilities $\geq$ 50%, which yields a sample of 3193 stars observed at two-minute cadence observed in Sectors 1-20 (Table 4.1). In this sample, 2345 of the stars were observed in a single sector, 609 in two sectors, 103 in $\geq$ 3 sectors, and 7 in 13 sectors (the continuous viewing zone) of *TESS* data.

4.2.2 TESS Light Curve Pre-Processing

We used `lightkurve`[6] to download the target pixel files (TPFs) for all stars in our sample. In general, the Science Processing Operations Center (SPOC) pre-processed light curves were used with the pipeline default aperture. However, we found for several faint $T_{\rm mag}$ $>$ 14 stars, the pipeline was returning higher than expected scatter or negative flux-value light curves. Specifically, we found the background model generated was over-correcting for some sources, seen in two examples in Figure 4.7, where the baseline background flux is not centered around 0.

To mitigate this issue, and for consistency, we completed our own light curve background subtraction and aperture photometry. We follow the 1D background estimation in [165], subtract this background model from the 2-minute TPFs, and extract photometry using the SPOC identified aperture for all sources.

In addition, we use the pipeline-assigned quality flags to mask bad regions in the light curve. We use cadences with quality flags 0 and 512. Upon visual inspection, we found that quality flag 512 ("impulsive outlier removed before cotrending") at times removes the peak

5. `https://github.com/jgagneastro/banyan_sigma`

6. `http://docs.lightkurve.org`

of flares across a range of amplitudes. To mitigate potential biases while calculating flare energies, we included this quality flag in the catalog. We additionally removed the first 200 cadences of each orbit to minimize Earthshine contamination.

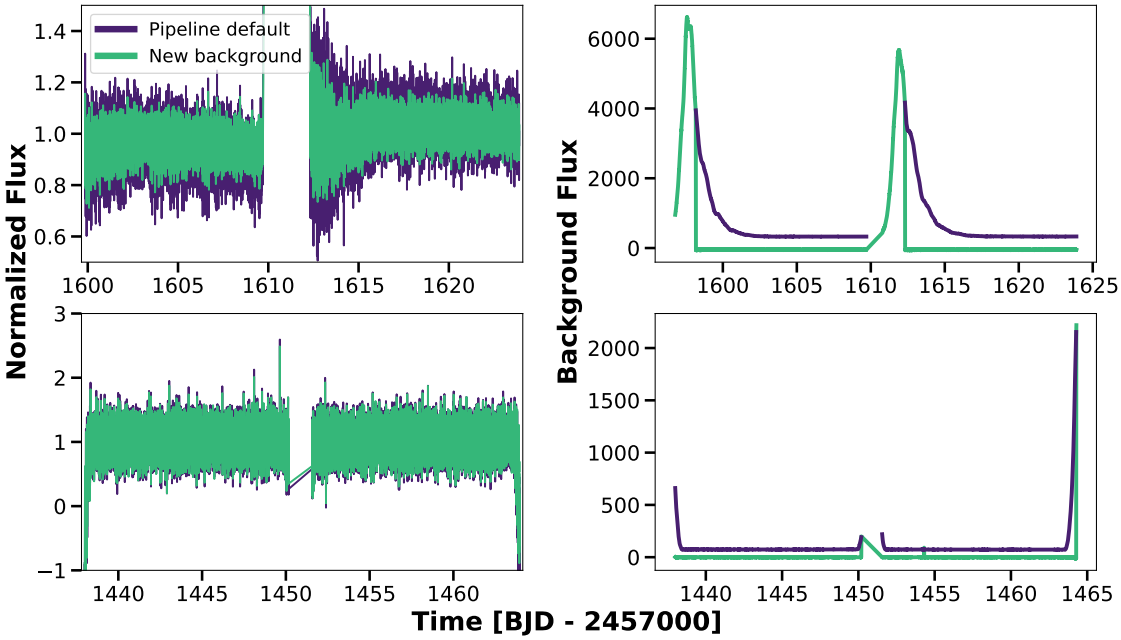

Figure 4.7 Localized background subtraction [green; based on 165] was performed to protect against background over-fitting (purple; default *TESS* pipeline background). Light curves are shown in the left column; background estimations are in the right column. The baseline background flux from the standard pipeline is greater than that of the localized background, suggesting over-fitting. Top is TIC 435801086 observed in Sector 11. Bottom is TIC 007652166 observed in Sector 5.

4.2.3 Measuring Rotation Periods

One of the primary goals of this work is study the correlation of flare events and starspots. The rotation period ($P_{\rm rot}$) of a star can be measured through photometric spot variability. Thus, we created a sub-sample of stars with measurable rotation periods to explore the relationship between flares and spots. Rotation periods for stars observed in multiple sectors were identified per sector. We limited measured periods to $P_{\rm rot} < 12$ days; we found the contamination from Earthshine at the end of each orbit resulted in a strong periodic signal.

Young stars are known to have short rotation periods, on the order of a few days, so this additional upper limit does not dramatically bias our sample [41]. Statistics of the stars in our entire sample can be seen in Figure 4.8 and Table 4.1.

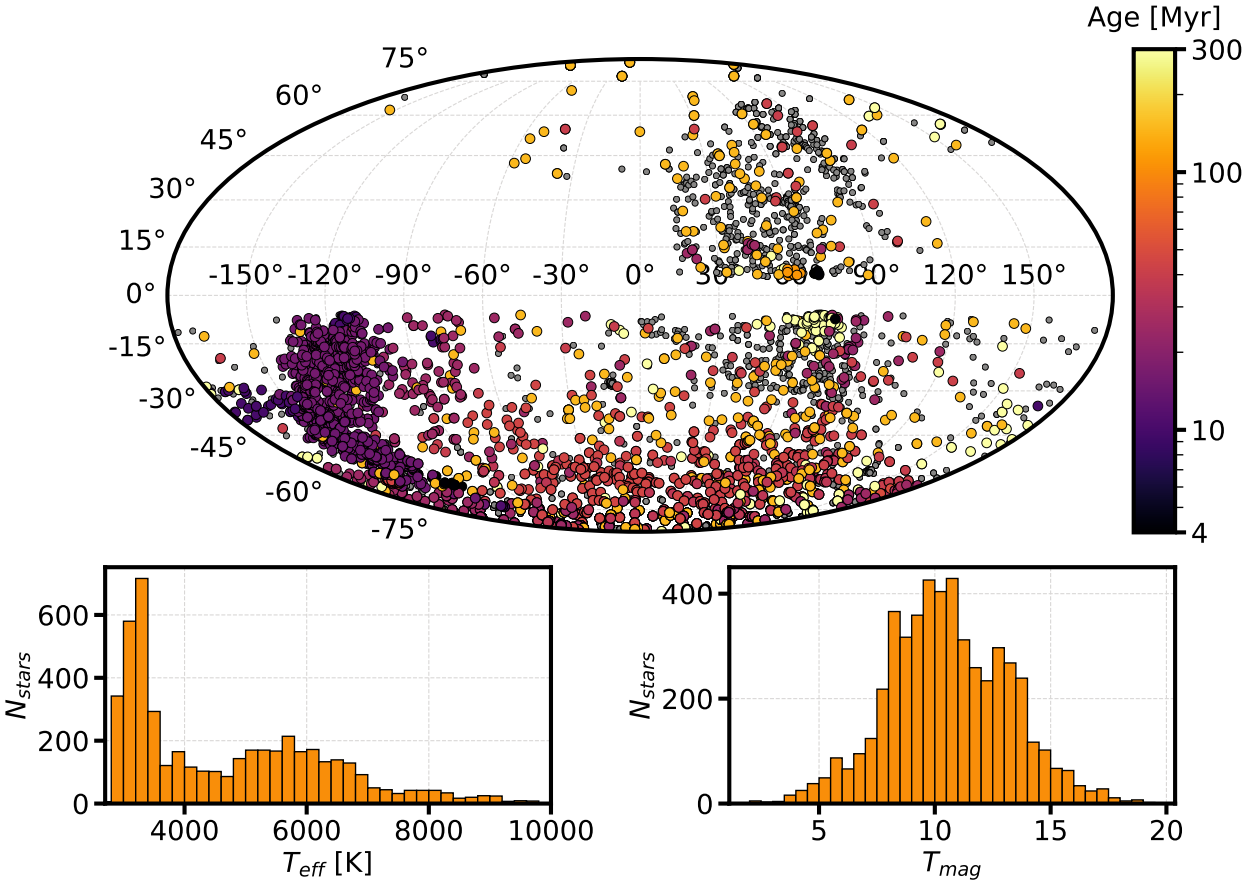

Figure 4.8 The sample of young stars selected in this study. The top plot displays the locations, colored by age, of the sample across the sky in RA and Dec. Gray points which do not meet $> 50\%$ probability of membership to a given young population. The bottom left plot is the distribution of $T_{\rm eff}$. The bottom right plot is the distribution of *TESS* magnitudes, $T_{\rm mag}$.

We used a Lomb-Scargle periodogram implemented in `astropy` to identify rotational signatures [319, 489]. We defined a set of criteria for the periodogram to pass in order to remove weak or non-existent rotation periods, highly unlikely rotation periods, or light curves that are dominated by noise or data gaps. The criteria as as follows: (A) the period must be less than 12 days; (B) the width of a Gaussian fit to the peak power must be less

than 40% of the peak period; (C) the secondary peak in the power spectrum must be 4% weaker than the primary peak. Letters above correspond to a row in Figure 4.9 as examples for each criterion: each one reduces the possibility of catching a light curve that does not have a rotation period.

Resonances of the peak period are masked before identifying the second strongest period in the periodogram. For stars observed in multiple sectors, we compare the rotation periods measured from each sector to the mode from all sectors. Additionally, we searched the second strongest power in the periodogram as we found, on occasion, the strongest period was caught by contamination in the light curve. Half the period and twice the period were each compared to the mode of the sample; if the period agreed within 0.1 days, it was considered a reliable measurement. In total, we measured rotation periods for 1513 stars. The resulting rotation periods for stars observed in multiple sectors can be see in Figure 4.10. The rotation periods are in good agreement across different sectors, sometimes varying as half or twice the periods, which is accounted for in the final median rotation period.

The rotation periods for all stars are plotted as a function of *Gaia* $B_p - R_p$ color and colored by age in Figure 4.11 (top). There is a clear artificially induced break at $P_{\rm rot} > 12$ days, as a result of our rotation period metrics. Stars $>$ 9000K were visually inspected for signs of rotation periods. It is possible that spot variability are from a binary companion to these hot stars, however for this analysis we assume this is not the case. The elbow at $B_p - R_p = 2$ is seen in other gyrochronology studies [e.g. 108]. The most likely associated young population membership were assigned by `BANYAN-`Σ and ages for each population is listed in Table 4.1.

4.2.4 Identifying Flares

The data used to train and validate the CNN required the flare to be at the center of each example. To predict where flares occur in other light curves, we used the CNN as a sliding box (with a baseline of 200 cadences) detector where each cadence is centered within the new

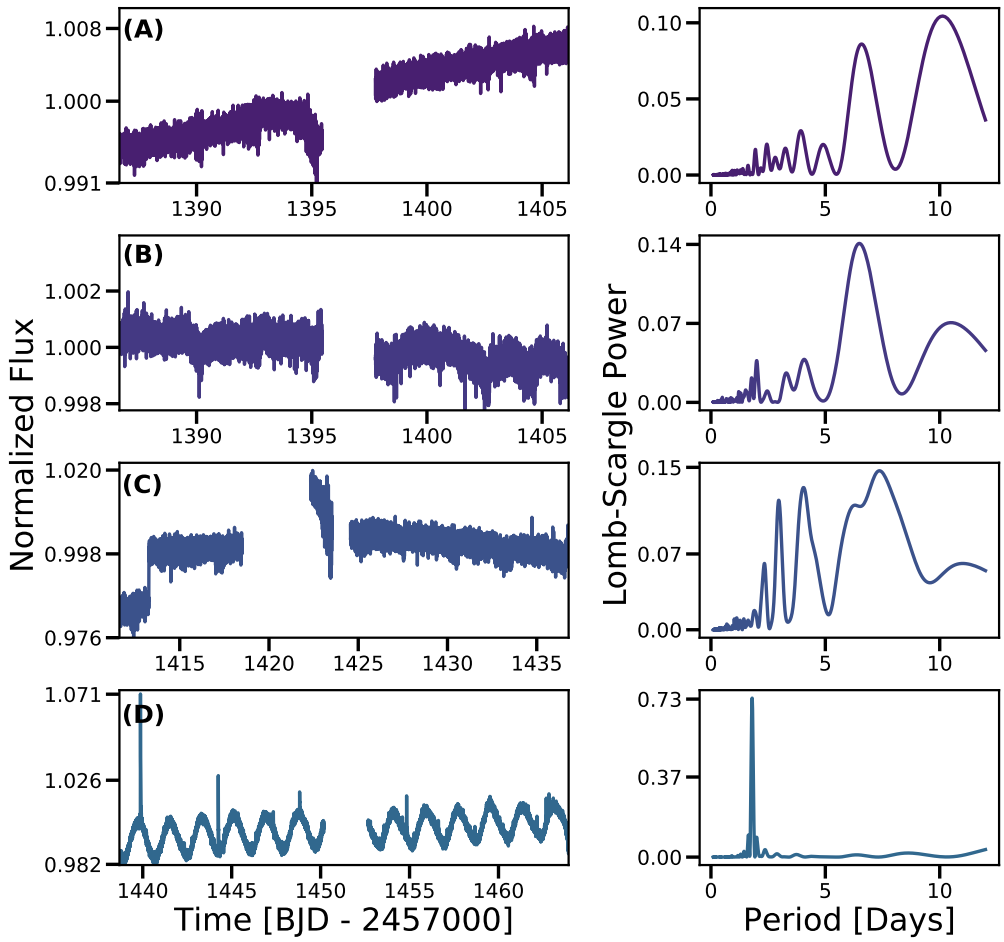

Figure 4.9 Examples of light curves (left column) and corresponding Lomb-Scargle periodogram (right column) that did not pass one of the criteria used to find reliable periods. (A) TIC 3837491. There was no period measured for this light curve, thus resulting in a best-fit period of 12. We limit rotation periods to $P_{\rm rot} < 12$ days to avoid periodic Earthshine signals at the beginning or end of each orbit in a given sector (B) TIC 408017296. A period of $P_{\rm rot} < 12$ days was measured, however the width of the power peak is greater than expected, and there is no noticeable periodic variability in the light curve. This may be due to poor background correction and large Earthshine contamination. (C) TIC 250419751. The periodogram shows 2 potentially strong periods, even after masking resonances of the most likely rotation period. (D) TIC 1273249. A reliably measured rotation period with clear variability in the light curve.

examples, similar to the methods of [429]. This removed biases for finding flares that may or may not have occurred in the center of an example if we evenly divided the light curve into 200 cadences. As flares appear towards the center of the sliding box, the probability assigned to that cadence increases, as seen in Figure 4.12. Each light curve was fed into the

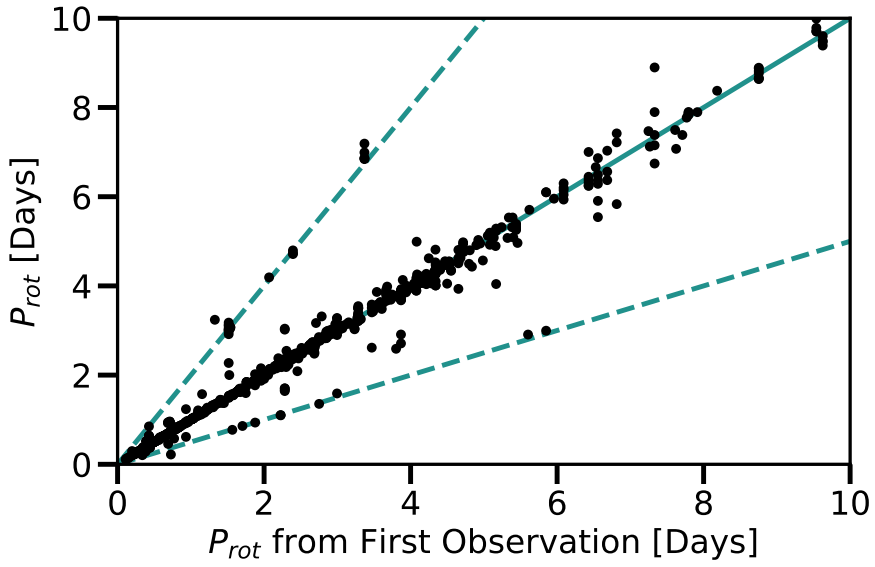

Figure 4.10 A comparison of measured rotation periods of the same star observed across multiple sectors. A one-to-one guiding line is plotted in green. Vertically aligned points represent measured rotation periods from the same star. 85% of rotation periods are consistent between sectors. Dashed lines represent periods that are twice and half the $P_{\rm rot}$ measured in the first observation.

10 `stella` models described in Section 4.1.4. The output predictions from each model were averaged per light curve and used for flare identification.

We considered every point in the "probability"-light curve above a threshold of 0.5 to be a potential flare. Consecutive cadences of greater than the threshold were considered to be part of the same flare. The amplitude of the flare is defined as the point in the series with either the highest probability or, if several cadences share the same probability, the corresponding maximum normalized flux. Examples of identified flares can be seen in Figure 4.12, where cadences are colored by the averaged probability identified with our ten CNN models. Both light curves were fed into the CNN as is. As the CNN requires 200 sequential cadences, without data gaps, the first and last 200 cadences of each orbit are ignored (Figure 4.12, "large" regions orange points).

Per each flare, we extract parameters by computing a χ^2-fit to an empirical flare model [114]. We chose to model the flares by a sharp Gaussian rise and an exponential decay. The

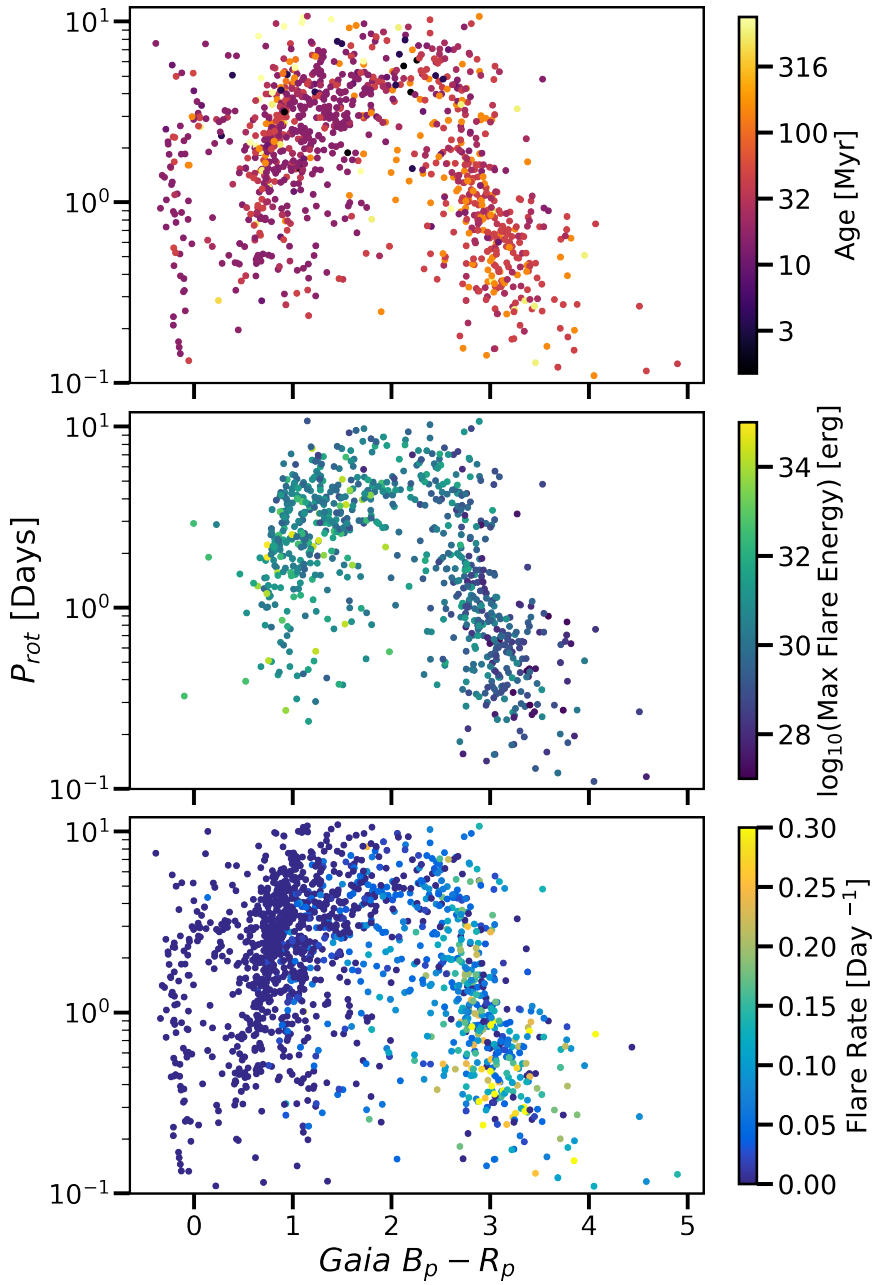

Figure 4.11 The rotation period distribution as a function of *Gaia* $B_p - R_p$ color. The top plot is colored by age; the middle plot is colored by maximum flare amplitude found on that star; and the bottom plot is colored by flare rate, where the flares are weighted by probability assigned by the CNN. $B_p - R_p = 2$ roughly corresponds to $T_{\rm eff} \approx 4000$K, as provided by *Gaia*. There is a clear drop-off in large flares at $T_{\rm eff} \approx 4000$K (bottom), where hotter stars do not have as strong flares, regardless of $P_{\rm rot}$.

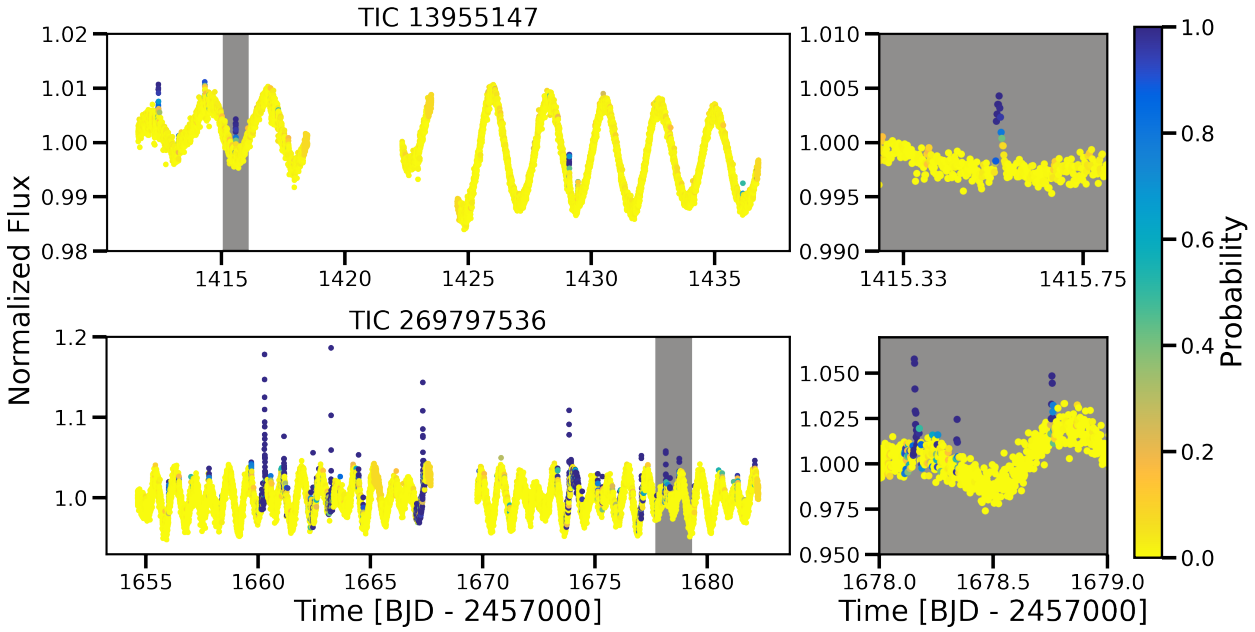

Figure 4.12 Examples of light curves colored by the average "probability" as determined by the ten ensembeled CNN models. An individual flare from each star is highlighted and displayed in the right column. The probability the cadence is part of a flare increases from yellow to purple. Orange areas at the beginnings and ends of continuous observations were ignored by the CNN due to large gaps in the data. Flares are seen to be easily distinguishable from differing spot modulation, which consistently has a low flare probability.

localized underlying stellar variability was removed before fitting the flare model by linearly interpolating across 100 cadences before and after the flare, where the flare itself is masked, and dividing this model from the light curve. Although flares sometimes show more complex structure, we found this simple model to result in reasonable fits to the flare amplitudes.

The CNN provides a good initial guess for where flares are located. However, due to a lack of completeness for flares down to low energies in the training set, we include minor additional checks that the event was a potential flare. Such checks include: (1) the amplitude of the flare must be $1.5\sigma \geq$ the locally detrended light curve, (2) the two cadences directly following the amplitude must be $1\sigma \geq$ the detrended light curve (i.e. at least 3 consecutive outlier points are considered part of a flare), (3) the cadence before and after the flare amplitude must be less than the amplitude, and (4) the amplitude must be $\geq 0.5\%$.

4.3 Results

In total, we identified 17,479 flares across the 3193 stars in our sample. Of these, 14,618 had amplitudes $< 5\%$ in the *TESS* bandpass. Figure 4.11 shows *Gaia* color plotted against $P_{\rm rot}$ colored by age (top), maximum flare energy (middle), and flare rate (bottom). There is a noticeable decrease in flare rate at *Gaia* $B_p - R_p < 2$, where $B_p - R_p = 2$ corresponds to $T_{\rm eff} \approx 4000$K. For Sun-like stars and hotter, there is a clear drop-off in flare energies, with many stars not experiencing any flares and are thus absent from the middle plot. [402] found a decrease in maximum flare energy with increasing rotation period for *Kepler* stars. Additionally, [548] observed the maximum flare energy as a function of rotation period for Solar-like stars in *TESS* data and found similar results. Magnetic activity is heightened for shorter rotation periods; it is interesting to note that we find no such relationship here with regards to the maximum flare energy as a function of rotation period. All young stars of the same color show similar flare energies across rotation periods.

4.3.1 Flare Rates as a Function of Age and Temperature

The flare rates are evaluated as a function of both stellar effective temperature and age. Figure 4.13 is binned by flare energy and colored by ages $t_{\rm age} \leq 50$ Myr (black) and $t_{\rm age} > 50$ Myr (blue); each subplot represents different spectral types. All flare analysis was weighted by the probability assigned by the CNN, as a flare with a 50% probability has an equal chance of being a flare or a non-flare. This figure is additionally binned in log-space and range in energies from $10^{29} - 10^{35}$ erg. The coolest stars exhibit greater flare rates across all energies and many more low-energy flares, with a tail extending out to 10^{35} ergs. There is a detection bias against low-energy flares with increasing $T_{\rm eff}$; the amplitudes of low-energy flares are smaller on hotter stars and therefore are undetectable. Our minimum flare amplitude is 0.5%, which has an equivalent duration (ED), or area under the flare light curve, ~ 1.5 s. For each temperature bin, we calculated the corresponding energy to such a flare. We found

a relation of $E_{\rm flare,min} = 0.01\,T_{\rm eff}^{8.65\pm1.61}$.

The tail extends across all ages, reffigbug with a more dominant presence in the ≤ 50 Myr stars. No flares were seen on $T_{\rm eff} \geq 6200$ K and age $t_{\rm age} > 50$ Myr. $T_{\rm eff} \sim 6200$ K roughly corresponds to the Kraft break [232]. Thus a change in internal structure may be the cause of such a lack of flares, although we note our sample has very few stars in this bin. There are only 132 stars in this temperature range, and only 3 of these are older than 50 Myr.

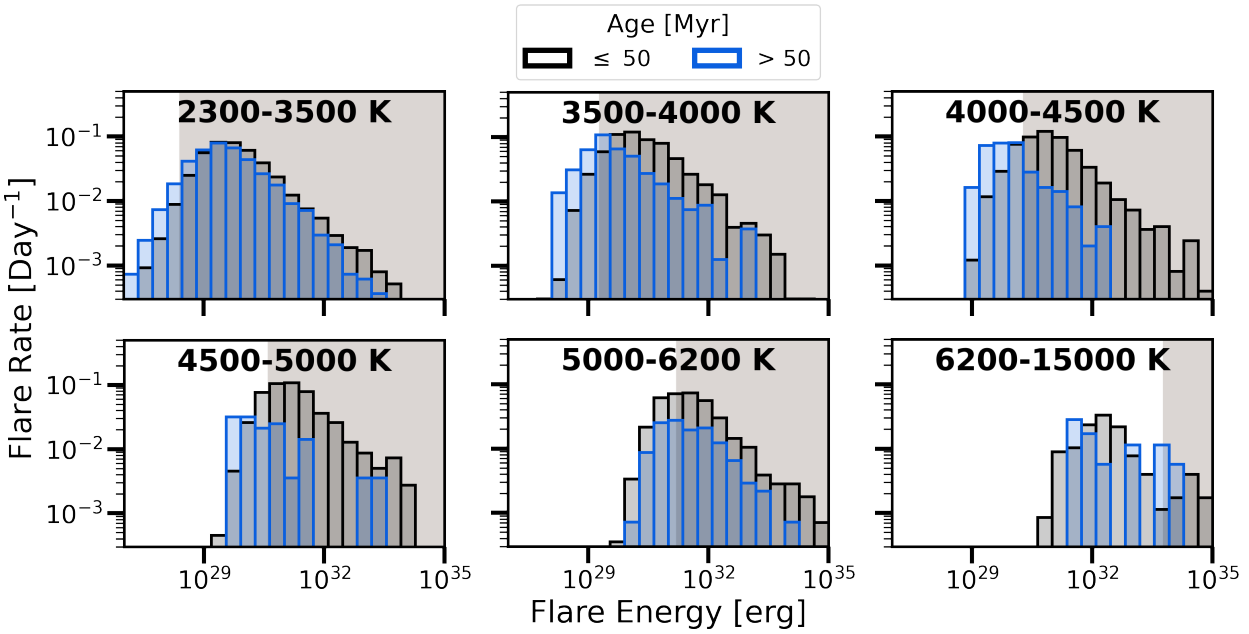

Figure 4.13 Flare rates broken down by effective temperature and colored by age, where black bins represent stars $t_{\rm age} \leq 50$ Myr and blue bins represent $t_{\rm age} > 50$ Myr. The gray shaded region corresponds to the energies at which we expect to be able to detect flares on all stars in that sub-panel. The flares are weighted by their assigned probability from the CNN. Temperature ranges are labeled in each subplot. There is a noticeable drop-off in flare rate and energy as the star's temperature increases. M and late K dwarfs ($2300 \leq T_{\rm eff} \leq 4000$ K) experience similar flare rates and energy across the entire range of our sample. We do not recover any flares on stars $6200 \leq T_{\rm eff} \leq 15000$ K older than 50 Myr.

Figure 4.14 evaluates flare rates by temperature, that which matches the maximum flare rate drop-off in Figure 4.11 (bottom panel), and binned in age ranges. Across all age ranges, stars hotter than 4000 K (green) uniformly display smaller flare rates. The cooler stars have relatively consistent flare rates for both low and high-energy flares in each age bin,

demonstrating an overall level of heightened activity for these stars. There may be a slight increase in high-energy flares and flare rates between 1-20 Myr and 30-45 Myr stars cooler than 4000 K. This may be due to the fact that low-mass stars evolve more slowly onto the main sequence. These results are similar to those presented in [251]. However, the ages explored in this sample are much younger than theirs.

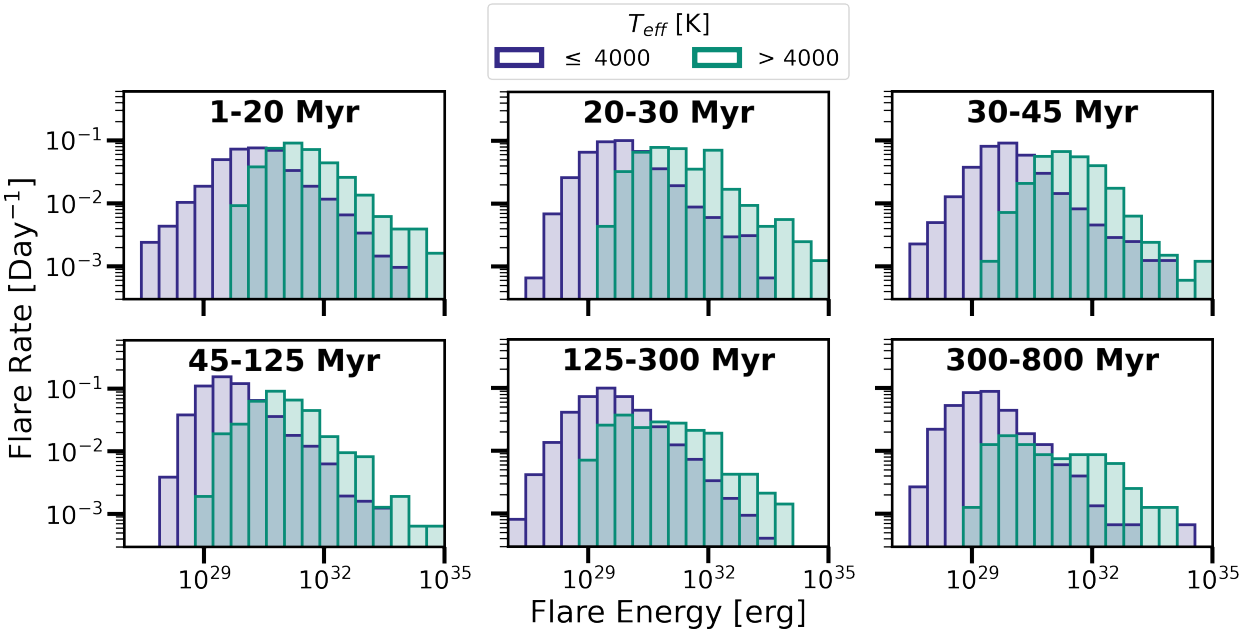

Figure 4.14 Flare rates for our sample broken down by age and colored by effective temperature, where purple bins represent $T_{\rm eff} \leq 4000$K and green bins represent $T_{\rm eff} > 4000$K. The flares are weighted by their assigned probability from the CNN. Cooler stars exhibit more low-energy flares due to detection biases. However, across all sub-panels, the cool stars show greater than or equal to flare rates compared to the hotter stars.

Additionally, we combined the subplots of Figure 4.14 into flare frequency distributions (FFD) for $T_{\rm eff} \leq 4000$ K and $T_{\rm eff} > 4000$ K. A power-law was fit to each FFD, with the same bin sizes. The slope of each was found to be $\alpha_{\leq 4000} = -1.59 \pm 0.03$ and $\alpha_{>4000} = -1.57 \pm 0.04$, which are within a 1.5σ agreement between the samples. We repeated the same calculation, but instead by fitting the FFD for $t_{\rm age} \leq 50$ Myr and $t_{\rm age} > 50$ Myr. We find the slope of each to be $\alpha_{\leq 50{\rm Myr}} = -1.58 \pm 0.03$ and $\alpha_{>50{\rm Myr}} = -1.52 \pm 0.08$. The FFDs binned by age are likely dominated by the flare rate of the coolest stars. With *TESS*'s

extended mission, more data on same and different young stars may reveal a more significant difference in FFD slope as a function of temperature and age.

4.3.2 Correlation between Spots and Flares

The phase of the light curve was then mapped using the best-fit or averaged (if observed in multiple sectors) rotation period. One full rotation period has a range of phases: $-0.5 < \phi < 0.5$, where the peak of the spot modulation is at $\phi = 0$. The phase was mapped at each orbit. Partial rotations near the beginning/end or orbit gap were extrapolated from the surrounding full rotation periods.

Figure 4.15 shows a histogram of flares with respect to phase, where the ϕ bin sizes are 0.04. Low- ($< 5\%$, purple) and high- ($\geq 5\%$, yellow) amplitude flares are separated. For both samples, there is a consistent spread in number of flares at each phase. These results are broadly consistent with those of [401, 138, 137, 136]. These previous studies have looked at flare rates versus phase for samples of size $\sim 100 - 200$, here we find the same effect with sample size 1500. Taken together, we interpret Figure 4.15 as evidence for magnetic active region coverage that is large and mostly uniformly distributed in longitude.

Starspots are dark regions on a star originating from a concentration of magnetic field lines in the photosphere. As such, it is believed that flares will likely occur near these concentrations, as seen on the Sun [144, 597]. By fitting a sine-wave to the overall sample of flares presented in Figure 4.15 at the same phase as the x-axis, we find a 3% difference in the flares between $\phi = 0$ and $\phi = \pm 0.5$. This small phase dependence means that the projected filling factor of stellar active regions remains relatively constant as seen from our viewing location. The on-average 2% spot-induced variability seen in the *TESS* light curves must be the result of a stars covered in starspots, with only slight differences between the most-spotted and least-spotted projected hemispheres.

In the *TESS* bandpass (600-1000 nm), the Sun would be observed to have part-per-thousand variability. The surfaces of the stars in our sample would be very different compared

to the Sun. Stellar active regions on this sample of young stars exhibit a large coverage fraction, with a large degree of longitudinal symmetry. Such symmetries can arise from potentially few, but large spots, very many small spots, circumpolar or polar spots on inclined stars, or active latitudes peppered with spots [455, 217]. The latitudinal distribution of starspots as a function of age is generally unknown, with evidence for circumpolar starspots on both young and evolved stars [133, 475]. Such high-latitude structures may act to mask the mapping from lightcurve amplitude to total starspot coverage [217] as spots remain in view on moderately inclined stars. Such viewing angle effects could explain the relatively uniform frequency of flares with rotational phase.

GJ 1243 is a known older active M dwarf and was found to have no correlation between starspots and flares [225]. That paper proposed two explanations: that there is either significant spot coverage or a large polar spot consistently in the field of view. While polar spots would have different effects as a function of inclination, the effects of high spot coverage would look broadly similar across a large sample of stars. As our sample contains a large selection of stars likely at a variety of inclinations, and we see no significant correlations across our sample, our results favor the high spot coverage scenario for GJ 1243 and other active systems.

Nearly 10 years of observations of the T Tauri star V410 Tau concluded in a relative coverage from 29-41% coverage on the less spotted hemisphere to 61-67% on the more spotted hemisphere [206]. LkCa 4 was found to have a total starspot coverage fraction of 74-86% on LkCa 4, for an asymmetric-to-total spot coverage ratio of 15% [214]. Detailed studies of low-mass members of the Pleiades ($\sim 112\,\mathrm{Myr}$) suggest $\sim 30\%$ and $\sim 50\%$ spot coverage may be common for young M and K dwarfs, respectively [523, 155]. With such varying differences of spot coverage star to star, but with consistency in significant coverage up to 112 Myr, detailed studies of each star with spot modulation would need to be completed to truly understand the underlying distribution of spots.

However, understanding the coverage fraction of spots does not provide insight into the

shape and nature of the spots. [455] modeled light curves with varying spot coverage levels with both small (Sun-like, $R_{spot} = 2°$) and large ($R_{spot} = 7°$). For the similar level of spot coverage, the large spots resulted in higher spot variability amplitudes than that of the small spots. They also concluded the relationship between spot coverage and observed variability is nonlinear.

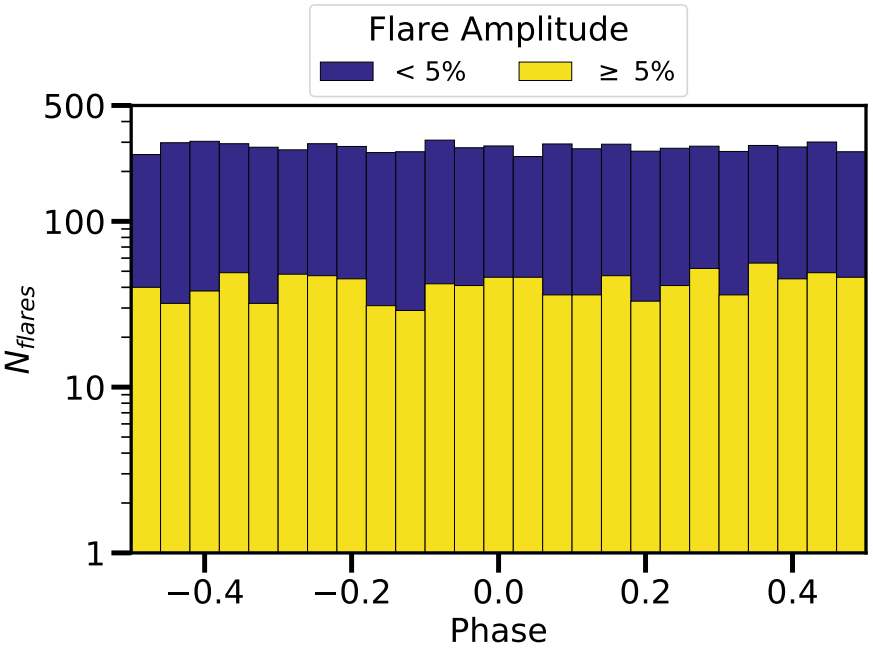

Figure 4.15 Histogram of flares as a function of phase along a light curve. Yellow are superflares ($\geq$ 5% flux increase) and purple are $<$ 5% flux increase. Flares are seen across all phases, which suggests both hemispheres could host spot groupings and the variability seen is the differences in spottiness. Bin sizes correspond to $\phi = 0.04$.

[382] estimated the spot coverage of 531 F-K type stars across 10 Myr - 4 Gyr finding spot coverage decreases exponentially as $\propto t^{-0.37}$, where t is stellar age given in Gyr. For the sample presented here, this would suggest a spot coverage of $1-13\%$ for the oldest to youngest stars. Even when broken down by age, Figure 4.15 remains relatively constant across phase. This suggests that even at older ages, the total spot coverage fraction must be very large and may be underestimated from light curve-based methods, which are largely only sensitive to hemispherical asymmetries and rely heavily on uncertain geometrical assumptions on the

longitudinal spot distribution.

4.4 Discussion

4.4.1 Comparing to Previous Flare Identification Methods

We completed an injection-recovery test to compare the results of the CNN to previous methods. `stella` was trained on real flare events; injected flares do not perfectly model such events. Therefore, we do not expect the performance of `stella` on this sample to be identical to the performance on real data, and the results of this test should be viewed as an imperfect estimate of the effectiveness of the predictive model. The results of this test thus do not provide a definite result of how well `stella` is doing compared to previous methods. In order to completely quantify the differences, a more detailed study would need to be completed, which is beyond the scope of this analysis.

The injected flare amplitudes were randomly chosen from a normal distribution centered around a 4% flux increase from the baseline light curve. Ten flares were injected in 2263 of the light curves, those with measured rotation periods, in our sample. The injected light curves were then processed using the `stella` CNN and flare identification module. To compare to previous methods, we chose to follow the methods of [89] (Equations 3a-d), which have been used for flare analyses for both *Kepler* and *K2* data [112, 252]. We used a Savitsky-Golay filter of window length = 15 [112], as implemented in `lightkurve`, to detrend the spot modulation in the light curves before applying the flare heuristics. An aggressively small kernel size was used to combat the range of rotation periods measured in the sample.

We used a probability threshold of 0.5 for positively identified flares with `stella`. The injected flares may not perfectly represent the real astrophysics behind a flare, which the CNN was originally trained on. As such, an injection recovery provides useful guidance for comparison between methods, and should *not* be interpreted as a definitive efficacy. Nevertheless, the injected flares can provide some insight into overall trends in flare detection.

While both methods recover all flares of amplitudes greater than 11% flux increase, there is a steep drop-off in recovered low-amplitude and generally lower energy flares for previous methods. The CNN is able to recover 80% of injected flares below 5% flux increase. The resulting distribution of recovered flares with `stella` is similar to the injected sample, while previous methods are more centered at higher-flare amplitudes and do not accurately represent the underlying distribution of injected flares.

4.4.2 Largest Discovered Flares

A selected sample of some of the highest amplitude flares recovered in this work are shown in Figure 4.16. The light curves have been normalized and are labeled by the best age estimation for that star. The best-fit young population membership and stellar parameters are presented in the figure caption. There is clear underlying spot modulation for most of the stars plotted (left column) and the superflare is highlighted with a different y-scale limit to the right. These four stars span a temperature range of $T_{\rm eff} = 2800 - 3200$ K and luminosity values between $0.001 - 0.02 L_{\odot}$, as provided in the TIC and are representative of all stars with flares amplitudes $\geq 100\%$.

The ED and the luminosity can be combined to estimate flare energy in the *TESS* band. We use the simple flare model described previously to estimate the ED. Note that the flare models used are a rough estimate. Large flares are sometimes found to be followed by lower-energy sympathetic flares, which extend the exponential decay [114]. The models used to estimate the ED and energy of these flares does not include this potential feature.

The resulting flare energies, in ascending age order for the targets displayed in Figure 4.16 (TIC 24721262, TIC 77954300, TIC 206544316, and TIC 44678751), are: 3×10^{35}, 1×10^{37}, 7×10^{36}, and 2×10^{37} erg. The 'Carrington' superflare event on the Sun in 1859 released $\sim 10^{32}$ erg, which is several orders of magnitude weaker than the strongest flares found in this work [80, 239]. Using the V, J, H magnitude relation in [521] and the measured flare amplitude, we find the change in magnitude for these stars during the flares to be $\Delta V = 3.22$,

4.11, 3.52, and 4.21 for the latter three targets. Flares are treated as a 9000 K blackbody [283]. As there was no V magnitude available for TIC 24721262, we used the G magnitude as an estimation.

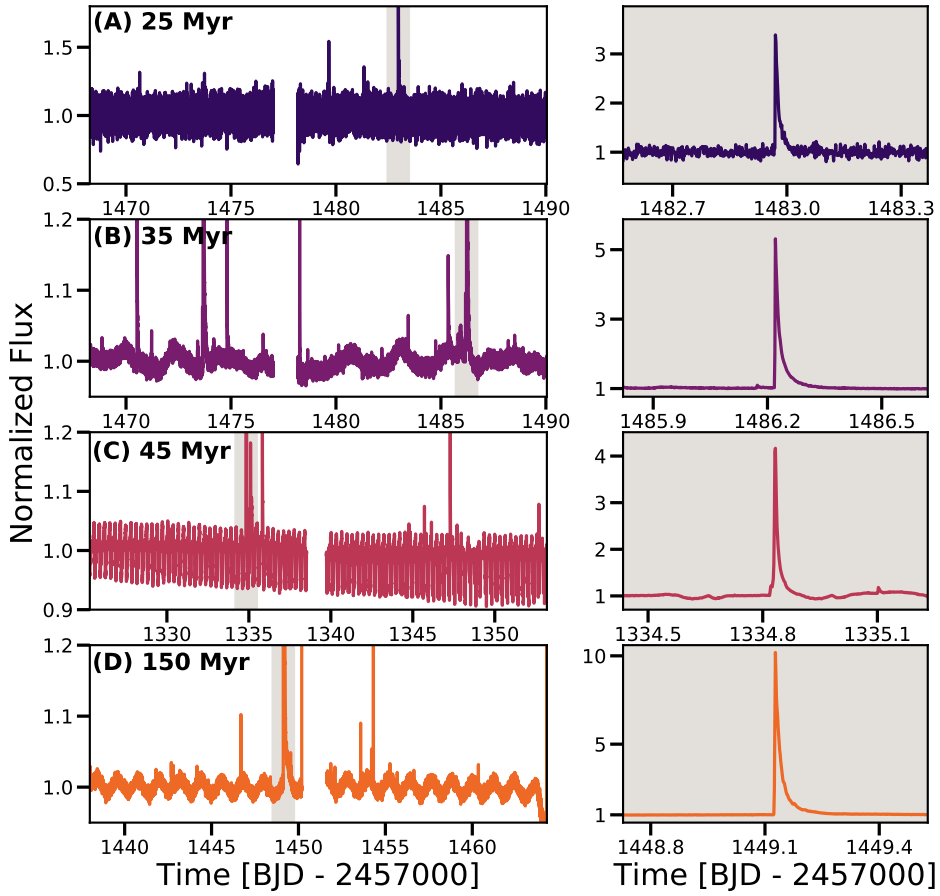

Figure 4.16 A few examples of the largest recovered flares in the sample in increasing age order. The flares are highlighted in gray and plotted with a different y-scale in the right column. (A) TIC 24721262 is a member of the β Pictoris moving group with $T_{\rm eff} = 2836$K and $L/L_{\odot} = 0.001$. (B) TIC 77954300 is a member of the Octans association with $T_{\rm eff} = 3171$K and $L/L_{\odot} = 0.017$. (C) TIC 206544316 is a member of the Tucana-Horologium association with $T_{\rm eff} = 3237$K and $L/L_{\odot} = 0.021$. (D) TIC 44678751 is a member of the AB Doradus moving group with $T_{\rm eff} = 3201$K and $L/L_{\odot} = 0.011$. Note the changes in y-axis, with the largest flare occurring on the oldest star of this sub-sample. Stellar parameters were obtained from TIC V8.

4.4.3 Repercussions for Exoplanets

As the confirmed number of low-mass stars hosting exoplanets increases [e.g. 166, 200, 215, 332, 275], so too does the need to understand the environment in which these planets grow and reside. High flare rates and high-energy radiation of main sequence stars have raised questions about the habitability of these planets. It could inhibit the evolution of life through the suppression or destruction of an atmosphere [541]. Or, flares could create prebiotic molecules to ignite complex chemistry required for life and allow for increased greenhouse warming [8].

Both the frequency and energy of the flares can affect exoplanet atmospheres. Simulations of the flares from AD Leo, an active M dwarf, on two different modeled planets found that a single high-energy flare [E$\sim 10^{34}$erg; 227] was sufficient enough to irreversibly alter the chemical composition of the atmospheres [556]. Specifically, the relative abundances of hydrogen, ammonia, carbon dioxide, nitric oxide, and hydroxide as a function of atmospheric pressure were significantly different $\sim 30,000$ years after a flare was injected, concluding that planets around very active stars are constantly and permanently altered by these events. The highest-amplitude flares in Figure 4.16 are 1-3 orders of magnitude larger than the flare for AD Leo. Although [500] found the enhanced UV radiation did not affect the habitability of an Earth-like planet around AD Leo, they did not account for short-duration high-energy flares. [560] analyzed the flares produced by TRAPPIST-1 in the available *K2* light curve and concluded that both the high frequency and energies are likely disadvantageous for life.

Only a handful of transiting exoplanets around young stars are known [e.g. K2-25, K2-33, DS Tuc Ab, and V1298 Tau bcde; 351, 116, 50, 115, 117, 397]. The atmospheres of these planets are believed to be highly extended and rapidly evolving. The "radius-gap" in *Kepler* planets at $\sim 1.6 R_{\oplus}$ has been theorized to the be result of significant photoevaporation of atmospheres within the first 100 Myr [415]. The models from [415] considered a higher background UV environment for the exoplanet atmospheres, but did not include flares. The results presented here suggest high flare rates and amplitudes within the first 125 Myr for

stars $T_{\rm eff} > 4000\,{\rm K}$. Cooler stars demonstrate high rates across 800 Myr.

We combined the methods described in [415] and [413] to study the evolution of atmospheric mass of an exoplanet over time. Additionally, the equations were modified to account for "flare-like" events, or short bursts of high-energy luminosity. We evaluated the potential impact of flares on V1298 Tau d, a 23 Myr old $6.41 R_\oplus$ planet at $a = 0.108\,{\rm AU}$ separation discovered with *K2* [115]. The following additional assumptions about the planet were made: (1) the iron fraction in the core, $X_{iron} = 1/3$; (2) the ice fraction in the core, $X_{ice} = 0$; (3) the mass of the core, $M_{core} = 5 M_\oplus$; (4) the mass loss efficiency, $\eta = 0.2$. The mass-loss rate due to photoevaporation is then given by

$$\dot{M} = \eta \frac{\pi R_p^3 L_{HE}}{4\pi a^2 G M_{core}} f(A), \tag{4.1}$$

where L_{HE} is the luminosity of high-energy photons from the star, R_p is the radius of the planet, a is the semi-major axis [415], and $f(A)$ is a factor of mass-loss rate increase as a function of flare amplitude, A. This factor in the presence of a flare follows the relations found in [60], and takes the form of $f(A) = 0.95 A^{2.6}$. We assumed a L_{HE} following Equation 22 in [415], which remains constant for the first 100 Myr and decays afterwards as ${\rm t}_{\rm age}^{-1.5}$. Although several studies have shown a correlation between flare rate and L_{HE} [342, 402], these were for solar-type stars and may not apply to young K dwarfs like V1298 Tau. Flare amplitudes were injected up to 100× the base luminosity as observed in the *TESS* bandpass. We include an additional parameter, s, which converts the observed flare amplitudes in *TESS* to the amplitude observed in broad UV wavelength range and was calculated by

$$s = \int_{TESS} \frac{B_\lambda(T_{\rm eff})}{B_\lambda(T_{\rm flare})} d\lambda \left[\int_{UV} \frac{B_\lambda(T_{\rm eff})}{B_\lambda(T_{\rm flare})} d\lambda \right]^{-1} \tag{4.2}$$

where $B_\lambda(T)$ is the Planck function, the *TESS* bandpass covers $600 - 1000\,{\rm nm}$, and the UV covers $66 - 365\,{\rm nm}$. We have assumed all flares can be represented as a 9000K blackbody [283]. For V1298 Tau, where $T_{\rm eff} = 4970\,{\rm K}$ [117], $s = 14.6$, which indicates flares would

appear 14.6× brighter if observed in the UV. At each time step, there was a $\sim 33\%$ chance of a flare being injected, which is a similar probability to observing a flare in the *TESS* light curves.

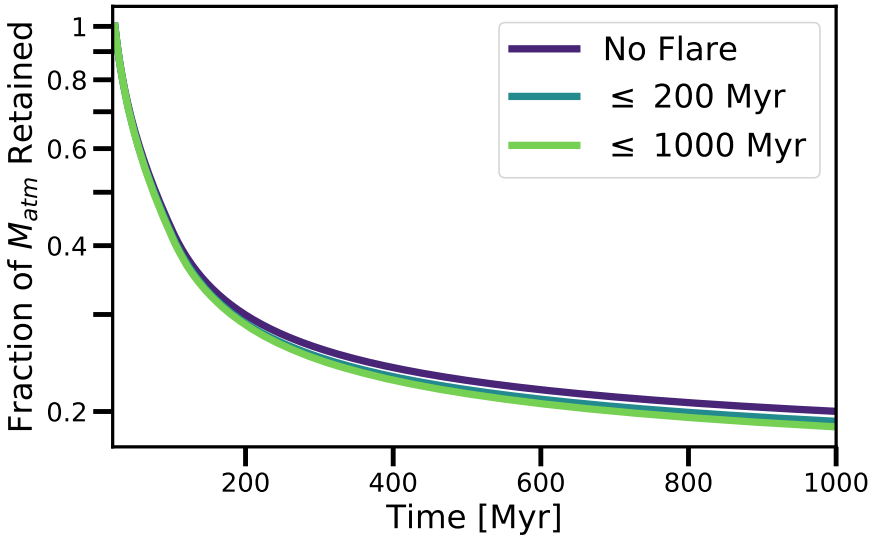

Figure 4.17 Combining the methods of [415] and [413], we calculated the atmospheric mass loss (bottom) for V1298 Tau d. Purple lines correspond to a high-energy luminosity without flares; blue corresponds to flares being present in the first 200 Myr; green corresponds to flares being present throughout all the 1000 Myr. The presence of flares affects the atmosphere mass, with flares present over a longer period of time removing more mass.

The evolution of the atmospheric mass as a function of time is shown in Figure 4.17 for three different scenarios: one with no flares (purple, following the original methods of [415] and [413]), one with flares present for the first 200 Myr (blue), and the third with flares present throughout 1000 Myr (green). The injection of flares does show an effect on the final atmosphere mass. In the case of flares present for the first 200 Myr, the planet loses 4% more atmosphere than without flares. For the case of flares persistent across 1000 Myr, the planet loses 7% more atmosphere. Because the only parameter changing between models is $f(A)$ and we are evaluating ratios, the composition assumptions above listed do not have an effect on these values.

As the mass-loss rate is linearly proportional the high-energy luminosity ($\dot{M} \propto f(A)$), we would expect the mass loss to increase with respect to flare amplitude. Thus stars that have

flares that are 40-60× the base flux [e.g. 427, 428] will increase the mass loss proportionally, thus resulting in even smaller fractional retention of the atmospheric mass. Additionally, the radius of the planet changes due to atmospheric loss changes, originally starting at $R_p = 6.41 R_\oplus$ and predicted to evolve to $R_{p,none} = 2.11 R_\oplus$. With the inclusion of flares, we find the final evolved radius to be $R_{p,200} = 2.10 R_\oplus$ and $R_{p,1000} = 2.09 R_\oplus$ for each model. Although these radius changes are smaller than the typical uncertainties in planet radii, these are physical changes brought about when including flares in atmospheric photoevaporation modeling.

The magnetic field of the planet should also be accounted for. [265] explored the impacts of M dwarf coronal-mass ejections, sometimes associated with flares, on exoplanets and found that rocky exoplanets would need to generate magnetic field strengths of a tens to hundreds of Gauss, much stronger than fields in the Solar System, to protect its atmosphere against these events. The presence of a magnetosphere will directly affect the amount of energy from the flare that reaches the atmosphere, which then directly affects the mass loss efficiency, η. Future analyses should consider flares when thinking about mass loss efficiencies.

4.4.4 Limitations & Future Work

Due to random alignments of stars with respect to our line of sight, one may a expect a handful of stars without measured $P_{\rm rot}$ which exhibit similar flare rates to those with measured $P_{\rm rot}$. These could be the result of either highly longitudinally symmetric spot distributions or a nearly pole-on stellar inclination, where polar starspots are consistently observed and thus show no obvious spot modulation. Additional follow-up of our sample with $v \sin i$ measurements could help to estimate the otherwise-difficult-to-measure latitudinal distribution of starspots. The presence of high-latitude spots could explain the lack of flare phase dependence (Figure 4.15) as polar spots are always visible. Sharp spectral lines in pole-on stars would make them amenable to direct measurement of starspot emission even for small coverage fractions of starspots since high spectral resolution can perceive individual

weak photospheric lines arising from collective starspot emission. Candidate pole-on stars in this sample would have to be reassessed to obtain $P_{\rm rot}$, since the measurement criteria discussed in Section 4.2.3 may have missed potentially weak rotation signatures.

There are a few instances where `stella` improperly characterizes a light curve feature as a flare. First, these improper characterizations are mainly constrained to stars with measurable rotation periods of ≤ 0.5 days, contact binaries with sharp modulation features, and generally noisy light curves. This may be due to a limited sample of such stars in the original training set of the CNN. Second, the metric results of our CNN could be improved by re-sampling the training set to over-sample the lowest-amplitude flares in each batch set. As such, we hope to improve the overall recovery rate of flares with `stella` by incorporating the new flare and non-flare examples identified in this work into the training, testing, and validation sets for future work. Third, users of `stella` who want the most complete flare-only catalog with minimal contamination from noise should explore using a higher threshold probability metric. If users want a small sample of high fidelity flares, they should explore different threshold values to obtain the desired flare results. This metric can be set in the `stella` code and will not affect the included pre-trained models.

The methods explored in this work provide hope for studying other events around young active stars, such as searching for exoplanet transits. Although this sample used real flares as the training set for the CNN, transits can be easily modeled and injected into young stellar light curves. CNNs have been trained to find transits in *K2* data [e.g. 429], however these searches have not been tailored towards young stars in *TESS*. We believe a similar CNN architecture to that created here would work well for transits and plan to explore this question in the near future.

The light curves processed in this work as well as the CNN models created will be hosted as a high-level science product (HLSP) at the Mikulski Archive for Space Telescopes (MAST). Additionally, `stella` is an open-source package that can be downloaded through GitHub or via the Python Package Index. `stella` includes the ability to create custom CNN model

architectures, as well as all of the rotation measurements and flare fitting described in this work. As the models were trained on *TESS* two-minute data, users can predict flares in their own light curves of the same format with our models.[7]

4.5 Conclusions

We have presented the use of a convolutional neural network to identify flares and understand flare rates across a range of young ($t_{\rm age} < 800$ Myr) ages in *TESS* two-minute light curves. Our key findings are the following:

1. CNNs are a promising method for flare detection and are able to recover more flares at lower energies ($< 5\%$ flare amplitude) than previously used light curve detrending and sigma-outlier methods.

2. There appears to be no preference for flare occurrence and spot phase across all flare energies. As flares and spots are both magnetically-driven events, this may be used to infer that neither hemisphere is spot-free, but rather the variability is driven by a different spot coverage fraction.

3. Low-mass stars ($T_{\rm eff} < 4000$ K) show higher flare rates and larger flare energies across all ages of our sample. Hotter stars show higher flare rates and larger flare amplitudes at $t_{\rm age} \leq 50$ Myr and evolve to slow rates and weaker flares as they age. Stars with $T_{\rm eff} = 6200 - 15000$ show no flares at any amplitude for ages $t_{\rm age} > 50$ Myr.

4. We find that across all ages, stars with $T_{\rm eff} \leq 4000$ K exhibit higher flare rates and flare energies than hotter stars. There is a slight increase in flare rate for cool stars in age bins $t_{\rm age} = 1$-20 Myr to 45-125 Myr. Low mass stars are believed to reach the zero age main sequence at 50 Myr [602]. The peak of this flare rate in the 45-125 Myr bin

7. `http://adina.feinste.in/stella`

may indicate the turn on of these stars to the main sequence. However, a larger study of cool stars may be needed to further explore this relation.

5. The largest flares were all found on late M dwarfs ($T_{\rm eff} \leq 3200\,{\rm K}$). As the fully convective boundary is at $T_{\rm eff} \sim 3300$ K [135], this suggests different internal processes driving the creation of such energetic flares.

6. Modeled atmosphere mass loss due to photoevaporation suggests the inclusion of flares decreases the final atmospheric mass and planet radius when compared to models not accounting for flares. Thus, flares should be accounted for in such models moving forward.

7. We hope to improve our CNN by incorporating our newly found flares and more examples of very fast (< 0.5 days) rotators in the training, validation, and test sets. We also plan on testing this CNN architecture and sliding box method to find new transiting exoplanets around young stars.

CHAPTER 5

SELF-ORGANIZED CRITICALITY IN STELLAR CORONAE

The concept of self-organized criticality [36] describes a class of dissipative dynamical systems which remain at a critical point with no intrinsic length or time scale.[1] The existence of the critical state requires a local instability, which occurs when some parameter exceeds its critical value and results in a dissipative transport process where this same parameter increases at neighboring sites. A simple physical analogy is a sand pile. As sand particles are added, the difference in height between neighboring sites on the pile increases. When the additional sand particles make the new height difference exceed a critical threshold, avalanche events occur. This system maintains a critical slope, representing a dynamical attractor that is insensitive to the initial conditions. This critical state is maintained via nonlinear avalanche events spanning all length scales triggered by perturbations.

While the sand pile analogy is simplistic by construction, self-organized criticality naturally manifests in a variety of physical systems. Applications have been found in hydrodynamical turbulence, forest fires and other percolation systems [549], landslides [32, 550], neuroscience [462, 235], climate fluctuations [209], rainfall [18], accretion disks [125], traffic jams [388], evolution [34], extinction [396], financial markets [33] and even Conway's game of Life [31], to name a non-comprehensive list. The theory also explains the Gutenberg-Richter [219] law for the distribution of earthquake energies [35, 517, 408],

$$\frac{dN}{dE} \sim E^{-\alpha}\,, \tag{5.1}$$

where N is the number of earthquakes, E is the energy released in the earthquake (where the earthquake magnitude $m \propto \log E$), and the power-law exponent $1.25 < \alpha \sim 1.5$. A 3-dimensional slip-stick model of tectonic events produces a critical exponent of $\alpha = 1.35$ [35], in reasonable agreement with the observed law. It is worth noting that scalar redistribution rules for the sandpile analogy have been generalized, and that the dynamics of the vectorial

1. This work is based on [164], which was co-authored by Darryl Z. Seligman, Maximilian N. Günther, and Fred C. Adams. A. Feinstein analyzed all data presented in this chapter. D. Seligman is credited with the initial hypothesis tested in this chapter. M. Günther ran `stella` [162] on the TESS stars and produced the catalog of flares. F. Adams provided useful guidance and insights to the manuscript.

case are quantitatively similar to those for the scalar-field case [471].

Even the solar coronal magnetic field may reside in a self-organized critical state [329]. This hypothesis naturally explains the power-law dependence of the magnitude of solar flares, which is of the same form as Equation (5.1), where $\alpha \approx 1.4$ [329]. This characteristic exponent and the subsequent temporal clustering are universal between earthquakes and solar flares [119].

Explosive events on the Sun are believed to be driven by the energy stored in twisted coronal magnetic field lines [425]. Such field configurations are generated through dynamo action in the fluid-dominated interior [94], and through convective and coriolis driven vortical subsurface plasma flows [421, 371, 320, 501]. The concentration of magnetic field lines can lead to the release and subsequent dissipation of energy via the process of magnetic reconnection [531]. These reconnection events could be triggered when the angle, θ, between neighboring magnetic field vectors is greater than a critical value, θ_c. The reconnection event changes the angles for neighboring field lines and can trigger additional events [531, 424, 529]. When $\theta < \theta_c$, a sequence of metastable states develops, allowing for the buildup of non-potential magnetic energy in the form of twisted field lines. Thus, this configuration satisfies all the requirements for a self-organized critical system, if given a source for energy injection.

Recent studies have begun to explore if flaring events on stars across all spectral types and evolutionary stages exhibit the same power-law distribution as in the Sun. This finding may suggest that other stars also maintain self-organized critical states in their coronal magnetic fields. However, this hypothesis has previously been difficult to test due to (i) the lack of a long observational baseline to capture a sufficient number of flaring events, (ii) the lack of observations of a large number of stars across spectral types, and (iii) the difficulty in observing, identifying and characterizing flares, especially those with low amplitudes relative to instrumental noise. Extra-solar surveys such as *Kepler/K2* [65] and the Transiting Exoplanet Survey Satellite [*TESS*; 466] have provided solutions to (i) and (ii). These missions have provided unprecedented, high precision, long-baseline light curves for hundreds of

thousands of stars.

Aschwanden & Güdel [24] identified a power-law dependence with $\alpha = 1.824 \pm 0.007$ in the cumulative distribution of flaring events observed in a set of stars across stellar types observed with *Kepler*. This suggests that the self-organized critical state observed in the Solar corona is ubiquitous. However, the published *Kepler* catalogs tend to be biased towards high-amplitude flares because of the inefficiency at identifying low-amplitude events of implemented flare-detection algorithms. Moreover, these catalogs are contaminated with other features easily mistaken for flaring events, such as rapidly rotating or variable stars [112]. Further complicating matters, the flares that are both observed and identified correctly in *Kepler* are not fully temporally resolved due to the 30-minute cadence of the observations. The *TESS* mission has recently provided 2-minute cadence light curves for ∼200,000 of the nearest and brightest stars. This data provides a full sample of spectral types across the main sequence to search for temporally-resolved flaring events [216].

Additionally, machine learning techniques curated to identify flares in *TESS* short cadence data have been developed to rectify issue (iii). These novel techniques are capable of identifying low-amplitude flares with high fidelity [162, 559]. This combination of unprecedented data and efficient identification techniques provides a new opportunity to expand the hypothesis of self-organized criticality in the solar corona to a sample of stars representative of the galactic census of spectral types and ages. In this letter, we provide a complementary search for indications of self-organized criticality in flaring events observed by *TESS*, using our newly created catalog of stellar flares from two years of data (Günther et al, in prep).

5.0.1 Observations with TESS

NASA's five-year *TESS* mission is currently performing time-series photometry of $\sim$ 90% of the sky [466]. The survey observes in $24^\circ \times 96^\circ$ sectors for $\sim$27 days at a time. During its primary 2-year mission, *TESS* observed ∼200,000 pre-selected stars at 2-minute cadence across both ecliptic hemispheres. *TESS* has been providing an unprecedented data set at

high temporal resolution with which to identify flaring events across stellar spectral types and ages. The light curves used in this study were processed by the Science Processing Operations Center (SPOC) pipeline operated at the NASA Ames Research Center, which performs optimized aperture selection and systematics detrending [257]. We applied pipeline-assigned quality flags to mask contaminated[2] regions of the light curves.

Flare Identification

As mentioned previously, flare identification in time series photometric data has proven challenging. Previous methods of flare identification have relied on detrended, or "cleaned", light curves and have heuristics for outlier detections. However, detrending often removes low-amplitude flares entirely, and the outlier-heuristics [e.g 89] are biased towards the identification of only the highest amplitude events. Conversely, more lenient heuristics produce a significant number of false positive events.

Neural networks are a class of supervised machine learning algorithm optimized for visualization problems such as identifying features in 1-dimensional time series [e.g. 19, 429, 559] or images [e.g. 532]. Here, we used the convolutional neural networks (CNN) developed in [162][3], which are accompanied by the open-source software package `stella` [160], and are easily scalable to a large number of *TESS* 2-minute light curves. `stella` is unique in that it provides a "probability" that any given cadence in a light curve is or is not part of a flaring event. We ran all 2-minute *TESS* light curves through 10 pre-trained `stella` models and averaged the probability outputs for our final catalog of flaring events. We require a probability ≥ 0.9 for an event, meaning the event has a 90% probability of being a true flare. We provide upper and lower limits by only including flaring events with a probability ≥ 0.50 and ≥ 0.99, respectively.

While `stella` recovers a high percentage of real flaring events, it was trained on the

2. Contamination can originate from cosmic rays, reaction wheel desaturation events, and other spacecraft sources. For more information see Table 28 in [536].

3. The pre-trained CNNs are available online: https://archive.stsci.edu/hlsp/stella.

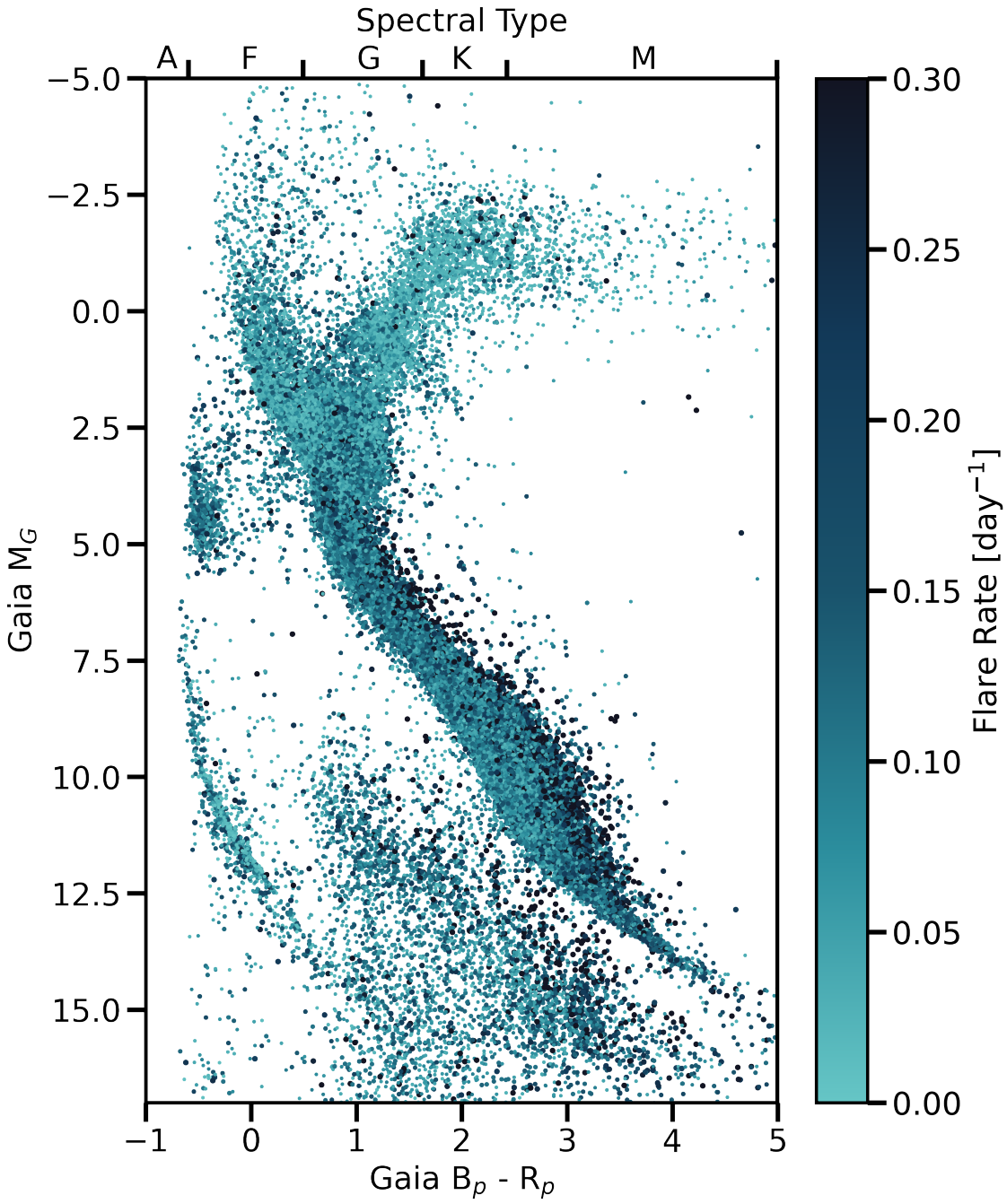

Figure 5.1 A color-magnitude diagram Gaia $B_{\rm p} - R_{\rm p}$ color and absolute Gaia G magnitude, M_G) for our sample colored by flare rate. The flare rate was calculated by weighting each flare by its output "probability" from `stella`. Here, we accounted for all identified flares, not just flares with probabilities ≥ 0.9. Stars towards the top of the main sequence tend to have higher flare rates. This trend could be due to being young and metal-rich or being binaries.

relatively small data set presented in [216], with limited examples of contaminating features such as variable and eclipsing binary stars, and noisy light curves. In Günther et al. (in prep) and this study, we therefore apply four quality control filters to the `stella` outputs, mitigating the risk of false positives:

1. *Signal-to-Noise Ratio Filter*: This filter removes any false positives originating from the increased photon noise of faint targets. To do this, we estimated the root-mean-square (RMS) noise of a given light curve. We first remove any variability using a biweight filter with a window size of 20 minutes and then take the RMS of the flattened light curve. We require stellar flare candidates to have an amplitude of $\geq 3\times$ RMS noise.

2. *Outliers*: This filter removes flaring events that appear in limited data points. We removed any flares with a fitted duration of ≤ 4 minutes which correspond to 2 *TESS* data points.

3. *Eclipsing Binaries (EBs)*: This filter removes false positives originating from EBs, where the ingress and egress of the eclipse events could be mis-classified as flare candidates. For this purpose, we use the entire *TESS* threshold-crossing-event (TCE) catalog provided by the SPOC pipeline. We check if the flare peak times are associated with known eclipses. If a flare candidate falls within the eclipse window (approximated as 3 times the TCE duration), we remove the flare from the catalog.

4. *Variability/Rotation*: This filter removes false positives originating from the peaks of fast-variable and fast-rotating targets. If the target has ≥ 10 flares, we compute a Lomb-Scargle periodogram of the target light curve and of the affiliated probability time series. If the variability detected from each data sets are within 2 days and have a false-alarm probability < 0.05, all flares from this target are removed.

After these filters are applied, we are left with a catalog of $N_{\rm flares} = 958,659$ originating from $N_{\rm stars} = 161,836$ for our analysis. A summary of our catalog is presented in Table 5.1

and the full catalogs are made available in Günther et al. (in prep.). We calculate the flare rate per star, $\beta_{\rm star}$, as

$$\beta_{\rm star} = \frac{1}{\tau_{\rm obs}} \left(\sum_{i=1}^{N} p_i \right), \tag{5.2}$$

where N is the number of flares for a given star, p_i is the `stella` probability for a given flare indexed by i, and $\tau_{\rm obs}$ is the total observed time. An overview of the flare rates for all stars in our sample is presented in Figure 5.1, on a Gaia color-magnitude diagram. Here, we use B_p - R_p as our color and the absolute Gaia G magnitude M_G. It is evident that stars with the highest flare rates ($\geq 0.3\,{\rm day}^{-1}$) fall along the upper edge of the main sequence (meaning they are brighter, i.e. have a lower absolute magnitude, than other stars of that given color). This trend could be indicative of binary star systems [248] or young, metal-rich stars [276]. For our analysis, we only account for stars along the main sequence and the red giant branch (RGB; stars that fork to the right at $1 \leq$ Gaia B_p-R_p and $M_G \leq 2.5$).

$B_p - R_p$	Mass ($M_\odot$)	$N_{\rm stars}$	$N_{\rm flares,\ p\geq0.5}$
$[2.78, 4.86]$	$[0.05, 0.3)$	9,241	59,150
$[2.13, 2.78)$	$[0.3, 0.5)$	20,124	108,963
$[1.21, 2.13)$	$[0.5, 0.8)$	17,914	139,445
$[0.327, 1.21)$	$[0.8, 1.7)$	85,609	571,556
$[-0.12, 0.327)$	$[1.7, 3.0]$	3,770	20,447
Red Giant Branch	[0.8, 1.8]	5,157	10,965

Table 5.1 Sample Summary Statistics. The relationship between Gaia $B_p - R_p$ and stellar mass was taken from [430]. Red giant branch stellar masses are adopted from [584].

5.0.2 Measured Flare Rates

We present our measured flare frequency distributions (FFDs) as a function of stellar mass and flare amplitude (Figure 5.2). The mass bins were selected based on spectral types/changes in interior stellar structure: stars with masses $M/M_\odot \lesssim 0.3$ are fully convective [87, 135], stars with masses $0.3 < M/M_\odot \lesssim 1.7$ have convective exteriors and radiative interiors, and stars with masses $M/M_\odot > 1.7$ have radiative exteriors and convective interiors [232].

We present these results in flare amplitude space, compared to energy, to remove any additional errors resulting from estimating stellar luminosities. In theory, the flare energy is more directly relevant to the predicted self-organized critical state. However, in practice, the uncertainty in mass and luminosity of each star makes the amplitude a more reliable quantity.

We measure the slope of each distribution, α, and associated error using a Markov Chain Monte Carlo (MCMC) approach with `emcee` [203, 178]. Our MCMC chains was initialized with 300 walkers and ran for 5000 steps. After visual inspection, we removed the first 800 burn-in steps and verified our chains converged following the method of [196]. We present our FFDs and measured slope with error in Figure 5.2. The black line in each sub-panel represents our fits that excluded incomplete bins. For example, several of the low-amplitude bins are incomplete because of (1) observational constraints, such as the cadence of the observations or stellar/systematic noise in the light curves and (2) limitations imposed by our definition of flare events in *TESS* data (see itemized list of filters in Section 5.0.1 for more details). Although it is theoretically feasible to quantify the incompleteness via injection-recovery tests, Feinstein et al. [162] stated that this method does not accurately represent the performance of the `stella` CNNs. This limitation is due to the uncertainty in generating synthetic flare photometric models, and the subsequent differences in real and injected flares. We note that Feinstein et al. [162] demonstrated that $\approx 80\%$ of flares with amplitudes $\leq 5\%$ were recovered, corresponding to the first four bins of each panel in Figure 5.2. For most of our sub-samples, these bins were not used for the fit. Finally, we note that the choice of excluded bins (here due to incompleteness) can affect the power-law slopes resulting from the fits.

We find that the FFDs for stars with masses $0.3 \leq M/M_{\odot} \lesssim 3.0$ appear as featureless power-laws. The measured slopes are consistent with models of flaring activity as self-organized critical systems [$\alpha \approx 1.4$ 329] and with that measured for the Sun [$\alpha = 1.65 \pm 0.1$; 119].

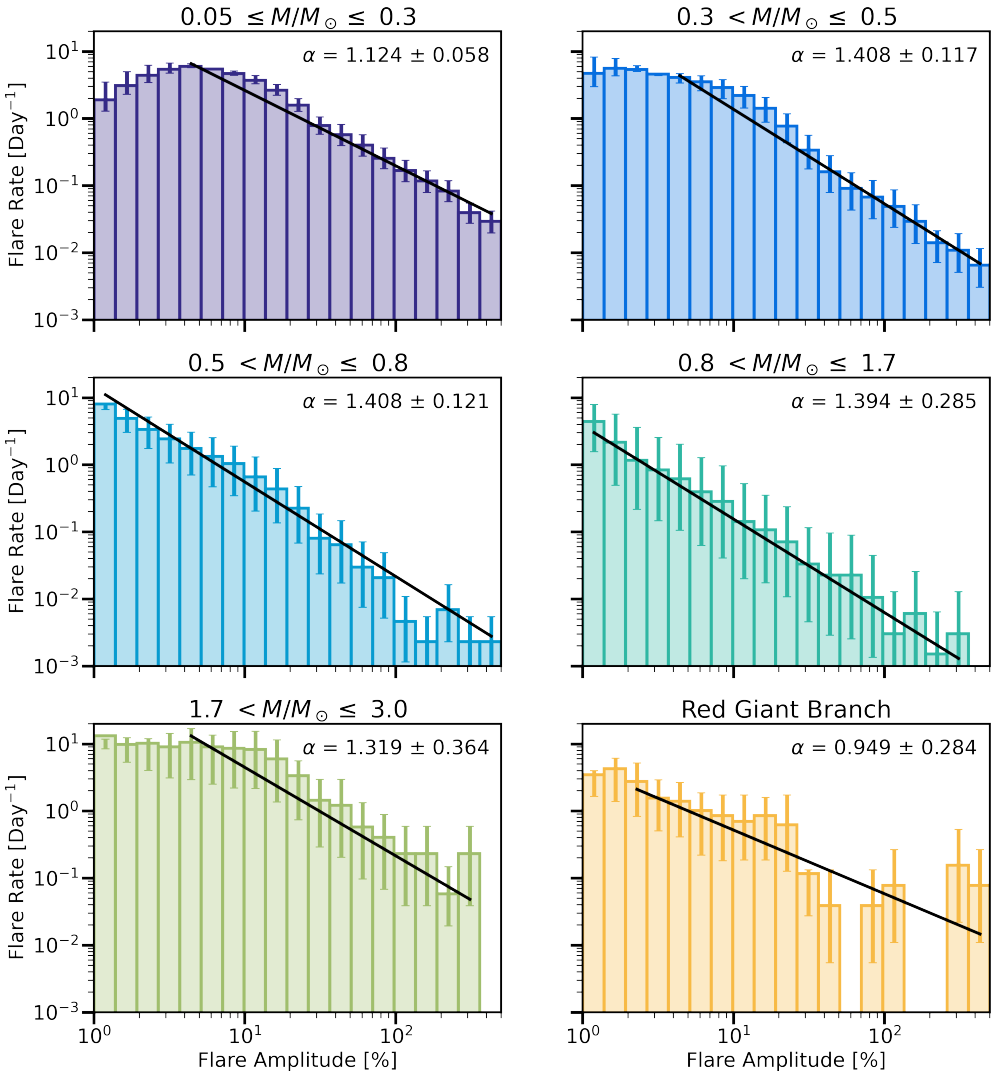

Figure 5.2 The cumulative flare frequency distributions (FFDs) in our sample of stars binned by the flare amplitude and subdivided into different mass bins; the slope, α, and error is given in the upper-right corner of each subpanel. The bins are the FFD for flares with a probability ≥ 0.9. The upper and lower errors on the FFD are defined as flares with probability ≥ 0.99 and ≥ 0.5. All bins exhibit clear power-laws, although some bins are incomplete for low-amplitude flares (e.g., $0.05 \leq M/M_{\odot} \leq 0.3$) or high-amplitude flares (e.g., Red Giant Branch) .

Our lowest mass bin ($0.05 \leq M/M_{\odot} \leq 0.3$) and our sample of RGB stars do not follow the same trends. Stars with $0.05 \leq M/M_{\odot} \leq 0.3$ show a featureless power-law for flare amplitudes $\geq 5\%$; while power-laws are indicative of a self-organized critical state, the difference in interior structure may result in a shallower flare rate (here, $\alpha \sim 1$). The most

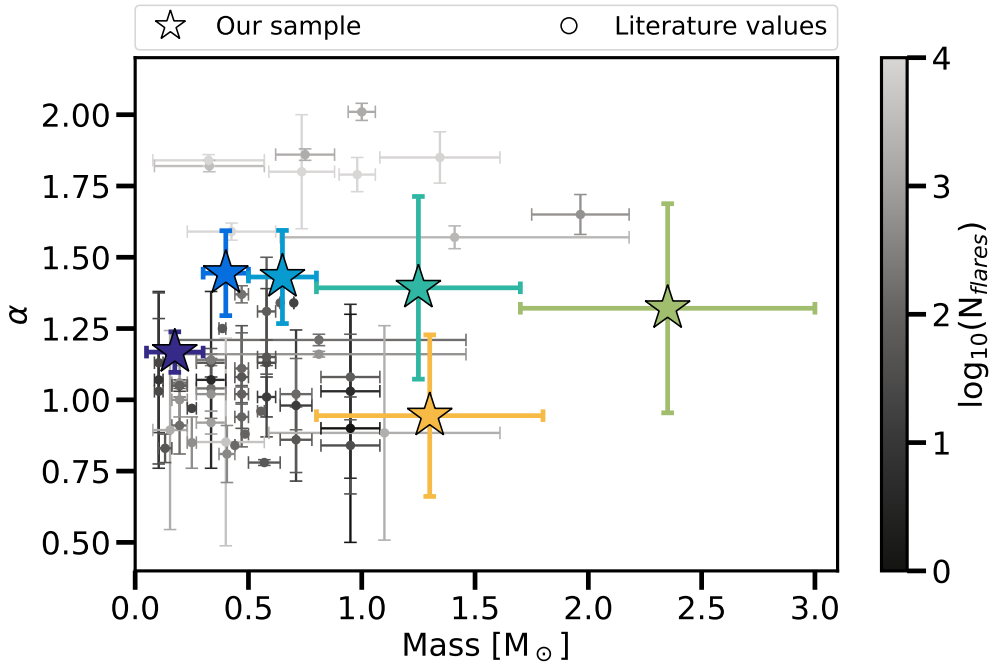

Figure 5.3 Comparison of measured cumulative distribution flare rate slopes, α, as a function of stellar mass. Our rates are plotted as stars. Literature values are plotted as circles and colored by the number of flares in the given sample, which range from single to 10^4 stars [507, 251, 308, 241, 586, 162, 216, 458, 253, 24]. The highest mass stars have higher flare rate indices (light green) than previously measured. Our RGB star (yellow) slope is within 1σ to that of main sequence stars in the same mass range. The remaining data points fall within the expected range of self-organized critical systems. We estimate the masses of our RGB stars using results from [584].

energetic flares have historically been observed on low-mass stars in this bin [162]. It is possible that because these stars are fully convective and therefore have larger convective cells than other main sequence stars, they produce more energetic flares. Similarly, red giants have larger convective cells and display even shallower slopes in their FFD. We also note that our bins of stars with $1.7 < M/M_{\odot} \leq 3.0$ and RGB stars have the fewest number of flares (Table 5.1) and while we are able to measure the slopes of these FFDs, they are incomplete to the lowest- and highest-amplitude flares.

Finally, we compare our measured FFD slopes from our cumulative distribution to those presented by previous authors in Figure 5.3. Previous studies used an order of magnitude fewer flaring events than ours, and tend to report shallower slopes ($\alpha \sim 1$) than the ones

measured here. The variation in measured slopes arises based on sample size/selection, and the cadence of the analyzed data (from 1- to 30-minute cadence). This discrepancy may also be explained by fewer high-amplitude events in the samples, given their rarity. In this study, we also extended our measurement of flare rates to include a broader stellar mass and evolutionary stage range.

5.0.3 Conclusions

In this letter, we analyzed the light curves of 161,836 stars that were observed by *TESS* at a 2-minute cadence. These light curves were processed and searched for flares using a novel machine learning algorithm [160, 162], resulting in a catalog of $\sim 10^6$ flaring events (Günther et al., in prep.). In Figure 5.1, we show how the flare rate changes as a function of location on a color-magnitude diagram. In Figure 5.2, we show the flare frequency distribution of stars as a function of stellar mass and compare it to that found in the literature (Figure 5.3). Main sequence stars with $M/M_\odot \geq 0.3$ exhibit power-law distributions of flare rates with slopes that are characteristic of self-organized critical systems ($\alpha \approx 1.4$). The resulting indices are somewhat smaller for stars with $M/M_\odot < 0.3$ and for red giant stars (which have slopes $\alpha \sim 1$). This discrepancy may be due to differences in the interior structure of these stars, which have larger convective cells compared to other main sequence stars, or due to the incompleteness of our sample of flares on red giant branch stars.

Although the measured slopes of the flare rates show some scatter, the results of this paper indicate a high degree of universality. In the working picture that emerges, subsurface convective regions efficiently inject sufficient energy in the form of twisted magnetic fields near the stellar surface. Subsequent reconnection events then act to produce flares and maintain the magnetic field topology in a self-organized critical state. For completeness, we note that power-law distributions can arise through a variety of mechanisms [395], not only via self-organized criticality, so that additional theoretical modeling of these systems is indicated.

TESS will continue to observe $\sim 90\%$ of the sky for the next three years. The full-frame images that observe $\sim 10^6$ stars per month will soon increase to a higher cadence, making flare identification more feasible for an order of magnitude more stars than presented herein. This increase should further complete the distribution of the rarest, high-energy events. The timing of sympathetic flares after a "main" flare event (defined by some amplitude threshold), can be used to further investigate if these systems maintain a self-organized critical state, as was observed for the Sun and for earthquake aftershocks [119]. Due to the short baseline of *TESS* (~ 1 month), this study may only be truly complete for stars within *TESS*'s continuous viewing zone, those that get ~ 1 year of continuous observations. Such a study could also be completed with the already available *Kepler* light curves, which have a baseline of 4-years to search for the timing of sympathetic flares.

CHAPTER 6

EARLY RELEASE SCIENCE OF THE EXOPLANET WASP-39B WITH JWST NIRISS

The Saturn-mass exoplanet WASP-39b has been the subject of extensive efforts to determine its atmospheric properties using transmission spectroscopy [170, 400, 568, 271].[1] However, these efforts have been hampered by modeling degeneracies between composition and cloud properties that are caused by limited data quality [547, 172, 435, 571, 370]. Here, we present the transmission spectrum of WASP-39 b obtained using the SOSS mode of the NIRISS instrument on JWST. This spectrum spans 0.6–2.8 μm in wavelength and reveals multiple water absorption bands, the potassium resonance doublet, and signatures of clouds. The precision and broad wavelength coverage of NIRISS-SOSS allows us to break model degeneracies between cloud properties and the atmospheric composition of WASP-39 b, favoring a heavy element enhancement ("metallicity") of $\sim$ 10–30$\times$ the solar value, a sub-solar carbon-to-oxygen (C/O) ratio, and a solar-to-super-solar potassium-to-oxygen (K/O) ratio. The observations are also best explained by wavelength-dependent, non-gray clouds with inhomogeneous coverage of the planet's terminator.

We observed a transit of WASP-39 b using the Near Infrared Imager and Slitless Spectrograph (NIRISS) [139] on the JWST as part of the Transiting Exoplanet Community Early Release Science Program (ERS) [525, 47]. Our observations spanned 8.2 hours starting on UTC July 26, 2022 20:45, covering the 2.8-hour transit as well as 3.0 hours prior to and 2.4 hours after the transit to establish a flux baseline. The data were taken in the Single Object Slitless Spectroscopy (SOSS) mode, which simultaneously covers the wavelength range from

1. This chapter is based on [168], which was co-authored by Michael R. Radica, Luis Welbanks, Catriona Anne Murray, Kazumasa Ohno, Louis-Philippe Coulombe, Néstor Espinoza, Jacob L. Bean, Johanna K. Teske. Björn Benneke, Michael R. Line, Zafar Rustamkulov, Arianna Saba, Angelos Tsiaras, and 74 others. Some specific contributions are listed as follows. N. Batalha, J. Bean, and K. Stevenson provided overall program leadership and management. A. Feinstein, M. Radica, L. Welbanks and J. Bean led the efforts for this manuscript. N. Espinoza provided instrument expertise. A. Feinstein, M. Radica, L. Welbanks, C. Murray, K. Ohno, J. Bean, and J. Teske contributed significantly to the writing of this manuscript, along with contributions in the Methods from L-P. Coulombe, B. Benneke, Z. Rustamkulov, A. Saba, and A. Tsiaras. A. Feinstein, M. Radica, C. Murray, L-P. Coulombe, N. Espinoza, Z. Rustamkulov, A. Saba, and A. Tsiaras contributed to the development of data analysis pipelines and/or provided the data analysis products used in this analysis i.e., reduced the data, modelled the light curves, and/or produced the planetary spectrum. L. Welbanks, K. Ohno, M. Line, and S. Moran generated theoretical model grids for comparison with data. A. Feinstein, L. Welbanks, and K. Ohno generated figures for this manuscript. J. Barstow, L. Dos Santos, J. Fortney, P. Gao, H. Knutson, R. MacDonald, T. Mikal-Evans, B. Rackham, and V. Parmentier provided significant feedback to the manuscript.

$0.6 - 2.8\,\mu$m across two spectral orders on the same detector. Order 1 contains the spectral range between $0.85 - 2.8\,\mu$m at an average resolving power of $R \equiv \lambda/\Delta\lambda = 700$, while Order 2 delivers the spectral range of $0.6 - 1.4\,\mu$m at an average resolving power of $R = 1400$. In the SOSS mode, the spectra are spread across more than 20 pixels in the cross-dispersion direction via a cylindrical defocusing lens (see Extended Data Fig. 6.5), thus allowing longer integration times and reducing the impact of pixel-level differences in the detector response. However, this defocus also results in the physical overlap of both orders on the detector. The time series observation was composed of 537 integrations of 49.4 seconds (nine groups per integration), corresponding to a duty cycle of 89%.

We extracted the stellar spectra from the time series observations using six different pipelines to test the impact of differences in spectral order tracing, $1/f$ noise correction, background removal, and spectrum extraction methodology (see Methods and Extended Data Figs. 6.6 and 6.7). We created spectrophotometric light curves per each pipeline (Fig. 6.1), and summed the data to create white-light curves per spectral order (Extended Data Fig. 6.8). The spectrophotometric and white-light curves are largely free of instrumental systematics except for a constant-rate linear trend in time and an exponential ramp effect within the first 15 minutes of the time series. The fitted transit depths were binned into 80 spectral wavelength changes in Order 1 and 20 in Order 2 to create transmission spectra at $R \sim 300$. We present the spectra from the `nirHiss`, `supreme-SPOON`, and `transitspectroscopy` reduction pipelines in Figure 6.2. We find consistent results between the pipelines, with the derived spectra also in agreement with previous Hubble Space Telescope (HST) observations (see also Extended Data Fig. 6.9).

We investigated the atmospheric properties of WASP-39b by comparing our measured transmission spectrum from the `nirHiss` pipeline to grids of one-dimensional, radiative-convective-thermochemical equilibrium models. These models explore the impact of atmospheric metallicity (M/H), carbon-to-oxygen ratio (C/O), potassium-to-oxygen ratio (K/O), heat redistribution (f), and cloud coverage on the transmission spectrum of the planet. We

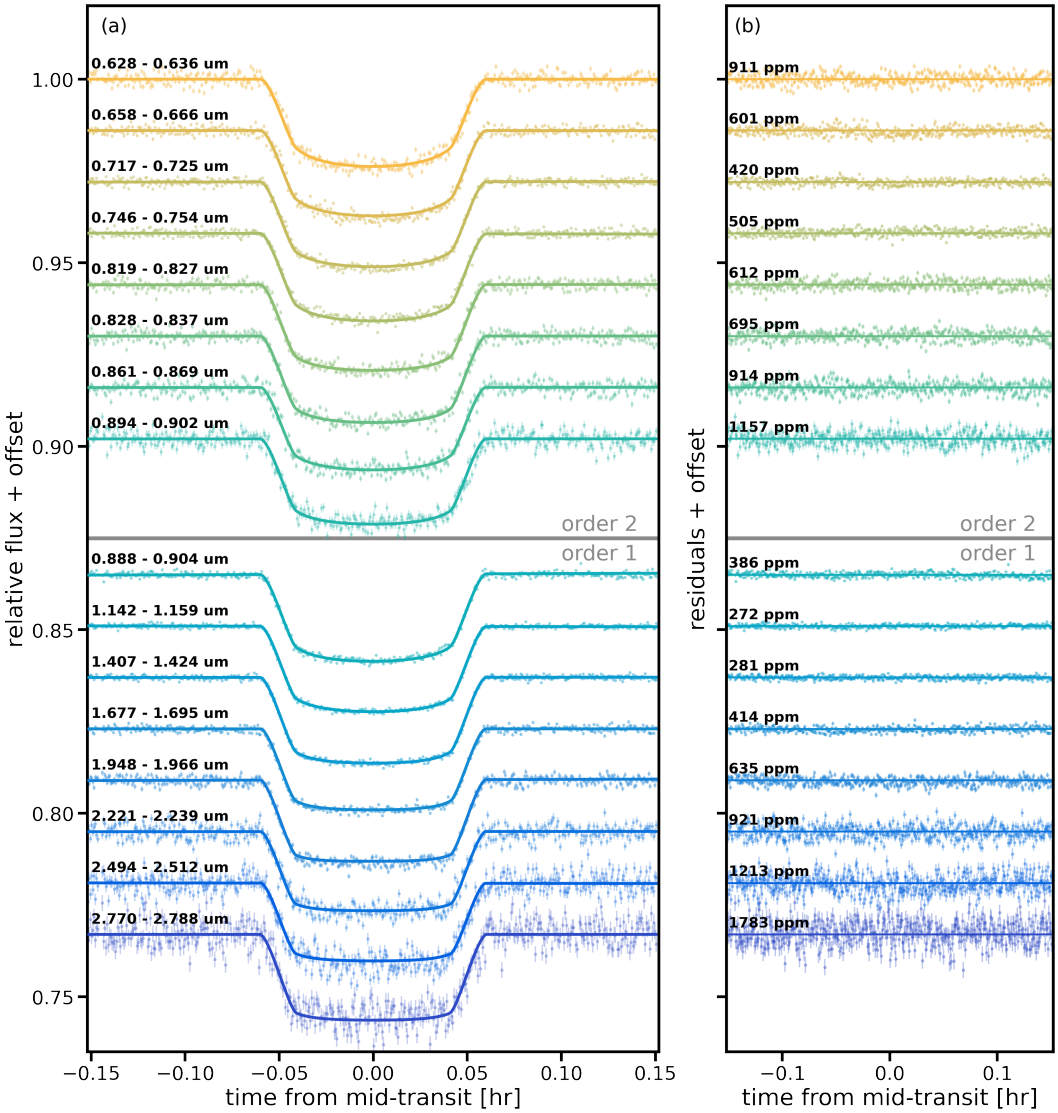

Figure 6.1 Selection of systematics-corrected spectrophotometric light curves and residuals for WASP-39b's transit observed with NIRISS-SOSS for Orders 1 and 2. a: An exoplanet transit model (solid line) was fitted to each light curve with `chromatic_fitting` using a quadratic limb-darkening law. The limb-darkening coefficients, planet-to-star radius ratio (R_p/R_*), and out-of-transit flux were varied in each wavelength channel, while all other parameters were fixed. b: The residuals to the best-fit models are shown for each light curve. The wavelength range per each channel is denoted on panel a, while parts-per-million (ppm) scatter in the residuals is denoted on panel b. We calculate the ppm as the standard deviation of the out-of-transit residuals. The reductions are from the `nirHiss` and `chromatic_fitting` routines described in the Methods. We define our errors as 1σ.

explored multiple cloud models ranging from parametric treatments [300, 311] to a droplet sedimentation model [2] that calculates the vertical distributions of cloud mass mixing ratio

and mean particle size from the balance between gravitational sedimentation and eddy diffusion of cloud particles. Using a Bayesian inference framework (see Methods), we compared these grids of models to the observations and inferred the range of M/H, C/O, K/O and f, that best explains the data while marginalizing over different cloud treatments. WASP-39, the host star, has a metallicity equal to that of the Sun within measurement precision [153, 349, 58, 443], so we reference the planet's atmospheric abundances to the solar pattern of elemental abundances [318]. We compared the grid spectra computed by various models (`PICASO`, `ATMO`, `Phoenix`, and `ScCHIMERA`) with an observational spectrum obtained from each data reduction pipeline and obtained broadly consistent results on the inferred atmospheric properties. In what follows, we introduce the results from the comparison between the spectrum from `nirHiss` data reduction and `ScCHIMERA` grid that allows the most comprehensive treatments of cloud properties.

Our best-fitting model to the NIRISS-SOSS transmission spectrum of WASP-39 b is presented in Figure 6.3. The spectral maxima at 0.9, 1.15, 1.4, and 1.8 μm due to water absorption result in a $> 30\sigma$ detection of the molecule (see Methods). Similarly, the potassium doublet at 0.768 μm is detected in the data at 6.8σ. Signatures of CO and/or CO_2 are identified due to their contribution to the spectrum past 2.3 μm. We find a 3.6σ significance model preference for CO and no significant preference for CO_2 (see Methods).

From the chemical equilibrium models considered, we find that the observations are best explained by a sub-solar C/O (see Fig. 6.4, panel a). Across the different spectroscopic resolutions and atmospheric models, the best-fit C/O is 0.2, which is the lowest ratio explored in the grid of models. We rule out super-solar C/O due to the lack of CH_4 features at ~ 1.7 μm and ~ 2.3 μm, where they would be expected for C/O $\gtrsim 0.7$. Overall, solar-to-super-solar C/O ratios fail to explain the transmission spectrum at the shortest ($\lesssim 1$ μm) and longest ($\gtrsim 2$ μm) wavelengths. Our best-fit C/O is broadly consistent with the observations of WASP-39b with NIRCam ($2.4-4\mu$m; Ahrer et al. submitted), NIRSpec G395H ($3-5\mu$m; Alderson et al. submitted), and NIRSpec PRISM ($0.5-5\mu$m; Rustamkulov et al. submitted).

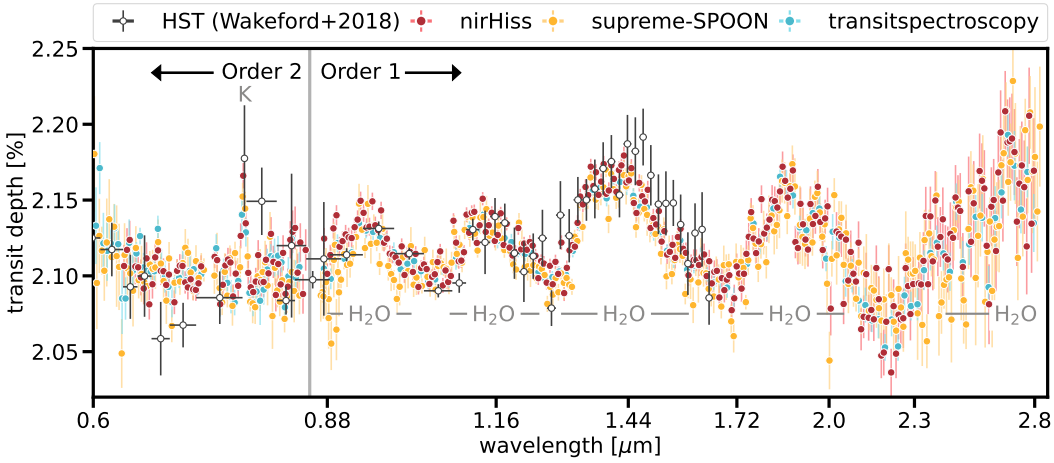

Figure 6.2 NIRISS transmission spectra for WASP-39b obtained by three data reduction pipelines. We find broad agreement in the overall structure of the transmission spectra between several reduction pipelines, a sample of which are presented here (see Extended Data Fig. 6.9 for all reductions). The JWST data are shown in the coloured points, while previous HST observations of WASP-39 b [568] are shown in white. We note that we only consider wavelengths $< 0.85\,\mu$m for Order 2, since Order 1 has much higher fidelity in the overlapping 0.85–1.0 μm range. We define our errors as the 1σ uncertainties extracted from the 16 and 84$^{\text{th}}$ percentiles of the transit depths fit from each pipeline. The JWST and HST data agree across the three broad H_2O features that they have in common. Additionally, [568] found evidence of a K absorption feature at 0.76 μm, which the new JWST data resolves in finer detail.

We also find that the observations are best explained by an atmospheric metallicity of 10–30× solar. Metallicity inferences over the wavelength range of these observations are largely driven by the size and shape of the water vapour features, with some minor contributions due to CO and/or CO_2 at longer wavelengths (> 2 μm; see Fig. 6.3 and Fig. 6.4, panel b). The preferred range of metallicities provides the best fit to the shape and size of the muted water vapour features shortward of 2 μm in combination with the larger water and CO/CO_2 feature longward of 2 μm, regardless of the assumed cloud treatment in our models.

Due to the simultaneous detection of potassium and water vapour, we are able to place constraints on K/O ratio, which is a refractory-to-volatile elemental ratio, being a solar-to-super-solar value. Since the refractory elements are condensed into solids in most parts of protoplanetary disks, the disk gas accretion tends to cause a sub-stellar refractory elemental abundance [495]. By contrast, solid accretion, such as planetesimal accretion, acts to increase

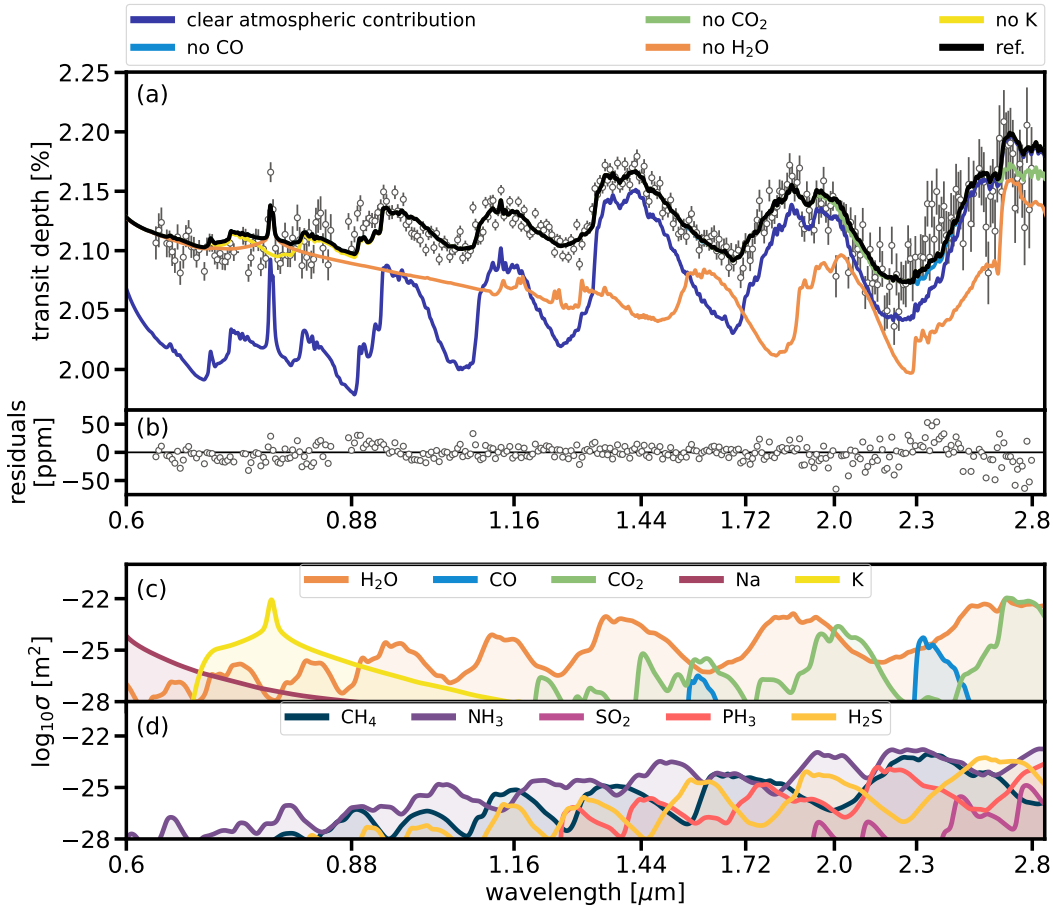

Figure 6.3 Interpretation of the constituents of the NIRISS WASP-39 b transmission spectrum. (a/b): The top panel shows the comparison of WASP-39 b's transmission spectrum from the `nirHiss` reduction (gray points) with respect to the best-fit reference model (black line). This model assumes an atmospheric metallicity of [M/H]=1.38 (23× the solar value), C/O=0.2 (0.55× solar value, [318]), [K/O]=0.1 (1.26× the solar value), full day-night heat redistribution (f=1), and flux-balanced clouds with inhomogeneous terminator coverage. Each colored line removes a key constituent found in our best-fit reference model to demonstrate how the spectrum would change were these features not included. The removal of clouds, and H_2O absorption from the reference model result in large-scale changes to the shape and depth of the transmission spectrum. Other sources of opacity with an impact on the spectrum are K, CO, and CO_2. Residuals between the data and the reference model are plotted below. (c/d): The two bottom panels show the molecular absorption cross-sections for a selection of gases observable within the NIRISS bandpass. The middle panel highlights gases inferred by our analysis of WASP-39 b's spectrum. The bottom panel highlights some gases that were not identified in these data, but that may be present in future observations of other exoplanets.

the refractory elemental abundance and refractory-to-volatile elemental ratio [220], though the latter depends on the composition of the accreted solids [324]. We anticipate that the

K/O ratio diagnoses to what degree the solid accretion enriched the atmosphere during the formation stage. All of our fitted models find that the WASP-39b observations are well described by solar-to-super-solar K/O ratios, which is in agreement with previous inferences for this planet obtained via observations with limited spectral coverage [573]. We do not expect the K feature to be impacted by stellar chromospheric magnetic activity given the effective temperature of the star [$\sim$ 5300 K, 470] and the general quietness of WASP-39 (see Ahrer et al. submitted) It is also in line with larger population studies of hot giant planets that broadly found solar-to-super-solar refractory abundances and solar-to-sub-solar H_2O abundances [573, 90]. The shape and strength of the potassium doublet are best explained by [K/O]$\sim$0.1–0.5, equivalent to 1–3$\times$ solar (see Extended Data Fig. 6.12). While the suggested K/O ratio might be a lower limit owing to the photoionization of K at upper atmospheres [298].

The NIRISS-SOSS observations enable the detection of clouds in the atmosphere of WASP-39b. Clear atmosphere models cannot explain the amplitudes of all of the water vapour features simultaneously, which strongly indicates the presence of clouds (see Methods and Extended Data Fig. 6.10). The atmospheric models explored here indicate the presence of non-gray and non-homogeneous clouds, with model preferences of 8σ and greater for models with both non-gray and non-homogeneous clouds over models with gray homogeneous clouds only. This model preference is driven by the decrease in transit depth between 2–2.3 μm (see Extended Data Fig. 6.11, panel a), which cannot be explained by gray clouds uniformly distributed along the terminator (see Extended Data Fig. 6.11, panel a). Moreover, within the various cloud treatments tested here (gray, gray + power-law, flux-balanced clouds, see Methods), both parametric and droplet sedimentation models indicate a preference for inhomogeneous cloud coverage of $\sim 50 - 70\%$ around the planetary day-night terminator because it better explains the decrease in transit depth between 2–2.3 μm.

Atmospheric circulation and cloud microphysical models have predicted that the cloud structure varies significantly along the terminators of hot Jupiters [426, 449, 479]. In par-

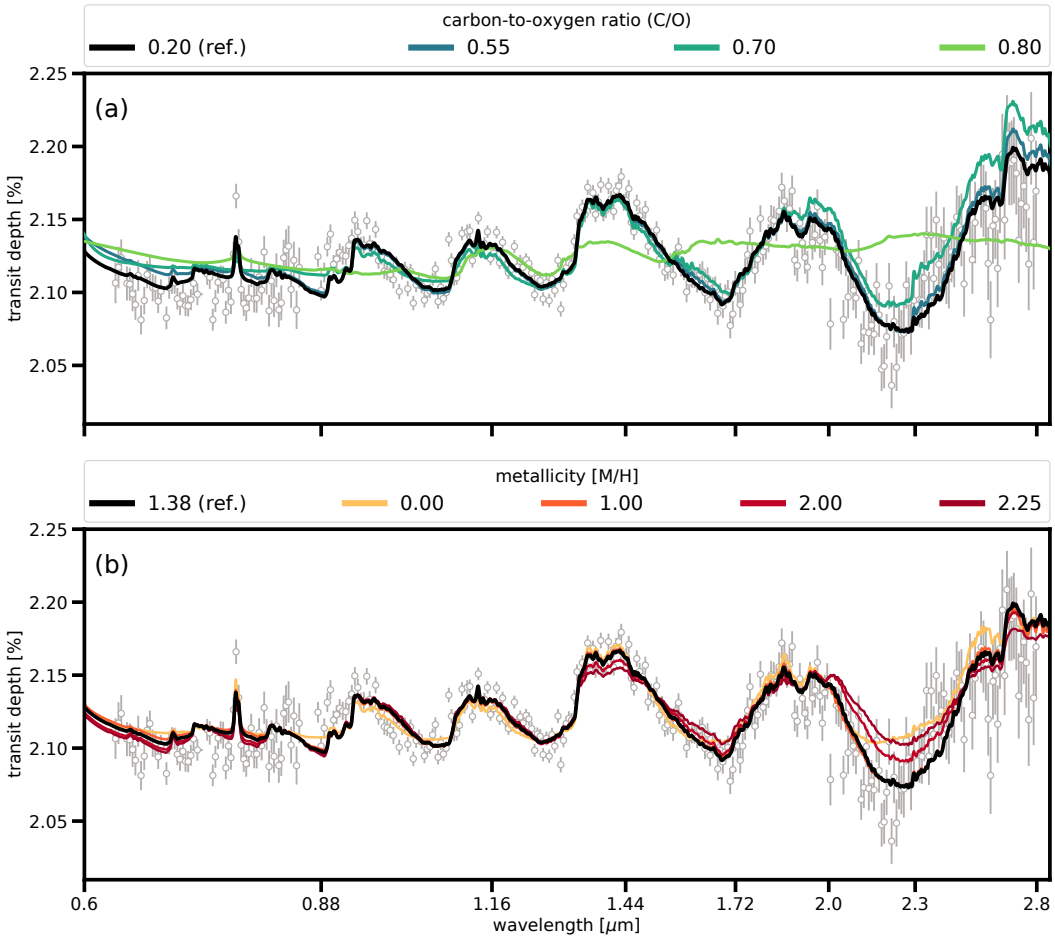

Figure 6.4 Impact of the carbon-to-oxygen ratio (C/O) and metallicity on the JWST-NIRISS spectrum of WASP-39 b. a: Variation of the C/O in the best-fit reference model, while keeping the metallicity, redistribution, and K/O parameters from the reference model the same, and fitting for the cloud parameters and scaled planetary radius to best explain the observations. Under these equilibrium conditions, increasing the C/O results in less H_2O and more CH_4, the latter having spectroscopic signatures incompatible with the observations. To mute these incompatible CH_4 features at high C/O, the model requires a higher degree of cloudiness that also mutes any remaining H_2O features in the spectrum. b: The same exercise as above, but instead we vary the metallicity parameter. The metallicity constraint is driven by the $\lambda > 2\mu$m data; the high-metallicity models ([M/H]$>$ 2) expect larger transit depths than what is seen in the data. The same reference model is plotted as a thick black line in both panels.

ticular, different compositions of clouds have different condensation temperatures and thus likely have different cloud coverage at the terminator [426]. Further studies combining temperature difference of east/west terminators to microphysical cloud models may be able to use the measured cloud coverage to determine the cloud composition of WASP-39b. Pre-

vious indications of non-gray or non-homogeneous clouds [124, 512, 337, 53, 43, 572] have relied on a single or small number of spectroscopic points, making our inference here for WASP-39b of non-gray cloud with inhomogeneous terminator coverage in the transmission spectrum of an exoplanetary atmosphere the most confident to date. These constraints on the physical properties of clouds, alongside the multiple spectral features across a broad wavelength coverage, are key to breaking well-known degeneracies between the metallicity and cloud-cover in atmospheric models [51, 311, 571] and deriving constraints on the bulk atmospheric properties.

The high precision of NIRISS-SOSS in combination with broadest wavelength coverage $< 2.8\mu$m for any JWST instrument, minimal systematics, and no issue with saturation allows us to obtain more precise and robust constraints on atmospheric composition and tracers of planet formation than most previous transmission spectroscopy observations. The super-solar metallicity of WASP-39 b and the solar-to-super-solar K/O are in agreement with previous studies of mass-metallicity trends in transiting exoplanets [282, 568, 435, 573]. If confirmed with further detailed modeling, a super-solar K/O ratio in WASP-39 b's atmosphere would likely indicate enrichment due to the accretion of planetesimals [573, 324, 220], although the measurements of potassium and oxygen abundances for the host star are also needed in order to establish this result. Similarly, the suggestion of sub-solar C/O and super-solar metallicity may be compatible with a planetesimal accretion scenario [e.g., 182, 341, 380]. The combination of a super-solar metallicity, super-solar K/O ratio, and sub-solar C/O ratio may suggest the planet formed beyond the H_2O snowline followed by inward migration, for which theory predicts efficient accretion of planetesimals at $\sim$ 2–10 AU [e.g., 220, 506]. At those orbital distances, the planetesimals likely contain K rock (e.g., alkali feldspar $KAlSi_3O_8$ [317, 578]) and H_2O ice but almost no CO ice [e.g., 404, 147], which explains the sub-solar C/O and super-solar K/O ratios along with a super-solar metallicity if a sufficient amount of planetesimals were accreted. However, fully understanding the possible formation pathways of this planet requires statistical constraints on the complete

chemical inventory of the planet and the relative abundances of the carbon- oxygen- and alkali- bearing species. Such efforts will be possible when applying retrieval techniques to the complete transmission spectrum of WASP-39b from 0.5 to 5.5μm that is being produced by the Transiting Exoplanet Community ERS Program. Our results validate JWST's NIRISS-SOSS as an instrument mode fully capable of producing exquisite exoplanet atmosphere measurements.

6.1 Data Reduction

Given the novelty of the data, we applied six independent data reduction and light curve fitting routines to the data: `nirHiss`, `supreme-SPOON`, `transitspectroscopy`, `NAMELESS`, `iraclis`, and FIREFly. Each pipeline extracts the stellar spectra from Orders 1 and 2 ($\lambda = 0.6 - 2.8\mu$m) with the exception of FIREFly, which only extracts data from Order 1. There is an additional Order 3 that has a spectral range of $\lambda = 0.6$–0.95μm [111]. However, the signal of Order 3 is generally weak and, since it provides no new wavelength information beyond what is covered in Orders 1 and 2, is not used by any of the presented pipelines. Below, we first describe the major reduction steps taken by each, followed by their light curve fitting methodologies. We note here that in each pipeline, the position of the SOSS trace was found to match near-perfectly with that measured during commissioning (Figure 6.5). Additionally, each pipeline trimmed the first 10–15 integrations to remove the effects of the exponential ramp in the fitting routines. We present a summary of all pipelines in Extended Data Table 6.1.

6.1.1 The `nirHiss` Pipeline

`nirHiss` is a Python open-source package that uses the Stage 2 outputs from the `Eureka!` pipeline and performs additional background and cosmic ray removal as well as extraction of the stellar spectra. For this analysis, we took the uncalibrated images and ran our own

Stages 1 and 2 calibration using `Eureka!` [49], an open-source package which performs spectral extraction and light curve fitting for several JWST instruments. We use the default steps presented in `Eureka!`, which includes detector-level corrections, production of count rate images, application of physical corrections, and calibrations to individual exposures.

Next `nirHiss` removes background noise sources in a multi-step process. The zodiacal background is first removed by applying the background model provided on the STScI JDox User Documentation website.[2] The background is scaled to a small region of each science integration where there was no contamination from any of the orders; in this case, x∈[190,250], y∈[200,500]. The average scaling—calculated here to be 0.881—is applied to all science integrations. Second, a model of 0^{th} order contaminants is built using the F277W integrations. The F277W integrations were taken after the transit of WASP-39b with the GR700XD/CLEAR pupil element and the F277W filter (throughput centered at $\lambda = 2.776\mu$m with a bandwidth of $\lambda = 0.715\mu$m). These observations consist of ten integrations with an exposure time of 49.4s. Observations with the F277W filter contain only the spectral trace of order 1 in the region where $x \leq 460$ pixels, thus allowing for the detection and modeling of 0^{th} order contaminants across the majority of the detector. A median F277W frame is created to identify and mask any bad data quality pixels.

To ensure no additional noise is added from the F277W median frame, we create a 2D background model map using `photutils.Background2D`. To identify regions of the background, we masked the upper-left corner, where the trace is located, and any regions with $> 1.5\sigma$, which includes the 0^{th} order sources. For `photutils.Background2D`, we used a filter size of (3,2) pixels and a box size of (2,2) pixels. Once the background is removed from the median F277W frame, we apply a Gaussian filter with a width of 2 to smooth out any additional small-scale background noise. To apply the median F277W frame to the Stage 2 science integrations, we scaled it to two isolated 0^{th} order sources in the science integrations at $x_1 \in$[900,1100], $y_1 \in$[150, 250] and $x_2 \in$[1800,2000], $y_2 \in$[150, 250]. We applied the aver-

2. `https://jwst-docs.stsci.edu/`

age scaling to all integrations. We found the average F277W background scaling to be 2.81. We apply the scaled background frame to each time-series integration (TSO) integration.

Once the 0^{th} order contaminants are removed, we trace the location of Orders 1 and 2. The spatial profile for NIRISS-SOSS along the column is double-peaked, with a slight dip in the middle. We developed a routine to identify the trace locations using a three-step approach to identifying each order. For each column in the first order trace, we identify the locations of the two peaks, or "ears" and assume the middle of the trace is the median row-pixel between the two "ears". We repeat this process for the third and second orders in that sequence, masking orders once they have been traced. We chose to identify the third order before the second order since it is better spatially resolved and does not overlap with any other orders. The routine creates one main set of traces from a median frame of all observations which is used to extract the stellar spectra. As an additional output, we track the changes in (x,y) pixel positions of each order on the detector across all integrations.

After the traces are identified, we continue our reduction to remove any additional noise and cosmic rays/bad pixels. We perform additional $1/f$ noise correction following the routine presented in `transitspectroscopy` (described below). Finally, `nirHiss` identifies and interpolates over cosmic rays. To identify cosmic rays we used the L.A. Cosmic technique wrapped into `ccdproc` [551, 105], which identifies pixels based on a variation of the Laplacian edge detection. We identify cosmic rays as pixels with $\sigma > 4$ via this method. We interpolate over any additional bad pixels by taking the median value of the two surrounding pixels along the column. We extract the spectra using a box extraction routine, and ignore any contaminants from overlapping orders or from any potential background orders. We use a box diameter of 24 pixels for both Orders 1 and 2. We do not extract the spectra from Order 3.

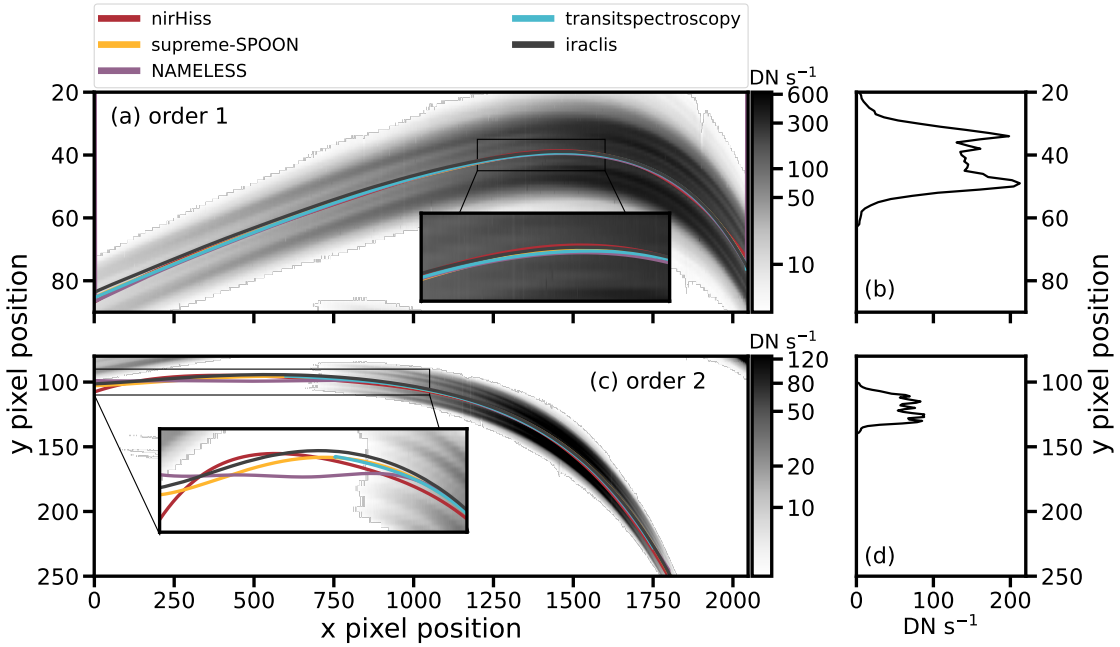

Figure 6.5 Comparison of (x,y) position of NIRISS Orders 1 and 2 across the detector as modeled from different reduction pipelines. (a/c): Each pipeline traces the curvature of Orders 1 and 2 using different methods. We show the best-fit trace for Order 1 in the top row, and Order 2 in the bottom row. We highlight zoomed-in regions to further examine differences. We note that `iraclis` uses the JWST-provided spectral trace. There is generally good agreement between the traces across the entire detector (< 1 pixel deviations), with the strongest deviations towards the ends of each trace (e.g., x pixel position < 500 for Orders 1 and 2. This demonstrates the reliability of order spectral traces across all pipelines. (b/d): We provide an example spatial profile along the column for Order 1 (b) and Order 2 (d) at $x = 1250$.

6.1.2 The `supreme-SPOON` Pipeline

In parallel, we reduce the WASP-39 b TSO with the independent `supreme-SPOON` (supreme-Steps to Process sOss ObservatioNs) pipeline, which processes SOSS TSOs from the raw, uncalibrated detector images to extracted 1D light curves. An outline of the specific steps is presented below.

For detector-level processing `supreme-SPOON` closely follows Stage 1 of the `jwst` pipeline. All default steps, up to and including the reference pixel correction, are run using their default settings. The reference pixel step is known to provide an inadequate correction of $1/f$ noise for SOSS observations; however, we include it in order to remove group-to-group

variations in the bias level, as well as even-odd row variations. At this stage, we remove the zodiacal background from each group. This is accomplished by first calculating a group-wise median frame, and scaling the model background provided in the STScI JDox to the flux level of each group in this median — yielding eight background models, one for each group. The region chosen to calculate the scaling was x∈[300,500], y∈[210,250], where there is minimal contamination from any of the SOSS orders. The n^{th} background model is then subtracted from the corresponding group of each integration.

We then proceed to a more in-depth treatment of $1/f$ noise. Unlike the other pipelines used in this work, `supreme-SPOON` treats $1/f$ noise at the group level instead of the integration level. $1/f$ noise is a time-varying noise source introduced by the voltage amplifiers during the readout of the detector, and therefore the $1/f$ pattern will vary from group-to-group, even within a given integration. To perform the $1/f$ correction, first a median out-of-transit frame is calculated for each group. This group-wise median is then scaled to the flux level of each frame in a given group via the transit curve, and subtracted off — revealing the characteristic $1/f$ striping in the residuals. A column-wise median of this residual map is then subtracted from the original frame. The trace residuals as well as any bad pixels are masked in the median calculation.

From this point we once again proceed with the standard Stage 1 steps of the `jwst` pipeline, with the exception of the `dark_current` step, to obtain the `supreme-SPOON` Stage 1 outputs. The dark current subtraction step is skipped as it was found to re-introduce $1/f$ noise into the data. The dark current level is additionally extremely small (several 10s of electrons/s compared to many thousands for the target signal) and can thus be safely ignored. `supreme-SPOON` only applies the `assign_wcs`, `srctype`, and `flat_field` steps of the Stage 2 `jwst` pipeline to the Stage 1 products. The background subtraction was already performed as part of Stage 1 calibrations. Furthermore, the flux calibration steps (`pathloss` which accounts for light incident on the telescope primary mirror which falls outside of the SUBSTRIP256 subarray, and `photom` which performs the actual photometric flux

calibration) are skipped, both because an absolute flux calibration is unnecessary for relative spectrophotometric measurements, and a wavelength-dependent flux calibration is nonsensical for SOSS where contributions from multiple wavelengths from all orders impact a single pixel. At this point, `supreme-SPOON` identifies any remaining hot pixels via median filtering of a median stack of all frames and interpolates them via the median of a surrounding box. These products are the `supreme-SPOON` Stage 2 results.

Stage 3 of the `supreme-SPOON` pipeline is the 1D extraction. This can be performed via two different methods: the first is a simple box aperture extraction on each order, ignoring the order contamination. The second uses `ATOCA` (Algorithm to Treat Order ContAmination) [111] to explicitly model the order contamination. Briefly, `ATOCA` constructs a linear model for each pixel on the detector, including contributions from the first and second diffraction orders, allowing for the decontamination of the SOSS detector — that is, `ATOCA` constructs models of both the first and second orders individually, thereby allowing a box extraction to be performed on each free from the effects of order contamination. Although the effects of this order contamination for differential measurements (e.g., exoplanet atmosphere observations) are predicted to be small ($\sim$1% of the amplitude of the expected spectral features) [111, 457], in the quest to obtain the most accurate possible transmission spectra, this contamination effect is important to take into account. `ATOCA` is currently built into the `extract1dstep` of the official `jwst` pipeline, although it not currently the default option and must be toggled to on via the "soss_atoca" parameter. To improve the performance of `ATOCA`, we do not use the default `specprofile` reference file included in the `jwst` pipeline, but instead construct estimates of the underlying spatial profiles of the first and second order, upon which `ATOCA` relies, using the `APPLESOSS` (A Producer of ProfiLEs for SOSS) algorithm [457]. We determine the centroid positions for each order on a median stack using the "edgetrigger" algorithm [457], and these positions are found to match to within a pixel with the default centroids contained in the jwst_niriss_spectrace_0023.fits reference file; the spectrace file is available on the JWST

Calibration Reference Data System (CRDS).[3] The SOSS trace position is furthermore highly stable over the course of this TSO, with RMS variations in x and y positions of ∼5 mpix, and RMS rotation of ∼0.3″. We therefore fix the "soss_transform" parameter to [0, 0, 0], and perform the extraction with a box size of 25 pixels. Any remaining $>5\sigma$ outliers in the resulting spectra are then identified and clipped. Currently, `supreme-SPOON` does not explicitly treat contamination from zeroth orders of background stars that intersect the trace.

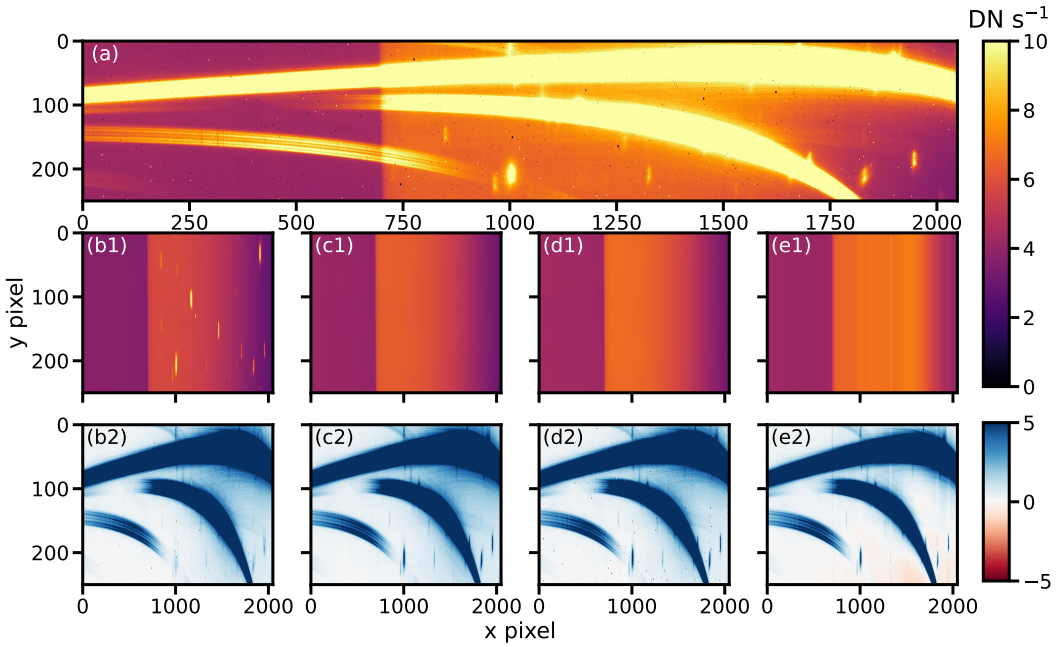

Figure 6.6 Comparison of averaged background frames computed for each reduction pipeline. a: A median out-of-transit (OOT) integration from the Stage 2 output files of the `jwst` pipeline in data numbers per second (DN s^{-1}). (b1/c1/d1/e1): Estimated median background frames for four example pipelines: (b) `nirHiss`, (c) `supreme-SPOON`, (d) `transitspectroscopy`, and (e) `iraclis`. All reduction pipelines use the predefined zodiacal background model provided on the STScI JDox User Documentation website. `nirHiss` estimates the 0$^{\text{th}}$ order contaminants by taking a smoothed median from the F277W filter integrations. We note that the background frame from `supreme-SPOON` (c1) for group eight is shown here, and was scaled by a factor of ∼0.02 to lie on the same scale as the background from the other three pipelines. `iraclis` subtracts a median per column to remove additional $1/f$ noise. (b2/c2/d2/e2): Background subtracted median integrations for each pipeline, plotted in [DN s^{-1}] but scaled from -5 to 5 to highlight subtle changes in the background. For these integrations, we define OOT as integrations $1-200$ and $400-518$.

3. `https://jwst-crds.stsci.edu/`

6.1.3 The `transitspectroscopy` *pipeline*

This third pipeline analysis combines the `jwst` pipeline Stage 1 "rateints.fits" files with `transitspectroscopy` [148].

`transitspectroscopy` completes stellar spectral extraction as well as transit fitting.

The trace positions for NIRISS orders 1 and 2 were determined using `transitspectroscopy.trace_spectrum`. This routine cross-correlates an input function with each column in the detector to find the center of the different traces via the maximum of the resulting cross-correlation function. In order to follow the shape of the NIRISS order profiles, an input function consisting of a double Gaussian was used with parameters that were trained on the NIRISS/SOSS observations of HAT-P-14 b (JWST Program ID 1541; PI Espinoza): $\mu_2 = -7.5; \sigma_1 = 3.0; \mu_2 = 7.5; \sigma_2 = 3.0$. The trace for order 2 was not fit for pixels ≤ 1040, as the throughput is not high enough for the method to robustly fit the trace without incorporating nearby contaminants. After identifying the trace positions with this method for both Order 1 and Order 2, both traces are smoothed using a series of spline functions. We find the best-fit parameters for Order 1, which were trained on the HAT-P-14 b observations are: $x_{\mathrm{knots},1} = [[6, 1200-5], [1200, 1500-5], [1500, 1700-5], [1700, 2041]]; n_{\mathrm{knots},1} = [4, 2, 3, 4]$ and for Order 2: $x_{\mathrm{knots},2} = [[601, 850-5], [850, 1100-5], [1100, 1749]]; n_{\mathrm{knots},2} = [2, 2, 5]$.

The zodiacal background was removed by scaling the model background provided on the STScI JDox User Documentation. This model was compared to a small region of the median science integrations where there was little to no contamination from the orders (x$\in$[500,800], y$\in$[210,250]). The ratio of all the pixels in this region versus the pixels in the background model was computed, ordered, and the median ratio of all the second quartile pixels was used as the scaling factor between the background model and the data, which was found to be 0.909. All the integrations had this scaled background subtracted.

Each integration is corrected for $1/f$ noise with the following procedure. First, all the out-of-transit, background-corrected integrations are median combined and scaled by the

relative flux decrease produced by the transit event at each integration (i.e., 1.0 for out-of-transit integrations, or about 0.976 for mid-transit). These scaled median frames are then subtracted from each individual integration, which then leaves in the frame only detector-level effects such as $1/f$ noise. We then go column by column and take the median of all pixels in this residual frames within a distance of 20 to 35 pixels from the center of the trace, and use this as an estimate of the contribution from $1/f$ noise to that given column. This value is then removed from each pixel within 20 pixels from the trace on that column. No correction for Order 1 contamination on Order 2 was made as the contribution is negligibly small in this case [111] — similarly for Order 1 contamination in Order 2 in our extraction.

To extract the resulting background and $1/f$-corrected spectrum, we used the `transitspectroscopy.spectroscopy.getSimpleSpectrum` routine with a 30-pixel total aperture for both orders. In order to handle obvious outliers in the resulting spectrum due to, e.g., uncorrected cosmic rays and/or deviating pixels, we median-normalized the spectra for each integration and combined them all to form a "master" 1D spectrum for both orders 1 and 2. The median was taken at each wavelength, as well as the error on that median, and this was then used to search for 5σ outliers on each individual integration at each wavelength. If outliers were found, they were replaced by the re-scaled version of this median "master" spectrum.

6.1.4 The NAMELESS Pipeline

Starting from the `jwst` pipeline Stage 1 products, we use the `NAMELESS` (Niriss dAta reduction MEthod for exopLanEt SpectroScopy) pipeline to go through the `jwst` pipeline Stage 2 with the addition of custom correction routines.

First, we go through the `assign_wcs`, `srctype`, and `flat_field` steps of the `jwst` pipeline Stage 2, opting for a custom background subtraction routine and skipping the `pathloss` and `photom` steps as absolute flux calibration is not needed. After flat-field correction, we scale the model background provided on the STScI JDox User Documentation to a region of the

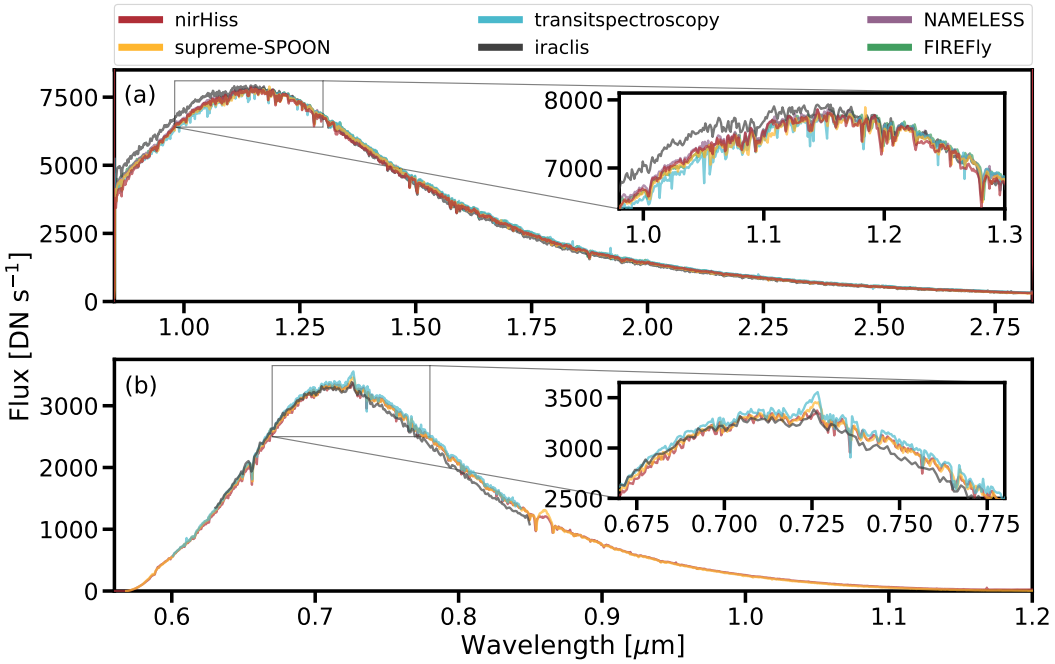

Figure 6.7 Example extracted stellar spectra from different reduction pipelines. The inset axes highlight the peak of the spectra. The `supreme-SPOON` spectra are scaled by a factor of 72 to compare the overall shape of the spectra, rather than the extracted flux counts. a: The extracted stellar spectra from Order 1. All pipelines are in relatively good agreement, while the shape of the `iraclis` data changes slightly at $\lambda < 1.1\mu$m. This is likely due to different traces which were used in the spectral extraction routine. b: The extracted stellar spectra from Order 2. Differences at $\lambda = 0.725$ and 0.86μm are due to differences in removing zeroth order contaminants in the background. The `iraclis` pipeline does not extract data out past $\lambda > 0.85\mu$m, which is where the order overlap region begins. Across all pipelines, the shape of the spectra, as well as overall absorption features, cosmic ray removal techniques, and noise levels are consistent.

median frame where the contribution from the tail of the three orders is lowest (x$\in$[200,250], y$\in$[400,600]). From the distribution of the scaling values of all pixels within the defined region, we take the 16$^{\text{th}}$ percentile as our scaling value and subtract the scaled background frame from all integrations.

We subsequently correct for $1/f$ noise by performing a column-by-column subtraction for each median frame subtracted integrations. The median frame is computed from the out-of-eclipse integrations (integration #$\in$[200,400]) and scaled to each individual integration by dividing the sum of the pixels within the first order by that of the median frame. We then subtract the scaled median frame from all integrations, perform the column-by-column

subtraction on the residual frames, and add back the scaled median frame to the corrected residual frames to obtain the $1/f$ corrected integrations.

We detect outliers frame-by-frame using the product of the second derivatives in the column and row directions. This method works particularly well for isolated outliers, as this leads to a strong inflexion that corresponds to a large second derivative. Because the spectral orders also lead to larger second derivative values, we divide the frames into windows of 4×4 pixels, compute the local second derivative median and standard deviation, and flag any pixel that is more than four standard deviations away from the median. Furthermore, we also flag pixels with null or negative flux. All identified outliers are set equal to the median value of the window it was identified in.

Finally, we proceed with spectral extraction of the corrected frames by first tracing the sections of the spectral orders that we wish to extract. We trace orders 1 and 2 from $x_1 \in$[4,2043] and $x_2 \in$[4,1830] respectively. The center of the traces is found for each individual column by performing a convolution of the profile with a gaussian filter, where we use the maximum of the convolved profile as the center of the trace. For the tracing of the second order, we keep the center of the trace fixed below x= 900 as the flux from the first order can bias the tracing method. Furthermore, we smooth the positions of the trace centroids using a spline function with 11 and 7 knots for the first and second order respectively. We perform spectral extraction of the first and second orders at all integrations using the `transitspectroscopy.spectroscopy.getSimpleSpectrum` routine with an aperture width of 30 pixels.

6.1.5 The `iraclis` Pipeline

We used the `jwst` pipeline Stage 1 "rateints.fits" files with modified routines from `iraclis` [547, 546], which was initially designed for HST. The modified routines will be part of the version 2 of `iraclis`, which will become publicly available in the near future. The routines

applied to the "rateints.fits" files were flat fielding, bad pixels and cosmic rays correction, sky background subtraction, $1/f$ noise correction, X- and Y-drifts detection, light curve extraction, light curve modeling and planetary spectrum decontamination.

We started our analysis by dividing the images by the appropriate flat field frame (jwst_niriss_flat_0275.fits), as provided by the JWST CRDS. The next step was the bad pixels and cosmic rays correction. As bad pixels we used those with a positive DQ flag in the "rateints.fits" files, excluding the warm pixels, as their large number did not allow for a reliable correction. We also identified extra outliers (cosmic rays or other artefacts) by calculating two flags for each pixel: the difference from the average of the ten horizontally neighboring pixels (x-flag) and the difference from the average of the ten vertically neighboring pixels (y-flag). If a pixel's x-flag was 5σ larger than the other pixels in the column and its y-flag 5σ larger than the other pixels in the row, it was identified as a cosmic ray (see also [546]). Both bad pixels and outliers were replaced with the value of a 2D interpolation function, created from the rest of the pixels, similarly to analyses with HST [546].

We then subtracted a column-based sky background frame and a column-based $1/f$ noise frame from each image. For each image, we first used a trace filter (value >0.001 in the jwst_niriss_spectrace_0023.fits, provided by the JWST CRDS), and a column-based 1×median absolute deviation filter to find the illuminated pixels. Then, we calculated the column-based median of the image—using only the unilluminated pixels—and subtracted it from the image. Finally, we calculated the column-based median of the IMFD (Image-MedianFrame Difference)—using only the unilluminated pixels—and subtracted it from the image. This process is not efficient in subtracting 100% of the background contamination, which was removed during the last analysis step (spectrum decontamination).

X- and Y-pixel trace drifts were detected relative to the first image by comparing the sums along the columns and the rows, respectively, similarly to HST [546]. The drifts are on the order of < 0.01 pixels without any evident trend in motion. Since this is below the subpixel size used in the `iraclis` extraction, we find there is no significant impact for not

correcting these drifts. For each spectroscopic image, we initially divided each pixel into a 100×100 grid of subpixels, and, for each subpixel, we calculated the distance from the trace (CD) and the wavelength (λ), creating the CD_{map} and the λ_{map}, respectively. λ was assigned to each subpixel directly from the wavelength solution (interpolated wavelength solution from the jwst_niriss_wavemap_0013.fits file, provided by the JWST CRDS, shifted by the detected X- and Y-drifts). CD was calculated as the distance between the center of the subpixel and the point of the trace with the same λ (interpolated trace from the jwst_niriss_spectrace_0023.fits file, provided by the JWST CRDS, shifted by the detected X- and Y-drifts). Our high-resolution bins had a λ-width of 10 Å, ranging between 0.62 and 0.85 μm for order 2 and between 0.85 and 2.8 μm for order 1, and a CD-width of 1.5 pixels, ranging from -25 to 25 pixels.

Finally, to construct the light curve of each bin, we applied the following smoothed aperture mask on each spectroscopic image and summed the values of all the subpixels. We chose a smoothed aperture, similarly to HST to reduce the effects of jitter noise:

$$APERTURE\_MASK = 0.5 \times \left[erf(\frac{CD_{map} - CD_1}{\sqrt{2}\sigma_{CD}}) - erf(\frac{CD_{map} - CD_2}{\sqrt{2}\sigma_{CD}}) \right] \times \left[erf(\frac{\lambda_{MAP} - \lambda_1}{\sqrt{2}\sigma_\lambda}) - erf(\frac{\lambda_{MAP} - \lambda_2}{\sqrt{2}\sigma_\lambda}) \right]$$

where CD_1, CD_2, and σ_{CD} are the bin boundaries and the smoothing factor along the cross-dispersion axis, λ_1, λ_2, and σ_λ are the bin boundaries and the smoothing factor along the dispersion axis. For the smoothing factors we used the values of $\sigma_{CD} = 0.015$ pixels and $\sigma_\lambda = 1$ Å—i.e., ∼10% of the bin size. We chose these values for the smoothing factors because lower values would effectively create a sharp-edge aperture, while larger values would force the bins to overlap substantially.

6.1.6 The FIREFly Pipeline

While FIREFLy (Fast InfraRed Exoplanet Fitting for Light curves) [484] was written and optimized for reducing NIRSpec-PRISM and G395H time series observations, it worked well on the NIRSISS-SOSS dataset, where it selected and processed the spectrophotometry from Order 1 only with minimal tuning or intervention. FIREFLy is not written in such a way to extract data from Order 2 ($\lambda < 0.9\mu$m). In our reduction, we perform standard calibrations on the raw data using the `jwst` Python pipeline for Stages 1 and 2 reduction. On the `jwst` Stage 2 outputs, we perform bad pixel and cosmic ray cleaning on each integration. We perform $1/f$ destriping and background subtraction using a pixel mask generated from the temporally-medianed image that selects regions of the data image below a specified count threshold. We extract the spectrophotometry using an optimized aperture extraction width that is constant in wavelength. The aperture width is selected such that the scatter of the resulting out-of-transit white-light photometry is minimized.

6.2 Light Curve Fitting and Transmission Spectra

We used a suite of light curve fitting routines to fit the extracted light curves. Each routine fit for orbital parameters from the broadband white-light curves per each order (see Extended Data Figure 6.8). We fixed the orbital period P to the best-fitting value from [$P = 4.05528$ d; 171] for all pipeline fits. For the spectroscopic light curves, most routines (`nirHiss/chromatic_fitting`, `supreme-SPOON/juliet`, `transispectroscopy/juliet`, and `NAMELESS/ExoTEP`) fixed the orbital parameters (that is the mid-transit time, t_0, semi-major axis to stellar radius ratio a/R_*, impact parameter b, eccentricity e) to the same values to ensure consistency. These parameters were fixed to their best-fitting values from the `transitspectroscopy/juliet` white light curve fit, except for t_0 which was fixed to the value obtained from the white light curve in each case. This left the planet-to-star radius ratio R_p/R_*, the limb-darkening coefficients, and parameters for any additional systematics

models to vary. These four routines also fit spectroscopic light curves at the native instrument resolution. However, two routines, `iraclis` and FIREFly instead fixed the orbital parameters in their spectroscopic fits to values obtained via their white light curve fits. `iraclis` also fit directly for the orbital inclination, i, as opposed to b and a/R_* like the other routines. `iraclis` fit for their spectrophotometric light curves at the pixel resolution, while FIREFly binned the spectroscopic light curves first and fit for the transit parameters. We present all of the best-fit white-light curve parameters for Order 1 in Extended Data Table 6.2. Additionally, for the spectroscopic light curve fits, we only considered the region of order 2 with wavelength <0.85 µm, as the 0.85 – 1.0 µm range is covered at higher SNR by order 1. All errors on each parameter are representative of 1σ (lower 16^{th} and upper 84^{th} percentiles) of the fit.

6.2.1 The `chromatic_fitting` routine

`chromatic_fitting` is an open-source Python tool for modelling multi-wavelength photometric light curves. This tool is built on the framework of `chromatic`, a package for importing, visualizing and comparing spectroscopic datasets from a variety of sources, including `Eureka!` and the `jwst` pipeline. In this paper we applied `chromatic_fitting` to the `nirHiss` reduction.

`chromatic_fitting` utilizes the `PyMC3` (NUTS) sampler [488] to fit the exoplanet transit model to the light curves. First, we fit the white light curves for order 1. The white light curve was generated using an inverse variance weighted average of the unbinned data. We fixed the orbital period to 4.05528 d [171] and assumed a circular orbit. We fit for the mid-transit epoch t_0, the stellar mass M_* and radius R_*, the impact parameter b, the planet-star radius ratio R_p/R_*, quadratic limb-darkening coefficients (u_1, u_2) and out-of-transit flux F_0. For the fitted parameters t_0, M_*, R_*, R_p/R_* and F_0, we assumed normal priors $\mathcal{N}(2459787.56, 0.02^2)$, $\mathcal{N}(0.934, 0.056^2)$, $\mathcal{N}(0.932, 0.014^2)$, $\mathcal{N}(0.146, 0.05^2)$ and $\mathcal{N}(1.0, 0.01^2)$ respectively. For b we used a uniform prior between 0 and 1.146, where $b \leq 1 + R_p/R_*$.

For the limb-darkening coefficients we calculated the theoretical values from 3D models in `ExoTIC-LD` [102, 511, 290] (based on the stellar parameters $T_{\rm eff} = 5512\,{\rm K}$, $\log g = 4.47\,{\rm dex}$ and Fe/H$= 0.0\,{\rm dex}$ [349]) and assumed normal priors around these values with $\sigma = 0.05$. We also included a second-order polynomial in time to describe the systematics with a fixed constant term of 0.0 and normal priors on the first and second-order coefficients c_1 and c_2 of $\mathcal{N}(0.0, (1e^{-4})^2)$. Using `PyMC3`'s NUTS implementation we ran 4000 tuning steps and 4000 draws, with 4 walkers, for the white light curve and the mean parameter values are shown in Extended Data Table 6.2. We checked for convergence using the rank normalized R-hat diagnostic [195, 555].

For each spectroscopic light curve we fixed the period P, transit epoch t_0, eccentricity e, semi-major axis in stellar radii a/R_* and impact parameter b to the white-light parameter values from the `transitspectroscopy/juliet` routine (Extended Data Table 6.2). We then fit for the planet-star radius ratio R_p/R_*, quadratic limb-darkening coefficients (u_1, u_2) and out-of-transit flux F_0 — for all of these parameters we assumed the same normal priors as for the white light curve. We also included a second-order polynomial in time with the same priors as the white light curve fit. For each wavelength we ran 2000 tuning steps and 2000 draws, also with 4 walkers. The final transmission spectrum was taken as the mean value drawn from the posterior distribution for the planet-star radius ratio with 1σ uncertainties extracted from the 16–84$^{\rm th}$ HDI (highest density interval) region.

The signal-to-noise (SNR) in the spectrophotometric light curves from `nirHiss` for Order 1 at 1.34μm is 165; the SNR for Order 2 at $0.71\,\mu$m is 103. We define the SNR as SNR$= \sqrt{n_{\rm bins}} \times \sigma_{\rm in\ transit}/\sigma_{\rm out\ of\ transit}$, where σ is the standard deviation.

6.2.2 The `juliet` routine

We applied the `juliet` package [151] for light curve fitting to the products of multiple reduction pipelines described above. Here, we give a general overview of the methods and include exact details per fit when appropriate.

For the `supreme-SPOON` reduced stellar spectra, we fit the white light curve for the mid-transit time, t_0, the impact parameter, b, the scaled orbital semi-major axis, a/R_*, and the scaled planetary radius, R_p/R_*; assuming a circular orbit. We also fit two parameters of a quadratic limb-darkening model following the parameterization of [270], as well as a jitter term added in quadrature to the error bars, and the two parameters of a linear trend with time. We therefore fit seven parameters to the white light curve for each order, using wide, flat priors for each case. We then proceeded to fit the light curves from each individual wavelength bin at the native detector resolution — that is two pixels per bin to roughly account for the extent of the PSF in the spectral direction. This results in 1020 bins for Order 1, and 520 bins for Order 2 as we only consider wavelengths $<$0.85 µm. For the spectroscopic fits, we fixed the central transit time to the white light curve value, and the other orbital parameters as described for `chromatic_fitting`. For the linear trend with time, we used the white light posterior for each of the two parameters as prior distributions for all wavelength bins, whereas for the limb-darkening parameters, we adopted a Gaussian prior centered around the predictions of the `ExoTiC-LD` package [290] with a width of 0.1. As the SOSS throughput files included with `ExoTiC-LD` did not cover the full wavelength range of both orders, we instead used the throughputs determined during commissioning and included in the `spectrace` reference file of the `jwst` pipeline. We truncated the Gaussian prior at 0 and 1, to prevent the limb-darkening parameters from straying into unphysical regions of the parameter space. We then used flat, uninformative priors for the remaining two parameters, the scaled planetary radius and the scalar jitter. The `supreme-SPOON` white light curve fits have $\chi^2_\nu = 1.15$ for Order 1, and $\chi^2_\nu = 1.11$ for Order 2.

For the `transitspectroscopy` reduced stellar spectra, we first fit the white-light light curves of Order 1 and 2 separately. For these, as suggested above, the period was fixed, but all the rest of the parameters were allowed to vary. In particular, we set a normal prior on the time-of-transit center of $\mathcal{N}(2459787.5, 0.2^2)$ days, where the first value denotes the mean and the second the variance of the prior. A normal prior was also set on $a/R_* \sim$

$\mathcal{N}(11.37, 0.5^2)$ and a truncated normal between 0 and 1 was set for the impact parameter $b \sim \mathcal{TN}(0.447, 0.1^2)$ where the means were set following the work of [339], but the variances are large to account for the variation of these parameters in the literature between different authors. We set a uniform prior for the planet-to-star radius ratio between 0 and 0.2, and fixed eccentricity to 0. In addition to those, we fit for a mean out-of-transit offset with a normal prior of $\mathcal{N}(0, 0.1^2)$, and a jitter term, as described above, with a log-uniform prior between 10 and 1000 ppm. To account for systematic trends in the data, we use a Gaussian Process (GP) via `celerite` [177] with a simple Matèrn 3/2 kernel to parametrize those trends. We set log-uniform priors for both the amplitude of this GP from 10^{-5} to 1000 ppm, and for the time-scale from 10^{-3} days to 0.5 days. We use the framework of [270] to parameterize limb-darkening via a square-root law, which, following [150], is one of the laws that should give the best results at this level of precision.

For the wavelength-dependent light curves we used a similar setup with two main differences. The first is that we fix the time-of-transit center, a/R_*, and b to their white light values. The second is that we set truncated normal priors on the transformed limb-darkening coefficients (q_1, q_2) between 0 and 1, with standard deviations of 0.1 and means obtained via the following method. First, we obtain the non-linear limb-darkening coefficients using an ATLAS stellar model with the closest properties to WASP-39's via the `limb-darkening` software [149]. Then, the square-root law limb-darkening coefficients are obtained following the algorithm of [244], and those are transformed to the (q_1, q_2) parameterization using the equations in [270]; these are then set as the mean for each wavelength-dependent light curve. We note that we fit the light curves at the pixel level, which means fitting one light curve per detector column. We fit them in parallel using the `transitspectroscopy.transitfitting.fit_lightcurves` routine.

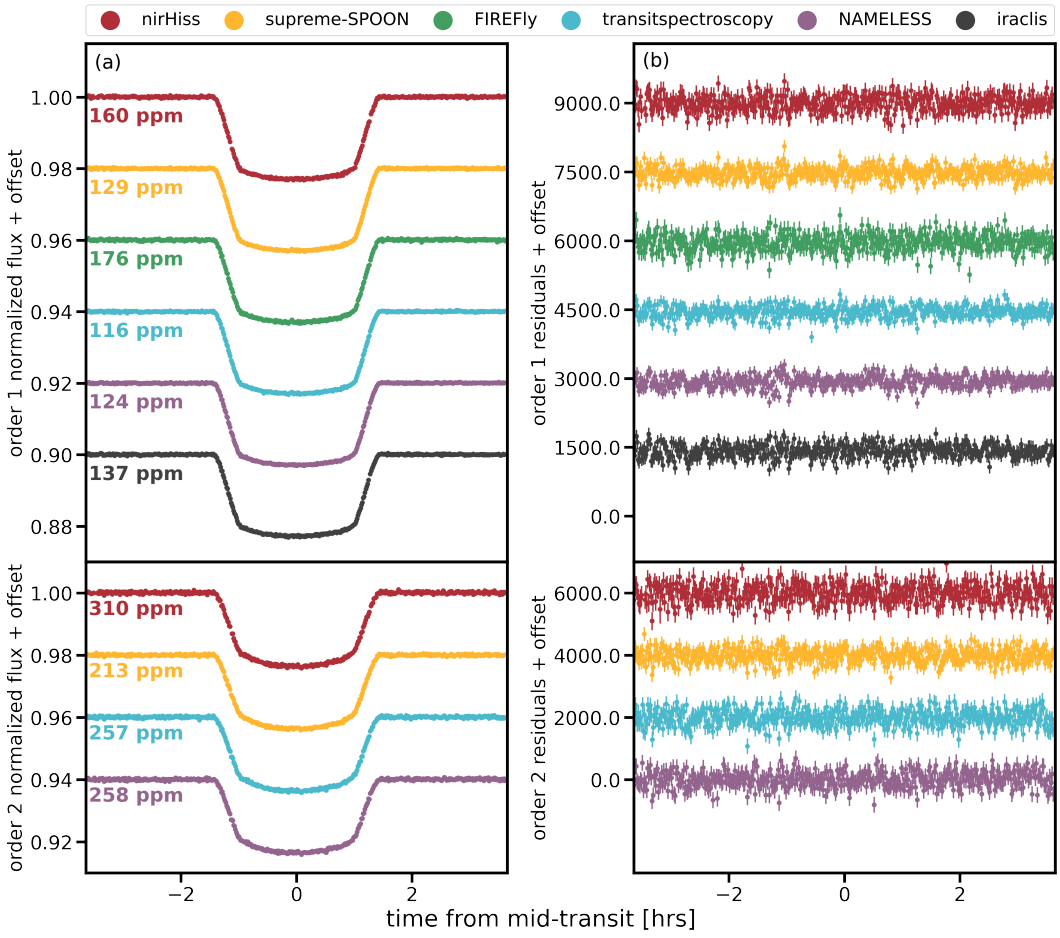

Figure 6.8 White light curves and residuals between the light curve and best-fit exoplanet transit model per each reduction pipeline. a: White light curves for Order 1 (top) and Order 2 (bottom) with the out-of-transit scatter noted in the figure text. These produced light curves are corrected based on each pipelines' treatment of systematics. b: The residuals, in ppm, between the plotted light curves and best-fit exoplanet transit model. Errors are representative of 1σ on each time step.

6.2.3 The ExoTEP routine

For the `NAMELESS` reduction, we perform light curve fitting on the extracted spectrophotometric observations using the ExoTEP framework [54]. We first fit the white light curves of both orders 1 and 2 separately. We fit for the mid-transit time t_0, the planet-to-star radius ratio R_p/R_*, and quadratic limb-darkening coefficients (u_1, u_2) [350, 281], while fixing the impact parameter b and semi-major axis a/R_* to the values of the best order 1 white light curve fit from the `transitspectroscopy/juliet` analysis. We also fit for the scatter σ, as

well as a linear systematics model with an offset c and slope v. Uniform priors are considered for all parameters. We additionally only discard the first 10 integrations to remove the exponential ramp. For all light curves, we compute the rolling median for a window size of 11 integrations and bring any data point that is more than four standard deviations away from it to the median value. We fit the light curves using the Markov chain Monte Carlo Ensemble sampler emcee [179] for 1,000 steps using four walkers per free parameter. The first 600 steps, 60% of the total amount, are discarded as burn-in. We then fit the spectroscopic light curves, keeping t_0 fixed to its white light value, at a resolution of three pixels per bin for order 1 (680 bins) and one pixel per bin for order 2 from ∼0.6–0.9 μm (675 bins). We used 1,000 steps for the spectroscopic fits, once again discarding the first 600 as burn-in.

6.2.4 The `iraclis` *routine*

We analysed all the light curves using the open source Python package PyLightcurve [545]. For every light curve, PyLightcurve: (I) calculates the limb-darkening coefficients using the ExoTETHyS package [381], the wavelength range of the bin, the response curves for each of the NIRISS orders
(jwst_niriss_spectrace_0023.fits file, provided by the JWST CRDS), and the stellar parameters ($T_{\rm eff}$=5540 K, $\log g$=4.42 cm/s^2, Fe/H=0.14 dex [233]); (II) finds the maximum-likelihood model for the data (an exposure-integrated transit model together with a quadratic trend model using the Nelder-Mead minimisation algorithm included in the SciPy package [564]; (III) removes outliers that deviate from the maximum-likelihood model by more than three times the standard deviation of the normalised residuals; (IV) scales the uncertainties by the RMS of the normalised residuals, to take into account any extra scatter; (V) and, finally, performs an MCMC optimisation process using the emcee package [179]. We initially modeled the first order white light curve (sum of all bins above 0.85 μm with out-of-transit fluxes above 20 DN s^{-1}) and fit for the white R_p/R_*, the orbital parameters, a/R_* and i,

and the transit mid-time. We then modeled the spectral light curves, fitting only for the R_p/R_*, fixing the orbital parameters, a/R_* and i, and the transit mid-time to the above white results. In both cases the models also included a quadratic de-trending function that was multiplied by the transit model. After modelling, we applied a spectral decontamination step, taking advantage of the varying total flux across the spectral traces. Due to the contamination we have: $(R_p/R_*)^2 * (TF - x)/TF$, where TF is the out-of-transit flux (star and contamination) and x is the flux of the contaminating source. Hence, for each wavelength we fitted for x and applied the correction: $(R_p/R_*)^2_{corr} = (R_p/R_*)^2 * TF/(TF - x)$. This procedure is effective in removing uniform contamination.The uniform contamination fixes issues of sky background over- or under-correction. It also corrects for order overlap. After the decontamination described above, there was still a contaminating source affecting the spectrum around $0.72\,\mu$m, which was not uniform due to the PSF. To separate this source we applied Independent Component Analysis (ICA) on the stellar spectra extracted from various distances from the trace. We used two components to describe the contaminating source and one to describe the stellar spectrum. Finally, we estimated the $(R_p/R_*)^2$ per wavelength bin using the weighted average of all the bins that had the same wavelength range. We only took into account the bins that had out-of-transit fluxes above 20 DN s^{-1}. This choice effectively applied an optimal aperture size for each wavelength bin.

6.2.5 The FIREFly routine

To extract the transmission spectrum, we bin the cleaned spectrophotometric light curves by wavelength first to create 120 variable-width spectral channels with roughly equal counts in each. We fit for the planet's transit depth in each channel using a joint light curve and systematics model. The systematics model accounts for spectral shifts in the X- and Y-directions [484]. We use the orbital parameters recovered from an MCMC fit to the white light curve, and fix them at each wavelength channel for our fit. We fit for the two quadratic

limb-darkening terms a and b at each wavelength channel. We find that the best-fit limb-darkening coefficients are uniquely determined, and deviate by a constant offset relative to model coefficients. Our fits are performed iteratively using the Python package `lmfit`. The light curves show a typical photometric scatter of 0.3% per integration, and the typical transit depth uncertainties vary between 150–300 ppm, which is in line with near photon-limited precision. More details of the FIREFly fitting routine can be found in [484] and in Rustamkulov et al. (in press).

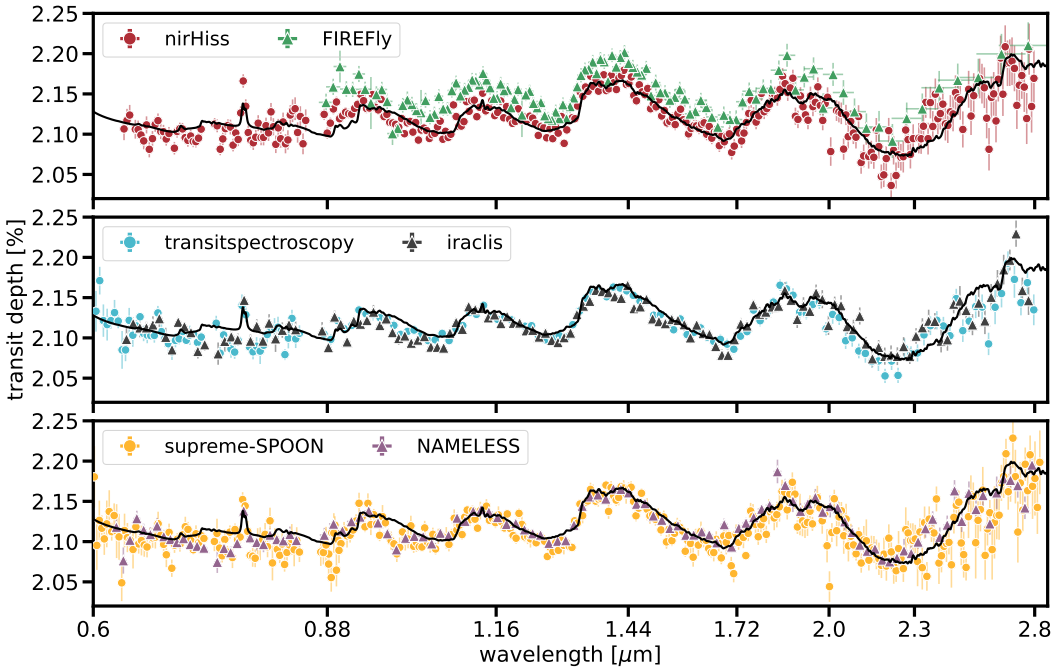

Figure 6.9 Transmission Spectra for WASP-39b for all reduction techniques.: Our best-fit reference model to the `nirHiss` spectrum (red) is plotted as a black solid line on both panels and the spectra are separated into three panels for ease of reading. Wavelengths which overlap with 0^{th} order contaminants are masked. Errors are representative of 1σ on each transit depth. We note that the spectra produced by the `nirHiss`, `supreme-SPOON`, and `transitspectroscopy` all performed similar $1/f$ noise treatment, and `supreme-SPOON` is the only pipeline which performed this removal on the group level. While the produced spectra all contain the same unambiguous water absorption features, further investigation into which method of $1/f$ noise removal produces the highest fidelity spectrum should be conducted.

6.3 Atmospheric Models

To interpret the measured transmission spectrum, we performed an extensive comparison with grids of synthetic transmission spectra. We tested several independent atmospheric models to avoid any model-dependent interpretation of the data. Unless otherwise noted, all of our grids have assumed radiative-convective-thermochemical equilibrium to estimate atmospheric compositions. The exploration of atmospheric models with fewer assumptions (e.g., without the assumption of chemical equilibrium with metallicity and C/O as free parameters) and those considering other effects of disequilibrium chemistry is left for future work.

We derive basic interpretations for the observed spectrum based on four independent model grids, `ATMO`, `PHOENIX`, `PICASO`, `ScCHIMERA` . Each grid contains pre-computed transmission spectra at various atmospheric properties, such as metallicity [M/H], carbon-to-oxygen C/O ratio, and cloud properties, using from gray to Mie-scattering cloud opacity (see next subsection for details). The `ScCHIMERA` grid considers additional model advancements 1) various cloud treatments, including a gray cloud, gray + power-law cloud opacity, and physically motivated (i.e., droplet sedimentation) cloud model, 2) the impact of inhomogeneous cloud coverage along the planetary terminator, and 3) the K/O ratio as a grid dimension. `ScCHIMERA` provides the best fit to the observations compared to the other three grids and informs the results presented in the main text.

6.3.1 Grid Search with Pre-Computed Forward Models

Here, we introduce the independent grids of pre-computed transmission spectra, their model description, and the main results from these grid fits. We first present the three grids that do assume horizontally homogeneous clouds.

ATMO

The atmospheric PT profile is computed using the 1D radiative-convective equilibrium model `ATMO` [543, 142, 204, 205]. The model includes the molecular/atomic opacity of CH_4, CO, CO_2, C_2H_2, Cs, FeH, HCN, H_2O, H_2S, K, Li, Na, NH_3, PH_3, Rb, SO_2, TiO, and VO, for which the adopted line list is summarized in [205]. The line lists of several key species are: H_2O [38], CH_4 [590], CO_2 [533], CO from HITEMP2010 [483], K from VALD3 [486]. We considered atmospheric metallicities of [M/H]=−1.0, +0.0, +1.0, +1.7, +2.0, +2.3, C/O ratios of C/O=0.35, 0.55, 0.7, 0.75, 1.0, 1.5, planetary intrinsic temperatures of $T_{\rm int}$ = 100, 200, 300, 400K, and day-night energy redistribution factors of 0.25, 0.50, 0.75, 1.0, where full heat redistribution corresponds to 0.5. The model varies O/H ratio for achieving each C/O ratio with C/H ratio fixed to that scaled by the metallicity from the solar abundance. The cloudy models include small particle opacity as the Rayleigh scattering gas opacity enhanced by a factor of either 0 or 10, while large particle opacity is equated to the H_2 Rayleigh scattering opacity at 0.35 μm enhanced by a factor of 0.5, 1.0, 5.0, 10.0, 30.0, and 50.0. In total, the `ATMO` grid consists of 484 cloud-free and 6292 cloudy atmosphere models. We only consider horizontally homogeneous clouds in the `ATMO` grid fits.

PHOENIX

The atmospheric PT profile is computed using the 1D radiative-convective equilibrium model `PHOENIX` [224, 39, 323]. We considered atmospheric metallicities of [M/H]=−1.0, +0.0, +1.0, +2.0; C/O ratios ranging from C/O=0.3 to 1 divided into 136 grid points, planetary intrinsic temperatures of $T_{\rm int}$ = 200 and 400K, and day-night energy redistribution factors of 0.172, 0.25, and 0.351, where full heat redistribution corresponds to 0.25. The model varies C/H ratio for achieving each C/O ratio with O/H ratio fixed to that scaled by the metallicity from the solar abundance. The model includes various chemical species: CH, CH_4, CN, CO, CO_2, COF, C_2, C_2H_2, C_2H_4, C_2H_6, CaH, CrH, FeH, HCN, HCl, HF, HI, HDO, HO_2, H_2, H_2S, H_2O, H_2O_2, H_3+, MgH, NH, NH_3, NO, N_2, N_2O, OH, O_2, O_3, PH_3, SF_6, SiH, SiO, SiO_2,

TiH, TiO, VO, and atoms up to U. The line list of H_2O is from BT2 [38], other molecular lines from HITRAN 2008 [482], and atomic lines from the database of Kurucz [287]. For cloudy models, the small non-gray cloud particle opacity is treated as a sum of Rayleigh scattering opacity of all gas species enhanced by a factor of either 0 (clear atmosphere) or 10; large gray particle opacity is treated as gray cloud deck pressure levels of 0.3, 3, and 10mbar. In total, the `PHOENIX` grid consists of 95 cloud-free and 380 cloudy atmosphere models. We only consider horizontally homogeneous clouds in the `PHOENIX` grid fits.

PICASO 3.0

Similarly to the grids of models presented above, we pre-computed atmospheric pressure-temperature (PT) profiles using the 1D radiative-convective equilibrium model `PICASO 3.0` [365, 358, 44, 383] for the atmospheric metallicity of [M/H]=−1.0, −0.5, +0.0, +0.5, +1.0, +1.5, +1.7, +2.0; atmospheric bulk C/O ratios of C/O=0.229, 0.458, 0.687, 1.1; planetary intrinsic temperatures of $T_{\rm int}$ = 100, 200, 300K; and heat redistribution factors of 0.5 and 0.4, where full heat redistribution corresponds to 0.5. The model fixes the sum of C and O abundances (i.e., (C+O)/H ratio) to that scaled by the metallicity from the solar C+O abundance when changing C/O ratio. The model includes 29 chemical species: CH_4, CO, CO_2, C_2H_2, C_2H_4, C_2H_6, CrH, Cs, Fe, FeH, HCN, H_2, H_2O, H_2S, H_3+, OCS, K, Li, LiCl, LiH, MgH, NH_3, N_2, Na, PH_3, Rb, SiO, TiO, and VO. The line lists of several key species are: H_2O [445], CH_4 [589], CO_2 [246], CO [306], K from VALD3 [486]. For cloudy models, we post-processed the computed PT profiles using the droplet sedimentation model `Virga` [3, 480] that determines the vertical distributions of cloud mass mixing ratio and mean particle size from the balance between downward mass flux of gravitational sedimentation and upward mass flux of eddy diffusion. We vary vertically-constant eddy diffusion coefficients of $K_{\rm zz} = 10^5$, 10^7, 10^9, 10^{11} and vertically-constant sedimentation parameters of $f_{\rm sed}$ = 0.6, 1.0, 3.0, 6.0, 10.0. The $f_{\rm sed}$ value is defined as the ratio of the mass-averaged sedimentation velocity of cloud particles to the mean upward velocity of the atmosphere, and a smaller $f_{\rm sed}$

yielding more vertically extended clouds [see e.g., 345, 480]. We have assumed horizontally homogeneous clouds and accounted for the formation of $MgSiO_3$, MnS, and Na_2S clouds. Then, we postprocessed the atmospheric properties to compute synthetic transmission spectra. We note that the optical properties of the flux-balanced cloud is computed by the Mie theory [e.g., 62] under the assumption of a log-normal particle size distribution with a mean particle size translated from $f_{\rm sed}$ [3]. In total, the `PICASO` grid consists of 192 cloud-free and 3840 cloudy atmosphere models.

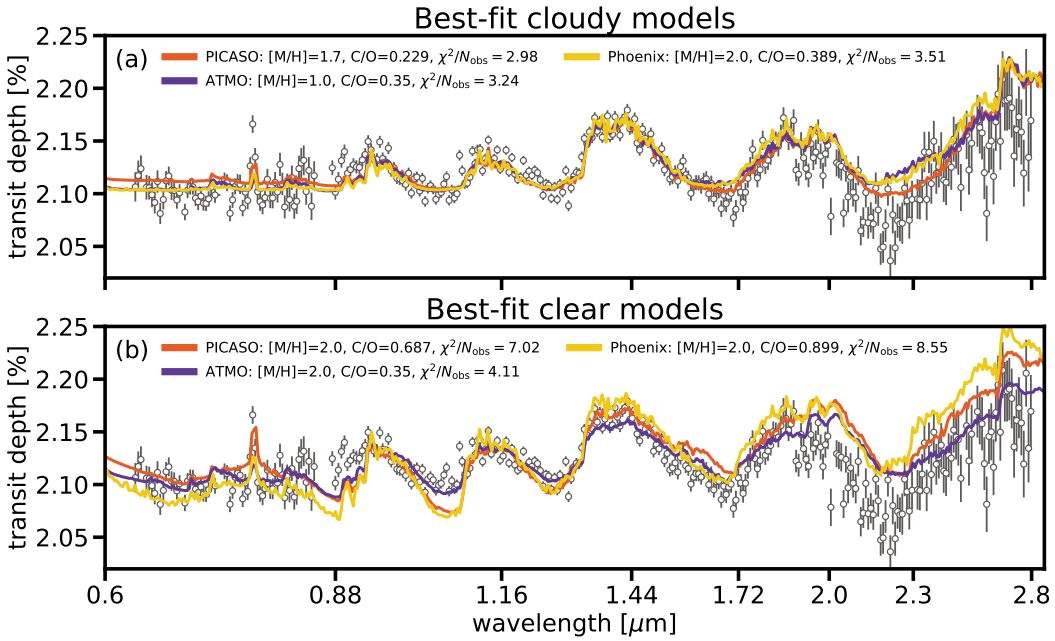

Figure 6.10 A summary of pre-computed forward model fits to NIRISS-SOSS spectrum: a: Each coloured line shows the best-fit spectrum from the `PICASO`, `ATMO`, and `PHOENIX` cloudy grid. The chi-squared values per number of data points ($N_{\rm obs}=327$) are $\chi^2/N_{\rm obs}=$ 2.98, 3.24, and 3.51 for the `PICASO`, `ATMO`, and `Phoenix` grids, respectively. All grid models consistently indicate a super-solar metallicity of [M/H]= 1–2 and a sub-solar C/O ratio. b: The same as the top panel, but for the best-fit clear atmosphere models. The clear models yield noticeably worse fits to the data: $\chi^2/N_{\rm obs}=7.02$, 4.11, and 8.55 for the `PICASO`, `ATMO`, and `Phoenix` grids, respectively, which strongly indicates the presence of clouds in the atmosphere.

We compare the NIRISS SOSS spectrum (binned to R=300) to each of these model grids and summarize the best fits in the top panel of Extended Data Fig. 6.10. For each cloudy and clear model we tested, we compute $\chi^2/N_{\rm obs}=2.98-8.55$ between the data and the

models, with specific values per model indicated in the legend of Extended Data Fig. 6.10. All of our forward model grids consistently indicate super-solar metallicity ([M/H]=1–2) and sub-solar C/O ratio. Each best-fit spectrum shows different structures at > 2 μm, as the spectra at these wavelengths are more sensitive to the treatment of cloud properties (see next subsection for details). The best-fit spectra from `PICASO`, `ATMO`, and `Phoenix` indicate atmospheric metallicities of [M/H]=1.7, 1.0, and 2.0, respectively. These models also consistently indicate C/O ratios between 0.229–0.389, corresponding to the lowest C/O ratio grid point in each grid (see the main text for why models prefer lower C/O ratios). Thus, the super-solar metallicity and sub-solar C/O ratio of WASP-39b are consistent across the different model interpretations of the NIRISS-SOSS transmission spectrum.

We also find that clear atmospheric models fail to fit the observed spectrum even at very high metallicity ([M/H]=2.0), as shown in the bottom panel of Extended Data Fig. 6.10. The clear models fail to match the amplitudes of H_2O absorption features at $\lambda = 0.9$, 1.15, 1.4, and 1.8 μm simultaneously. The clear `ATMO` models fit the data better than the clear `PICASO` and `Phoenix` models because the `ATMO` grid allows lower heat redistribution factors (i.e., cooler atmosphere). The clear models also overestimate the transit depth at $\lambda \sim 2$ μm because of a strong CO_2 absorption resulting from the inferred high metallicity ([M/H]=2.0). The inability of clear atmosphere models to fit the overall NIRISS spectrum strongly indicates the presence of clouds in the atmosphere, and emphasizes the ability of the NIRISS wavelength coverage to break the cloud property-metallicity degeneracy. The best-fit cloud properties are $f_{\rm sed} = 1$ and $K_{\rm zz} = 10^9 {\rm cm}^{-2}{\rm s}^{-1}$ for `Virga` clouds in `PICASO`, a gray cloud opacity of 5$\times$ the H_2 Rayleigh scattering opacity at 0.35 μm for `ATMO`, and a gray cloud top pressure of 3×10^{-4}bar for `Phoenix`.

6.3.2 Grid Search with ScCHIMERA

The NIRISS transmission spectrum offers key insights into the atmospheric properties of WASP-39b over a broad wavelength range. The simultaneous detection of H_2O and K,

alongside possible indications of carbon-bearing species, allows us to explore equilibrium models for which the potassium-to-oxygen (K/O) ratio is an additional dimension besides the commonly employed C/O and metallicity parameters. Furthermore, as explained in the previous subsection (see also Figure 6.3 demonstrating how clouds contribute to the NIRISS spectrum), the broad wavelength coverage of these NIRISS observations makes it possible to explore more complex cloud models beyond traditional gray and homogeneous cloud models. To explore these considerations, we implement the `ScCHIMERA` grid as explained below.

Previous implementations of this framework include [21, 436, 356], where the methods are described in detail. Implementations of this procedure to JWST data include ref. [537]. For a given set of planetary parameters, our methods pre-compute the temperature-pressure structure of the planetary atmosphere and the thermochemical equilibrium gas mixing ratio profiles. The computations are performed on a grid of atmospheric metallicity ([M/H], e.g., $\log_{10}$ enrichment relative to solar [318]) spaced at 0.125 dex values between 0 and 2.25 (e.g., 1 to 177×solar) and carbon-to-oxygen (C/O) ratios at values of 0.2, 0.35, 0.45, 0.55, 0.65, 0.7, and 0.8. Unlike previous implementations of this framework, and to better understand the NIRISS-SOSS observations presented, we include a dimension to our grid exploring the potassium-to-oxygen ratio ([K/O], i.e., $\log_{10}$ enrichment relative to solar [318]) with spacing of 0.5 dex between -1 and 0, and 0.1 dex between 0 and 1, overall spanning a range from -1 to 1, or 0.1 to 10×solar. In these calculations, the atmospheric metallicity (M/H) scales the sum of K, C and O. This sum determines the final elemental abundances after scaling M/H, C/O and K/O. That is, the total oxygen elemental abundance is $O' = \frac{M/H}{K/O+C/O+1}$, the total carbon elemental abundance is $C' = O' \times C/O$, and the total potassium elemental abundance is $K' = O' \times K/O$. Additionally, we explore the energy redistribution (f) between the day and night sides of the planet [181], with values of 0.657, 0.721, 0.791, 0.865, 1.0 , 1.03 , 1.12 , 1.217, 1.319 in our grid, where $f = 1.0$ and 2.0 correspond to full day-to-night heat redistribution and dayside only redistribution, respectively.

The transmission spectrum of the planet is computed with CHIMERA [312, 254, 345]

using the converged atmospheric structures. We compare the observations to these models in a Bayesian inference framework using the nested sampling algorithm MultiNest [169] through its python implementation PyMultiNest [74], and obtain an optimal [M/H], C/O, [K/O], and f via nearest neighbor search in the grid. When computing the transmission spectrum for a given set of ([M/H], C/O, [K/O], f), we additionally adjust the 1 bar planetary radius controlling the absolute transit depth (an arbitrary pressure with no direct impact on the inferred properties, see e.g.,Welbanks & Madhusudhan [571]), and model different cloud treatments. The opacity sources considered are H_2-H_2 and H_2-He CIA [463], H_2O [445, 187], CO_2 [187], CO [483], CH_4 [483], H_2S [30], HCN [37], Na [280, 14], and K [280, 13], and were computed following the methods described in [197, 210]. The cloud models considered are 1) a basic cloud model with a gray, uniformly vertically distributed cloud opacity (κ_{cloud}); 2) a gray+power-law cloud model that accounts for non-gray opacity of small-size particles as a vertically uniform power-law opacity (i.e., a parameter for the scattering slope and and a Rayleigh-enhancement factor, e.g, [301, 337, 572, 406]) in addition to gray cloud component, which is expressed by gray cloud-deck of infinite opacity at a given atmospheric pressure; and 3) a droplet sedimentation model [3] (assuming enstatite grains) where parameters capture the eddy diffusion coefficient and the ratio of sedimentation velocity to characteristic vertical mixing velocity (see also the description of `PICASO` above). For cloud treatments 2 and 3, we also consider the possibility of inhomogeneities around the planetary limb by considering a linear combination of clear and cloudy models [e.g. 311], key for breaking degeneracies between metallicity and cloud properties (e.g., [51, 571]). We assume the same PT profile for both cloudy and clear limbs in the inhomogeneous cloud models and leave an investigation on the possibility of different PT profiles on those regions to future studies.

Identification of Absorbers and Model Selection

We perform our Bayesian inference using all model combinations with the `ScCHIMERA` grid on four different data resolutions for the `nirHiss` transmission spectrum: R=100, R=300, native

instrument resolution ($R_{\text{Order 1}}$=910; $R_{\text{Order 2}}$=830), and pixel-level resolution ($R_{\text{Order 1}}$=1820; $R_{\text{Order 2}}$=1660). Resolutions are given at the reference wavelengths of $\lambda = 1.791\mu$m for Order 1 and 0.744μm for Order 2. We test the robustness of our inferences against different binning and convolution strategies and find the results, i.e., the bulk atmospheric properties [M/H], C/O, and K/O, consistent regardless of the resolution of the data. We find a fiducial combination of parameters that can best explain the spectrum (that we call the reference model) with full redistribution (f=1, matching predictions that planets in this temperature regime are unlikely to possess strong day-to-night temperature contrast [432, 274, 596]), [M/H]=1.375 (i.e., $\sim 20\times$ solar), C/O=0.2, and [K/O]=0.1. With these atmospheric properties, the data are best explained by the droplet sedimentation model (`ScCHIMERA` cloud model 3) and inhomogeneous cover. However, the gray+power-law model (`ScCHIMERA` cloud model 2) with inhomogeneous cover provides a comparable fit to the data. We compare sets of models by computing their Bayes factor and converting to a 'sigma' detection significance using the prescription in [51] (see also [572]). Using R=300 data, the homogeneous droplet sedimentation model (model 3) is preferred over homogeneous gray cloud (model 1) at $\gtrsim 8\sigma$, which strongly indicates the non-gray nature of cloud opacity. Meanwhile, the inhomogeneous droplet sedimentation model is preferred over the homogeneous droplet sedimentation model cloud at 5σ. This is evidence that for the same model 3 inhomogeneous cloud coverage is preferred. The inhomogeneous droplet sedimentation model is preferred over all other tested models across all aforementioned resolutions we tested.

We explore the contribution of different chemical species to our reference model by performing the Bayesian inference using the inhomogeneous cloud model 3 and artificially disabling the contribution of a selected chemical species, one at a time. By redoing the Bayesian inference, we are able to compare the Bayesian evidence and converting to a 'sigma' detection significance as described above. We detected H_2O at $> 30\sigma$, K at 6.8σ, CO at 3.6σ, and no significant detections of Na, CH_4, CO_2, HCN, and H_2S. The best-fit metallicity across all models is $\sim$ 10–30$\times$ solar, the best fit K/O ratio 1–2$\times$ solar, and C/O ratio 0.2. Taking the

average and standard deviation of the best-fit results for all 20 runs (i.e., 5 models on 4 data resolutions) we find an average M/H=19× solar with a standard deviation of 5× solar and an average K/O=1.5× solar with a standard deviation of 0.26× solar.

Wavelength Sensitivity to Inferences

We investigate the dependence of the inferred atmospheric properties on the spectral range of the observations by performing the same Bayesian inferences described above on the spectrum blue-ward of 2 μm (see panel b of Extended Data Fig. 6.11). This exercise is repeated on all 20 models-data-combinations from `ScCHIMERA` . With the exception of the solar-to-super-solar K/O ratio, inferences about the atmospheric metallicity, C/O ratio, and clouds are primarily driven by the shallower transit depth seen between $\lambda = 2.1 - 2.3 \mu m$. This wavelength region is where the traces of Orders 1 and 2 overlap on the detector. To assess the robustness of our results, we explore different data treatments that could affect the final spectrum. First, we find there are no zeroth order background contaminants that could be diluting the transit depth in this region. Second, we extract the transmission spectra and fit for dilution between the orders (`supreme-SPOON` data reduction) and without accounting for the overlap (`supreme-SPOON`, `nirHiss` and `transitspectroscopy`). The evidence for minimal dilution stems from reducing the data through both methods with the same pipeline (`supreme-SPOON`), which uses the same steps for the entire reduction process along the way, with the exception of fitting and not fitting for dilution. Both techniques yield similar results between $\lambda = 2.1 - 2.3\,\mu m$. We note that the contamination from Order 2 into Order 1 was previously shown to be between 8 – 12 ppm [111] and is therefore negligible.

We find that without the data red-wards of 2 μm, the [M/H] value is more scattered across models and resolutions with an average metallicity of 61×solar for the 20 runs and a standard deviation of 28× solar. On the other hand, the inference on the C/O ratio remains consistently 0.2 across all models and resolutions. Similarly, the K/O ratio remains solar-to-super-solar with an average of 1.89× solar and a standard deviation of 0.29× solar.

These results confirm the necessity for the NIRISS broad wavelength coverage to constrain the atmospheric metallicity of a planet [51, 311, 571]. Without the transit depth decrease at 2.1 μm, our models do not exhibit a preference for cloud models 2 and 3 over cloud model 1, nor do they prefer the presence of inhomogeneities in the cloud cover. Without these constraints on the cloud properties, a wide range of metallicities can provide an equally good fit to the observations blue-wards of 2 μm when combined with different cloud properties, preventing reliable constraints on the metallicity.

The exploration of these models is summarized in Extended Data Figure 6.11. The top panel shows the different cloud treatments and their goodness of fit to the data. Overall, models with inhomogeneous cloud cover best explain the data, with the flux-balanced cloud of model 3 giving the lowest χ^2. The bottom panel contrasts the reference model against the results from all cloud models when using data blue-wards of 2 μm only. Without the information contained in the dip in transit depth at 2.1 μm, all cloud treatments provide an equally good fit and overestimate the transit depth between 2.0 μm and 2.3 μm.

K/O Inferences

We explore the possibility of constraining the potassium-to-oxygen ratio using NIRISS-SOSS. As explained above, across different models and data resolutions, our results suggest that the observations of WASP-39b are best explained by a solar-to-super-solar K/O ratio. To further explore this, we repeat our Bayesian inference for all 20 model-data configurations (5 models $\times$ 4 resolutions) using the observations blue-wards of 0.8 μm. From high-resolution to low-resolution observations and for all cloud model configurations, we find that all 20 runs prefer models with solar or super-solar K/O ratios for WASP-39b ranging from 1 to 10$\times$ solar. The average across the 20 runs is 2.12$\times$ solar and a standard deviation of 2.33$\times$ solar, with the relatively larger standard deviation resulting from two inferences of highly super solar K/O ratios of 7$\times$ solar or greater for observations at the pixel-level resolution.

Using the reference model atmospheric properties, (e.g., [M/H]=1.37, C/O=0.2, full re-

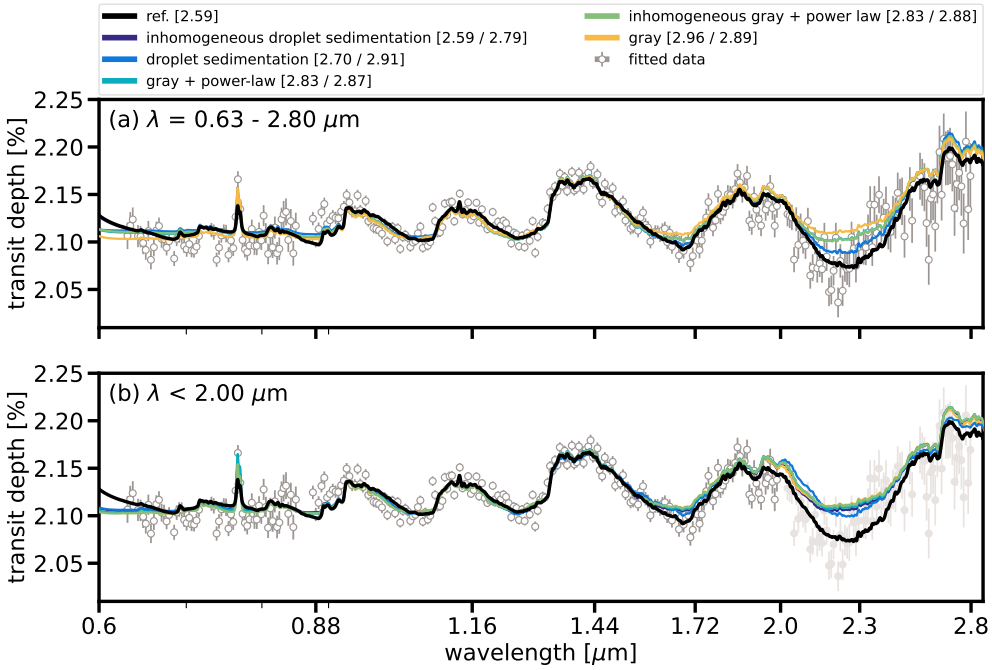

Figure 6.11 A demonstration of how the redder wavelength coverage of NIRISS-SOSS drives the inference on cloud structure for WASP-39b: We fit the NIRISS-SOSS spectrum (gray) using a suite of cloud models to derive the best-fit C/O and metallicity. Here, we demonstrate how the best-fit model for each cloud treatment changes as a function of what wavelength region we fit. a: The best-fit models when using the entire wavelength coverage of NIRISS-SOSS. b: The best-fit models when using $\lambda < 2\mu$m, which excludes the overlapping region between orders on the detector. The reference spectrum (black) on both panels corresponds to the best-fit inhomogeneous droplet sedimentation model for the entire wavelength coverage. The fitted data are presented as dark gray points. The quoted numbers in brackets in the legend are the respective χ^2/N for each fit for the top (left value) and bottom (right value). The difference between cloud models is within the noise of the NIRISS-SOSS data when fitting to $\lambda < 2\mu$m. It is clear that fitting the entire NIRISS-SOSS wavelength coverage results in a lower χ^2/N and better fit.

distribution f=1), we search for the best-fit [K/O] while simultaneously adjusting the 1 bar radius and the parameters for the inhomogeneous cloud model 3, when only using the observations blue-wards of 0.8 μm. The best-fit [K/O]=0.4 is consistent with the inferences using all the data and the data blue-wards of 2.0 μm only. This model is shown in Extended Data Figure 6.12 in green. For the best fit cloud parameters and 1 bar radius, we compute a series of K/O ratios spanning sub-solar and super-solar values. We compute the fit of each model to the data using chi-squared statistics. We then convert the resulting χ^2 value to a p-value.

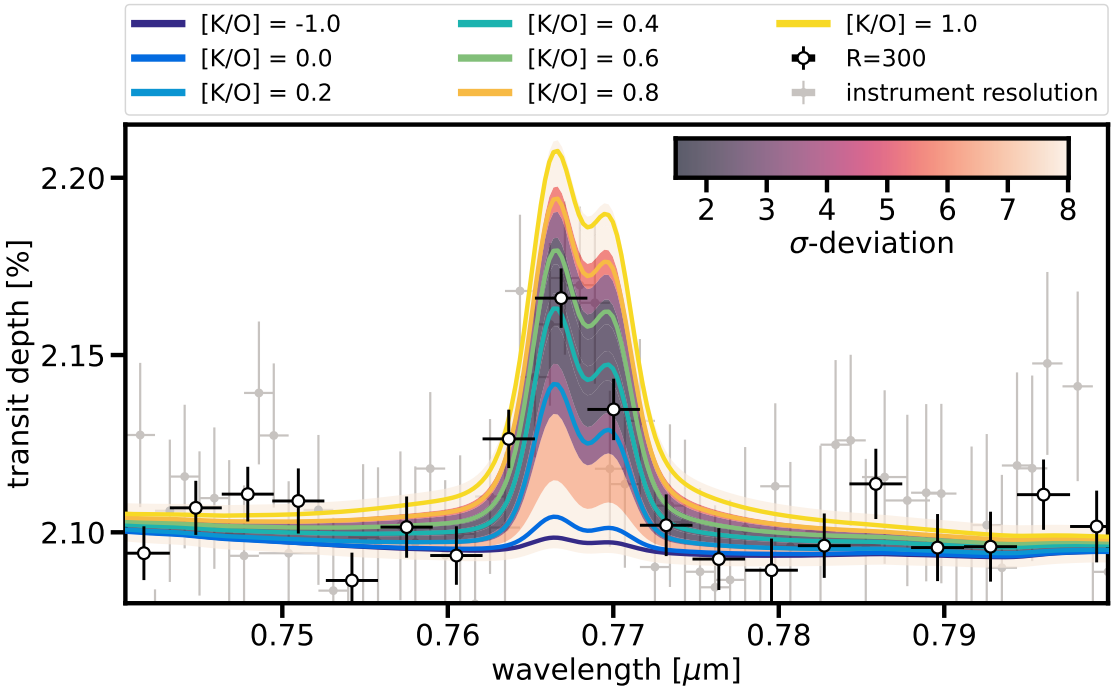

Figure 6.12 Evidence for super-solar [K/O] in WASP-39 b: We fit for [K/O] while keeping the rest of the model parameters (e.g., C/O, metallicity, and redistribution) the same as our reference model and fitting for the cloud parameters and scaled planetary radius. Here, we present the different [K/O] models (solid lines) we fit against the transmission spectrum at R=300 (black and white points). We represent each model's respective fit in the orange shading.

These p-values allow us to estimate the agreement between each model and the data. Our results find that sub-solar K/O ratios are disfavoured to 2σ, while super-solar values $\gtrsim 0.7$ are disfavoured to 5σ.

Pipeline	JDox bkg model	F277W filter	$1/f$ removal	Spectral extraction	Fitting process	Limb darkening
`nirHiss`	x	x	int	box (24)	`chromatic_fitting`; MCMC	quadratic, fit, (priors from `ExoTiC-LD`)
`supreme-SPOON`	x		group	ATOCA (removes order overlap)	`juliet`; LM(t)	quadratic, fit (priors from `ExoTiC-LD`)
`transitspectroscopy`	x			box (30)	`juliet`; GP	truncated normal, (priors from `limb-darkening`)
`NAMELESS`	x		int	box (30)	ExoTEP; MCMC	quadratic (uniform priors)
`iraclis`				smoothed optimal	`iraclis`; MCMC/emcee	quadratic (priors from ExoTETHyS)
FIREFly				optimal	FIREFly MCMC	

Table 6.1 An outline of reduction and fitting pipelines used to produce transmission spectra for WASP-39b with NIRISS/SOSS. All spectra are publicly available.

Table 6.2 White-light curve best-fit orbital parameters from NIRISS Order 1. The errors presented on each fit are the 16^{th} and 84^{th} percentile fits to the transit parameter.

Pipeline	$t_0 - 2459787$ [BJD]	R_p/R_{star}	a/R_*	b
`nirHiss`	0.556779 ± 0.000012	$0.14541^{+0.00020}_{-0.00017}$	$11.345^{+0.020}_{-0.021}$	0.4591 ± 0.0041
`supreme-SPOON`	0.556742 ± 0.000015	0.14588 ± 0.00020	$11.3795^{+0.0253}_{-0.0263}$	$0.4530^{+0.0053}_{-0.0052}$
`transitspectroscopy`	0.556743 ± 0.000020	0.14530 ± 0.00035	$11.388^{+0.028}_{-0.027}$	$0.4496^{+0.0057}_{-0.0060}$
`NAMELESS`	0.556740 ± 0.000014	0.14587 ± 0.00018	11.400 ± 0.024	$0.4510^{+0.0047}_{-0.0049}$
`iraclis`	$0.556724^{+0.000017}_{-0.000019}$	$0.145083^{+0.000090}_{-0.000083}$	11.419 ± 0.026	0.4439 ± 0.0062
FIREFly	0.556737 ± 0.000020	0.145982 ± 0.00025	11.402 ± 0.033	0.4519 ± 0.0067

CHAPTER 7

CONCLUSION

"*Why would I quit now? All my friends who quit are dead.*"

— Diana Gross

7.1 Searching for escaping atmospheric metal lines in the FUV

Young planets are actively evolving. One unique characteristic of these planets is that their radii tend to be larger, or inflated, with respect to older planets on similar orbital periods (see Figure 1.2 as a reference). If these atmospheres are inflated, then they provide a unique environment to test mechanisms which could be driving atmospheric escape. There are several theories for what could cause an atmosphere to lose a significant amount of mass. The first is photoevaporation, where high-energy (XUV) irradiation from the host star strips the primordial H/He envelope [414, 415]. The second is core-powered mass-loss, where the latent heat of formation retained in the core heats the atmosphere, resulting in such atmospheric expansion that it becomes unbound [201, 218]. Photoevaporation is predicted to be the dominant source of atmospheric stripping during the first $\sim 100\,\mathrm{Myr}$, when the star has an elevated XUV irradiation. Meanwhile, core-powered mass-loss could continue out to $\sim 1\,\mathrm{Gyr}$, depending on the cooling properties of the core [477]. By measuring the atmospheric escape of young planets, we can determine whether photoevaportion drives the majority of mass-loss, or if it is driven by core-powered mass-loss.

There have been several campaigns to date which have attempted to measure the atmospheric mass-loss for young planets. Many of these studies have been reliant on transmission observations of H I Ly-α and Hα, and He I metastable triplet at $1083.3\,\mathrm{nm}$, as each of these lines would trace the primordial H/He envelope. Each of these lines come with strong limitations. Several short-period planets have had observed transits in the UV with Ly-α [e.g. HD 189733 b 304, 70]. However, Ly-α is strongly absorbed and obscured by the inter-

stellar medium, and therefore can be an unreliable tracer of atmospheric outflows. In the optical, Hα could be an good tracer for H I; however it has been demonstrated in several archival studies, as well as in Chapter 3, that Hα is strongly correlated with stellar activity. Therefore, Hα is an unreliable tracer of planetary material. Finally, He I in the NIR has been proposed as a tracer for the He present in the primordial envelope [407], and several He I transits have been observed for intermediate and old-aged planets [e.g. 355, 595, 594]. Additionally, it was recently demonstrated that He I can trend with stellar iron coronal abundances, leading to detections and non-detections of specific atmospheres [446]. Several campaigns have been undertaken to observe He I in young planetary atmospheres; all have yielded either non- or tentative detections [237, 565]. A potentially more reliable way to search for and subsequently measure atmospheric mass-loss could be through metal lines in the UV.

UV observations of the first transiting exoplanet, HD 209458 b [91] yielded significant insights into atmospheric mass-loss. Initially, *Hubble Space Telescope* (*HST*) Space Telescope Imaging Spectrograph (STIS) discovered a $\sim$ 15% transit depth observed with Lyman-α [Ly-α; 562]. The corresponding radius from the transit depth is beyond the Roche lobe of HD 209458 b, implying it was losing its atmosphere. Follow-up revealed a $7.5 \pm 3.5\%$ transit depth in the C II 1335 Å doublet [563]. Additionally, higher signal-to-noise observations of a transit of HD 209458 b revealed a consistent transit depth in the C II 1335 Å doublet and an $8.2 \pm 1.4\%$ transit depth in the Si III 1206.500 Å line [313]. By measuring transit depths in these metal lines, [562, 563, 313] all provided a novel, and perhaps more reliable, method for detecting atmospheric escape compared to Ly-α, which can be attenuated or obscured by the interstellar medium. In this section, I will discuss an ongoing effort to detect metals lines in the atmospheres of AU Mic b ($4.159 R_\oplus$; 23 Myr) and V1298 Tau c ($5.044 R_\oplus$; $30-40$ Myr) with the *HST* Cosmic Origins Spectrograph (COS).

7.1.1 *FUV Transits of the 23 Myr planet AU Mic b*

Three transits of AU Mic b were observed with the *HST*/COS on 28 May 2021, 23 Sep 2021, and 09 Oct 2022 as part of GO 16164 (PI Cauley). Each observation used the G130M filter with a central wavelength of $\lambda = 1222\,\text{Å}$ and has an exposure time of $\sim 11,970\,\text{s}$. The phase-folded light curve, summed over the C II doublet is presented in Figure 7.1. I used the 30 s light curves for Visits 1 and 2 from [167] and generated the new light curves for Visit 3 at the same cadence. The observations were scheduled in such a way that resulted in minimal sampling over the entire transit, but rather are isolated to times prior to and just after transit midpoint. There were no observations taken during ingress, egress, or mid-point. Flares are marked as outlined points. As seen, there were 9 flares observed during the transit observations, which could potentially lead to significant contamination when trying to extract information about the planet's atmosphere.

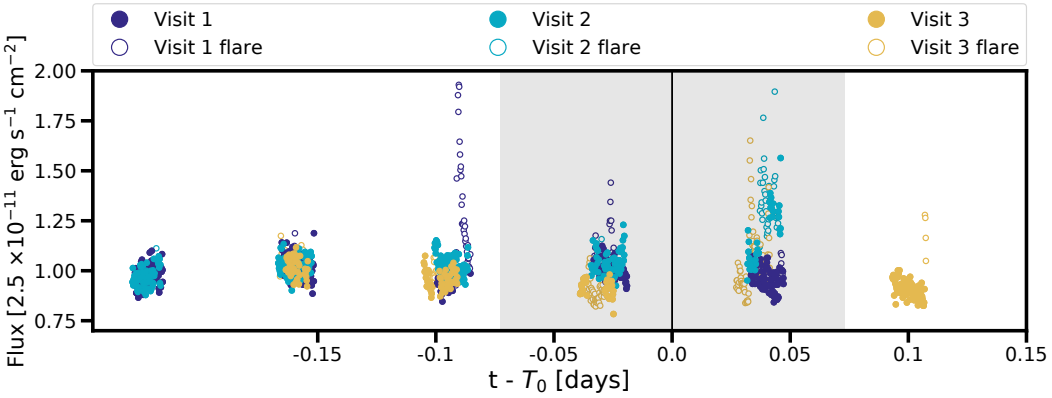

Figure 7.1 Light curve in the C II 1334.532 Å doublet for the transit of AU Mic b with *HST*/COS. The entire transit is marked with the shaded gray region; T_0 is marked with the vertical black line. All three visits sample the same phase of the transit, just prior to and after transit mid-point. There were no data obtained during transit ingress or egress. Data contaminated by flares are marked by outlined points.

To investigate whether or not AU Mic b is experiencing atmospheric mass loss via metals in its atmosphere, I followed the methods of [313]. Namely, I searched for excess absorption in three doublets: C II at 1335 Å, Si III at 1296 Å, and N V at 1240 Å. These lines were selected as the highest signal-to-noise emission features in the observations for these

particular species. N V is a highly ionized species with a high formation temperature of $10^{5.2}$ K. This doublet is likely to originate in the stellar atmosphere and not be contaminated by the planet's atmosphere, given its high formation temperature. Therefore, N V acts as a tracer for stellar activity in this analysis. I did not include any spectra which were taken during flare events. The resulting line profiles are presented in Figure 7.2.

N V appears relatively well behaved during Visits 1 and 3 (magenta and green), while Visit 2 (blue) has excess absorption during the transit from -30 to $30\,\mathrm{km\,s^{-1}}$. An excess of absorption in the C II and Si III doublets can be seen at a similar velocity range as N V during Visit 2, likely indicating that this visit is overrun with stellar activity. For Visits 1 and 3, there does not appear to be any excess absorption during the transit in either the C II or Si III doublets. The difference between in- and out-of-transit observations are either 1σ consistent with a flat line or $\sim 2\sigma$ consistent with excess emission. The combined profile from all three visits (right column of Figure 7.2) are all consistent with a flat line, yielding no indication of excess absorption during the transit of AU Mic b.

While these results are tentative, they do not prove promising for any detection of escaping metal lines for AU Mic b. One source of potential issue with this analysis could be that not all in-flare observations were fully removed, resulting in remaining sources of activity still being present in the line profiles. Flares can evolve on timescales of $< 30\,\mathrm{s}$, which is the current cadence of the light curves evaluated here. It is possible that there are still trace amounts of a flare decay in some of the observations used to perform this work. Future work will include generating shorter cadence light curves to ensure that all observations associated with the many flares observed during these three transits of AU Mic b are completely removed. If any trace of excess absorption is seen during any of the transits, this would justify future *HST* /COS observations of AU Mic b to further sample the transit at different phases.

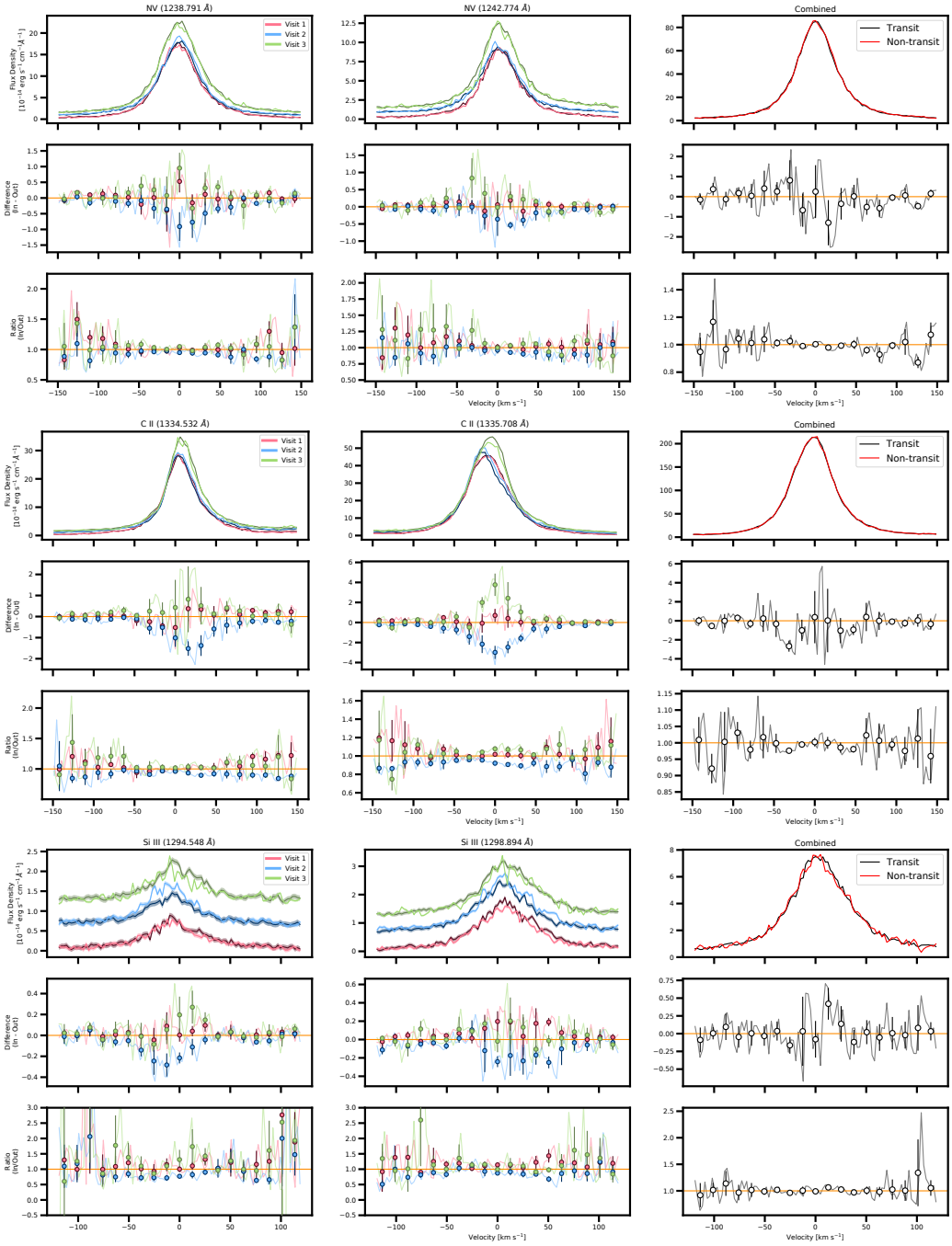

Figure 7.2 Comparison of the line profiles for the in- versus out-of-transit *HST*/COS observations of AU Mic b. Magenta represents data from Visit 1, blue from Visit 2, and green from Visit 3. The darker shade of each color represents the in-transit profile; the lighter shade of each color represents the out-of-transit profile. The combined line profile from each visit is shown on the right in black and red. The top three rows are for the N V 1240 Å doublet; the middle three rows are for the C II 1335 Å doublet; the bottom three rows are for the Si III 1296 Å doublet. Lines from each visit are offset to ease readability.

7.1.2 FUV Transits of the 30 - 40 Myr planet V1298 Tau c

Three transits of V1298 Tau c were observed with the *HST*/COS on 17 Jan 2022, 02 Feb 2022, and 26 July 2022 as part of GO 16163 (PI Cauley). Each observation used the G130M filter with a central wavelength of $\lambda = 1291$ Å and has an exposure time of $\sim 12,030$ s. The V1298 Tau planets have been seen to have large transit-timing variations (TTV) on the order of several hours for V1298 Tau c. I used an updated TTV model to predict where the transits occurred during the three *HST* visits [161, Livingston et al. in prep]. The TTVs were not accounted for when scheduling these observations. This lead to having no pre-transit or transit ingress coverage in the observations (Figure 7.3).

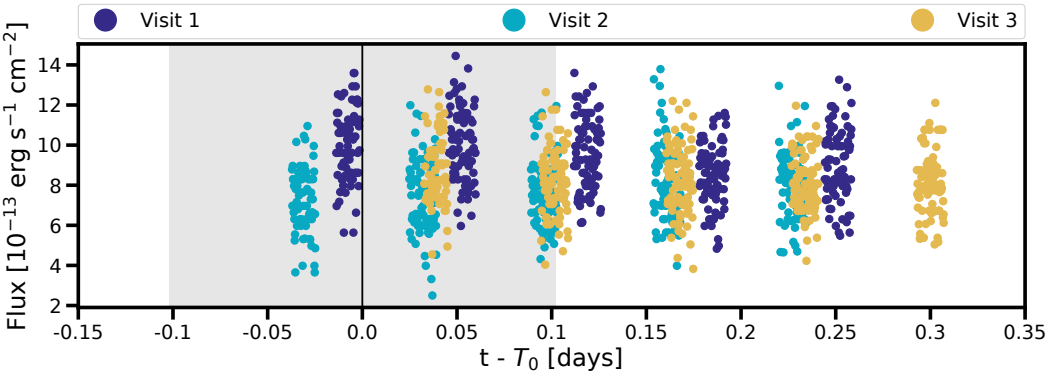

Figure 7.3 Light curve in in the C II 1334.532 Å doublet for the transit of V1298 Tau c with *HST*/COS. The entire transit is marked with the shaded gray region; T_0 is marked with the vertical black line. All three visits sample just before transit mid-point and transit egress well. However, there is no information about transit ingress due to the TTVs of V1298 Tau c. No flares were identified during these visits.

To investigate whether or not V1298 Tau c is losing metals in its atmosphere, I followed the methods of [313]. Namely, I searched for excess absorption in three lines: the Si IV 1393.76 Å and 1402.77 Å doublet, the C II 1335 Å doublet, and the Si III 1206.5 Å line. The highly ionized Si IV doublet will act as a tracer for stellar activity, as its formation temperature means it is unlikely to be present in the exoplanet atmosphere or extended wind. The excess absorption was explored by searching for differences in the line profiles from the in- versus the out-of-transit observations. By subtracting and diving the in- by the

out-of-transit observations, if the element is present in the atmosphere, excess absorption should be seen. As an additional test, and to increase the signal-to-noise, I transformed the spectra from wavelength to velocity, and combined the doublet lines. The preliminary results can be seen in Figure 7.4.

The first thing to note is that there appears to be excess absorption in C II and Si III during Visit 3 from $\sim 0 - 50\,\mathrm{km\,s^{-1}}$ (magenta lines). However, this is directly correlated to excess absorption in Si IV at the same velocity, indicating that this could be stellar in origin. By combining the line profiles from each visit, there is some excess absorption seen. The same calculation was completed for just Visits 2 and 3, where Si IV appears relatively stable, and there is no excess absorption seen, further suggesting the origin of this feature is from the star. The combined line profiles for all visits for C II and Si III are consistent with no excess absorption during the transits of V1298 Tau c.

The preliminary results for AU Mic b and V1298 Tau c as observed with *HST* /COS yield non-detections of both atmospheres. There are several steps forward for further analyzing these two unique FUV data sets. First, it would be useful to test whether or not a transit model can be fit to the light curve for individual lines/doublets. This analysis could yield insights into whether or not a transit model is a better fit to the data over a non-detection (flat line). This is relatively easy to implement using the `exoplanet` open-source software package [180], which performs transit fits given a set of system parameters and performs Markov chain Monte Carlo (MCMC) for sampling from a probability distribution to determine the best-fit values for parameters such as the planet-to-star radius ratio $R_p/R_\star$, impact parameter b, and time of transit mid-point T_0. Second, I will explore using the shape of the stellar-only lines (high formation temperatures) to try and detrend traces of activity seen in lines which could originate from the planet's atmosphere. The ionic emission generally traces across all lines, as seen in correlations between the excess in absorption in N V (Figure 7.2) and Si IV (Figure 7.4), and excess absorption seen in less ionized lines. Therefore, it may be possible to use a scaled version of the stellar-only lines to remove the intrinsic stellar variability seen

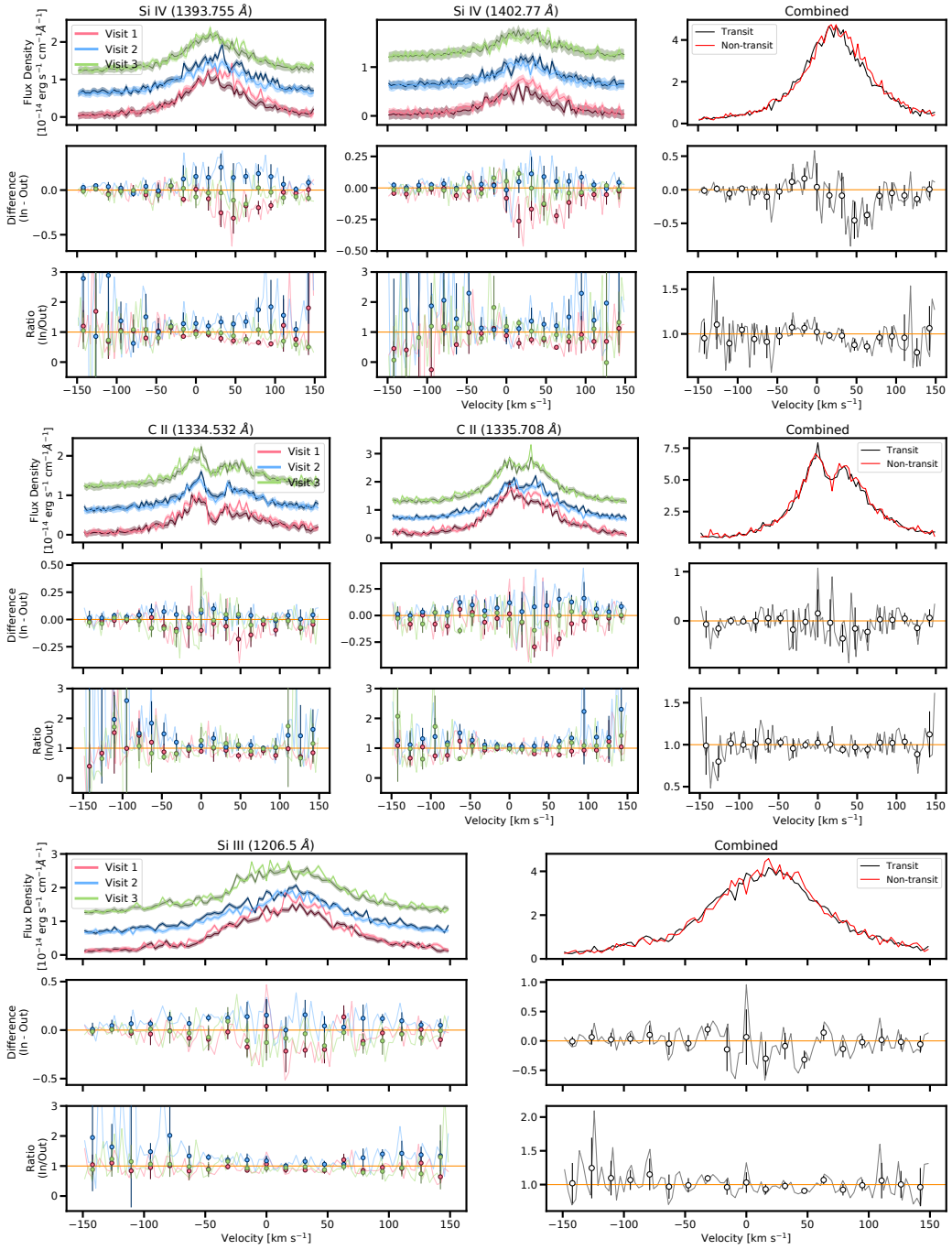

Figure 7.4 Comparison of the line profiles for the in- versus out-of-transit *HST*/COS observations of V1298 Tau c. Magenta represents data from Visit 1, blue from Visit 2, and green from visit 3. The darker shade of each color represents the in-transit profile; the lighter shade of each color represents the out-of-transit profile. The combined line profile from each visit is shown on the right in black and red. The top three rows are for the Si IV 1397.5 Å doublet; the middle three rows are for the C II 1335 Å doublet; the bottom three rows are for the Si III 1206.5 Å line. Lines from each visit are offset to ease readability.

in other lines.

7.2 Chemical compositions of young planetary atmospheres

7.2.1 Using high-resolution ground-based instruments

Section 7.2.2 discussed the future of using low resolution transmission spectra to understand young planetary atmospheres. On the other end of the spectrum, high-resolution ground-based spectroscopy ($R \approx 25,000 - 100,000$) has enabled an additional means of understanding atmospheres. High resolution observations allow for the detailed understanding of the dense forest of molecular absorption features, which would otherwise me unresolved in lower resolution observations. This method is biased towards short-period planets, as it relies on the principle that the molecular features from the planet's atmosphere will undergo large Doppler-shifts during the planet's orbit, while the stellar and telluric lines will remain relatively constant, allowing for the reliable extraction of the planetary signal [see Figure 1 in 59].

To explore the feasibility of using high-resolution ground-based observations for understanding young planetary atmospheres, we observed two planets using IGRINS ($R \approx 45,000$) on Gemini-S. The primary objective of these observations is to measure the C/O abundance of these unique planets to further understand their formation histories. We obtained a single transit of the Jupiter-radius planet HIP 67522 b [469], which orbits a young (17 Myr) solar analogue with a period of 6.96 days (PI A. Feinstein). The transit was observed on 04 May 2022. Simultaneous observations of this transit of HIP 67522 b were obtained with the Next Generation Survey Telescope to allow for a more precise transit time in our analysis. Additionally, we obtained a single transit of the Saturn-radius planet DS Tuc Ab [397], which orbits a young ($30 - 40$ Myr) solar analogue with a period of 8.14 days (PI M. Mansfield). The transit was observed on 02 November 2022. Both transits were observed with the standard IGRINS observing strategy with an ABBA nodding pattern and an on-slit separation

of 2.5" and under favorable weather consitions. The large $v \sin i$ of HIP 67522 (54.2 km s^{-1}) and DS Tuc A (17.8 km s^{-1}) and resulting smooth spectrum should allow for an easy extraction the fast-moving features from both planets.

The data were reduced as follows: First, I evaluated the signal-to-noise ratio (SNR) for each of the 54 orders available in the IGRINS observations. I removed all orders with SNR$<$ 100, which was a total of 15 orders. I removed the first and last 100 data points per order. Next, wavelength calibration was performed on each observation. The calibration includes a simple wavelength shift or stretch to fit each spectrum to the template spectrum, where the template is a median of the first few out-of-transit observations. After, principal component analysis (PCA) was performed to remove the common stellar and telluric lines. This method relies on the idea that the stellar and telluric lines will not change substantially over the night. For HIP 67522 b, we removed the first 10 shared components; for DS Tuc A b, we removed the first 7 shared components. The results of the PCA removal are shown in Figure 7.5.

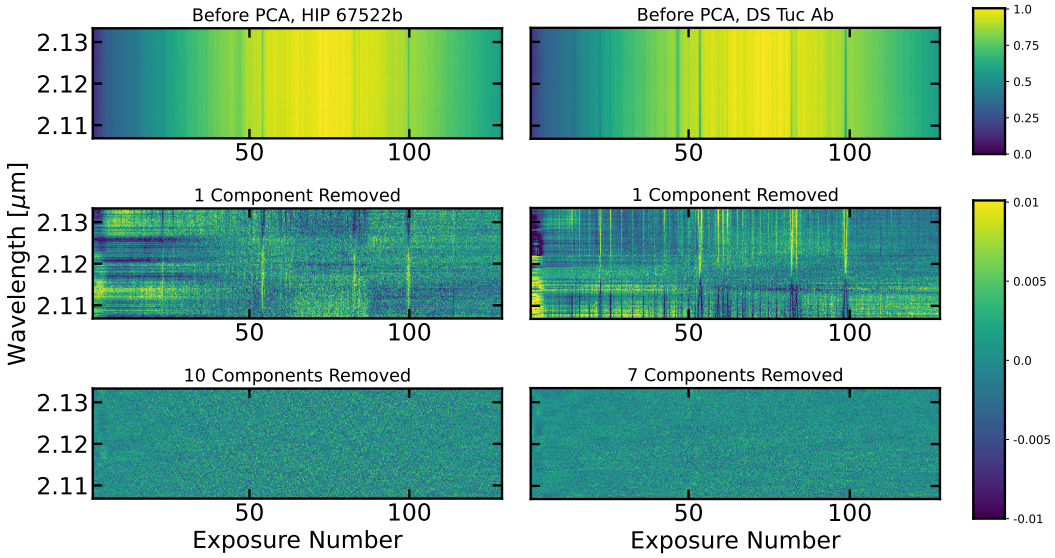

Figure 7.5 The results of the PCA removal of stellar and telluric lines for the IGRINS transit observations of HIP 67522 b (left) and DS Tuc A b (right). Here, we show the results for Order 10 ($\lambda = 2.107 - 2.133 \mu$m) as an example for both data sets.

I explored using the cross-correlation technique to detect H_2O, CH_4, and CO in the

atmosphere of both planets. All three compounds exhibit strong absorption features covered within the IGRINS bandpass and are the primary carriers of carbon and oxygen. The cross-correlation technique uses a template spectrum for the planet atmosphere, scans through the residuals of the observation, and compares how well the template matches specific line positions and depths in the planet rest frame. Here, the residuals are the result of using principal component analysis to remove both telluric and stellar absorption lines, leaving just the signal of the planet (Figure 7.5).

The models were generated assuming $M_{p\text{HIP 67522b}} = 30M_{\oplus}$ and $M_{p\text{DS Tuc Ab}} = 20M_{\oplus}$. These masses are much lower than that predicted for planets of their given radii [99]. However, because they are young and therefore inflated, their masses may be more aligned with that of a Neptune-sized planet (Livingston et al. in prep). Preliminary results of the cross-correlation technique are presented in Figures 7.6 and 7.7.

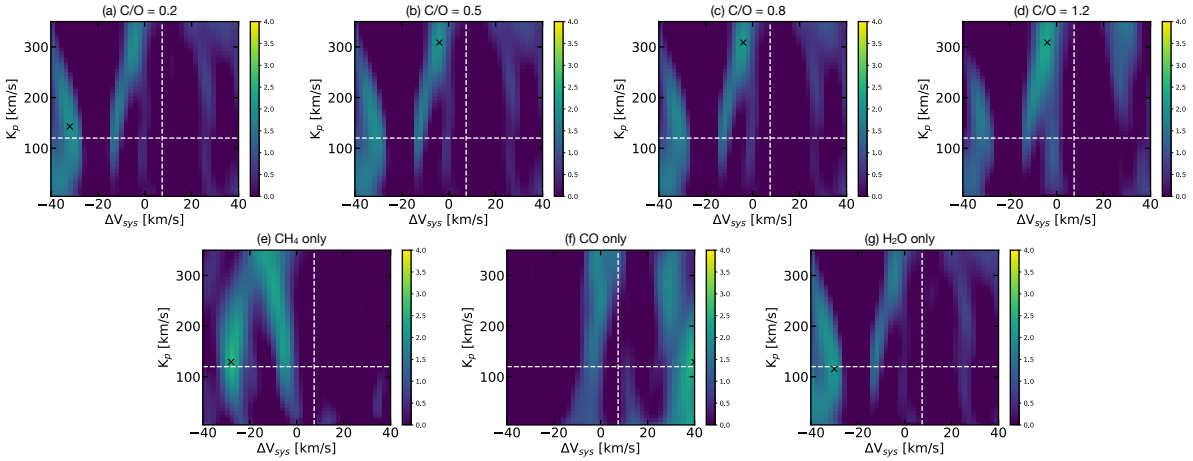

Figure 7.6 The results of the CCF technique for HIP 67522 b. Seven models different models were cross-correlated with the data. (a) Model assuming the carbon-to-oxygen ratio (C/O) = 0.2; (b) Model assuming C/O = 0.5; (c) Model assuming C/O = 0.8; (d) Model assuming C/O = 1.2. Additionally, I searched for signatures from specific molecules: (e) CH_4; (f) CO; and (g) H_2O. The white dashed lines mark where the signal should be with respect to the systemic velocity ($V_{\rm sys}$) and planet orbital velocity (K_p). The colors represents the strength of the detection, σ, and the black x marks where the peak of the signal is. These figures were generated using a resolution of 41×51.

These results are preliminary and therefore should not be accepted as the final solution. One of the challenges of the CCF technique is that it relies on an accurate atmospheric model,

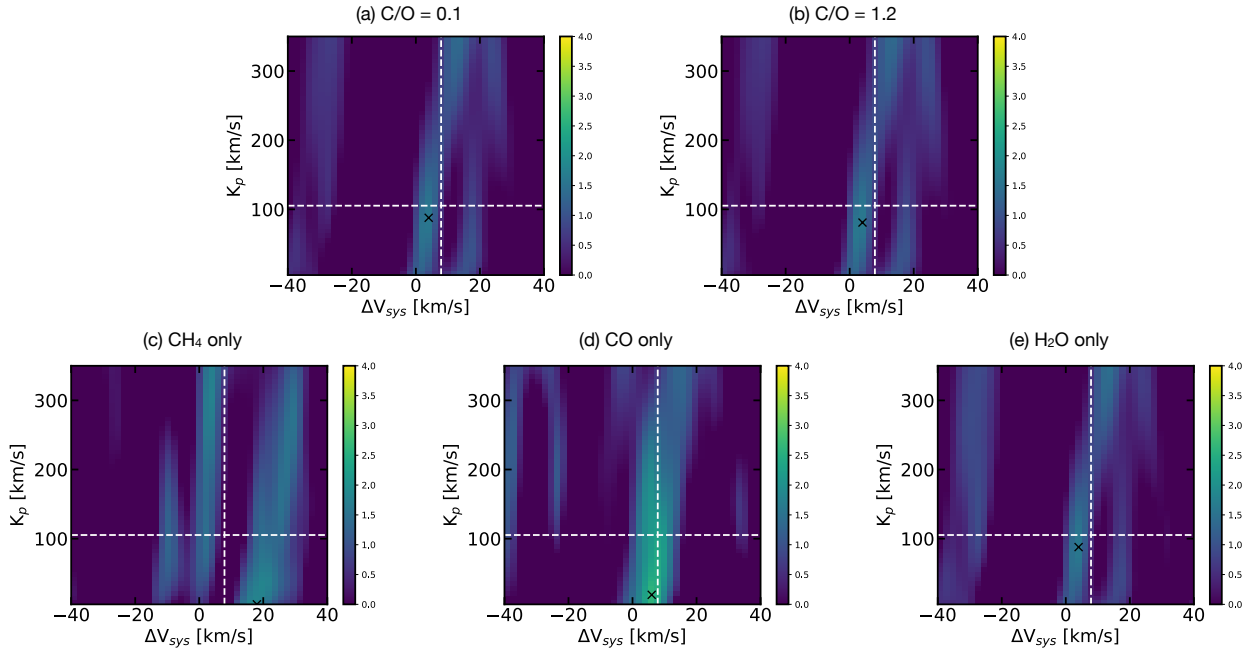

Figure 7.7 The results of the CCF technique for DS Tuc A b. Seven models different models were cross-correlated with the data. (a) Model assuming the carbon-to-oxygen ratio (C/O) = 0.1; and (b) Model assuming C/O = 1.2. Additionally, I searched for signatures from specific molecules: (c) CH_4; (d) CO; and (e) H_2O. The white dashed lines mark where the signal should be with respect to the systemic velocity ($V_{\rm sys}$) and planet orbital velocity (K_p). The colors represents the strength of the detection, σ, and the black x marks where the peak of the signal is.

one which captures the features buried in the data. However, the results from DS Tuc A b are promising.

Moving forward, I will interpret the data using the Bayesian retrieval framework outlined in [72]. Additionally, I will test if transmission spectroscopy can be used to further constrain the mass of young planets. Empirical mass-radius relationships for mature planets, HIP 67522 b's large radius implies that it has a mass of $M_p = 80$ $M_\oplus$ [99]. However, young planets are believed to be inflated, with larger radii and smaller masses ($<$15 $M_\oplus$) before undergoing thermal contraction. Our proposed observations will clarify whether HIP 67522 b is (i) a Neptune-sized planet progenitor, whose inflated atmosphere will undergo mass loss [452] or (ii) a young Jupiter analogue. We will infer the mass of HIP 67522 b via the strength of the spectral features, which is a function of atmospheric scale height and planetary mass

[121].

7.2.2 Using JWST

JWST offers the ability to perform unprecedented transmission spectroscopy of short period ($P < 20$ day) transiting planets. JWST has already demonstrated significant advancements in our understanding of the molecular inventory of gas giant planet inventories through the JWST Transiting Early Release Science Program [525, 47]. Using all available near-infrared spectrographs, JWST has revealed an abundance of H_2O [7, 168], CO_2 [11, 485, 538], CO [168, 485], potassium [168], and even a new species: SO_2 [11, 485, 544]. In Cycle 1 (10 July 2022 - 2023), three young planets will be observed with NIRSpec G395H/F290LP: V1298 Tau bc ($30 - 40$ Myr) and HIP 67522 b (17 Myr; GO 2149, 2498). These observations will have wavelength coverage of $\lambda = 2.87$–5.14μm, which could yield detections of CO_2, CO, H_2O, SO_2, and trace amounts of CH_4. This could allow for a reliable constraint on the carbon-to-oxygen ratio (C/O) of these planets, constraining their initial formation locations. Future observations with a broader wavelength coverage would be beneficial to provide stronger constraints on the C/O, metallicity, and cloud properties of young planets. While observing any young planetary atmosphere would be interesting and advance our understanding of the early stages of planet formation, here I will highlight three particularly interesting systems that would benefit from JWST observations: TOI-1227 b, HD 109833 bc, and AU Mic b.

TOI-1227 b: a first comparison between short- and long-period exoplanets

TOI-1227 b is a $0.85R_{\rm Jup}$ planet orbiting a low-mass star [$0.17M_\odot$; 354]. The kinematics of the system have been found in agreement with that of the Musca group (11 ± 2 Myr) which is a subgroup of the Lower Centaurus Crux (LCC) OB association. TOI-1227 b is the youngest, large-radius giant planet orbiting a low-mass star identified to-date. Radial velocity monitoring of the system has yielded an upper mass constraint of $\leq 0.5M_J$ [354]. The

extended atmosphere of the planet makes it an ideal laboratory to understand the chemical composition of the planet. Therefore, a single transit of TOI-1227 b with NIRSpec/PRISM could be used to constrain its initial formation location by measuring its C/O. As the primordial atmosphere has been directly accreted from the protoplanetary disk, TOI-1227 b has the potential to constrain the initial formation location of young gas-rich short-period exoplanets around low-mass stars. The composition of its atmosphere is a spectroscopic clue to where in the disk TOI-1227 b underwent runaway growth. To date, TOI-1227 b is the youngest gas-giant planet discovered around a low-mass star, therefore it is currently our only benchmark to further our understanding of planet formation in such an environment. Future observations of TOI-1227 b are directly synergistic to those of directly imaged planets, allowing for the first time, a direct comparison of measured C/O between short- and long-period planets in the same stellar association. For example, observations of TOI-1227 b are directly comparative to two JWST Cycle 1 direct imaging programs: GO 1195 and 2044. GO 1195 will observe HD 95086 b with NIRCam ($2.4 - 5\mu$m), and GO 2044 will observe two Jovian exoplanets in the TYC 8998-760-1 planetary system with NIRSpec/PRISM and MIRI LRS ($1 - 12\mu$m). TYC 8998-760-1 was identified as a member of the LCC subgroup, the same subgroup as the target of this proposal [61]. The two companions observed in GO 2044 have semi-major axes of 160 and 320 AU, respectively. TOI-1227 b has a semi-major axis of 0.0886 AU [352]. Therefore, observations of TOI-1227 b, in combination with Cycle 1 observations of TYC 8998-760-1 bc, will allow us to test atmospheric compositions of large, young gas-rich planets in the same stellar association as a function of semi-major axis. TOI-1227 b is the only known short-period exoplanet to complete this study with.

Uncovering the true nature of sub-Neptune sized planets with HD 109833 bc

The radius gap is a prominent trend seen in exoplanet radii, which can be described as a clear bimodal distribution centered around "super-Earths" ($\approx 1.5R_\oplus$) and "sub-Neptunes" ($\approx 2.5R_\oplus$) with a deficiency in planets in between for FGK type stars [189, 552, 57]. The

origin of the gap is debated: is it a byproduct of planetary nature? Or stellar nurture? If the gap is the result of nature, this would indicate that super-Earths and sub-Neptunes are the result of fundamentally different formation mechanisms. In this theory, super-Earths are a scaled-up version of Earth with cores composed of primarily rock and iron, while sub-Neptunes, or water worlds, are a scaled-up version of the Solar System's icy moons with cores composed of primarily rock and ice [141, 478, 592]. Alternatively, the gap can be explained as a byproduct of atmospheric evolution. In this theory, sub-Neptunes, or gas dwarfs, have large hydrogen and helium dominated envelopes, which are lost during the first ~ 100 Myr after their formation due to high-energy irradiation from the host star [415, 414, 322, 97].

To date, all of these new young (< 50 Myr) systems have radii $R_p \geq 3.3 R_\oplus$ except for HD 109833 b and c. These two planets have radii of 2.9 and $2.6 R_\oplus$ and orbital periods of 9.2 and 13.9 days, respectively [581]. These two planets are unique benchmarks for determining whether the radius gap is sculpted by different bulk compositions or atmospheric evolution because they are young enough that they should still host their primordial atmospheres. Since this is a multi-planet system, we have the opportunity for comparative exoplanetology of two similarly sized planets in the sub-Neptune mode of the radius distribution with different $T_{\rm eq}$. Understanding whether both planets are water worlds or gas dwarfs, or one of each would be transformative to our understanding of planetary formation and evolution [129].

One key absorption feature to observe when trying to distinguish between water worlds and gas dwarfs is water. It has been demonstrated that at $R \sim 100$ that the wing steepness and relative depths of H_2O absorption can lead to an unambiguous distinction between cloudy-H/He dominated atmospheres and cloud-free H_2O atmospheres [52]. It has already been readily demonstrated that cloud-free H/He-dominated atmospheres would display larger absorption features than atmospheres dominated in H_2O, CO, CO_2, and CH_4 [369]. This is the result of the atmosphere having a lower mean molecular weight and larger scale height. This distinction was demonstrated on *HST* observations of GJ 1214 b [282], but required the

errors to be reduced by a factor of ~ 3 [52]. Now, JWST has the capability for high-fidelity detections of H_2O and other molecules, while also probing the atmospheric cloud properties, therefore a single transit of both HD 109833 b and c with JWST/NIRISS [168] could answer the groundbreaking question of if these young planets are water worlds or gas dwarfs.

The challenging opportunity to distinguish between the atmosphere of AU Mic b and the starspots of AU Mic

AU Mic b is the youngest Neptune-sized planet ever discovered. Attempts at ground-based transmission spectroscopy have reported non-detections in the optical [419] and He I, which places an upper limit on the amount of atmospheric escape of $0.15 - 0.45 M_{\oplus}\,\mathrm{Gyr}^{-1}$ [237]. Previous atmospheric observations of evolved sub-Neptune and Neptune sized planets have been taken with the *Hubble* and *Spitzer*, with some exhibiting clear H_2O absorption (e.g. HAT-P-11 b and HAT-P-26 b). However, weak to no absorption has been measured in systems such as TOI-674 b, GJ 3470 b, and GJ 436 b. The lack of water absorption in these planets could be the result of either obscuring clouds, hazes, or high metallicity. However, each Neptune-sized exoplanet that has been observed with *HST* is significantly more evolved than AU Mic b (> 1 Gyr). Therefore, the chemical compositions of these exoplanet atmospheres may have been significantly processed due to stellar irradiation [413] or even cometary enrichment [502]. Our best opportunity to resolve the true initial conditions of planet formation is to obtain compositional measurements of *young* planetary systems that are as close to the primordial formation compositions as possible. Therefore, AU Mic b provides a unique window into the progenitors of the more evolved exoplanet population.

AU Mic b can be observed with JWST NIRCam to measure key absorption features of H_2O, CH_4, CO, and CO_2 to infer the protoplanetary disk conditions of the planet during formation [221]. The C/O and metallicity of the atmosphere can also be measured using the aforementioned species. Atmospheric measurements of AU Mic b indicative of formation at large stellocentric distances will constrain migration timescales of Neptune-sized planets for

the first time. These migration timescales are critical for our understanding of the formation and atmospheric evolution of short-period Neptune-sized planets because they allow us to trace the high energy irradiation history of these planets.

We need to understand the ambient environment in which planets reside to understand their true nature. Young stars — and M stars in particular — exhibit high levels of activity driven by stellar inhomogeneity in their photospheres such as starspots and facular regions [214, 162, 382]. These features pose a challenge for the characterization of planets orbiting young and/or M-type stars, which we are equipped to mitigate. However, within this "noise" we have the opportunity to detect interesting signatures of stellar activity. The observations proposed here will constrain the photospheric covering fraction of heterogeneities and the temperature of those regions, which can only be done via spectroscopic observations.

Atmospheric retrievals have been developed to account for stellar surface inhomogeneity coverage fraction and temperatures, and has been proven to recover stellar and starspot properties while marginalizing over the atmospheric abundances of particular molecules. The heterogeneity temperature and coverage fraction inferred using these observations will be the first assessment of contamination of transmission spectra for young, active stars.

7.3 Stellar flares as probes into stellar dynamos

Instantaneously, stellar flares can have detrimental effects to atmospheric chemistry and mass-loss rates. However, in the context of understanding the full evolution of planets, longer timescales must be accounted for: that of stellar cycles. It is through long-term monitoring of the Sun that we learned the Sun goes through solar cycles, or 11-year timescales of higher and lower magnetic activity [497]. Through these cycles, the Sun is seen to have an increased number of and stronger solar flares; it is believed that other stars go through these long-term cycles as well [134]. Therefore, when evaluating the long term evolution of exoplanets which account for the high-energy luminosity of the star, the cycles of magnetic activity and flare rates/energies must be accounted for.

While we know a significant amount about the Sun, it is still unclear what drives the solar cycle. By searching for signatures of stellar cycles on other stars, we will not only better understand the effects of longer timescale activity cycles on atmospheric removal, but also shed light on the mechanisms driving our own Sun. It is currently believed that the timescale of the solar cycle is proportional to the rotation period of the Sun and inversely proportional to the convective turn-over timescale, or stellar mass [583, 131]. Stars are known to spin-down as they age [515]. If stellar cycles are correlated with the rotation period of a given star, then the stellar cycles for young, rapidly rotating stars should be shorter than the 11 year cycle we see for the Sun ($P_{\rm rot} \approx 30$ days). Using stellar flares to approximate cycles of strong and weak magnetic activity is one of the only ways to approach the question that has alluded us for so long: what drives the length of stellar cycles?

From the Sun, we know that two properties of solar flares change during solar minimum and maximum: the pure counting number of flares and the maximum energy of flares. Both of these will manifest in changing the overall flare rate distribution as a function of flare energy. Case studies have been completed for select *Kepler* stars [498]. The pilot study presented the best candidate for flare activity variation across *Kepler* quarters: KIC 8507979, a dM3e star with a rotation period of 1.2 days. While no unambiguous evidence for a stellar cycle length was demonstrated, the variation was consistent with a cyclic behavior of over a decade. *Kepler* targets had a limited baseline of 4 years before the reaction wheels of the observatory broke, therefore limiting the baseline on searching for variations in flare rates. Additionally, the small field-of-view limited the number of targets to search for variations in flare rates over.

Now, TESS is about to enter Year 6 of its extended mission, therefore providing us with a longer baseline to search for flare variations from year to year. TESS is an all-sky survey, therefore allowing us to survey changes in flare rates across a large range of stellar rotation periods and spectral types. Additionally, the orientation of TESS has resulted in the northern and southern ecliptic hemispheres being observed every other year across 6 years. Targets

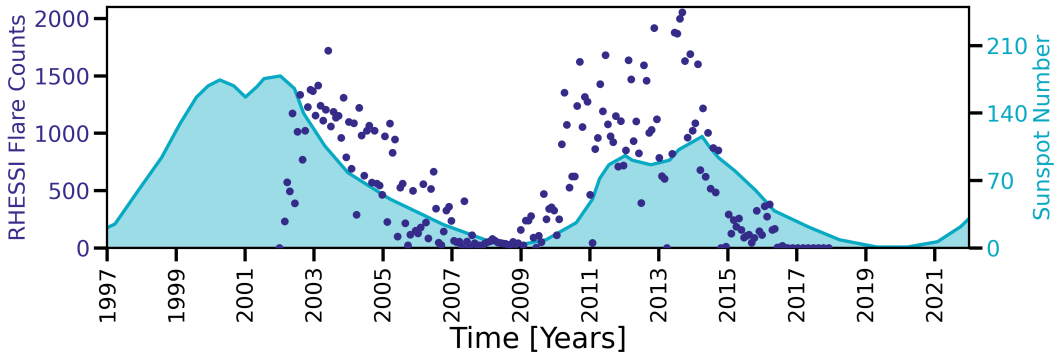

Figure 7.8 A comparison of the number of X-ray solar flares from the RHESSI mission (purple) and sunspots (blue) as a function of time. While sunspots are often used to characterize the long-term solar cycle, it is clear that solar flare counts trace the cycle as well.

that of are particular interest are those located in the continuous viewing zone (CVZ), which are located at the ecliptic poles and have ~ 1 year of continuous observations. Therefore, it is extremely timely to begin using stellar flares to measure or constrain the length of stellar cycles of stars other than the Sun.

Once all *TESS* data is available, it would be interesting to target young stars within the CVZ to search for evidence of stellar cycle lengths. Young stars are of particular interest because the length of the stellar cycle is believed to be correlated with the rotation period of the star. In theory, the shorter the rotation period, the shorter the stellar cycle. I have identified 64 targets within the CVZ which were identified as high probability members of various nearby young moving groups, young open clusters, OB associations, and star forming regions with Banyan-Σ [190]. By evaluating the fractional luminosity emitted in flares $L_{\rm flare}/L_{\rm TESS} \equiv \xi_{\rm tot}/t_{\rm exp}$, where $\xi_{\rm tot}$ is the equivalent duration of the flare and $t_{\rm exp}$ is the total exposure time of the observation [336, 498], we can compare the flare frequency distribution (FFD) on various different timescales (months to a year) to search for evidence of either (a) fewer flares in each luminosity bin or (b) a shallower FFD, indicative of fewer high energy flares. Either signature could be evidence of a stellar cycle, and is more reliable than using pure photometric variability, which is what has generally been used in the past.

REFERENCES

[1] Abadi, M., Agarwal, A., Barham, P., et al. 2016, ArXiv e-prints, arXiv:1603.04467

[2] Ackerman, A. S., & Marley, M. S. 2001, ApJ, 556, 872

[3] —. 2001, ApJ, 556, 872

[4] Addison, B., Wright, D. J., Wittenmyer, R. A., et al. 2019, PASP, 131, 115003

[5] Addison, B. C., Horner, J., Wittenmyer, R. A., et al. 2020, arXiv e-prints, arXiv:2006.13675

[6] Aggarwal, C. C. 2014, Data classification: algorithms and applications (CRC press)

[7] Ahrer, E.-M., Stevenson, K. B., Mansfield, M., et al. 2023, Nature, 614, 653–658

[8] Airapetian, V. S., Glocer, A., Gronoff, G., Hébrard, E., & Danchi, W. 2016, Nature Geoscience, 9, 452

[9] Airapetian, V. S., Barnes, R., Cohen, O., et al. 2020, International Journal of Astrobiology, 19, 136

[10] Albrecht, S., Winn, J. N., Marcy, G. W., et al. 2013, ApJ, 771, 11

[11] Alderson, L., Wakeford, H. R., Alam, M. K., et al. 2023, Nature, 614, 664–669

[12] Alfven, H. 1950, Cosmical electrodynamics

[13] Allard, N. F., Spiegelman, F., & Kielkopf, J. F. 2016, A&A, 589, A21

[14] Allard, N. F., Spiegelman, F., Leininger, T., & Molliere, P. 2019, A&A, 628, A120

[15] Allart, R., Bourrier, V., Lovis, C., et al. 2019, A&A, 623, A58

[16] Alvarado-Gómez, J. D., Drake, J. J., Moschou, S. P., et al. 2019, ApJ, 884, L13

[17] Alvarado-Gómez, J. D., Cohen, O., Drake, J. J., et al. 2022, ApJ, 928, 147

[18] Andrade, R. F. S., Schellnhuber, H. J., & Claussen, M. 1998, Physica A Statistical Mechanics and its Applications, 254, 557

[19] Ansdell, M., Ioannou, Y., Osborn, H. P., et al. 2018, ApJ, 869, L7

[20] Antonova, L. A., & Nusinov, A. A. 1998, Sol. Phys., 177, 197

[21] Arcangeli, J., Désert, J.-M., Line, M. R., et al. 2018, ApJ, 855, L30

[22] Arney, G., Domagal-Goldman, S. D., Meadows, V. S., et al. 2016, Astrobiology, 16, 873

[23] Arney, G. N., Meadows, V. S., Domagal-Goldman, S. D., et al. 2017, ApJ, 836, 49

[24] Aschwanden, M. J., & Güdel, M. 2021, The Astrophysical Journal, 910, 41

[25] Aschwanden, M. J., Kosugi, T., Hanaoka, Y., Nishio, M., & Melrose, D. B. 1999, ApJ, 526, 1026

[26] Aschwanden, M. J., Tarbell, T. D., Nightingale, R. W., et al. 2000, ApJ, 535, 1047

[27] Astropy Collaboration, Robitaille, T. P., Tollerud, E. J., et al. 2013, A&A, 558, A33

[28] Audard, M., Güdel, M., & Guinan, E. F. 1999, ApJ, 513, L53

[29] Augereau, J. C., & Beust, H. 2006, A&A, 455, 987

[30] Azzam, A. A. A., Tennyson, J., Yurchenko, S. N., & Naumenko, O. V. 2016, MNRAS, 460, 4063

[31] Bak, P., Chen, K., & Creutz, M. 1989, Nature, 342, 780

[32] Bak, P., Chen, K., & Tang, C. 1990, Physics Letters A, 147, 297

[33] Bak, P., Paczuski, M., & Shubik, M. 1997, Physica A Statistical Mechanics and its Applications, 246, 430

[34] Bak, P., & Sneppen, K. 1993, Phys. Rev. Lett., 71, 4083

[35] Bak, P., & Tang, C. 1989, J. Geophys. Res., 94, 15,635

[36] Bak, P., Tang, C., & Wiesenfeld, K. 1988, Phys. Rev. A, 38, 364

[37] Barber, R. J., Strange, J. K., Hill, C., et al. 2014, MNRAS, 437, 1828

[38] Barber, R. J., Tennyson, J., Harris, G. J., & Tolchenov, R. N. 2006, MNRAS, 368, 1087

[39] Barman, T. S., Hauschildt, P. H., & Allard, F. 2001, ApJ, 556, 885

[40] Barnes, J. R., Haswell, C. A., Staab, D., & Anglada-Escudé, G. 2016, Monthly Notices of the RAS, 462, 1012

[41] Barnes, S. A. 2003, ApJ, 586, 464

[42] Barrado y Navascués, D., Stauffer, J. R., & Jayawardhana, R. 2004, ApJ, 614, 386

[43] Barstow, J. K. 2020, MNRAS, 497, 4183

[44] Batalha, N. E., Marley, M. S., Lewis, N. K., & Fortney, J. J. 2019, ApJ, 878, 70

[45] Bate, M. R., Lubow, S. H., Ogilvie, G. I., & Miller, K. A. 2003, MNRAS, 341, 213

[46] Bean, J. L., Raymond, S. N., & Owen, J. E. 2021, Journal of Geophysical Research (Planets), 126, e06639

[47] Bean, J. L., Stevenson, K. B., Batalha, N. M., et al. 2018, PASP, 130, 114402

[48] Bell, C. P. M., Mamajek, E. E., & Naylor, T. 2015, Monthly Notices of the RAS, 454, 593

[49] Bell, T. J., Ahrer, E.-M., Brande, J., et al. 2022, arXiv e-prints, arXiv:2207.03585

[50] Benatti, S., Nardiello, D., Malavolta, L., et al. 2019, A&A, 630, A81

[51] Benneke, B., & Seager, S. 2012, ApJ, 753, 100

[52] —. 2013, ApJ, 778, 153

[53] Benneke, B., Knutson, H. A., Lothringer, J., et al. 2019, Nature Astronomy, 3, 813

[54] Benneke, B., Wong, I., Piaulet, C., et al. 2019, The Astrophysical Journal Letters, 887, L14, publisher: American Astronomical Society

[55] Benz, A. O., & Güdel, M. 2010, ARA&A, 48, 241

[56] Berdyugina, S. V., Solanki, S. K., & Frutiger, C. 2003, A&A, 412, 513

[57] Berger, T. A., Huber, D., Gaidos, E., van Saders, J. L., & Weiss, L. M. 2020, AJ, 160, 108

[58] Biazzo, K., D'Orazi, V., Desidera, S., et al. 2022, A&A, 664, A161

[59] Birkby, J. L. 2018, arXiv e-prints, arXiv:1806.04617

[60] Bisikalo, D. V., Shematovich, V. I., Cherenkov, A. A., Fossati, L., & Möstl, C. 2018, ApJ, 869, 108

[61] Bohn, A. J., Kenworthy, M. A., Ginski, C., et al. 2020, ApJ, 898, L16

[62] Bohren, C. F., & Huffman, D. R. 1983, Absorption and scattering of light by small particles

[63] Bondar', N. I., & Katsova, M. M. 2020, Geomagnetism and Aeronomy, 60, 942

[64] Borucki, W. J., & Others. 2010, Science, 327, 977

[65] Borucki, W. J., Koch, D., Basri, G., et al. 2010, Science, 327, 977

[66] Boss, A. P. 1997, Science, 276, 1836

[67] Bouma, L. G., Curtis, J. L., Masuda, K., et al. 2022, AJ, 163, 121

[68] Bourrier, V., Lecavelier des Etangs, A., Ehrenreich, D., Tanaka, Y. A., & Vidotto, A. A. 2016, A&A, 591, A121

[69] Bourrier, V., Lecavelier des Etangs, A., Ehrenreich, D., et al. 2018, A&A, 620, A147

[70] Bourrier, V., Wheatley, P. J., Lecavelier des Etangs, A., et al. 2020, MNRAS, 493, 559

[71] Brandt, T. D., & Huang, C. X. 2015, ApJ, 807, 24

[72] Brogi, M., & Line, M. R. 2019, AJ, 157, 114

[73] Brueckner, G. E. 1976, Philosophical Transactions of the Royal Society of London Series A, 281, 443

[74] Buchner, J., Georgakakis, A., Nandra, K., et al. 2014, A&A, 564, A125

[75] Burke, C. J., Bryson, S. T., Mullally, F., et al. 2014, ApJS, 210, 19

[76] Butler, C. J., Rodono, M., & Linsky, J. L. 1986, in ESA Special Publication, Vol. 263, New Insights in Astrophysics. Eight Years of UV Astronomy with IUE, ed. E. J. Rolfe & R. Wilson, 229

[77] Cale, B. L., Reefe, M., Plavchan, P., et al. 2021, AJ, 162, 295

[78] Candelaresi, S., Hillier, A., Maehara, H., Brand enburg, A., & Shibata, K. 2014, ApJ, 792, 67

[79] Carleo, I., Desidera, S., Nardiello, D., et al. 2021, A&A, 645, A71

[80] Carrington, R. C. 1859, MNRAS, 20, 13

[81] Castelli, F., & Kurucz, R. L. 1994, A&A, 281, 817

[82] Catalano, S., Biazzo, K., Frasca, A., & Marilli, E. 2002, A&A, 394, 1009

[83] Cauley, P. W., Kuckein, C., Redfield, S., et al. 2018, AJ, 156, 189

[84] Cauley, P. W., Redfield, S., & Jensen, A. G. 2017, AJ, 153, 217

[85] Cauley, P. W., Shkolnik, E. L., Llama, J., Bourrier, V., & Moutou, C. 2018, AJ, 156, 262

[86] Cauley, P. W., Shkolnik, E. L., Llama, J., & Lanza, A. F. 2019, Nature Astronomy, 3, 1128

[87] Chabrier, G., & Baraffe, I. 1997, A&A, 327, 1039

[88] Chabrier, G., Johansen, A., Janson, M., & Rafikov, R. 2014, in Protostars and Planets VI, ed. H. Beuther, R. S. Klessen, C. P. Dullemond, & T. Henning, 619–642

[89] Chang, S. W., Byun, Y. I., & Hartman, J. D. 2015, ApJ, 814, 35

[90] Changeat, Q., Edwards, B., Al-Refaie, A. F., et al. 2022, ApJS, 260, 3

[91] Charbonneau, D., Brown, T. M., Latham, D. W., & Mayor, M. 2000, ApJ, 529, L45

[92] Charbonneau, D., Brown, T. M., Noyes, R. W., & Gilliland, R. L. 2002, ApJ, 568, 377

[93] Charbonneau, D., Berta, Z. K., Irwin, J., et al. 2009, Nature, 462, 891

[94] Charbonneau, P. 2010, Living Reviews in Solar Physics, 7, 3

[95] Chassefière, E., & Leblanc, F. 2004, Planet. Space Sci., 52, 1039

[96] Chassefière, E., Leblanc, F., & Langlais, B. 2007, Planet. Space Sci., 55, 343

[97] Chen, H., & Rogers, L. A. 2016, ApJ, 831, 180

[98] Chen, H., Zhan, Z., Youngblood, A., et al. 2021, Nature Astronomy, 5, 298

[99] Chen, J., & Kipping, D. 2017, ApJ, 834, 17

[100] Chene, A.-N., Padzer, J., Barrick, G., et al. 2014, in Society of Photo-Optical Instrumentation Engineers (SPIE) Conference Series, Vol. 9151, Advances in Optical and Mechanical Technologies for Telescopes and Instrumentation, ed. R. Navarro, C. R. Cunningham, & A. A. Barto, 915147

[101] Chollet, F., & others. 2018, Keras: The Python Deep Learning library, ascl:1806.022

[102] Claret, A. 2000, A&A, 363, 1081

[103] Cohen, O., Drake, J., Alvarado Gomez, J., et al. 2022, in Bulletin of the American Astronomical Society, Vol. 54, 102.280

[104] Cohen, O., Drake, J. J., Glocer, A., et al. 2014, ApJ, 790, 57

[105] Craig, M., Crawford, S., Seifert, M., et al. 2017, astropy/ccdproc: v1.3.0.post1, doi:10.5281/zenodo.1069648

[106] Cranmer, S. R., Wilner, D. J., & MacGregor, M. A. 2013, ApJ, 772, 149

[107] Cully, S. L., Siegmund, O. H. W., Vedder, P. W., & Vallerga, J. V. 1993, ApJ, 414, L49

[108] Curtis, J. L., Agüeros, M. A., Mamajek, E. E., Wright, J. T., & Cummings, J. D. 2019, AJ, 158, 77

[109] Czesla, S., Klocová, T., Khalafinejad, S., Wolter, U., & Schmitt, J. H. M. M. 2015, A&A, 582, A51

[110] Dahm, S. E. 2015, ApJ, 813, 108

[111] Darveau-Bernier, A., Albert, L., Talens, G. J., et al. 2022, PASP, 134, 094502

[112] Davenport, J. R. A. 2016, ApJ, 829, 23

[113] Davenport, J. R. A., Covey, K. R., Clarke, R. W., et al. 2019, ApJ, 871, 241

[114] Davenport, J. R. A., Hawley, S. L., Hebb, L., et al. 2014, ApJ, 797, 122

[115] David, T. J., Petigura, E. A., Luger, R., et al. 2019, ApJ, 885, L12

[116] David, T. J., Hillenbrand, L. A., Petigura, E. A., et al. 2016, Nature, 534, 658

[117] David, T. J., Cody, A. M., Hedges, C. L., et al. 2019, AJ, 158, 79

[118] Dawson, R. I., & Johnson, J. A. 2018, ARA&A, 56, 175

[119] de Arcangelis, L., Godano, C., Lippiello, E., & Nicodemi, M. 2006, Phys. Rev. Lett., 96, 051102

[120] de Gasperin, F., Lazio, T. J. W., & Knapp, M. 2020, A&A, 644, A157

[121] de Wit, J., & Seager, S. 2013, Science, 342, 1473

[122] Del Zanna, G., Dere, K. P., Young, P. R., & Landi, E. 2021, ApJ, 909, 38

[123] Del Zanna, G., Landini, M., & Mason, H. E. 2002, A&A, 385, 968

[124] Demory, B.-O., de Wit, J., Lewis, N., et al. 2013, ApJ, 776, L25

[125] Dendy, R. O., Helander, P., & Tagger, M. 1998, A&A, 337, 962

[126] Dennis, B. R., & Zarro, D. M. 1993, Sol. Phys., 146, 177

[127] Dere, K. P., Landi, E., Mason, H. E., Monsignori Fossi, B. C., & Young, P. R. 1997, A&AS, 125, 149

[128] Diamond-Lowe, H., Youngblood, A., Charbonneau, D., et al. 2021, AJ, 162, 10

[129] Diamond-Lowe, H., Kreidberg, L., Harman, C. E., et al. 2022, AJ, 164, 172

[130] Dissauer, K., Veronig, A. M., Temmer, M., Podladchikova, T., & Vanninathan, K. 2018, ApJ, 863, 169

[131] Distefano, E., Lanzafame, A. C., Lanza, A. F., Messina, S., & Spada, F. 2017, A&A, 606, A58

[132] Dobbie, P. D., Lodieu, N., & Sharp, R. G. 2010, MNRAS, 409, 1002

[133] Donati, J. F., & Landstreet, J. D. 2009, ARA&A, 47, 333

[134] Donati, J. F., Collier Cameron, A., Semel, M., et al. 2003, MNRAS, 345, 1145

[135] Dorman, B., Nelson, L. A., & Chau, W. Y. 1989, ApJ, 342, 1003

[136] Doyle, L., Ramsay, G., & Doyle, J. G. 2020, arXiv e-prints, arXiv:2003.14410

[137] Doyle, L., Ramsay, G., Doyle, J. G., & Wu, K. 2019, MNRAS, 489, 437

[138] Doyle, L., Ramsay, G., Doyle, J. G., Wu, K., & Scullion, E. 2018, MNRAS, 480, 2153

[139] Doyon, R., Hutchings, J. B., Beaulieu, M., et al. 2012, in Society of Photo-Optical Instrumentation Engineers (SPIE) Conference Series, Vol. 8442, Space Telescopes and Instrumentation 2012: Optical, Infrared, and Millimeter Wave, ed. M. C. Clampin, G. G. Fazio, H. A. MacEwen, & J. Oschmann, Jacobus M., 84422R

[140] Drake, J. J., Brown, A., Bowyer, S., et al. 1994, in Astronomical Society of the Pacific Conference Series, Vol. 64, Cool Stars, Stellar Systems, and the Sun, ed. J.-P. Caillault, 35

[141] Dressing, C. D., Charbonneau, D., Dumusque, X., et al. 2015, ApJ, 800, 135

[142] Drummond, B., Tremblin, P., Baraffe, I., et al. 2016, A&A, 594, A69

[143] Dubinin, E., Winningham, D., Fränz, M., et al. 2006, Icarus, 182, 343

[144] Dun, J., Kurokawa, H., Ishii, T. T., Liu, Y., & Zhang, H. 2007, ApJ, 657, 577

[145] Durisen, R. H., Boss, A. P., Mayer, L., et al. 2007, in Protostars and Planets V, ed. B. Reipurth, D. Jewitt, & K. Keil, 607

[146] Duvvuri, G. M., Sebastian Pineda, J., Berta-Thompson, Z. K., et al. 2021, ApJ, 913, 40

[147] Eistrup, C., Walsh, C., & van Dishoeck, E. F. 2016, A&A, 595, A83

[148] Espinoza, N. 2022, TransitSpectroscopy, doi:10.5281/zenodo.6960924

[149] Espinoza, N., & Jordán, A. 2015, MNRAS, 450, 1879

[150] —. 2016, MNRAS, 457, 3573

[151] Espinoza, N., Kossakowski, D., & Brahm, R. 2019, Monthly Notices of the Royal Astronomical Society, 490, 2262

[152] Fabrycky, D., & Tremaine, S. 2007, ApJ, 669, 1298

[153] Faedi, F., Barros, S. C. C., Anderson, D. R., et al. 2011, A&A, 531, A40

[154] Faherty, J. K., Bochanski, J. J., Gagné, J., et al. 2018, ApJ, 863, 91

[155] Fang, X.-S., Zhao, G., Zhao, J.-K., Chen, Y.-Q., & Bharat Kumar, Y. 2016, MNRAS, 463, 2494

[156] Fares, R., Donati, J. F., Moutou, C., et al. 2010, MNRAS, 406, 409

[157] Fedele, D., van den Ancker, M. E., Henning, T., Jayawardhana, R., & Oliveira, J. M. 2010, A&A, 510, A72

[158] Feigelson, E., Townsley, L., Güdel, M., & Stassun, K. 2007, in Protostars and Planets V, ed. B. Reipurth, D. Jewitt, & K. Keil, 313

[159] Feigelson, E. D., & Montmerle, T. 1999, ARA&A, 37, 363

[160] Feinstein, A., Montet, B., & Ansdell, M. 2020, The Journal of Open Source Software, 5, 2347

[161] Feinstein, A. D., David, T. J., Montet, B. T., et al. 2022, ApJ, 925, L2

[162] Feinstein, A. D., Montet, B. T., Ansdell, M., et al. 2020, AJ, 160, 219

[163] Feinstein, A. D., Montet, B. T., Johnson, M. C., et al. 2021, AJ, 162, 213

[164] Feinstein, A. D., Seligman, D. Z., Günther, M. N., & Adams, F. C. 2022, ApJ, 925, L9

[165] Feinstein, A. D., Montet, B. T., Foreman-Mackey, D., et al. 2019, PASP, 131, 094502

[166] Feinstein, A. D., Schlieder, J. E., Livingston, J. H., et al. 2019, AJ, 157, 40

[167] Feinstein, A. D., France, K., Youngblood, A., et al. 2022, AJ, 164, 110

[168] Feinstein, A. D., Radica, M., Welbanks, L., et al. 2023, Nature, 614, 670–675

[169] Feroz, F., Hobson, M. P., & Bridges, M. 2009, MNRAS, 398, 1601

[170] Fischer, P. D., Knutson, H. A., Sing, D. K., et al. 2016, ApJ, 827, 19

[171] —. 2016, ApJ, 827, 19

[172] Fisher, C., & Heng, K. 2018, MNRAS, 481, 4698

[173] Fitzgerald, M. P., Kalas, P. G., Duchêne, G., Pinte, C., & Graham, J. R. 2007, ApJ, 670, 536

[174] Flagg, L., Johns-Krull, C., France, K., et al. 2022, arXiv e-prints, arXiv:2206.02636

[175] Flores Soriano, M., Strassmeier, K. G., & Weber, M. 2015, A&A, 575, A57

[176] Ford, E. B. 2014, Proceedings of the National Academy of Science, 111, 12616

[177] Foreman-Mackey, D., Agol, E., Ambikasaran, S., & Angus, R. 2017, AJ, 154, 220

[178] Foreman-Mackey, D., Hogg, D. W., Lang, D., & Goodman, J. 2013, PASP, 125, 306

[179] Foreman-Mackey, D., Hogg, D. W., Lang, D., & Goodman, J. 2013, Publications of the Astronomical Society of the Pacific, 125, 306

[180] Foreman-Mackey, D., Luger, R., Agol, E., et al. 2021, arXiv e-prints, arXiv:2105.01994

[181] Fortney, J. J. 2005, MNRAS, 364, 649

[182] Fortney, J. J., Mordasini, C., Nettelmann, N., et al. 2013, ApJ, 775, 80

[183] France, K., Linsky, J. L., Tian, F., Froning, C. S., & Roberge, A. 2012, ApJ, 750, L32

[184] France, K., Loyd, R. O. P., Youngblood, A., et al. 2016, ApJ, 820, 89

[185] France, K., Duvvuri, G., Egan, H., et al. 2020, AJ, 160, 237

[186] Fraunhofer, J. 1817, Annalen der Physik, 56, 264

[187] Freedman, R. S., Lustig-Yaeger, J., Fortney, J. J., et al. 2014, ApJS, 214, 25

[188] Froning, C. S., Kowalski, A., France, K., et al. 2019, ApJ, 871, L26

[189] Fulton, B. J., Petigura, E. A., Howard, A. W., et al. 2017, AJ, 154, 109

[190] Gagné, J., Mamajek, E. E., Malo, L., et al. 2018, ApJ, 856, 23

[191] Gaia Collaboration, Prusti, T., de Bruijne, J. H. J., et al. 2016, A&A, 595, A1

[192] Gaia Collaboration, Brown, A. G. A., Vallenari, A., et al. 2018, A&A, 616, A1

[193] Garcia-Sage, K., Glocer, A., Drake, J. J., Gronoff, G., & Cohen, O. 2017, ApJ, 844, L13

[194] Gautier, Thomas N., I., Charbonneau, D., Rowe, J. F., et al. 2012, ApJ, 749, 15

[195] Gelman, A., & Rubin, D. B. 1992, Statistical Science, 7, 457

[196] Geweke, J. 1992, Bayesian Statistics IV. Oxford: Clarendon Press, ed. J. M. Bernardo, 169

[197] Gharib-Nezhad, E., Iyer, A. R., Line, M. R., et al. 2021, ApJS, 254, 34

[198] Gilbert, E. A., Barclay, T., Quintana, E. V., et al. 2022, AJ, 163, 147

[199] Gilbert, J., Bergmann, C., Bloxham, G., et al. 2018, in Society of Photo-Optical Instrumentation Engineers (SPIE) Conference Series, Vol. 10702, Ground-based and Airborne Instrumentation for Astronomy VII, ed. C. J. Evans, L. Simard, & H. Takami, 107020Y

[200] Gillon, M., Triaud, A. H. M. J., Demory, B.-O., et al. 2017, Nature, 542, 456

[201] Ginzburg, S., Schlichting, H. E., & Sari, R. 2018, MNRAS, 476, 759

[202] Goldreich, P., & Tremaine, S. 1979, ApJ, 233, 857

[203] Goodman, J., & Weare, J. 2010, Communications in Applied Mathematics and Computational Science, 5, 65

[204] Goyal, J. M., Mayne, N., Sing, D. K., et al. 2018, MNRAS, 474, 5158

[205] Goyal, J. M., Mayne, N., Drummond, B., et al. 2020, MNRAS, 498, 4680

[206] Grankin, K. N. 1999, Astronomy Letters, 25, 526

[207] Gray, D. F. 2008, The Observation and Analysis of Stellar Photospheres

[208] Gray, R. O., & Corbally, C. J. 1994, AJ, 107, 742

[209] Grieger, B. 1992, Physica A Statistical Mechanics and its Applications, 191, 51

[210] Grimm, S. L., Malik, M., Kitzmann, D., et al. 2021, ApJS, 253, 30

[211] Gronoff, G., Arras, P., Baraka, S., et al. 2020, Journal of Geophysical Research (Space Physics), 125, e27639

[212] Gryciuk, M., Siarkowski, M., Sylwester, J., et al. 2017, Sol. Phys., 292, 77

[213] Guilluy, G., Andretta, V., Borsa, F., et al. 2020, A&A, 639, A49

[214] Gully-Santiago, M. A., Herczeg, G. J., Czekala, I., et al. 2017, ApJ, 836, 200

[215] Günther, M. N., Pozuelos, F. J., Dittmann, J. A., et al. 2019, Nature Astronomy, 3, 1099

[216] Günther, M. N., Zhan, Z., Seager, S., et al. 2020, AJ, 159, 60

[217] Guo, Z., Gully-Santiago, M., & Herczeg, G. J. 2018, ApJ, 868, 143

[218] Gupta, A., & Schlichting, H. E. 2019, MNRAS, 487, 24

[219] Gutenberg, B., & Richter, C. F. 1956, Annals of Geophysics, 53, doi:10.4401/ag-4588

[220] Hands, T. O., & Helled, R. 2022, MNRAS, 509, 894

[221] —. 2022, MNRAS, 509, 894

[222] Harman, C. E., Kopparapu, R. K., Stefánsson, G., et al. 2022, , 3, 45

[223] Harra, L. K., Schrijver, C. J., Janvier, M., et al. 2016, Sol. Phys., 291, 1761

[224] Hauschildt, P. H., Allard, F., & Baron, E. 1999, ApJ, 512, 377

[225] Hawley, S. L., Davenport, J. R. A., Kowalski, A. F., et al. 2014, ApJ, 797, 121

[226] Hawley, S. L., & Pettersen, B. R. 1991, ApJ, 378, 725

[227] —. 1991, ApJ, 378, 725

[228] Hawley, S. L., Fisher, G. H., Simon, T., et al. 1995, ApJ, 453, 464

[229] Hawley, S. L., Allred, J. C., Johns-Krull, C. M., et al. 2003, ApJ, 597, 535

[230] Hazra, G., Vidotto, A. A., Carolan, S., Villarreal D'Angelo, C., & Manchester, W. 2022, MNRAS, 509, 5858

[231] He, K., Zhang, X., Ren, S., & Sun, J. 2016, in 14th European Conference on Computer Vision (ECCV), Vol. 5 (Springer), 630–645

[232] Heger, A., Langer, N., & Woosley, S. E. 2000, ApJ, 528, 368

[233] Hellier, C., Anderson, D. R., Collier Cameron, A., et al. 2014, MNRAS, 440, 1982

[234] Henry, T. J., Jao, W.-C., Subasavage, J. P., et al. 2006, AJ, 132, 2360

[235] Hesse, J., & Gross, T. 2014, Frontiers in Systems Neuroscience, 8, 166

[236] Hippke, M., David, T. J., Mulders, G. D., & Heller, R. 2019, AJ, 158, 143

[237] Hirano, T., Krishnamurthy, V., Gaidos, E., et al. 2020, ApJ, 899, L13

[238] Hoch, K. K. W., Konopacky, Q. M., Theissen, C. A., et al. 2022, arXiv e-prints, arXiv:2212.04557

[239] Hodgson, R. 1859, MNRAS, 20, 15

[240] Holman, M., Touma, J., & Tremaine, S. 1997, Nature, 386, 254

[241] Howard, W. S., Corbett, H., Law, N. M., et al. 2019, ApJ, 881, 9

[242] Howard, W. S., & MacGregor, M. A. 2022, ApJ, 926, 204

[243] Howard, W. S., Corbett, H., Law, N. M., et al. 2020, ApJ, 895, 140

[244] Howarth, I. D. 2011, MNRAS, 418, 1165

[245] Howell, S. B., Sobeck, C., Haas, M., et al. 2014, PASP, 126, 398

[246] Huang, X., Gamache, R., Freedman, R., Schwenke, D., & Lee, T. 2014, Journal of Quantitative Spectroscopy & Radiative Transfer, 147, 134

[247] Hudson, H. S., Acton, L. W., & Freeland, S. L. 1996, ApJ, 470, 629

[248] Hurley, J., & Tout, C. A. 1998, Monthly Notices of the RAS, 300, 977

[249] Husser, T. O., Wende-von Berg, S., Dreizler, S., et al. 2013, A&A, 553, A6

[250] Ida, S., & Lin, D. N. C. 2008, ApJ, 673, 487

[251] Ilin, E., Schmidt, S. J., Davenport, J. R. A., & Strassmeier, K. G. 2019, A&A, 622, A133

[252] —. 2019, A&A, 622, A133

[253] Ilin, E., Schmidt, S. J., Poppenhäger, K., et al. 2021, A&A, 645, A42

[254] Iyer, A. R., & Line, M. R. 2020, ApJ, 889, 78

[255] Jakosky, B. M., Pepin, R. O., Johnson, R. E., & Fox, J. L. 1994, Icarus, 111, 271

[256] Jenkins, J. M., Caldwell, D. A., Chandrasekaran, H., et al. 2010, ApJ, 713, L87

[257] Jenkins, J. M., Twicken, J. D., McCauliff, S., et al. 2016, in Society of Photo-Optical Instrumentation Engineers (SPIE) Conference Series, Vol. 9913, Software and Cyberinfrastructure for Astronomy IV, 99133E

[258] Johnson, L. J., Norris, C. N., Unruh, Y. C., et al. 2021, arXiv e-prints, arXiv:2104.11544

[259] Johnson, M. C., Cochran, W. D., Addison, B. C., Tinney, C. G., & Wright, D. J. 2017, AJ, 154, 137

[260] Johnson, M. C., Cochran, W. D., Albrecht, S., et al. 2014, ApJ, 790, 30

[261] Johnstone, C. P., Güdel, M., Stökl, A., et al. 2015, ApJ, 815, L12

[262] Jones, J., White, R. J., Boyajian, T., et al. 2015, ApJ, 813, 58

[263] Kalas, P., Liu, M. C., & Matthews, B. C. 2004, Science, 303, 1990

[264] Kavanagh, R. D., Vidotto, A. A., Klein, B., et al. 2021, MNRAS, 504, 1511

[265] Kay, C., Opher, M., & Kornbleuth, M. 2016, ApJ, 826, 195

[266] Kempton, E. M. R., Lupu, R., Owusu-Asare, A., Slough, P., & Cale, B. 2017, PASP, 129, 044402

[267] Kempton, E. M. R., Bean, J. L., Louie, D. R., et al. 2018, PASP, 130, 114401

[268] Kenyon, S. J., & Hartmann, L. 1995, ApJS, 101, 117

[269] Kingma, D. P., & Ba, J. 2014, ArXiv e-prints, arXiv:1412.6980

[270] Kipping, D. M. 2013, Monthly Notices of the Royal Astronomical Society, 435, 2152

[271] Kirk, J., López-Morales, M., Wheatley, P. J., et al. 2019, AJ, 158, 144

[272] Klein, B., Donati, J.-F., Moutou, C., et al. 2021, MNRAS, 502, 188

[273] Kochukhov, O., & Reiners, A. 2020, ApJ, 902, 43

[274] Komacek, T. D., & Showman, A. P. 2016, ApJ, 821, 16

[275] Kostov, V. B., Schlieder, J. E., Barclay, T., et al. 2019, AJ, 158, 32

[276] Kotoneva, E., Flynn, C., & Jimenez, R. 2002, Monthly Notices of the RAS, 335, 1147

[277] Kowalski, A. F., Hawley, S. L., Wisniewski, J. P., et al. 2013, ApJS, 207, 15

[278] Kozai, Y. 1962, AJ, 67, 591

[279] Kramida, A., Ralchenko, Y., Reader, J., & NIST ASD Team. 2021, doi:https://doi.org/10.18434/T4W30F

[280] Kramida, A., Yu. Ralchenko, Reader, J., & and NIST ASD Team. 2018, NIST Atomic Spectra Database (ver. 5.6.1), [Online]. Available: `https://physics.nist.gov/asd` [2019, February 6]. National Institute of Standards and Technology, Gaithersburg, MD.

[281] Kreidberg, L. 2015, Publications of the Astronomical Society of the Pacific, 127, 1161

[282] Kreidberg, L., Bean, J. L., Désert, J.-M., et al. 2014, ApJ, 793, L27

[283] Kretzschmar, M. 2011, A&A, 530, A84

[284] Krizhevsky, A., Sutskever, I., & Hinton, G. E. 2012, in Advances in neural information processing systems, 1097–1105

[285] Kubyshkina, D., Fossati, L., Erkaev, N. V., et al. 2018, ApJ, 866, L18

[286] Kupka, F. G., Ryabchikova, T. A., Piskunov, N. E., Stempels, H. C., & Weiss, W. W. 2000, Baltic Astronomy, 9, 590

[287] Kurucz, R., & Bell, B. 1995, Atomic Line Data (R.L. Kurucz and B. Bell) Kurucz CD-ROM No. 23. Cambridge, 23

[288] Kurucz, R. L. 1979, ApJS, 40, 1

[289] —. 1993, SYNTHE spectrum synthesis programs and line data

[290] Laginja, I., & Wakeford, H. 2020, The Journal of Open Source Software, 5, 2281

[291] Lai, D. 2014, MNRAS, 440, 3532

[292] Lambrechts, M., & Johansen, A. 2012, A&A, 544, A32

[293] Lammer, H., Selsis, F., Ribas, I., et al. 2003, ApJ, 598, L121

[294] Lammer, H., Stumptner, W., & Bauer, S. J. 1996, Geophys. Res. Lett., 23, 3353

[295] Lammer, H., Lichtenegger, H. I. M., Kulikov, Y. N., et al. 2007, Astrobiology, 7, 185

[296] Landi, E., Del Zanna, G., Young, P. R., Dere, K. P., & Mason, H. E. 2012, ApJ, 744, 99

[297] Lanza, A. F. 2012, A&A, 544, A23

[298] Lavvas, P., Koskinen, T., & Yelle, R. V. 2014, ApJ, 796, 15

[299] Leblanc, F., & Johnson, R. E. 2002, Journal of Geophysical Research (Planets), 107, 5010

[300] Lecavelier Des Etangs, A., Pont, F., Vidal-Madjar, A., & Sing, D. 2008, A&A, 481, L83

[301] —. 2008, A&A, 481, L83

[302] Lecavelier des Etangs, A., Sirothia, S. K., Gopal-Krishna, & Zarka, P. 2013, A&A, 552, A65

[303] Lecavelier Des Etangs, A., Ehrenreich, D., Vidal-Madjar, A., et al. 2010, A&A, 514, A72

[304] Lecavelier des Etangs, A., Bourrier, V., Wheatley, P. J., et al. 2012, A&A, 543, L4

[305] LeCun, Y., Bengio, Y., & Hinton, G. 2015, Nature, 521, 436

[306] Li, G., Gordon, I. E., Rothman, L. S., et al. 2015, ApJS, 216, 15

[307] Lidov, M. L. 1962, Planet. Space Sci., 9, 719

[308] Lin, C. L., Ip, W. H., Hou, W. C., Huang, L. C., & Chang, H. Y. 2019, The Astrophysical Journal, 873, 97

[309] Lin, H.-T., Chen, W.-P., Liu, J., et al. 2022, AJ, 163, 164

[310] Lin, M., Chen, Q., & Yan, S. 2013, arXiv e-prints, arXiv:1312.4400

[311] Line, M. R., & Parmentier, V. 2016, ApJ, 820, 78

[312] Line, M. R., Wolf, A. S., Zhang, X., et al. 2013, ApJ, 775, 137

[313] Linsky, J. L., Yang, H., France, K., et al. 2010, ApJ, 717, 1291

[314] Liu, M. C. 2004, Science, 305, 1442

[315] Liu, M. C., Matthews, B. C., Williams, J. P., & Kalas, P. G. 2004, ApJ, 608, 526

[316] Livingston, J. H., Endl, M., Dai, F., et al. 2018, AJ, 156, 78

[317] Lodders, K. 2003, ApJ, 591, 1220

[318] Lodders, K., Palme, H., & Gail, H. P. 2009, Landolt Börnstein, 4B, 712

[319] Lomb, N. R. 1976, Ap&SS, 39, 447

[320] Longcope, D. W., Fisher, G. H., & Pevtsov, A. A. 1998, ApJ, 507, 417

[321] Lopez, E. D., & Fortney, J. J. 2013, ApJ, 776, 2

[322] —. 2014, ApJ, 792, 1

[323] Lothringer, J. D., & Barman, T. S. 2020, AJ, 159, 289

[324] Lothringer, J. D., Rustamkulov, Z., Sing, D. K., et al. 2021, ApJ, 914, 12

[325] Loyd, R. O. P., Shkolnik, E. L., Schneider, A. C., et al. 2018, ApJ, 867, 70

[326] —. 2020, ApJ, 890, 23

[327] Loyd, R. O. P., France, K., Youngblood, A., et al. 2016, ApJ, 824, 102

[328] —. 2018, ApJ, 867, 71

[329] Lu, E. T., & Hamilton, R. J. 1991, ApJ, 380, L89

[330] Luger, R., Agol, E., Foreman-Mackey, D., et al. 2019, AJ, 157, 64

[331] Luger, R., Foreman-Mackey, D., Hedges, C., & Hogg, D. W. 2021, arXiv e-prints, arXiv:2102.00007

[332] Luger, R., Sestovic, M., Kruse, E., et al. 2017, Nature Astronomy, 1, 0129

[333] Luhman, K. L. 2018, AJ, 156, 271

[334] Luhmann, J. G., & Kozyra, J. U. 1991, J. Geophys. Res., 96, 5457

[335] Lundin, R., Lammer, H., & Ribas, I. 2007, Space Sci. Rev., 129, 245

[336] Lurie, J. C., Davenport, J. R. A., Hawley, S. L., et al. 2015, ApJ, 800, 95

[337] MacDonald, R. J., & Madhusudhan, N. 2017, MNRAS, 469, 1979

[338] MacGregor, M. A., Weinberger, A. J., Loyd, R. O. P., et al. 2021, ApJ, 911, L25

[339] Maciejewski, G., Dimitrov, D., Mancini, L., et al. 2016, J Acta Astronomica, 66, 55

[340] MacNeice, P., Pallavicini, R., Mason, H. E., et al. 1985, Sol. Phys., 99, 167

[341] Madhusudhan, N., Amin, M. A., & Kennedy, G. M. 2014, ApJ, 794, L12

[342] Maehara, H., Notsu, Y., Notsu, S., et al. 2017, PASJ, 69, 41

[343] Maehara, H., Shibayama, T., Notsu, Y., et al. 2015, Earth, Planets and Space, 67, 59

[344] Maehara, H., Notsu, Y., Namekata, K., et al. 2021, PASJ, 73, 44

[345] Mai, C., & Line, M. R. 2019, ApJ, 883, 144

[346] Malik, M., Kitzmann, D., Mendonça, J. M., et al. 2019, AJ, 157, 170

[347] Malik, M., Grosheintz, L., Mendonça, J. M., et al. 2017, AJ, 153, 56

[348] Mamajek, E. E., & Bell, C. P. M. 2014, MNRAS, 445, 2169

[349] Mancini, L., Esposito, M., Covino, E., et al. 2018, A&A, 613, A41

[350] Mandel, K., & Agol, E. 2002, ApJ, 580, L171

[351] Mann, A. W., Newton, E. R., Rizzuto, A. C., et al. 2016, The Astronomical Journal, 152, 61

[352] Mann, A. W., Johnson, M. C., Vanderburg, A., et al. 2020, AJ, 160, 179

[353] Mann, A. W., Wood, M. L., Schmidt, S. P., et al. 2022, AJ, 163, 156

[354] —. 2022, AJ, 163, 156

[355] Mansfield, M., Bean, J. L., Oklopčić, A., et al. 2018, ApJ, 868, L34

[356] Mansfield, M., Line, M. R., Bean, J. L., et al. 2021, Nature Astronomy, 5, 1224

[357] Maran, S. P., Robinson, R. D., Shore, S. N., et al. 1994, ApJ, 421, 800

[358] Marley, M. S., & McKay, C. P. 1999, Icarus, 138, 268

[359] Martioli, E., Hébrard, G., Correia, A. C. M., Laskar, J., & Lecavelier des Etangs, A. 2021, A&A, 649, A177

[360] Martioli, E., Teeple, D., Manset, N., et al. 2012, in Society of Photo-Optical Instrumentation Engineers (SPIE) Conference Series, Vol. 8451, Software and Cyberinfrastructure for Astronomy II, ed. N. M. Radziwill & G. Chiozzi, 84512B

[361] Martioli, E., Hébrard, G., Moutou, C., et al. 2020, A&A, 641, L1

[362] Mason, J. P., Attie, R., Arge, C. N., Thompson, B., & Woods, T. N. 2019, ApJS, 244, 13

[363] Matsuo, T., Greene, T. P., Johnson, R. R., et al. 2019, PASP, 131, 124502

[364] McClymont, A. N., & Canfield, R. C. 1986, ApJ, 305, 936

[365] McKay, C. P., Pollack, J. B., & Courtin, R. 1989, Icarus, 80, 23

[366] McQuillan, A., Mazeh, T., & Aigrain, S. 2014, ApJS, 211, 24

[367] McTiernan, J. M., Caspi, A., & Warren, H. P. 2019, ApJ, 881, 161

[368] Metchev, S. A., Eisner, J. A., Hillenbrand, L. A., & Wolf, S. 2005, ApJ, 622, 451

[369] Miller-Ricci, E., Seager, S., & Sasselov, D. 2009, ApJ, 690, 1056

[370] Min, M., Ormel, C. W., Chubb, K., Helling, C., & Kawashima, Y. 2020, A&A, 642, A28

[371] Moffatt, H. K. 1978, Magnetic field generation in electrically conducting fluids

[372] Moldovan, R., Matthews, J. M., Gladman, B., Bottke, W. F., & Vokrouhlický, D. 2010, ApJ, 716, 315

[373] Monsignori Fossi, B. C., & Landini, M. 1994, A&A, 284, 900

[374] Monsignori Fossi, B. C., Landini, M., Del Zanna, G., & Bowyer, S. 1996, ApJ, 466, 427

[375] Montet, B. T., Tovar, G., & Foreman-Mackey, D. 2017, ApJ, 851, 116

[376] Montet, B. T., Johnson, J. A., Muirhead, P. S., et al. 2015, ApJ, 800, 134

[377] Montet, B. T., Feinstein, A. D., Luger, R., et al. 2020, AJ, 159, 112

[378] Moore, T. E., Lundin, R., Alcayde, D., et al. 1999, Space Sci. Rev., 88, 7

[379] Moos, H. W., Cash, W. C., Cowie, L. L., et al. 2000, ApJ, 538, L1

[380] Mordasini, C., van Boekel, R., Mollière, P., Henning, T., & Benneke, B. 2016, ApJ, 832, 41

[381] Morello, G., Claret, A., Martin-Lagarde, M., et al. 2020, AJ, 159, 75

[382] Morris, B. M. 2020, arXiv e-prints, arXiv:2002.09135

[383] Mukherjee, S., Batalha, N. E., Fortney, J. J., & Marley, M. S. 2022, arXiv e-prints, arXiv:2208.07836

[384] Mullan, D. J., & Bais, H. P. 2018, ApJ, 865, 101

[385] Murphy, M. T., Udem, T., Holzwarth, R., et al. 2007, MNRAS, 380, 839

[386] Murphy, S. J., & Lawson, W. A. 2015, MNRAS, 447, 1267

[387] Murphy, S. J., Lawson, W. A., & Bessell, M. S. 2013, MNRAS, 435, 1325

[388] Nagel, K., & Herrmann, H. J. 1993, Physica A Statistical Mechanics and its Applications, 199, 254

[389] Naoz, S., Farr, W. M., Lithwick, Y., Rasio, F. A., & Teyssandier, J. 2011, Nature, 473, 187

[390] Narang, M., Manoj, P., Ishwara Chandra, C. H., et al. 2021, MNRAS, 500, 4818

[391] Neff, J. E., O'Neal, D., & Saar, S. H. 1995, ApJ, 452, 879

[392] Nelson, R. P., Papaloizou, J. C. B., Masset, F., & Kley, W. 2000, MNRAS, 318, 18

[393] Neupert, W. M. 1968, ApJ, 153, L59

[394] Neves Ribeiro do Amaral, L., Barnes, R., Segura, A., & Luger, R. 2022, arXiv e-prints, arXiv:2203.10127

[395] Newman, M. E. J. 2005, Contemporary Physics, 46, 323

[396] Newman, M. E. J., & Sneppen, K. 1996, Phys. Rev. E, 54, 6226

[397] Newton, E. R., Mann, A. W., Tofflemire, B. M., et al. 2019, ApJ, 880, L17

[398] Newville, M., Otten, R., Nelson, A., et al. 2021, lmfit/lmfit-py 1.0.2, doi:10.5281/zenodo.4516651

[399] Niculescu-Mizil, A., & Caruana, R. 2005, in ICML '05

[400] Nikolov, N., Sing, D. K., Gibson, N. P., et al. 2016, ApJ, 832, 191

[401] Notsu, Y., Shibayama, T., Maehara, H., et al. 2013, ApJ, 771, 127

[402] Notsu, Y., Maehara, H., Honda, S., et al. 2019, ApJ, 876, 58

[403] Noyes, R. W., Hartmann, L. W., Baliunas, S. L., Duncan, D. K., & Vaughan, A. H. 1984, ApJ, 279, 763

[404] Öberg, K. I., Murray-Clay, R., & Bergin, E. A. 2011, ApJ, 743, L16

[405] Oh, S., Price-Whelan, A. M., Hogg, D. W., Morton, T. D., & Spergel, D. N. 2017, AJ, 153, 257

[406] Ohno, K., & Kawashima, Y. 2020, ApJ, 895, L47

[407] Oklopčić, A., & Hirata, C. M. 2018, ApJ, 855, L11

[408] Olami, Z., Feder, H. J. S., & Christensen, K. 1992, Phys. Rev. Lett., 68, 1244

[409] Orrall, F. Q., & Zirker, J. B. 1976, ApJ, 208, 618

[410] Osten, R. A., Crosley, M. K., Gudel, M., et al. 2018, arXiv e-prints, arXiv:1803.05345

[411] Osten, R. A., Hawley, S. L., Allred, J. C., Johns-Krull, C. M., & Roark, C. 2005, ApJ, 621, 398

[412] Owen, J. E. 2019, Annual Review of Earth and Planetary Sciences, 47, 67

[413] Owen, J. E., & Campos Estrada, B. 2020, MNRAS, 491, 5287

[414] Owen, J. E., & Wu, Y. 2013, ApJ, 775, 105

[415] —. 2017, ApJ, 847, 29

[416] Pagano, I., Linsky, J. L., Carkner, L., et al. 2000, ApJ, 532, 497

[417] Pallavicini, R., Cutispoto, G., Randich, S., & Gratton, R. 1993, A&A, 267, 145

[418] Pallavicini, R., Randich, S., & Giampapa, M. S. 1992, A&A, 253, 185

[419] Palle, E., Oshagh, M., Casasayas-Barris, N., et al. 2020, A&A, 643, A25

[420] Paragas, K., Vissapragada, S., Knutson, H. A., et al. 2021, ApJ, 909, L10

[421] Parker, E. N. 1955, ApJ, 122, 293

[422] —. 1958, ApJ, 128, 664

[423] —. 1988, ApJ, 330, 474

[424] —. 1988, ApJ, 330, 474

[425] —. 1989, Sol. Phys., 121, 271

[426] Parmentier, V., Fortney, J. J., Showman, A. P., Morley, C., & Marley, M. S. 2016, ApJ, 828, 22

[427] Paudel, R. R., Gizis, J. E., Mullan, D. J., et al. 2018, ApJ, 861, 76

[428] —. 2019, MNRAS, 486, 1438

[429] Pearson, K. A., Palafox, L., & Griffith, C. A. 2018, MNRAS, 474, 478

[430] Pecaut, M. J., & Mamajek, E. E. 2013, ApJS, 208, 9

[431] —. 2016, MNRAS, 461, 794

[432] Perez-Becker, D., & Showman, A. P. 2013, ApJ, 776, 134

[433] Perri, F., & Cameron, A. G. W. 1974, Icarus, 22, 416

[434] Pineda, J. S., Bottom, M., & Johnson, J. A. 2013, ApJ, 767, 28

[435] Pinhas, A., Madhusudhan, N., Gandhi, S., & MacDonald, R. 2019, MNRAS, 482, 1485

[436] Piskorz, D., Buzard, C., Line, M. R., et al. 2018, AJ, 156, 133

[437] Piso, A.-M. A., Youdin, A. N., & Murray-Clay, R. A. 2015, ApJ, 800, 82

[438] Platais, I., Kozhurina-Platais, V., & van Leeuwen, F. 1998, AJ, 116, 2423

[439] Plavchan, P., Werner, M. W., Chen, C. H., et al. 2009, ApJ, 698, 1068

[440] Plavchan, P., Barclay, T., Gagné, J., et al. 2020, Nature, 582, 497

[441] Pöhnl, H., & Paunzen, E. 2010, A&A, 514, A81

[442] Poland, A. I., Orwig, L. E., Mariska, J. T., Auer, L. H., & Nakatsuka, R. 1984, ApJ, 280, 457

[443] Polanski, A. S., Crossfield, I. J. M., Howard, A. W., Isaacson, H., & Rice, M. 2022, Research Notes of the American Astronomical Society, 6, 155

[444] Pollack, J. B., Hubickyj, O., Bodenheimer, P., et al. 1996, Icarus, 124, 62

[445] Polyansky, O. L., Kyuberis, A. A., Zobov, N. F., et al. 2018, MNRAS, 480, 2597

[446] Poppenhaeger, K. 2022, MNRAS, 512, 1751

[447] Poppenhaeger, K., Ketzer, L., & Mallonn, M. 2021, MNRAS, 500, 4560

[448] Porter, J. G., Fontenla, J. M., & Simnett, G. M. 1995, ApJ, 438, 472

[449] Powell, D., Louden, T., Kreidberg, L., et al. 2019, ApJ, 887, 170

[450] Preibisch, T., Brown, A. G. A., Bridges, T., Guenther, E., & Zinnecker, H. 2002, AJ, 124, 404

[451] Preibisch, T., Guenther, E., & Zinnecker, H. 2001, AJ, 121, 1040

[452] Preibisch, T., Kim, Y.-C., Favata, F., et al. 2005, ApJS, 160, 401

[453] Price-Whelan, A. M., Sipőcz, B. M., Günther, H. M., et al. 2018, AJ, 156, 123

[454] Quin, D. A., Doyle, J. G., Butler, C. J., Byrne, P. B., & Swank, J. H. 1993, A&A, 272, 477

[455] Rackham, B. V., Apai, D., & Giampapa, M. S. 2018, ApJ, 853, 122

[456] Rackham, B. V., Espinoza, N., Berdyugina, S. V., et al. 2022, arXiv e-prints, arXiv:2201.09905

[457] Radica, M., Albert, L., Taylor, J., et al. 2022, PASP, 134, 104502

[458] Raetz, S., Stelzer, B., Damasso, M., & Scholz, A. 2020, Astronomy and Astrophysics, 637, A22

[459] Ranjan, S., Wordsworth, R., & Sasselov, D. D. 2017, ApJ, 843, 110

[460] Redfield, S., Linsky, J. L., Ake, T. B., et al. 2002, ApJ, 581, 626

[461] Reinhold, T., & Gizon, L. 2015, A&A, 583, A65

[462] Ribeiro, T. L., Copelli, M., Caixeta, F., et al. 2010, PLoS ONE, 5, e14129

[463] Richard, C., Gordon, I. E., Rothman, L. S., et al. 2012, J. Quant. Spec. Radiat. Transf., 113, 1276

[464] Richey-Yowell, T., Shkolnik, E. L., Schneider, A. C., et al. 2019, The Astrophysical Journal, 872, 17

[465] Ricker, G. R., Winn, J. N., Vanderspek, R., et al. 2014, in Proc. SPIE, Vol. 9143, Space Telescopes and Instrumentation 2014: Optical, Infrared, and Millimeter Wave, 914320

[466] Ricker, G. R., Winn, J. N., Vanderspek, R., et al. 2015, Journal of Astronomical Telescopes, Instruments, and Systems, 1, 014003

[467] Riedel, A. R., Alam, M. K., Rice, E. L., Cruz, K. L., & Henry, T. J. 2017, ApJ, 840, 87

[468] Rimmer, P. B., Xu, J., Thompson, S. J., et al. 2018, Science Advances, 4, eaar3302

[469] Rizzuto, A. C., Newton, E. R., Mann, A. W., et al. 2020, AJ, 160, 33

[470] Robertson, P., Bender, C., Mahadevan, S., Roy, A., & Ramsey, L. W. 2016, ApJ, 832, 112

[471] Robinson, P. A. 1994, Phys. Rev. E, 49, 1984

[472] Robinson, R. D., Carpenter, K. G., Woodgate, B. E., & Maran, S. P. 1993, ApJ, 414, 872

[473] Rockcliffe, K. E., Newton, E. R., Youngblood, A., et al. 2021, AJ, 162, 116

[474] Roettenbacher, R. M., & Vida, K. 2018, ApJ, 868, 3

[475] Roettenbacher, R. M., Monnier, J. D., Korhonen, H., et al. 2016, Nature, 533, 217

[476] Rogers, J. G., Gupta, A., Owen, J. E., & Schlichting, H. E. 2021, MNRAS, 508, 5886

[477] Rogers, J. G., & Owen, J. E. 2021, MNRAS, 503, 1526

[478] Rogers, L. A. 2015, ApJ, 801, 41

[479] Roman, M. T., Kempton, E. M. R., Rauscher, E., et al. 2021, ApJ, 908, 101

[480] Rooney, C. M., Batalha, N. E., Gao, P., & Marley, M. S. 2022, ApJ, 925, 33

[481] Rosenblatt, F. 1961, Principles of neurodynamics. perceptrons and the theory of brain mechanisms, Tech. rep., Cornell Aeronautical Lab Inc Buffalo NY

[482] Rothman, L., Gordon, I., Barbe, A., et al. 2009, Journal of Quantitative Spectroscopy and Radiative Transfer, 110, 533, hITRAN

[483] Rothman, L. S., Gordon, I. E., Barber, R. J., et al. 2010, J. Quant. Spec. Radiat. Transf., 111, 2139

[484] Rustamkulov, Z., Sing, D. K., Liu, R., & Wang, A. 2022, ApJ, 928, L7

[485] Rustamkulov, Z., Sing, D. K., Mukherjee, S., et al. 2023, Nature, 614, 659–663

[486] Ryabchikova, T., Piskunov, N., Kurucz, R. L., et al. 2015, Phys. Scr, 90, 054005

[487] Sahnow, D. J., Moos, H. W., Ake, T. B., et al. 2000, ApJ, 538, L7

[488] Salvatier, J., Wiecki, T. V., & Fonnesbeck, C. 2016, PeerJ Computer Science, 2, e55

[489] Scargle, J. D. 1982, ApJ, 263, 835

[490] Schlawin, E., Leisenring, J., Misselt, K., et al. 2020, AJ, 160, 231

[491] Schlawin, E., Leisenring, J., McElwain, M. W., et al. 2021, AJ, 161, 115

[492] Schmelz, J. T., Reames, D. V., von Steiger, R., & Basu, S. 2012, ApJ, 755, 33

[493] Schneider, A. C., & Shkolnik, E. L. 2018, AJ, 155, 122

[494] Schneider, A. C., Shkolnik, E. L., Allers, K. N., et al. 2019, AJ, 157, 234

[495] Schneider, A. D., & Bitsch, B. 2021, A&A, 654, A72

[496] Schrijver, C. J., & Title, A. M. 2011, Journal of Geophysical Research (Space Physics), 116, A04108

[497] Schwabe, M. 1844, Astronomische Nachrichten, 21, 233

[498] Scoggins, M. T., Davenport, J. R. A., & Covey, K. R. 2019, Research Notes of the AAS, 3, 137

[499] Seager, S., & Sasselov, D. D. 2000, ApJ, 537, 916

[500] Segura, A., Walkowicz, L. M., Meadows, V., Kasting, J., & Hawley, S. 2010, Astrobiology, 10, 751

[501] Seligman, D., Petrie, G. J. D., & Komm, R. 2014, ApJ, 795, 113

[502] Seligman, D. Z., Becker, J., Adams, F. C., Feinstein, A. D., & Rogers, L. A. 2022, arXiv e-prints, arXiv:2204.12653

[503] Seligman, D. Z., Rogers, L. A., Feinstein, A. D., et al. 2022, ApJ, 929, 54

[504] Shallue, C. J., & Vanderburg, A. 2018, AJ, 155, 94

[505] Shibata, K. 1996, Advances in Space Research, 17, 9

[506] Shibata, S., Helled, R., & Ikoma, M. 2020, A&A, 633, A33

[507] Shibayama, T., Maehara, H., Notsu, S., et al. 2013, The Astrophysical Journals, 209, 5

[508] Shkolnik, E., Bohlender, D. A., Walker, G. A. H., & Collier Cameron, A. 2008, ApJ, 676, 628

[509] Shkolnik, E. L., Allers, K. N., Kraus, A. L., Liu, M. C., & Flagg, L. 2017, AJ, 154, 69

[510] Shkolnik, E. L., & Barman, T. S. 2014, AJ, 148, 64

[511] Sing, D. K. 2010, A&A, 510, A21

[512] Sing, D. K., Fortney, J. J., Nikolov, N., et al. 2016, Nature, 529, 59

[513] Sinukoff, E., Howard, A. W., Petigura, E. A., et al. 2016, ApJ, 827, 78

[514] Smith, K., Pestalozzi, M., Güdel, M., Conway, J., & Benz, A. O. 2003, A&A, 406, 957

[515] Soderblom, D. R. 2010, ARA&A, 48, 581

[516] Soderblom, D. R., Jones, B. F., Balachandran, S., et al. 1993, AJ, 106, 1059

[517] Sornette, A., & Sornette, D. 1989, EPL (Europhysics Letters), 9, 197

[518] Spake, J. J., Sing, D. K., Evans, T. M., et al. 2018, Nature, 557, 68

[519] Spearman, C. 1907, The American journal of psychology, 161

[520] Srivastava, N., Hinton, G., Krizhevsky, A., Sutskever, I., & Salakhutdinov, R. 2014, Journal of Machine Learning Research, 15, 1929

[521] Stassun, K. G., Collins, K. A., & Gaudi, B. S. 2017, AJ, 153, 136

[522] Stassun, K. G., Oelkers, R. J., Pepper, J., et al. 2018, AJ, 156, 102

[523] Stauffer, J. R., Jones, B. F., Backman, D., et al. 2003, AJ, 126, 833

[524] Sterling, A. C., & Hudson, H. S. 1997, ApJ, 491, L55

[525] Stevenson, K. B., Lewis, N. K., Bean, J. L., et al. 2016, PASP, 128, 094401

[526] Stock, J. W., Kitzmann, D., Patzer, A. B. C., & Sedlmayr, E. 2018, MNRAS, 479, 865

[527] Strassmeier, K. G. 2009, A&A Rev., 17, 251

[528] Sturrock, P. A., Dixon, W. W., Klimchuk, J. A., & Antiochos, S. K. 1990, ApJ, 356, L31

[529] —. 1990, ApJ, 356, L31

[530] Sturrock, P. A., Kaufman, P., Moore, R. L., & Smith, D. F. 1984, Sol. Phys., 94, 341

[531] —. 1984, Sol. Phys., 94, 341

[532] Tanoglidis, D., Ćiprijanović, A., & Drlica-Wagner, A. 2021, Astronomy and Computing, 35, 100469

[533] Tashkun, S., & Perevalov, V. 2011, Journal of Quantitative Spectroscopy and Radiative Transfer, 112, 1403

[534] Teal, D. J., Kempton, E. M. R., Bastelberger, S., Youngblood, A., & Arney, G. 2022, ApJ, 927, 90

[535] Teeple, D. 2014, OPERA: Open-source Pipeline for Espadons Reduction and Analysis, ascl:1411.004

[536] Tenenbaum, P., & Jenkins, J. M. 2018

[537] The JWST Transiting Exoplanet Community Early Release Science Team, Ahrer, E.-M., Alderson, L., et al. 2022, arXiv e-prints, arXiv:2208.11692

[538] —. 2023, Nature, 649–652

[539] Tian, F., Kasting, J. F., Liu, H.-L., & Roble, R. G. 2008, Journal of Geophysical Research (Planets), 113, E05008

[540] Tilley, M. A., Harnett, E. M., & Winglee, R. M. 2016, ApJ, 827, 77

[541] Tilley, M. A., Segura, A., Meadows, V., Hawley, S., & Davenport, J. 2019, Astrobiology, 19, 64

[542] Tovar Mendoza, G., Davenport, J. R. A., Agol, E., Jackman, J. A. G., & Hawley, S. L. 2022, arXiv e-prints, arXiv:2205.05706

[543] Tremblin, P., Amundsen, D. S., Mourier, P., et al. 2015, ApJ, 804, L17

[544] Tsai, S.-M., Lee, E. K. H., Powell, D., et al. 2023, arXiv e-prints, arXiv:2211.10490

[545] Tsiaras, A., Waldmann, I., Rocchetto, M., et al. 2016, ascl:1612.018

[546] Tsiaras, A., Waldmann, I. P., Rocchetto, M., et al. 2016, ApJ, 832, 202

[547] Tsiaras, A., Waldmann, I. P., Zingales, T., et al. 2018, AJ, 155, 156

[548] Tu, Z.-L., Yang, M., Zhang, Z. J., & Wang, F. Y. 2020, The Astrophysical Journal, 890, 46

[549] Turcotte, D. L. 1999, Reports on Progress in Physics, 62, 1377

[550] Turcotte, D. L., Malamud, B. D., Guzzetti, F., & Reichenbach, P. 2002, Proceedings of the National Academy of Sciences, 99, 2530

[551] van Dokkum, P. G. 2001, PASP, 113, 1420

[552] Van Eylen, V., Agentoft, C., Lundkvist, M. S., et al. 2018, MNRAS, 479, 4786

[553] Vanderburg, A., Latham, D. W., Buchhave, L. A., et al. 2016, ApJS, 222, 14

[554] Vanninathan, K., Veronig, A. M., Dissauer, K., & Temmer, M. 2018, ApJ, 857, 62

[555] Vehtari, A., Gelman, A., Simpson, D., Carpenter, B., & Bürkner, P.-C. 2019, arXiv e-prints, arXiv:1903.08008

[556] Venot, O., Rocchetto, M., Carl, S., Roshni Hashim, A., & Decin, L. 2016, ApJ, 830, 77

[557] Veronig, A. M., Odert, P., Leitzinger, M., et al. 2021, Nature Astronomy, 5, 697

[558] Veronig, A. M., Rybák, J., Gömöry, P., et al. 2010, ApJ, 719, 655

[559] Vida, K., Bódi, A., Szklenár, T., & Seli, B. 2021, Astronomy and Astrophysics, 652, A107

[560] Vida, K., Kővári, Z., Pál, A., Oláh, K., & Kriskovics, L. 2017, ApJ, 841, 124

[561] Vida, K., & Roettenbacher, R. M. 2018, A&A, 616, A163

[562] Vidal-Madjar, A., Lecavelier des Etangs, A., Désert, J. M., et al. 2003, Nature, 422, 143

[563] Vidal-Madjar, A., Désert, J. M., Lecavelier des Etangs, A., et al. 2004, ApJ, 604, L69

[564] Virtanen, P., Gommers, R., Burovski, E., et al. 2020, scipy/scipy: SciPy 1.5.3, Zenodo, doi:10.5281/zenodo.4100507

[565] Vissapragada, S., Stefánsson, G., Greklek-McKeon, M., et al. 2021, AJ, 162, 222

[566] Vogt, S. S., Penrod, G. D., & Hatzes, A. P. 1987, ApJ, 321, 496

[567] Volkov, A. N., Johnson, R. E., Tucker, O. J., & Erwin, J. T. 2011, ApJ, 729, L24

[568] Wakeford, H. R., Sing, D. K., Deming, D., et al. 2018, AJ, 155, 29

[569] Walkowicz, L. M., Basri, G., Batalha, N., et al. 2011, AJ, 141, 50

[570] Warren, H. P., Brooks, D. H., Ugarte-Urra, I., et al. 2018, ApJ, 854, 122

[571] Welbanks, L., & Madhusudhan, N. 2019, AJ, 157, 206

[572] —. 2021, ApJ, 913, 114

[573] Welbanks, L., Madhusudhan, N., Allard, N. F., et al. 2019, ApJ, 887, L20

[574] Wheatley, P. J., Collier Cameron, A., Harrington, J., et al. 2010, arXiv e-prints, arXiv:1004.0836

[575] Wichmann, R., Krautter, J., Schmitt, J. H. M. M., et al. 1996, A&A, 312, 439

[576] Wichmann, R., Torres, G., Melo, C. H. F., et al. 2000, A&A, 359, 181

[577] Wöhl, H. 1971, Sol. Phys., 16, 362

[578] Woitke, P., Helling, C., Hunter, G. H., et al. 2018, A&A, 614, A1

[579] Wolk, S. J., Pillitteri, I., Kashyap, V., et al. 2011, in Astronomical Society of the Pacific Conference Series, Vol. 448, 16th Cambridge Workshop on Cool Stars, Stellar Systems, and the Sun, ed. C. Johns-Krull, M. K. Browning, & A. A. West, 1317

[580] Wood, B. E., Müller, H.-R., Redfield, S., et al. 2021, ApJ, 915, 37

[581] Wood, M. L., Mann, A. W., Barber, M. G., et al. 2023, AJ, 165, 85

[582] Woodgate, B. E., Robinson, R. D., Carpenter, K. G., Maran, S. P., & Shore, S. N. 1992, ApJ, 397, L95

[583] Wright, J. T., Veras, D., Ford, E. B., et al. 2011, ApJ, 730, 93

[584] Wu, Y., Xiang, M., Zhao, G., et al. 2019, Monthly Notices of the RAS, 484, 5315

[585] Wyttenbach, A., Ehrenreich, D., Lovis, C., Udry, S., & Pepe, F. 2015, A&A, 577, A62

[586] Yang, H., & Liu, J. 2019, The Astrophysical Journals, 241, 29

[587] Youngblood, A., France, K., Loyd, R. O. P., et al. 2016, ApJ, 824, 101

[588] —. 2017, ApJ, 843, 31

[589] Yurchenko, S. N., Amundsen, D. S., Tennyson, J., & Waldmann, I. P. 2017, A&A, 605, A95

[590] Yurchenko, S. N., & Tennyson, J. 2014, MNRAS, 440, 1649

[591] Zellem, R. T., Swain, M. R., Roudier, G., et al. 2017, ApJ, 844, 27

[592] Zeng, L., Jacobsen, S. B., Sasselov, D. D., et al. 2019, Proceedings of the National Academy of Science, 116, 9723

[593] Zeng, Z., Qiu, J., Cao, W., & Judge, P. G. 2014, ApJ, 793, 87

[594] Zhang, M., Knutson, H. A., Dai, F., et al. 2023, AJ, 165, 62

[595] Zhang, M., Knutson, H. A., Wang, L., Dai, F., & Barragán, O. 2022, AJ, 163, 67

[596] Zhang, X. 2020, Research in Astronomy and Astrophysics, 20, 099

[597] Zhang, Y., Liu, J., & Zhang, H. 2008, Sol. Phys., 247, 39

[598] Zhou, G., Winn, J. N., Newton, E. R., et al. 2020, ApJ, 892, L21

[599] Zicher, N., Barragán, O., Klein, B., et al. 2022, MNRAS, 512, 3060

[600] Zuckerman, B. 2019, ApJ, 870, 27

[601] Zuckerman, B., Bessell, M. S., Song, I., & Kim, S. 2006, ApJ, 649, L115

[602] Zuckerman, B., Song, I., & Bessell, M. S. 2004, ApJ, 613, L65

REFERENCES

[1] Abadi, M., Agarwal, A., Barham, P., et al. 2016, ArXiv e-prints, arXiv:1603.04467

[2] Ackerman, A. S., & Marley, M. S. 2001, ApJ, 556, 872

[3] —. 2001, ApJ, 556, 872

[4] Addison, B., Wright, D. J., Wittenmyer, R. A., et al. 2019, PASP, 131, 115003

[5] Addison, B. C., Horner, J., Wittenmyer, R. A., et al. 2020, arXiv e-prints, arXiv:2006.13675

[6] Aggarwal, C. C. 2014, Data classification: algorithms and applications (CRC press)

[7] Ahrer, E.-M., Stevenson, K. B., Mansfield, M., et al. 2023, Nature, 614, 653–658

[8] Airapetian, V. S., Glocer, A., Gronoff, G., Hébrard, E., & Danchi, W. 2016, Nature Geoscience, 9, 452

[9] Airapetian, V. S., Barnes, R., Cohen, O., et al. 2020, International Journal of Astrobiology, 19, 136

[10] Albrecht, S., Winn, J. N., Marcy, G. W., et al. 2013, ApJ, 771, 11

[11] Alderson, L., Wakeford, H. R., Alam, M. K., et al. 2023, Nature, 614, 664–669

[12] Alfven, H. 1950, Cosmical electrodynamics

[13] Allard, N. F., Spiegelman, F., & Kielkopf, J. F. 2016, A&A, 589, A21

[14] Allard, N. F., Spiegelman, F., Leininger, T., & Molliere, P. 2019, A&A, 628, A120

[15] Allart, R., Bourrier, V., Lovis, C., et al. 2019, A&A, 623, A58

[16] Alvarado-Gómez, J. D., Drake, J. J., Moschou, S. P., et al. 2019, ApJ, 884, L13

[17] Alvarado-Gómez, J. D., Cohen, O., Drake, J. J., et al. 2022, ApJ, 928, 147

[18] Andrade, R. F. S., Schellnhuber, H. J., & Claussen, M. 1998, Physica A Statistical Mechanics and its Applications, 254, 557

[19] Ansdell, M., Ioannou, Y., Osborn, H. P., et al. 2018, ApJ, 869, L7

[20] Antonova, L. A., & Nusinov, A. A. 1998, Sol. Phys., 177, 197

[21] Arcangeli, J., Désert, J.-M., Line, M. R., et al. 2018, ApJ, 855, L30

[22] Arney, G., Domagal-Goldman, S. D., Meadows, V. S., et al. 2016, Astrobiology, 16, 873

[23] Arney, G. N., Meadows, V. S., Domagal-Goldman, S. D., et al. 2017, ApJ, 836, 49

[24] Aschwanden, M. J., & Güdel, M. 2021, The Astrophysical Journal, 910, 41

[25] Aschwanden, M. J., Kosugi, T., Hanaoka, Y., Nishio, M., & Melrose, D. B. 1999, ApJ, 526, 1026

[26] Aschwanden, M. J., Tarbell, T. D., Nightingale, R. W., et al. 2000, ApJ, 535, 1047

[27] Astropy Collaboration, Robitaille, T. P., Tollerud, E. J., et al. 2013, A&A, 558, A33

[28] Audard, M., Güdel, M., & Guinan, E. F. 1999, ApJ, 513, L53

[29] Augereau, J. C., & Beust, H. 2006, A&A, 455, 987

[30] Azzam, A. A. A., Tennyson, J., Yurchenko, S. N., & Naumenko, O. V. 2016, MNRAS, 460, 4063

[31] Bak, P., Chen, K., & Creutz, M. 1989, Nature, 342, 780

[32] Bak, P., Chen, K., & Tang, C. 1990, Physics Letters A, 147, 297

[33] Bak, P., Paczuski, M., & Shubik, M. 1997, Physica A Statistical Mechanics and its Applications, 246, 430

[34] Bak, P., & Sneppen, K. 1993, Phys. Rev. Lett., 71, 4083

[35] Bak, P., & Tang, C. 1989, J. Geophys. Res., 94, 15,635

[36] Bak, P., Tang, C., & Wiesenfeld, K. 1988, Phys. Rev. A, 38, 364

[37] Barber, R. J., Strange, J. K., Hill, C., et al. 2014, MNRAS, 437, 1828

[38] Barber, R. J., Tennyson, J., Harris, G. J., & Tolchenov, R. N. 2006, MNRAS, 368, 1087

[39] Barman, T. S., Hauschildt, P. H., & Allard, F. 2001, ApJ, 556, 885

[40] Barnes, J. R., Haswell, C. A., Staab, D., & Anglada-Escudé, G. 2016, Monthly Notices of the RAS, 462, 1012

[41] Barnes, S. A. 2003, ApJ, 586, 464

[42] Barrado y Navascués, D., Stauffer, J. R., & Jayawardhana, R. 2004, ApJ, 614, 386

[43] Barstow, J. K. 2020, MNRAS, 497, 4183

[44] Batalha, N. E., Marley, M. S., Lewis, N. K., & Fortney, J. J. 2019, ApJ, 878, 70

[45] Bate, M. R., Lubow, S. H., Ogilvie, G. I., & Miller, K. A. 2003, MNRAS, 341, 213

[46] Bean, J. L., Raymond, S. N., & Owen, J. E. 2021, Journal of Geophysical Research (Planets), 126, e06639

[47] Bean, J. L., Stevenson, K. B., Batalha, N. M., et al. 2018, PASP, 130, 114402

[48] Bell, C. P. M., Mamajek, E. E., & Naylor, T. 2015, Monthly Notices of the RAS, 454, 593

[49] Bell, T. J., Ahrer, E.-M., Brande, J., et al. 2022, arXiv e-prints, arXiv:2207.03585

[50] Benatti, S., Nardiello, D., Malavolta, L., et al. 2019, A&A, 630, A81

[51] Benneke, B., & Seager, S. 2012, ApJ, 753, 100

[52] —. 2013, ApJ, 778, 153

[53] Benneke, B., Knutson, H. A., Lothringer, J., et al. 2019, Nature Astronomy, 3, 813

[54] Benneke, B., Wong, I., Piaulet, C., et al. 2019, The Astrophysical Journal Letters, 887, L14, publisher: American Astronomical Society

[55] Benz, A. O., & Güdel, M. 2010, ARA&A, 48, 241

[56] Berdyugina, S. V., Solanki, S. K., & Frutiger, C. 2003, A&A, 412, 513

[57] Berger, T. A., Huber, D., Gaidos, E., van Saders, J. L., & Weiss, L. M. 2020, AJ, 160, 108

[58] Biazzo, K., D'Orazi, V., Desidera, S., et al. 2022, A&A, 664, A161

[59] Birkby, J. L. 2018, arXiv e-prints, arXiv:1806.04617

[60] Bisikalo, D. V., Shematovich, V. I., Cherenkov, A. A., Fossati, L., & Möstl, C. 2018, ApJ, 869, 108

[61] Bohn, A. J., Kenworthy, M. A., Ginski, C., et al. 2020, ApJ, 898, L16

[62] Bohren, C. F., & Huffman, D. R. 1983, Absorption and scattering of light by small particles

[63] Bondar', N. I., & Katsova, M. M. 2020, Geomagnetism and Aeronomy, 60, 942

[64] Borucki, W. J., & Others. 2010, Science, 327, 977

[65] Borucki, W. J., Koch, D., Basri, G., et al. 2010, Science, 327, 977

[66] Boss, A. P. 1997, Science, 276, 1836

[67] Bouma, L. G., Curtis, J. L., Masuda, K., et al. 2022, AJ, 163, 121

[68] Bourrier, V., Lecavelier des Etangs, A., Ehrenreich, D., Tanaka, Y. A., & Vidotto, A. A. 2016, A&A, 591, A121

[69] Bourrier, V., Lecavelier des Etangs, A., Ehrenreich, D., et al. 2018, A&A, 620, A147

[70] Bourrier, V., Wheatley, P. J., Lecavelier des Etangs, A., et al. 2020, MNRAS, 493, 559

[71] Brandt, T. D., & Huang, C. X. 2015, ApJ, 807, 24

[72] Brogi, M., & Line, M. R. 2019, AJ, 157, 114

[73] Brueckner, G. E. 1976, Philosophical Transactions of the Royal Society of London Series A, 281, 443

[74] Buchner, J., Georgakakis, A., Nandra, K., et al. 2014, A&A, 564, A125

[75] Burke, C. J., Bryson, S. T., Mullally, F., et al. 2014, ApJS, 210, 19

[76] Butler, C. J., Rodono, M., & Linsky, J. L. 1986, in ESA Special Publication, Vol. 263, New Insights in Astrophysics. Eight Years of UV Astronomy with IUE, ed. E. J. Rolfe & R. Wilson, 229

[77] Cale, B. L., Reefe, M., Plavchan, P., et al. 2021, AJ, 162, 295

[78] Candelaresi, S., Hillier, A., Maehara, H., Brand enburg, A., & Shibata, K. 2014, ApJ, 792, 67

[79] Carleo, I., Desidera, S., Nardiello, D., et al. 2021, A&A, 645, A71

[80] Carrington, R. C. 1859, MNRAS, 20, 13

[81] Castelli, F., & Kurucz, R. L. 1994, A&A, 281, 817

[82] Catalano, S., Biazzo, K., Frasca, A., & Marilli, E. 2002, A&A, 394, 1009

[83] Cauley, P. W., Kuckein, C., Redfield, S., et al. 2018, AJ, 156, 189

[84] Cauley, P. W., Redfield, S., & Jensen, A. G. 2017, AJ, 153, 217

[85] Cauley, P. W., Shkolnik, E. L., Llama, J., Bourrier, V., & Moutou, C. 2018, AJ, 156, 262

[86] Cauley, P. W., Shkolnik, E. L., Llama, J., & Lanza, A. F. 2019, Nature Astronomy, 3, 1128

[87] Chabrier, G., & Baraffe, I. 1997, A&A, 327, 1039

[88] Chabrier, G., Johansen, A., Janson, M., & Rafikov, R. 2014, in Protostars and Planets VI, ed. H. Beuther, R. S. Klessen, C. P. Dullemond, & T. Henning, 619–642

[89] Chang, S. W., Byun, Y. I., & Hartman, J. D. 2015, ApJ, 814, 35

[90] Changeat, Q., Edwards, B., Al-Refaie, A. F., et al. 2022, ApJS, 260, 3

[91] Charbonneau, D., Brown, T. M., Latham, D. W., & Mayor, M. 2000, ApJ, 529, L45

[92] Charbonneau, D., Brown, T. M., Noyes, R. W., & Gilliland, R. L. 2002, ApJ, 568, 377

[93] Charbonneau, D., Berta, Z. K., Irwin, J., et al. 2009, Nature, 462, 891

[94] Charbonneau, P. 2010, Living Reviews in Solar Physics, 7, 3

[95] Chassefière, E., & Leblanc, F. 2004, Planet. Space Sci., 52, 1039

[96] Chassefière, E., Leblanc, F., & Langlais, B. 2007, Planet. Space Sci., 55, 343

[97] Chen, H., & Rogers, L. A. 2016, ApJ, 831, 180

[98] Chen, H., Zhan, Z., Youngblood, A., et al. 2021, Nature Astronomy, 5, 298

[99] Chen, J., & Kipping, D. 2017, ApJ, 834, 17

[100] Chene, A.-N., Padzer, J., Barrick, G., et al. 2014, in Society of Photo-Optical Instrumentation Engineers (SPIE) Conference Series, Vol. 9151, Advances in Optical and Mechanical Technologies for Telescopes and Instrumentation, ed. R. Navarro, C. R. Cunningham, & A. A. Barto, 915147

[101] Chollet, F., & others. 2018, Keras: The Python Deep Learning library, ascl:1806.022

[102] Claret, A. 2000, A&A, 363, 1081

[103] Cohen, O., Drake, J., Alvarado Gomez, J., et al. 2022, in Bulletin of the American Astronomical Society, Vol. 54, 102.280

[104] Cohen, O., Drake, J. J., Glocer, A., et al. 2014, ApJ, 790, 57

[105] Craig, M., Crawford, S., Seifert, M., et al. 2017, astropy/ccdproc: v1.3.0.post1, doi:10.5281/zenodo.1069648

[106] Cranmer, S. R., Wilner, D. J., & MacGregor, M. A. 2013, ApJ, 772, 149

[107] Cully, S. L., Siegmund, O. H. W., Vedder, P. W., & Vallerga, J. V. 1993, ApJ, 414, L49

[108] Curtis, J. L., Agüeros, M. A., Mamajek, E. E., Wright, J. T., & Cummings, J. D. 2019, AJ, 158, 77

[109] Czesla, S., Klocová, T., Khalafinejad, S., Wolter, U., & Schmitt, J. H. M. M. 2015, A&A, 582, A51

[110] Dahm, S. E. 2015, ApJ, 813, 108

[111] Darveau-Bernier, A., Albert, L., Talens, G. J., et al. 2022, PASP, 134, 094502

[112] Davenport, J. R. A. 2016, ApJ, 829, 23

[113] Davenport, J. R. A., Covey, K. R., Clarke, R. W., et al. 2019, ApJ, 871, 241

[114] Davenport, J. R. A., Hawley, S. L., Hebb, L., et al. 2014, ApJ, 797, 122

[115] David, T. J., Petigura, E. A., Luger, R., et al. 2019, ApJ, 885, L12

[116] David, T. J., Hillenbrand, L. A., Petigura, E. A., et al. 2016, Nature, 534, 658

[117] David, T. J., Cody, A. M., Hedges, C. L., et al. 2019, AJ, 158, 79

[118] Dawson, R. I., & Johnson, J. A. 2018, ARA&A, 56, 175

[119] de Arcangelis, L., Godano, C., Lippiello, E., & Nicodemi, M. 2006, Phys. Rev. Lett., 96, 051102

[120] de Gasperin, F., Lazio, T. J. W., & Knapp, M. 2020, A&A, 644, A157

[121] de Wit, J., & Seager, S. 2013, Science, 342, 1473

[122] Del Zanna, G., Dere, K. P., Young, P. R., & Landi, E. 2021, ApJ, 909, 38

[123] Del Zanna, G., Landini, M., & Mason, H. E. 2002, A&A, 385, 968

[124] Demory, B.-O., de Wit, J., Lewis, N., et al. 2013, ApJ, 776, L25

[125] Dendy, R. O., Helander, P., & Tagger, M. 1998, A&A, 337, 962

[126] Dennis, B. R., & Zarro, D. M. 1993, Sol. Phys., 146, 177

[127] Dere, K. P., Landi, E., Mason, H. E., Monsignori Fossi, B. C., & Young, P. R. 1997, A&AS, 125, 149

[128] Diamond-Lowe, H., Youngblood, A., Charbonneau, D., et al. 2021, AJ, 162, 10

[129] Diamond-Lowe, H., Kreidberg, L., Harman, C. E., et al. 2022, AJ, 164, 172

[130] Dissauer, K., Veronig, A. M., Temmer, M., Podladchikova, T., & Vanninathan, K. 2018, ApJ, 863, 169

[131] Distefano, E., Lanzafame, A. C., Lanza, A. F., Messina, S., & Spada, F. 2017, A&A, 606, A58

[132] Dobbie, P. D., Lodieu, N., & Sharp, R. G. 2010, MNRAS, 409, 1002

[133] Donati, J. F., & Landstreet, J. D. 2009, ARA&A, 47, 333

[134] Donati, J. F., Collier Cameron, A., Semel, M., et al. 2003, MNRAS, 345, 1145

[135] Dorman, B., Nelson, L. A., & Chau, W. Y. 1989, ApJ, 342, 1003

[136] Doyle, L., Ramsay, G., & Doyle, J. G. 2020, arXiv e-prints, arXiv:2003.14410

[137] Doyle, L., Ramsay, G., Doyle, J. G., & Wu, K. 2019, MNRAS, 489, 437

[138] Doyle, L., Ramsay, G., Doyle, J. G., Wu, K., & Scullion, E. 2018, MNRAS, 480, 2153

[139] Doyon, R., Hutchings, J. B., Beaulieu, M., et al. 2012, in Society of Photo-Optical Instrumentation Engineers (SPIE) Conference Series, Vol. 8442, Space Telescopes and Instrumentation 2012: Optical, Infrared, and Millimeter Wave, ed. M. C. Clampin, G. G. Fazio, H. A. MacEwen, & J. Oschmann, Jacobus M., 84422R

[140] Drake, J. J., Brown, A., Bowyer, S., et al. 1994, in Astronomical Society of the Pacific Conference Series, Vol. 64, Cool Stars, Stellar Systems, and the Sun, ed. J.-P. Caillault, 35

[141] Dressing, C. D., Charbonneau, D., Dumusque, X., et al. 2015, ApJ, 800, 135

[142] Drummond, B., Tremblin, P., Baraffe, I., et al. 2016, A&A, 594, A69

[143] Dubinin, E., Winningham, D., Fränz, M., et al. 2006, Icarus, 182, 343

[144] Dun, J., Kurokawa, H., Ishii, T. T., Liu, Y., & Zhang, H. 2007, ApJ, 657, 577

[145] Durisen, R. H., Boss, A. P., Mayer, L., et al. 2007, in Protostars and Planets V, ed. B. Reipurth, D. Jewitt, & K. Keil, 607

[146] Duvvuri, G. M., Sebastian Pineda, J., Berta-Thompson, Z. K., et al. 2021, ApJ, 913, 40

[147] Eistrup, C., Walsh, C., & van Dishoeck, E. F. 2016, A&A, 595, A83

[148] Espinoza, N. 2022, TransitSpectroscopy, doi:10.5281/zenodo.6960924

[149] Espinoza, N., & Jordán, A. 2015, MNRAS, 450, 1879

[150] —. 2016, MNRAS, 457, 3573

[151] Espinoza, N., Kossakowski, D., & Brahm, R. 2019, Monthly Notices of the Royal Astronomical Society, 490, 2262

[152] Fabrycky, D., & Tremaine, S. 2007, ApJ, 669, 1298

[153] Faedi, F., Barros, S. C. C., Anderson, D. R., et al. 2011, A&A, 531, A40

[154] Faherty, J. K., Bochanski, J. J., Gagné, J., et al. 2018, ApJ, 863, 91

[155] Fang, X.-S., Zhao, G., Zhao, J.-K., Chen, Y.-Q., & Bharat Kumar, Y. 2016, MNRAS, 463, 2494

[156] Fares, R., Donati, J. F., Moutou, C., et al. 2010, MNRAS, 406, 409

[157] Fedele, D., van den Ancker, M. E., Henning, T., Jayawardhana, R., & Oliveira, J. M. 2010, A&A, 510, A72

[158] Feigelson, E., Townsley, L., Güdel, M., & Stassun, K. 2007, in Protostars and Planets V, ed. B. Reipurth, D. Jewitt, & K. Keil, 313

[159] Feigelson, E. D., & Montmerle, T. 1999, ARA&A, 37, 363

[160] Feinstein, A., Montet, B., & Ansdell, M. 2020, The Journal of Open Source Software, 5, 2347

[161] Feinstein, A. D., David, T. J., Montet, B. T., et al. 2022, ApJ, 925, L2

[162] Feinstein, A. D., Montet, B. T., Ansdell, M., et al. 2020, AJ, 160, 219

[163] Feinstein, A. D., Montet, B. T., Johnson, M. C., et al. 2021, AJ, 162, 213

[164] Feinstein, A. D., Seligman, D. Z., Günther, M. N., & Adams, F. C. 2022, ApJ, 925, L9

[165] Feinstein, A. D., Montet, B. T., Foreman-Mackey, D., et al. 2019, PASP, 131, 094502

[166] Feinstein, A. D., Schlieder, J. E., Livingston, J. H., et al. 2019, AJ, 157, 40

[167] Feinstein, A. D., France, K., Youngblood, A., et al. 2022, AJ, 164, 110

[168] Feinstein, A. D., Radica, M., Welbanks, L., et al. 2023, Nature, 614, 670–675

[169] Feroz, F., Hobson, M. P., & Bridges, M. 2009, MNRAS, 398, 1601

[170] Fischer, P. D., Knutson, H. A., Sing, D. K., et al. 2016, ApJ, 827, 19

[171] —. 2016, ApJ, 827, 19

[172] Fisher, C., & Heng, K. 2018, MNRAS, 481, 4698

[173] Fitzgerald, M. P., Kalas, P. G., Duchêne, G., Pinte, C., & Graham, J. R. 2007, ApJ, 670, 536

[174] Flagg, L., Johns-Krull, C., France, K., et al. 2022, arXiv e-prints, arXiv:2206.02636

[175] Flores Soriano, M., Strassmeier, K. G., & Weber, M. 2015, A&A, 575, A57

[176] Ford, E. B. 2014, Proceedings of the National Academy of Science, 111, 12616

[177] Foreman-Mackey, D., Agol, E., Ambikasaran, S., & Angus, R. 2017, AJ, 154, 220

[178] Foreman-Mackey, D., Hogg, D. W., Lang, D., & Goodman, J. 2013, PASP, 125, 306

[179] Foreman-Mackey, D., Hogg, D. W., Lang, D., & Goodman, J. 2013, Publications of the Astronomical Society of the Pacific, 125, 306

[180] Foreman-Mackey, D., Luger, R., Agol, E., et al. 2021, arXiv e-prints, arXiv:2105.01994

[181] Fortney, J. J. 2005, MNRAS, 364, 649

[182] Fortney, J. J., Mordasini, C., Nettelmann, N., et al. 2013, ApJ, 775, 80

[183] France, K., Linsky, J. L., Tian, F., Froning, C. S., & Roberge, A. 2012, ApJ, 750, L32

[184] France, K., Loyd, R. O. P., Youngblood, A., et al. 2016, ApJ, 820, 89

[185] France, K., Duvvuri, G., Egan, H., et al. 2020, AJ, 160, 237

[186] Fraunhofer, J. 1817, Annalen der Physik, 56, 264

[187] Freedman, R. S., Lustig-Yaeger, J., Fortney, J. J., et al. 2014, ApJS, 214, 25

[188] Froning, C. S., Kowalski, A., France, K., et al. 2019, ApJ, 871, L26

[189] Fulton, B. J., Petigura, E. A., Howard, A. W., et al. 2017, AJ, 154, 109

[190] Gagné, J., Mamajek, E. E., Malo, L., et al. 2018, ApJ, 856, 23

[191] Gaia Collaboration, Prusti, T., de Bruijne, J. H. J., et al. 2016, A&A, 595, A1

[192] Gaia Collaboration, Brown, A. G. A., Vallenari, A., et al. 2018, A&A, 616, A1

[193] Garcia-Sage, K., Glocer, A., Drake, J. J., Gronoff, G., & Cohen, O. 2017, ApJ, 844, L13

[194] Gautier, Thomas N., I., Charbonneau, D., Rowe, J. F., et al. 2012, ApJ, 749, 15

[195] Gelman, A., & Rubin, D. B. 1992, Statistical Science, 7, 457

[196] Geweke, J. 1992, Bayesian Statistics IV. Oxford: Clarendon Press, ed. J. M. Bernardo, 169

[197] Gharib-Nezhad, E., Iyer, A. R., Line, M. R., et al. 2021, ApJS, 254, 34

[198] Gilbert, E. A., Barclay, T., Quintana, E. V., et al. 2022, AJ, 163, 147

[199] Gilbert, J., Bergmann, C., Bloxham, G., et al. 2018, in Society of Photo-Optical Instrumentation Engineers (SPIE) Conference Series, Vol. 10702, Ground-based and Airborne Instrumentation for Astronomy VII, ed. C. J. Evans, L. Simard, & H. Takami, 107020Y

[200] Gillon, M., Triaud, A. H. M. J., Demory, B.-O., et al. 2017, Nature, 542, 456

[201] Ginzburg, S., Schlichting, H. E., & Sari, R. 2018, MNRAS, 476, 759

[202] Goldreich, P., & Tremaine, S. 1979, ApJ, 233, 857

[203] Goodman, J., & Weare, J. 2010, Communications in Applied Mathematics and Computational Science, 5, 65

[204] Goyal, J. M., Mayne, N., Sing, D. K., et al. 2018, MNRAS, 474, 5158

[205] Goyal, J. M., Mayne, N., Drummond, B., et al. 2020, MNRAS, 498, 4680

[206] Grankin, K. N. 1999, Astronomy Letters, 25, 526

[207] Gray, D. F. 2008, The Observation and Analysis of Stellar Photospheres

[208] Gray, R. O., & Corbally, C. J. 1994, AJ, 107, 742

[209] Grieger, B. 1992, Physica A Statistical Mechanics and its Applications, 191, 51

[210] Grimm, S. L., Malik, M., Kitzmann, D., et al. 2021, ApJS, 253, 30

[211] Gronoff, G., Arras, P., Baraka, S., et al. 2020, Journal of Geophysical Research (Space Physics), 125, e27639

[212] Gryciuk, M., Siarkowski, M., Sylwester, J., et al. 2017, Sol. Phys., 292, 77

[213] Guilluy, G., Andretta, V., Borsa, F., et al. 2020, A&A, 639, A49

[214] Gully-Santiago, M. A., Herczeg, G. J., Czekala, I., et al. 2017, ApJ, 836, 200

[215] Günther, M. N., Pozuelos, F. J., Dittmann, J. A., et al. 2019, Nature Astronomy, 3, 1099

[216] Günther, M. N., Zhan, Z., Seager, S., et al. 2020, AJ, 159, 60

[217] Guo, Z., Gully-Santiago, M., & Herczeg, G. J. 2018, ApJ, 868, 143

[218] Gupta, A., & Schlichting, H. E. 2019, MNRAS, 487, 24

[219] Gutenberg, B., & Richter, C. F. 1956, Annals of Geophysics, 53, doi:10.4401/ag-4588

[220] Hands, T. O., & Helled, R. 2022, MNRAS, 509, 894

[221] —. 2022, MNRAS, 509, 894

[222] Harman, C. E., Kopparapu, R. K., Stefánsson, G., et al. 2022, , 3, 45

[223] Harra, L. K., Schrijver, C. J., Janvier, M., et al. 2016, Sol. Phys., 291, 1761

[224] Hauschildt, P. H., Allard, F., & Baron, E. 1999, ApJ, 512, 377

[225] Hawley, S. L., Davenport, J. R. A., Kowalski, A. F., et al. 2014, ApJ, 797, 121

[226] Hawley, S. L., & Pettersen, B. R. 1991, ApJ, 378, 725

[227] —. 1991, ApJ, 378, 725

[228] Hawley, S. L., Fisher, G. H., Simon, T., et al. 1995, ApJ, 453, 464

[229] Hawley, S. L., Allred, J. C., Johns-Krull, C. M., et al. 2003, ApJ, 597, 535

[230] Hazra, G., Vidotto, A. A., Carolan, S., Villarreal D'Angelo, C., & Manchester, W. 2022, MNRAS, 509, 5858

[231] He, K., Zhang, X., Ren, S., & Sun, J. 2016, in 14th European Conference on Computer Vision (ECCV), Vol. 5 (Springer), 630–645

[232] Heger, A., Langer, N., & Woosley, S. E. 2000, ApJ, 528, 368

[233] Hellier, C., Anderson, D. R., Collier Cameron, A., et al. 2014, MNRAS, 440, 1982

[234] Henry, T. J., Jao, W.-C., Subasavage, J. P., et al. 2006, AJ, 132, 2360

[235] Hesse, J., & Gross, T. 2014, Frontiers in Systems Neuroscience, 8, 166

[236] Hippke, M., David, T. J., Mulders, G. D., & Heller, R. 2019, AJ, 158, 143

[237] Hirano, T., Krishnamurthy, V., Gaidos, E., et al. 2020, ApJ, 899, L13

[238] Hoch, K. K. W., Konopacky, Q. M., Theissen, C. A., et al. 2022, arXiv e-prints, arXiv:2212.04557

[239] Hodgson, R. 1859, MNRAS, 20, 15

[240] Holman, M., Touma, J., & Tremaine, S. 1997, Nature, 386, 254

[241] Howard, W. S., Corbett, H., Law, N. M., et al. 2019, ApJ, 881, 9

[242] Howard, W. S., & MacGregor, M. A. 2022, ApJ, 926, 204

[243] Howard, W. S., Corbett, H., Law, N. M., et al. 2020, ApJ, 895, 140

[244] Howarth, I. D. 2011, MNRAS, 418, 1165

[245] Howell, S. B., Sobeck, C., Haas, M., et al. 2014, PASP, 126, 398

[246] Huang, X., Gamache, R., Freedman, R., Schwenke, D., & Lee, T. 2014, Journal of Quantitative Spectroscopy & Radiative Transfer, 147, 134

[247] Hudson, H. S., Acton, L. W., & Freeland, S. L. 1996, ApJ, 470, 629

[248] Hurley, J., & Tout, C. A. 1998, Monthly Notices of the RAS, 300, 977

[249] Husser, T. O., Wende-von Berg, S., Dreizler, S., et al. 2013, A&A, 553, A6

[250] Ida, S., & Lin, D. N. C. 2008, ApJ, 673, 487

[251] Ilin, E., Schmidt, S. J., Davenport, J. R. A., & Strassmeier, K. G. 2019, A&A, 622, A133

[252] —. 2019, A&A, 622, A133

[253] Ilin, E., Schmidt, S. J., Poppenhäger, K., et al. 2021, A&A, 645, A42

[254] Iyer, A. R., & Line, M. R. 2020, ApJ, 889, 78

[255] Jakosky, B. M., Pepin, R. O., Johnson, R. E., & Fox, J. L. 1994, Icarus, 111, 271

[256] Jenkins, J. M., Caldwell, D. A., Chandrasekaran, H., et al. 2010, ApJ, 713, L87

[257] Jenkins, J. M., Twicken, J. D., McCauliff, S., et al. 2016, in Society of Photo-Optical Instrumentation Engineers (SPIE) Conference Series, Vol. 9913, Software and Cyberinfrastructure for Astronomy IV, 99133E

[258] Johnson, L. J., Norris, C. N., Unruh, Y. C., et al. 2021, arXiv e-prints, arXiv:2104.11544

[259] Johnson, M. C., Cochran, W. D., Addison, B. C., Tinney, C. G., & Wright, D. J. 2017, AJ, 154, 137

[260] Johnson, M. C., Cochran, W. D., Albrecht, S., et al. 2014, ApJ, 790, 30

[261] Johnstone, C. P., Güdel, M., Stökl, A., et al. 2015, ApJ, 815, L12

[262] Jones, J., White, R. J., Boyajian, T., et al. 2015, ApJ, 813, 58

[263] Kalas, P., Liu, M. C., & Matthews, B. C. 2004, Science, 303, 1990

[264] Kavanagh, R. D., Vidotto, A. A., Klein, B., et al. 2021, MNRAS, 504, 1511

[265] Kay, C., Opher, M., & Kornbleuth, M. 2016, ApJ, 826, 195

[266] Kempton, E. M. R., Lupu, R., Owusu-Asare, A., Slough, P., & Cale, B. 2017, PASP, 129, 044402

[267] Kempton, E. M. R., Bean, J. L., Louie, D. R., et al. 2018, PASP, 130, 114401

[268] Kenyon, S. J., & Hartmann, L. 1995, ApJS, 101, 117

[269] Kingma, D. P., & Ba, J. 2014, ArXiv e-prints, arXiv:1412.6980

[270] Kipping, D. M. 2013, Monthly Notices of the Royal Astronomical Society, 435, 2152

[271] Kirk, J., López-Morales, M., Wheatley, P. J., et al. 2019, AJ, 158, 144

[272] Klein, B., Donati, J.-F., Moutou, C., et al. 2021, MNRAS, 502, 188

[273] Kochukhov, O., & Reiners, A. 2020, ApJ, 902, 43

[274] Komacek, T. D., & Showman, A. P. 2016, ApJ, 821, 16

[275] Kostov, V. B., Schlieder, J. E., Barclay, T., et al. 2019, AJ, 158, 32

[276] Kotoneva, E., Flynn, C., & Jimenez, R. 2002, Monthly Notices of the RAS, 335, 1147

[277] Kowalski, A. F., Hawley, S. L., Wisniewski, J. P., et al. 2013, ApJS, 207, 15

[278] Kozai, Y. 1962, AJ, 67, 591

[279] Kramida, A., Ralchenko, Y., Reader, J., & NIST ASD Team. 2021, doi:https://doi.org/10.18434/T4W30F

[280] Kramida, A., Yu. Ralchenko, Reader, J., & and NIST ASD Team. 2018, NIST Atomic Spectra Database (ver. 5.6.1), [Online]. Available: `https://physics.nist.gov/asd` [2019, February 6]. National Institute of Standards and Technology, Gaithersburg, MD.

[281] Kreidberg, L. 2015, Publications of the Astronomical Society of the Pacific, 127, 1161

[282] Kreidberg, L., Bean, J. L., Désert, J.-M., et al. 2014, ApJ, 793, L27

[283] Kretzschmar, M. 2011, A&A, 530, A84

[284] Krizhevsky, A., Sutskever, I., & Hinton, G. E. 2012, in Advances in neural information processing systems, 1097–1105

[285] Kubyshkina, D., Fossati, L., Erkaev, N. V., et al. 2018, ApJ, 866, L18

[286] Kupka, F. G., Ryabchikova, T. A., Piskunov, N. E., Stempels, H. C., & Weiss, W. W. 2000, Baltic Astronomy, 9, 590

[287] Kurucz, R., & Bell, B. 1995, Atomic Line Data (R.L. Kurucz and B. Bell) Kurucz CD-ROM No. 23. Cambridge, 23

[288] Kurucz, R. L. 1979, ApJS, 40, 1

[289] —. 1993, SYNTHE spectrum synthesis programs and line data

[290] Laginja, I., & Wakeford, H. 2020, The Journal of Open Source Software, 5, 2281

[291] Lai, D. 2014, MNRAS, 440, 3532

[292] Lambrechts, M., & Johansen, A. 2012, A&A, 544, A32

[293] Lammer, H., Selsis, F., Ribas, I., et al. 2003, ApJ, 598, L121

[294] Lammer, H., Stumptner, W., & Bauer, S. J. 1996, Geophys. Res. Lett., 23, 3353

[295] Lammer, H., Lichtenegger, H. I. M., Kulikov, Y. N., et al. 2007, Astrobiology, 7, 185

[296] Landi, E., Del Zanna, G., Young, P. R., Dere, K. P., & Mason, H. E. 2012, ApJ, 744, 99

[297] Lanza, A. F. 2012, A&A, 544, A23

[298] Lavvas, P., Koskinen, T., & Yelle, R. V. 2014, ApJ, 796, 15

[299] Leblanc, F., & Johnson, R. E. 2002, Journal of Geophysical Research (Planets), 107, 5010

[300] Lecavelier Des Etangs, A., Pont, F., Vidal-Madjar, A., & Sing, D. 2008, A&A, 481, L83

[301] —. 2008, A&A, 481, L83

[302] Lecavelier des Etangs, A., Sirothia, S. K., Gopal-Krishna, & Zarka, P. 2013, A&A, 552, A65

[303] Lecavelier Des Etangs, A., Ehrenreich, D., Vidal-Madjar, A., et al. 2010, A&A, 514, A72

[304] Lecavelier des Etangs, A., Bourrier, V., Wheatley, P. J., et al. 2012, A&A, 543, L4

[305] LeCun, Y., Bengio, Y., & Hinton, G. 2015, Nature, 521, 436

[306] Li, G., Gordon, I. E., Rothman, L. S., et al. 2015, ApJS, 216, 15

[307] Lidov, M. L. 1962, Planet. Space Sci., 9, 719

[308] Lin, C. L., Ip, W. H., Hou, W. C., Huang, L. C., & Chang, H. Y. 2019, The Astrophysical Journal, 873, 97

[309] Lin, H.-T., Chen, W.-P., Liu, J., et al. 2022, AJ, 163, 164

[310] Lin, M., Chen, Q., & Yan, S. 2013, arXiv e-prints, arXiv:1312.4400

[311] Line, M. R., & Parmentier, V. 2016, ApJ, 820, 78

[312] Line, M. R., Wolf, A. S., Zhang, X., et al. 2013, ApJ, 775, 137

[313] Linsky, J. L., Yang, H., France, K., et al. 2010, ApJ, 717, 1291

[314] Liu, M. C. 2004, Science, 305, 1442

[315] Liu, M. C., Matthews, B. C., Williams, J. P., & Kalas, P. G. 2004, ApJ, 608, 526

[316] Livingston, J. H., Endl, M., Dai, F., et al. 2018, AJ, 156, 78

[317] Lodders, K. 2003, ApJ, 591, 1220

[318] Lodders, K., Palme, H., & Gail, H. P. 2009, Landolt Börnstein, 4B, 712

[319] Lomb, N. R. 1976, Ap&SS, 39, 447

[320] Longcope, D. W., Fisher, G. H., & Pevtsov, A. A. 1998, ApJ, 507, 417

[321] Lopez, E. D., & Fortney, J. J. 2013, ApJ, 776, 2

[322] —. 2014, ApJ, 792, 1

[323] Lothringer, J. D., & Barman, T. S. 2020, AJ, 159, 289

[324] Lothringer, J. D., Rustamkulov, Z., Sing, D. K., et al. 2021, ApJ, 914, 12

[325] Loyd, R. O. P., Shkolnik, E. L., Schneider, A. C., et al. 2018, ApJ, 867, 70

[326] —. 2020, ApJ, 890, 23

[327] Loyd, R. O. P., France, K., Youngblood, A., et al. 2016, ApJ, 824, 102

[328] —. 2018, ApJ, 867, 71

[329] Lu, E. T., & Hamilton, R. J. 1991, ApJ, 380, L89

[330] Luger, R., Agol, E., Foreman-Mackey, D., et al. 2019, AJ, 157, 64

[331] Luger, R., Foreman-Mackey, D., Hedges, C., & Hogg, D. W. 2021, arXiv e-prints, arXiv:2102.00007

[332] Luger, R., Sestovic, M., Kruse, E., et al. 2017, Nature Astronomy, 1, 0129

[333] Luhman, K. L. 2018, AJ, 156, 271

[334] Luhmann, J. G., & Kozyra, J. U. 1991, J. Geophys. Res., 96, 5457

[335] Lundin, R., Lammer, H., & Ribas, I. 2007, Space Sci. Rev., 129, 245

[336] Lurie, J. C., Davenport, J. R. A., Hawley, S. L., et al. 2015, ApJ, 800, 95

[337] MacDonald, R. J., & Madhusudhan, N. 2017, MNRAS, 469, 1979

[338] MacGregor, M. A., Weinberger, A. J., Loyd, R. O. P., et al. 2021, ApJ, 911, L25

[339] Maciejewski, G., Dimitrov, D., Mancini, L., et al. 2016, J Acta Astronomica, 66, 55

[340] MacNeice, P., Pallavicini, R., Mason, H. E., et al. 1985, Sol. Phys., 99, 167

[341] Madhusudhan, N., Amin, M. A., & Kennedy, G. M. 2014, ApJ, 794, L12

[342] Maehara, H., Notsu, Y., Notsu, S., et al. 2017, PASJ, 69, 41

[343] Maehara, H., Shibayama, T., Notsu, Y., et al. 2015, Earth, Planets and Space, 67, 59

[344] Maehara, H., Notsu, Y., Namekata, K., et al. 2021, PASJ, 73, 44

[345] Mai, C., & Line, M. R. 2019, ApJ, 883, 144

[346] Malik, M., Kitzmann, D., Mendonça, J. M., et al. 2019, AJ, 157, 170

[347] Malik, M., Grosheintz, L., Mendonça, J. M., et al. 2017, AJ, 153, 56

[348] Mamajek, E. E., & Bell, C. P. M. 2014, MNRAS, 445, 2169

[349] Mancini, L., Esposito, M., Covino, E., et al. 2018, A&A, 613, A41

[350] Mandel, K., & Agol, E. 2002, ApJ, 580, L171

[351] Mann, A. W., Newton, E. R., Rizzuto, A. C., et al. 2016, The Astronomical Journal, 152, 61

[352] Mann, A. W., Johnson, M. C., Vanderburg, A., et al. 2020, AJ, 160, 179

[353] Mann, A. W., Wood, M. L., Schmidt, S. P., et al. 2022, AJ, 163, 156

[354] —. 2022, AJ, 163, 156

[355] Mansfield, M., Bean, J. L., Oklopčić, A., et al. 2018, ApJ, 868, L34

[356] Mansfield, M., Line, M. R., Bean, J. L., et al. 2021, Nature Astronomy, 5, 1224

[357] Maran, S. P., Robinson, R. D., Shore, S. N., et al. 1994, ApJ, 421, 800

[358] Marley, M. S., & McKay, C. P. 1999, Icarus, 138, 268

[359] Martioli, E., Hébrard, G., Correia, A. C. M., Laskar, J., & Lecavelier des Etangs, A. 2021, A&A, 649, A177

[360] Martioli, E., Teeple, D., Manset, N., et al. 2012, in Society of Photo-Optical Instrumentation Engineers (SPIE) Conference Series, Vol. 8451, Software and Cyberinfrastructure for Astronomy II, ed. N. M. Radziwill & G. Chiozzi, 84512B

[361] Martioli, E., Hébrard, G., Moutou, C., et al. 2020, A&A, 641, L1

[362] Mason, J. P., Attie, R., Arge, C. N., Thompson, B., & Woods, T. N. 2019, ApJS, 244, 13

[363] Matsuo, T., Greene, T. P., Johnson, R. R., et al. 2019, PASP, 131, 124502

[364] McClymont, A. N., & Canfield, R. C. 1986, ApJ, 305, 936

[365] McKay, C. P., Pollack, J. B., & Courtin, R. 1989, Icarus, 80, 23

[366] McQuillan, A., Mazeh, T., & Aigrain, S. 2014, ApJS, 211, 24

[367] McTiernan, J. M., Caspi, A., & Warren, H. P. 2019, ApJ, 881, 161

[368] Metchev, S. A., Eisner, J. A., Hillenbrand, L. A., & Wolf, S. 2005, ApJ, 622, 451

[369] Miller-Ricci, E., Seager, S., & Sasselov, D. 2009, ApJ, 690, 1056

[370] Min, M., Ormel, C. W., Chubb, K., Helling, C., & Kawashima, Y. 2020, A&A, 642, A28

[371] Moffatt, H. K. 1978, Magnetic field generation in electrically conducting fluids

[372] Moldovan, R., Matthews, J. M., Gladman, B., Bottke, W. F., & Vokrouhlický, D. 2010, ApJ, 716, 315

[373] Monsignori Fossi, B. C., & Landini, M. 1994, A&A, 284, 900

[374] Monsignori Fossi, B. C., Landini, M., Del Zanna, G., & Bowyer, S. 1996, ApJ, 466, 427

[375] Montet, B. T., Tovar, G., & Foreman-Mackey, D. 2017, ApJ, 851, 116

[376] Montet, B. T., Johnson, J. A., Muirhead, P. S., et al. 2015, ApJ, 800, 134

[377] Montet, B. T., Feinstein, A. D., Luger, R., et al. 2020, AJ, 159, 112

[378] Moore, T. E., Lundin, R., Alcayde, D., et al. 1999, Space Sci. Rev., 88, 7

[379] Moos, H. W., Cash, W. C., Cowie, L. L., et al. 2000, ApJ, 538, L1

[380] Mordasini, C., van Boekel, R., Mollière, P., Henning, T., & Benneke, B. 2016, ApJ, 832, 41

[381] Morello, G., Claret, A., Martin-Lagarde, M., et al. 2020, AJ, 159, 75

[382] Morris, B. M. 2020, arXiv e-prints, arXiv:2002.09135

[383] Mukherjee, S., Batalha, N. E., Fortney, J. J., & Marley, M. S. 2022, arXiv e-prints, arXiv:2208.07836

[384] Mullan, D. J., & Bais, H. P. 2018, ApJ, 865, 101

[385] Murphy, M. T., Udem, T., Holzwarth, R., et al. 2007, MNRAS, 380, 839

[386] Murphy, S. J., & Lawson, W. A. 2015, MNRAS, 447, 1267

[387] Murphy, S. J., Lawson, W. A., & Bessell, M. S. 2013, MNRAS, 435, 1325

[388] Nagel, K., & Herrmann, H. J. 1993, Physica A Statistical Mechanics and its Applications, 199, 254

[389] Naoz, S., Farr, W. M., Lithwick, Y., Rasio, F. A., & Teyssandier, J. 2011, Nature, 473, 187

[390] Narang, M., Manoj, P., Ishwara Chandra, C. H., et al. 2021, MNRAS, 500, 4818

[391] Neff, J. E., O'Neal, D., & Saar, S. H. 1995, ApJ, 452, 879

[392] Nelson, R. P., Papaloizou, J. C. B., Masset, F., & Kley, W. 2000, MNRAS, 318, 18

[393] Neupert, W. M. 1968, ApJ, 153, L59

[394] Neves Ribeiro do Amaral, L., Barnes, R., Segura, A., & Luger, R. 2022, arXiv e-prints, arXiv:2203.10127

[395] Newman, M. E. J. 2005, Contemporary Physics, 46, 323

[396] Newman, M. E. J., & Sneppen, K. 1996, Phys. Rev. E, 54, 6226

[397] Newton, E. R., Mann, A. W., Tofflemire, B. M., et al. 2019, ApJ, 880, L17

[398] Newville, M., Otten, R., Nelson, A., et al. 2021, lmfit/lmfit-py 1.0.2, doi:10.5281/zenodo.4516651

[399] Niculescu-Mizil, A., & Caruana, R. 2005, in ICML '05

[400] Nikolov, N., Sing, D. K., Gibson, N. P., et al. 2016, ApJ, 832, 191

[401] Notsu, Y., Shibayama, T., Maehara, H., et al. 2013, ApJ, 771, 127

[402] Notsu, Y., Maehara, H., Honda, S., et al. 2019, ApJ, 876, 58

[403] Noyes, R. W., Hartmann, L. W., Baliunas, S. L., Duncan, D. K., & Vaughan, A. H. 1984, ApJ, 279, 763

[404] Öberg, K. I., Murray-Clay, R., & Bergin, E. A. 2011, ApJ, 743, L16

[405] Oh, S., Price-Whelan, A. M., Hogg, D. W., Morton, T. D., & Spergel, D. N. 2017, AJ, 153, 257

[406] Ohno, K., & Kawashima, Y. 2020, ApJ, 895, L47

[407] Oklopčić, A., & Hirata, C. M. 2018, ApJ, 855, L11

[408] Olami, Z., Feder, H. J. S., & Christensen, K. 1992, Phys. Rev. Lett., 68, 1244

[409] Orrall, F. Q., & Zirker, J. B. 1976, ApJ, 208, 618

[410] Osten, R. A., Crosley, M. K., Gudel, M., et al. 2018, arXiv e-prints, arXiv:1803.05345

[411] Osten, R. A., Hawley, S. L., Allred, J. C., Johns-Krull, C. M., & Roark, C. 2005, ApJ, 621, 398

[412] Owen, J. E. 2019, Annual Review of Earth and Planetary Sciences, 47, 67

[413] Owen, J. E., & Campos Estrada, B. 2020, MNRAS, 491, 5287

[414] Owen, J. E., & Wu, Y. 2013, ApJ, 775, 105

[415] —. 2017, ApJ, 847, 29

[416] Pagano, I., Linsky, J. L., Carkner, L., et al. 2000, ApJ, 532, 497

[417] Pallavicini, R., Cutispoto, G., Randich, S., & Gratton, R. 1993, A&A, 267, 145

[418] Pallavicini, R., Randich, S., & Giampapa, M. S. 1992, A&A, 253, 185

[419] Palle, E., Oshagh, M., Casasayas-Barris, N., et al. 2020, A&A, 643, A25

[420] Paragas, K., Vissapragada, S., Knutson, H. A., et al. 2021, ApJ, 909, L10

[421] Parker, E. N. 1955, ApJ, 122, 293

[422] —. 1958, ApJ, 128, 664

[423] —. 1988, ApJ, 330, 474

[424] —. 1988, ApJ, 330, 474

[425] —. 1989, Sol. Phys., 121, 271

[426] Parmentier, V., Fortney, J. J., Showman, A. P., Morley, C., & Marley, M. S. 2016, ApJ, 828, 22

[427] Paudel, R. R., Gizis, J. E., Mullan, D. J., et al. 2018, ApJ, 861, 76

[428] —. 2019, MNRAS, 486, 1438

[429] Pearson, K. A., Palafox, L., & Griffith, C. A. 2018, MNRAS, 474, 478

[430] Pecaut, M. J., & Mamajek, E. E. 2013, ApJS, 208, 9

[431] —. 2016, MNRAS, 461, 794

[432] Perez-Becker, D., & Showman, A. P. 2013, ApJ, 776, 134

[433] Perri, F., & Cameron, A. G. W. 1974, Icarus, 22, 416

[434] Pineda, J. S., Bottom, M., & Johnson, J. A. 2013, ApJ, 767, 28

[435] Pinhas, A., Madhusudhan, N., Gandhi, S., & MacDonald, R. 2019, MNRAS, 482, 1485

[436] Piskorz, D., Buzard, C., Line, M. R., et al. 2018, AJ, 156, 133

[437] Piso, A.-M. A., Youdin, A. N., & Murray-Clay, R. A. 2015, ApJ, 800, 82

[438] Platais, I., Kozhurina-Platais, V., & van Leeuwen, F. 1998, AJ, 116, 2423

[439] Plavchan, P., Werner, M. W., Chen, C. H., et al. 2009, ApJ, 698, 1068

[440] Plavchan, P., Barclay, T., Gagné, J., et al. 2020, Nature, 582, 497

[441] Pöhnl, H., & Paunzen, E. 2010, A&A, 514, A81

[442] Poland, A. I., Orwig, L. E., Mariska, J. T., Auer, L. H., & Nakatsuka, R. 1984, ApJ, 280, 457

[443] Polanski, A. S., Crossfield, I. J. M., Howard, A. W., Isaacson, H., & Rice, M. 2022, Research Notes of the American Astronomical Society, 6, 155

[444] Pollack, J. B., Hubickyj, O., Bodenheimer, P., et al. 1996, Icarus, 124, 62

[445] Polyansky, O. L., Kyuberis, A. A., Zobov, N. F., et al. 2018, MNRAS, 480, 2597

[446] Poppenhaeger, K. 2022, MNRAS, 512, 1751

[447] Poppenhaeger, K., Ketzer, L., & Mallonn, M. 2021, MNRAS, 500, 4560

[448] Porter, J. G., Fontenla, J. M., & Simnett, G. M. 1995, ApJ, 438, 472

[449] Powell, D., Louden, T., Kreidberg, L., et al. 2019, ApJ, 887, 170

[450] Preibisch, T., Brown, A. G. A., Bridges, T., Guenther, E., & Zinnecker, H. 2002, AJ, 124, 404

[451] Preibisch, T., Guenther, E., & Zinnecker, H. 2001, AJ, 121, 1040

[452] Preibisch, T., Kim, Y.-C., Favata, F., et al. 2005, ApJS, 160, 401

[453] Price-Whelan, A. M., Sipőcz, B. M., Günther, H. M., et al. 2018, AJ, 156, 123

[454] Quin, D. A., Doyle, J. G., Butler, C. J., Byrne, P. B., & Swank, J. H. 1993, A&A, 272, 477

[455] Rackham, B. V., Apai, D., & Giampapa, M. S. 2018, ApJ, 853, 122

[456] Rackham, B. V., Espinoza, N., Berdyugina, S. V., et al. 2022, arXiv e-prints, arXiv:2201.09905

[457] Radica, M., Albert, L., Taylor, J., et al. 2022, PASP, 134, 104502

[458] Raetz, S., Stelzer, B., Damasso, M., & Scholz, A. 2020, Astronomy and Astrophysics, 637, A22

[459] Ranjan, S., Wordsworth, R., & Sasselov, D. D. 2017, ApJ, 843, 110

[460] Redfield, S., Linsky, J. L., Ake, T. B., et al. 2002, ApJ, 581, 626

[461] Reinhold, T., & Gizon, L. 2015, A&A, 583, A65

[462] Ribeiro, T. L., Copelli, M., Caixeta, F., et al. 2010, PLoS ONE, 5, e14129

[463] Richard, C., Gordon, I. E., Rothman, L. S., et al. 2012, J. Quant. Spec. Radiat. Transf., 113, 1276

[464] Richey-Yowell, T., Shkolnik, E. L., Schneider, A. C., et al. 2019, The Astrophysical Journal, 872, 17

[465] Ricker, G. R., Winn, J. N., Vanderspek, R., et al. 2014, in Proc. SPIE, Vol. 9143, Space Telescopes and Instrumentation 2014: Optical, Infrared, and Millimeter Wave, 914320

[466] Ricker, G. R., Winn, J. N., Vanderspek, R., et al. 2015, Journal of Astronomical Telescopes, Instruments, and Systems, 1, 014003

[467] Riedel, A. R., Alam, M. K., Rice, E. L., Cruz, K. L., & Henry, T. J. 2017, ApJ, 840, 87

[468] Rimmer, P. B., Xu, J., Thompson, S. J., et al. 2018, Science Advances, 4, eaar3302

[469] Rizzuto, A. C., Newton, E. R., Mann, A. W., et al. 2020, AJ, 160, 33

[470] Robertson, P., Bender, C., Mahadevan, S., Roy, A., & Ramsey, L. W. 2016, ApJ, 832, 112

[471] Robinson, P. A. 1994, Phys. Rev. E, 49, 1984

[472] Robinson, R. D., Carpenter, K. G., Woodgate, B. E., & Maran, S. P. 1993, ApJ, 414, 872

[473] Rockcliffe, K. E., Newton, E. R., Youngblood, A., et al. 2021, AJ, 162, 116

[474] Roettenbacher, R. M., & Vida, K. 2018, ApJ, 868, 3

[475] Roettenbacher, R. M., Monnier, J. D., Korhonen, H., et al. 2016, Nature, 533, 217

[476] Rogers, J. G., Gupta, A., Owen, J. E., & Schlichting, H. E. 2021, MNRAS, 508, 5886

[477] Rogers, J. G., & Owen, J. E. 2021, MNRAS, 503, 1526

[478] Rogers, L. A. 2015, ApJ, 801, 41

[479] Roman, M. T., Kempton, E. M. R., Rauscher, E., et al. 2021, ApJ, 908, 101

[480] Rooney, C. M., Batalha, N. E., Gao, P., & Marley, M. S. 2022, ApJ, 925, 33

[481] Rosenblatt, F. 1961, Principles of neurodynamics. perceptrons and the theory of brain mechanisms, Tech. rep., Cornell Aeronautical Lab Inc Buffalo NY

[482] Rothman, L., Gordon, I., Barbe, A., et al. 2009, Journal of Quantitative Spectroscopy and Radiative Transfer, 110, 533, hITRAN

[483] Rothman, L. S., Gordon, I. E., Barber, R. J., et al. 2010, J. Quant. Spec. Radiat. Transf., 111, 2139

[484] Rustamkulov, Z., Sing, D. K., Liu, R., & Wang, A. 2022, ApJ, 928, L7

[485] Rustamkulov, Z., Sing, D. K., Mukherjee, S., et al. 2023, Nature, 614, 659–663

[486] Ryabchikova, T., Piskunov, N., Kurucz, R. L., et al. 2015, Phys. Scr, 90, 054005

[487] Sahnow, D. J., Moos, H. W., Ake, T. B., et al. 2000, ApJ, 538, L7

[488] Salvatier, J., Wiecki, T. V., & Fonnesbeck, C. 2016, PeerJ Computer Science, 2, e55

[489] Scargle, J. D. 1982, ApJ, 263, 835

[490] Schlawin, E., Leisenring, J., Misselt, K., et al. 2020, AJ, 160, 231

[491] Schlawin, E., Leisenring, J., McElwain, M. W., et al. 2021, AJ, 161, 115

[492] Schmelz, J. T., Reames, D. V., von Steiger, R., & Basu, S. 2012, ApJ, 755, 33

[493] Schneider, A. C., & Shkolnik, E. L. 2018, AJ, 155, 122

[494] Schneider, A. C., Shkolnik, E. L., Allers, K. N., et al. 2019, AJ, 157, 234

[495] Schneider, A. D., & Bitsch, B. 2021, A&A, 654, A72

[496] Schrijver, C. J., & Title, A. M. 2011, Journal of Geophysical Research (Space Physics), 116, A04108

[497] Schwabe, M. 1844, Astronomische Nachrichten, 21, 233

[498] Scoggins, M. T., Davenport, J. R. A., & Covey, K. R. 2019, Research Notes of the AAS, 3, 137

[499] Seager, S., & Sasselov, D. D. 2000, ApJ, 537, 916

[500] Segura, A., Walkowicz, L. M., Meadows, V., Kasting, J., & Hawley, S. 2010, Astrobiology, 10, 751

[501] Seligman, D., Petrie, G. J. D., & Komm, R. 2014, ApJ, 795, 113

[502] Seligman, D. Z., Becker, J., Adams, F. C., Feinstein, A. D., & Rogers, L. A. 2022, arXiv e-prints, arXiv:2204.12653

[503] Seligman, D. Z., Rogers, L. A., Feinstein, A. D., et al. 2022, ApJ, 929, 54

[504] Shallue, C. J., & Vanderburg, A. 2018, AJ, 155, 94

[505] Shibata, K. 1996, Advances in Space Research, 17, 9

[506] Shibata, S., Helled, R., & Ikoma, M. 2020, A&A, 633, A33

[507] Shibayama, T., Maehara, H., Notsu, S., et al. 2013, The Astrophysical Journals, 209, 5

[508] Shkolnik, E., Bohlender, D. A., Walker, G. A. H., & Collier Cameron, A. 2008, ApJ, 676, 628

[509] Shkolnik, E. L., Allers, K. N., Kraus, A. L., Liu, M. C., & Flagg, L. 2017, AJ, 154, 69

[510] Shkolnik, E. L., & Barman, T. S. 2014, AJ, 148, 64

[511] Sing, D. K. 2010, A&A, 510, A21

[512] Sing, D. K., Fortney, J. J., Nikolov, N., et al. 2016, Nature, 529, 59

[513] Sinukoff, E., Howard, A. W., Petigura, E. A., et al. 2016, ApJ, 827, 78

[514] Smith, K., Pestalozzi, M., Güdel, M., Conway, J., & Benz, A. O. 2003, A&A, 406, 957

[515] Soderblom, D. R. 2010, ARA&A, 48, 581

[516] Soderblom, D. R., Jones, B. F., Balachandran, S., et al. 1993, AJ, 106, 1059

[517] Sornette, A., & Sornette, D. 1989, EPL (Europhysics Letters), 9, 197

[518] Spake, J. J., Sing, D. K., Evans, T. M., et al. 2018, Nature, 557, 68

[519] Spearman, C. 1907, The American journal of psychology, 161

[520] Srivastava, N., Hinton, G., Krizhevsky, A., Sutskever, I., & Salakhutdinov, R. 2014, Journal of Machine Learning Research, 15, 1929

[521] Stassun, K. G., Collins, K. A., & Gaudi, B. S. 2017, AJ, 153, 136

[522] Stassun, K. G., Oelkers, R. J., Pepper, J., et al. 2018, AJ, 156, 102

[523] Stauffer, J. R., Jones, B. F., Backman, D., et al. 2003, AJ, 126, 833

[524] Sterling, A. C., & Hudson, H. S. 1997, ApJ, 491, L55

[525] Stevenson, K. B., Lewis, N. K., Bean, J. L., et al. 2016, PASP, 128, 094401

[526] Stock, J. W., Kitzmann, D., Patzer, A. B. C., & Sedlmayr, E. 2018, MNRAS, 479, 865

[527] Strassmeier, K. G. 2009, A&A Rev., 17, 251

[528] Sturrock, P. A., Dixon, W. W., Klimchuk, J. A., & Antiochos, S. K. 1990, ApJ, 356, L31

[529] —. 1990, ApJ, 356, L31

[530] Sturrock, P. A., Kaufman, P., Moore, R. L., & Smith, D. F. 1984, Sol. Phys., 94, 341

[531] —. 1984, Sol. Phys., 94, 341

[532] Tanoglidis, D., Ćiprijanović, A., & Drlica-Wagner, A. 2021, Astronomy and Computing, 35, 100469

[533] Tashkun, S., & Perevalov, V. 2011, Journal of Quantitative Spectroscopy and Radiative Transfer, 112, 1403

[534] Teal, D. J., Kempton, E. M. R., Bastelberger, S., Youngblood, A., & Arney, G. 2022, ApJ, 927, 90

[535] Teeple, D. 2014, OPERA: Open-source Pipeline for Espadons Reduction and Analysis, ascl:1411.004

[536] Tenenbaum, P., & Jenkins, J. M. 2018

[537] The JWST Transiting Exoplanet Community Early Release Science Team, Ahrer, E.-M., Alderson, L., et al. 2022, arXiv e-prints, arXiv:2208.11692

[538] —. 2023, Nature, 649–652

[539] Tian, F., Kasting, J. F., Liu, H.-L., & Roble, R. G. 2008, Journal of Geophysical Research (Planets), 113, E05008

[540] Tilley, M. A., Harnett, E. M., & Winglee, R. M. 2016, ApJ, 827, 77

[541] Tilley, M. A., Segura, A., Meadows, V., Hawley, S., & Davenport, J. 2019, Astrobiology, 19, 64

[542] Tovar Mendoza, G., Davenport, J. R. A., Agol, E., Jackman, J. A. G., & Hawley, S. L. 2022, arXiv e-prints, arXiv:2205.05706

[543] Tremblin, P., Amundsen, D. S., Mourier, P., et al. 2015, ApJ, 804, L17

[544] Tsai, S.-M., Lee, E. K. H., Powell, D., et al. 2023, arXiv e-prints, arXiv:2211.10490

[545] Tsiaras, A., Waldmann, I., Rocchetto, M., et al. 2016, ascl:1612.018

[546] Tsiaras, A., Waldmann, I. P., Rocchetto, M., et al. 2016, ApJ, 832, 202

[547] Tsiaras, A., Waldmann, I. P., Zingales, T., et al. 2018, AJ, 155, 156

[548] Tu, Z.-L., Yang, M., Zhang, Z. J., & Wang, F. Y. 2020, The Astrophysical Journal, 890, 46

[549] Turcotte, D. L. 1999, Reports on Progress in Physics, 62, 1377

[550] Turcotte, D. L., Malamud, B. D., Guzzetti, F., & Reichenbach, P. 2002, Proceedings of the National Academy of Sciences, 99, 2530

[551] van Dokkum, P. G. 2001, PASP, 113, 1420

[552] Van Eylen, V., Agentoft, C., Lundkvist, M. S., et al. 2018, MNRAS, 479, 4786

[553] Vanderburg, A., Latham, D. W., Buchhave, L. A., et al. 2016, ApJS, 222, 14

[554] Vanninathan, K., Veronig, A. M., Dissauer, K., & Temmer, M. 2018, ApJ, 857, 62

[555] Vehtari, A., Gelman, A., Simpson, D., Carpenter, B., & Bürkner, P.-C. 2019, arXiv e-prints, arXiv:1903.08008

[556] Venot, O., Rocchetto, M., Carl, S., Roshni Hashim, A., & Decin, L. 2016, ApJ, 830, 77

[557] Veronig, A. M., Odert, P., Leitzinger, M., et al. 2021, Nature Astronomy, 5, 697

[558] Veronig, A. M., Rybák, J., Gömöry, P., et al. 2010, ApJ, 719, 655

[559] Vida, K., Bódi, A., Szklenár, T., & Seli, B. 2021, Astronomy and Astrophysics, 652, A107

[560] Vida, K., Kővári, Z., Pál, A., Oláh, K., & Kriskovics, L. 2017, ApJ, 841, 124

[561] Vida, K., & Roettenbacher, R. M. 2018, A&A, 616, A163

[562] Vidal-Madjar, A., Lecavelier des Etangs, A., Désert, J. M., et al. 2003, Nature, 422, 143

[563] Vidal-Madjar, A., Désert, J. M., Lecavelier des Etangs, A., et al. 2004, ApJ, 604, L69

[564] Virtanen, P., Gommers, R., Burovski, E., et al. 2020, scipy/scipy: SciPy 1.5.3, Zenodo, doi:10.5281/zenodo.4100507

[565] Vissapragada, S., Stefánsson, G., Greklek-McKeon, M., et al. 2021, AJ, 162, 222

[566] Vogt, S. S., Penrod, G. D., & Hatzes, A. P. 1987, ApJ, 321, 496

[567] Volkov, A. N., Johnson, R. E., Tucker, O. J., & Erwin, J. T. 2011, ApJ, 729, L24

[568] Wakeford, H. R., Sing, D. K., Deming, D., et al. 2018, AJ, 155, 29

[569] Walkowicz, L. M., Basri, G., Batalha, N., et al. 2011, AJ, 141, 50

[570] Warren, H. P., Brooks, D. H., Ugarte-Urra, I., et al. 2018, ApJ, 854, 122

[571] Welbanks, L., & Madhusudhan, N. 2019, AJ, 157, 206

[572] —. 2021, ApJ, 913, 114

[573] Welbanks, L., Madhusudhan, N., Allard, N. F., et al. 2019, ApJ, 887, L20

[574] Wheatley, P. J., Collier Cameron, A., Harrington, J., et al. 2010, arXiv e-prints, arXiv:1004.0836

[575] Wichmann, R., Krautter, J., Schmitt, J. H. M. M., et al. 1996, A&A, 312, 439

[576] Wichmann, R., Torres, G., Melo, C. H. F., et al. 2000, A&A, 359, 181

[577] Wöhl, H. 1971, Sol. Phys., 16, 362

[578] Woitke, P., Helling, C., Hunter, G. H., et al. 2018, A&A, 614, A1

[579] Wolk, S. J., Pillitteri, I., Kashyap, V., et al. 2011, in Astronomical Society of the Pacific Conference Series, Vol. 448, 16th Cambridge Workshop on Cool Stars, Stellar Systems, and the Sun, ed. C. Johns-Krull, M. K. Browning, & A. A. West, 1317

[580] Wood, B. E., Müller, H.-R., Redfield, S., et al. 2021, ApJ, 915, 37

[581] Wood, M. L., Mann, A. W., Barber, M. G., et al. 2023, AJ, 165, 85

[582] Woodgate, B. E., Robinson, R. D., Carpenter, K. G., Maran, S. P., & Shore, S. N. 1992, ApJ, 397, L95

[583] Wright, J. T., Veras, D., Ford, E. B., et al. 2011, ApJ, 730, 93

[584] Wu, Y., Xiang, M., Zhao, G., et al. 2019, Monthly Notices of the RAS, 484, 5315

[585] Wyttenbach, A., Ehrenreich, D., Lovis, C., Udry, S., & Pepe, F. 2015, A&A, 577, A62

[586] Yang, H., & Liu, J. 2019, The Astrophysical Journals, 241, 29

[587] Youngblood, A., France, K., Loyd, R. O. P., et al. 2016, ApJ, 824, 101

[588] —. 2017, ApJ, 843, 31

[589] Yurchenko, S. N., Amundsen, D. S., Tennyson, J., & Waldmann, I. P. 2017, A&A, 605, A95

[590] Yurchenko, S. N., & Tennyson, J. 2014, MNRAS, 440, 1649

[591] Zellem, R. T., Swain, M. R., Roudier, G., et al. 2017, ApJ, 844, 27

[592] Zeng, L., Jacobsen, S. B., Sasselov, D. D., et al. 2019, Proceedings of the National Academy of Science, 116, 9723

[593] Zeng, Z., Qiu, J., Cao, W., & Judge, P. G. 2014, ApJ, 793, 87

[594] Zhang, M., Knutson, H. A., Dai, F., et al. 2023, AJ, 165, 62

[595] Zhang, M., Knutson, H. A., Wang, L., Dai, F., & Barragán, O. 2022, AJ, 163, 67

[596] Zhang, X. 2020, Research in Astronomy and Astrophysics, 20, 099

[597] Zhang, Y., Liu, J., & Zhang, H. 2008, Sol. Phys., 247, 39

[598] Zhou, G., Winn, J. N., Newton, E. R., et al. 2020, ApJ, 892, L21

[599] Zicher, N., Barragán, O., Klein, B., et al. 2022, MNRAS, 512, 3060

[600] Zuckerman, B. 2019, ApJ, 870, 27

[601] Zuckerman, B., Bessell, M. S., Song, I., & Kim, S. 2006, ApJ, 649, L115

[602] Zuckerman, B., Song, I., & Bessell, M. S. 2004, ApJ, 613, L65